ATB
Agrartechnik Bornim

Control Applications in Post-Harvest and Processing Technology (CAPPT 2006)

4th IFAC / CIGR Workshop
26th to 29th of March 2006

Bornimer Agrartechnische Berichte
Heft 55

Potsdam-Bornim 2006

Herausgeber/Published by

Leibniz-Institut für Agrartechnik
Potsdam-Bornim e. V. (ATB)
Max-Eyth-Allee 100
14469 Potsdam
☏ 0331 5699-0
Fax 0331 5699-849
E-Mail atb@atb-potsdam.de
Internet www.atb-potsdam.de

July 2006

Redaktion/Editors

Dr. Klaus Gottschalk

Typografische Gestaltung/Layout:

Caroline Eichmann und Andrea Gabbert

Herausgegeben vom Leibniz-Institut für Agrartechnik Potsdam-Bornim e.V. (ATB) mit Förderung des Bundesministeriums für Ernährung, Landwirtschaft und Verbraucherschutz und des Ministeriums für Ländliche Entwicklung, Umwelt und Verbraucherschutz des Landes Brandenburg.

Für den Inhalt der Beiträge zeichnen die Autoren verantwortlich.

Published by the Leibniz-Institute for Agricultural Engineering Potsdam-Bornim e. V. (ATB) with the support of the Federal Ministry of Consumer Protection, Food and Agriculture as well as of the Ministry of Agriculture, Environment Conservation and Regional Policy of the State Brandenburg.

Contents do not necessarily reflect the publisher or editors views in this area.

ISSN 0947-7314

Inhaltsverzeichnis
Table of contents

Seite
page

Objectives of the Workshop **5**
K. Gottschalk

Multiscale Modelling of Gas Transport During Controlled Atmosphere Storage of Fruit **7**
B. M. Nicolaï, N.T. Anh, Q.T. Ho, H.K. Mebatsion, F. Mendoza, P. Verboven, B. Verlinden and M. Wevers

Artificial Intelligence as a Tool for Modelling of Post-Harvest Processes **18**
I. Farkas

Weather Generator a Tool for Supporting Agricultural Modelling **39**
L. Kuchar

Impact of Weather Forecast Uncertainty in Optimal Climate Control of Storehouses **46**
T.G. Doeswijk, K.J. Keesman and G. van Straten

Optimal Control of a Finite-Capacity Fresh-Food Distribution Network **58**
F. Dabbene P. Gay and N. Sacco

Robust Control of Thermal Treatments in Can Industry **72**
A. Baños, P. García and L. Checa

A Monitoring and Distributed Control System for Wine Fermentation Via Ethernet/Ip **84**
M. Gil-Martínez, R. Martín and C. Elvira

Nondestructive Quality Assessment of Pickling Cucumbers Using Visible and Near Infrared Spectroscopy **97**
I. Kavdir, R. Lu, D. Ariana and M. Ngouajio

Optimal Climate Control to Anticipate Future Weather and Energy Tariffs **109**
L. Lukasse, A.-J. van der Voort and J. de Kramer-Cuppen

Measuring Possibilities of Low Range Air Speed in Dryers and Storehouses **123**
I. Seres, L. Kocsis, A. Wójcicki, K. Gottschalk and I. Farkas

A Hybrid Model for Coupled Transport Processes Through Porous Media **136**
Cs. Mészáros, Á. Bálint, I. Kirschner, K. Gottschalk and I. Farkas

Bruise Detection on Apples Using Hyperspectral Imaging System 150
J. Xing and J. De Baerdemaeker

Phenolics and Antioxidant Activity of Wines During the Winemaking Process 161
J. Lachman and M. Šulc

Impact of Pulsed Electric Field Treatment on Polyphenolic Content of Grapes 169
A. Balasa, S. Toepfl and D. Knorr

Evaluation of Modified Phototransistor as Radiation Sensor 175
A. Wójcicki and I. Farkas

Determination of Optimum Conditions for Half Fruit Drying Kinetics of Tomato 181
M. A. Hossain and K. Gottschalk

A Simulation to Design Solar Dryer with Controlled Drying Air Conditions 198
B. M. A. Amer and K. Gottschalk

Separation of Potato, Stones and Clods in the Air Flow 215
J. Fér and V. Mayer

A New Method to Model a 3D Shape of Biomaterials for Using in Post-Harvest Modelling 223
J. Kafashan, B.Tijskens, D. Moshou,
C. Bravo, J. De Baerdemaeker and H. Ramon

Crop Conceptual Model for Predicting Productivity of Bread Wheat in Semi-Arid Kenya 230
P. K. Kimurto, K. Gottschalk, J. B. O. Ogola, M. G. Kinyua, J. K. Macharia and W. B. Herppich

Mathematical Model of Mixed-Flow Grain Drying, Experimental Validation and Concept of a Model-Based Bontrol 245
J. Mellmann, I.-G. Richter and W. Maltry

Objectives of the Workshop

The workshop continues the tradition of this specific meeting within the IFAC activities inaugurated in 1995 in Oostende, Belgium and lately organized in 2001 by our colleagues in Tokyo.

The Workshop gives all visitors the opportunity to present their scientific works and to inform about the state of the art in the application of control methods in storage and processes of agricultural and horticultural products. That is also a good possibility to join a productive and interesting forum for discussion and derive new ideas in the field of control applications in Post-Harvest technology.

Main Topics of this Workshop

- Measurement and modelling of crop or product responses for quality enhancement during storage or processing
- Identification of control structures based on product responses - intelligent, crop based decision criteria
- Effect of product variability on control strategy
- Compartments and instruments for controls in processing technology
- Man-machine interaction in post harvest technology
- Economic and management evaluation of advanced control systems in post-harvest
- Social effects of automatic control in storage and processing
- Optimal control; intelligent control

Programme Committee

Gerrit van Straten (Chair)	NL
István Farkas (Vice-Chair)	HU
Josse de Baerdemaker (Vice-Chair)	BE
Nick Sigrimis (Vice-Chair)	GR
Haruhiko Murase (Vice-Chair)	J
Seiichi Oshita	J
Hans-Jürgen Tantau	D
Yasushi Hashimoto	J
Kiyohiko Toyoda	J
Hans Werner Griepentrog	DK
Bernd Herold	D
Klaus Gottschalk (Editor)	D

Sponsored by

IFAC	International Federation of Automatic Control
CIGR	Commission Internationale du Génie Rural (International Commission of Agricultural Engineering)
VDI / VDE-GMA	Verein der Ingenieure / Verband der Elektrotechnik Elektronik Informationstechnik e.V. - VDI / VDE-Gesellschaft Mess- und Automatisierungstechnik
MEG	Max-Eyth-Gesellschaft Agrartechnik im VDI

Klaus Gottschalk

Multiscale Modelling of Gas Transport During Controlled Atmosphere Storage of Fruit

B.M. Nicolaï[1], N.T. Anh, Q.T. Ho[1], H. K. Mebatsion[1], F. Mendoza[1], P. Verboven[1], B. Verlinden[1] and M. Wevers[2]

[1] Flanders Centre of Postharvest Technology / BIOSYST – MeBioS, Catholic University of Leuven, de Croylaan 42, B-3001 Leuven, Belgium
E-Mail: bart.nicolai@biw.kuleuven.be

[2] Department of Metallurgy and Materials Engineering (MTM), Catholic University of Leuven, Kasteelpark Arenberg 44, B-3001 Leuven, Belgium

Abstract: *The success of controlled atmosphere storage of fruit critically depends on the gas composition of the storage atmosphere. Gas transport models can be used advantageously to evaluate the effect of gas composition on product quality and to optimise and control the storage process. In this paper we will discuss gas and moisture transport models of increasing complexity. We will focus on recent advances in multiscale transport models. Such models are basically a hierarchy of models which describe the transport phenomena at different spatial scales in such a way that the submodels are interconnected. We will pay particular attention to methods to measure product topology and material properties at the micro- and nanoscale. Copyright © 2006 IFAC*

Keywords: *distributed models, transport properties, gas, fruit, controlled atmosphere, storage, multiscale*

1 Introduction

Apples and pears are perishable commodities whose storage life depends on, amongst other factors, the respiratory activity of the fruit. Commercial storage is essentially based on reducing the respiration as much as possible without causing adverse effects such as off-flavours and storage disorders due to fermentation processes. In *controlled atmosphere storage,* the fruit are hereto stored at a low temperature (typically around 0°C) in combination with a reduced O_2 and increased CO_2 partial pressure (so-called “Controlled Atmosphere (CA) storage”). In this way the storage life of some apple and pear cultivars can be extended to up to one year.

For a proper operation of the controlled atmosphere cool rooms a more profound insight in the metabolic reactions and transport processes inside the stored fruit is mandatory. A mechanistic modelling approach seems most appropriate, as it provides more insight into the physiological phenomena related to storage disorders. In this paper we will present an overview of recent advances in modelling of gas and moisture transport processes in fruit, with particular attention to multiscale models.

2 Controlled Atmosphere Storage

In controlled atmosphere storage the O_2 and CO_2 concentration are maintained at a well-defined set point level. This set point is often close to the anaerobic compensation point, the O_2 partial pressure at which the CO_2 production rate is at its minimum. The optimal gas composition is critical, as too low an O_2 partial pressure in combination with too high a CO_2 partial pressure induces a fermentative metabolism in the fruit (BEAUDRY 1999, YEARSLEY *et al.* 1996). This causes off-flavours (e.g., ethanol) and storage disorders (e.g., core breakdown in pear). For this reason, the O_2 and CO_2 partial pressure in commercial cool stores is kept at a safe and steady value. The optimal storage temperature depends on the produce and is in general the lowest temperature preventing the produce from chilling injury or freezing damage.

The O_2 can be reduced by respiration as such, and by injecting N_2 gas produced from ordinary air by removing ("scrubbing") the O_2 and CO_2. Storage under controlled atmosphere is widely used to store all kinds of horticultural produce. In ultra low oxygen (ULO) the O_2 concentration is below 2%. Some optimal gas compositions for long term storage of fruit and vegetables are summarised in **Table 1**.

Table 1: Optimal gas compositions for long term storage of apple and pear cultivars (KADER & SEAVER 2001)

Cultivar	T (°C)	O_2 (%)	CO_2 (%)
Apple			
Braeburn	0.5	3	<1
Cox's Orange Pippin	4	1.3	0.7
Golden Delicious	0.5	2.5	1
Red Delicious	0 to 0.5	2.5	4.5
Jonagold	1	1	4.5
Pear			
Conference	-1	2.5	0.7
Packham's Triumph	-0.5	1.5	2.5
Williams Bon Chretien	0 to -0.5	1	0

Modified atmosphere packaging is a technique in which the produce is kept fresh for a longer period, using a gas permeable foil allowing, to some extent, gas exchange between the internal micro atmosphere in the package and the external atmosphere. The micro atmosphere is usually generated through respiration of the produce, but often a gas mixture is injected into the package to obtain a faster equilibrium.

3 Gas Transport

If the local gas composition inside the fruit is too extreme, storage disorders may occur. An example of such disorders is core breakdown. This storage disorder is characterised by the development of brown tissue which will further develop into cavities so that the fruit can no longer be commercialised. The harvest time, the O_2 and CO_2 concentration in the cool room, the storage temperature, the size of the pear and their interactions are the most critical factors which affect the development of the disorder. The antioxidant content also affects the susceptibility of the pear to core breakdown. The exact mechanism of the disorder is not well understood, but it is believed to be caused by an imbalance in the energy metabolism in the cells due to too low an O_2 or too high a CO_2 concentration. This leads to membrane damage and decompartmentalisation. Phenolic compounds are then enzymatically oxidised to brown coloured compounds. Eventually, water diffuses from the centre towards the boundary of the pear and a cavity is created.

As limited gas transport inside the fruit is probably the prime cause of disorders such as core breakdown, several attempts have been made to model this process. Models to describe gas exchange of fruit and vegetables are usually based on enzyme kinetics according to Michaëlis-Menten:

$$\frac{d}{dt}[O_2] = -\frac{m}{V} V_{O_2,\max} \frac{[O_2]}{K_m + [O_2]} \qquad (1)$$

where m is the mass of the fruit, V the volume of the enclosure in which the fruit is kept, $V_{O_2,\max}$ the maximum oxygen consumption rate, and K_m the Michaëlis-Menten constant or the concentration at which its activity is half of $V_{O_2,\max}$.

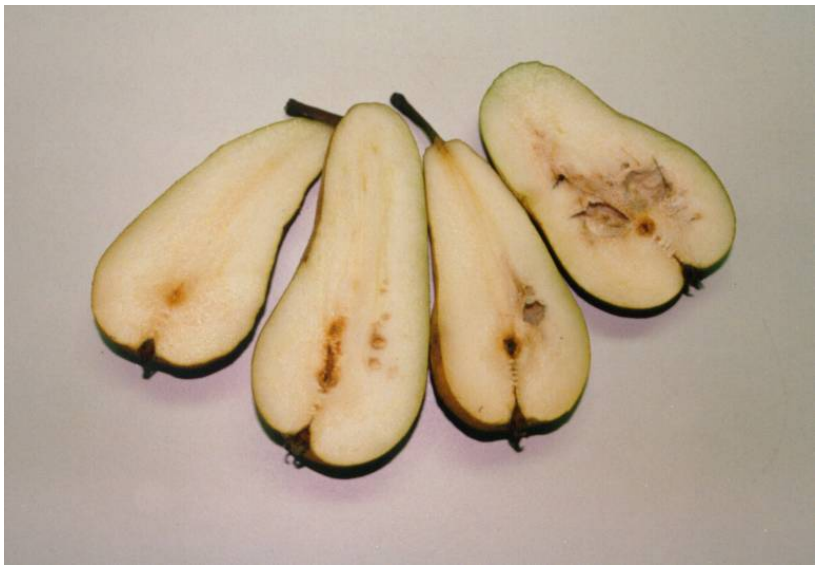

Figure 1: Core breakdown in Conference pear. Brown spots (left) gradually evolve into cavities (right)

Equation (1) disregards transport phenomena in or at the surface of the fruit. However, the critical partial pressures beyond which undesireable phenomena develop are often much higher then one would expect from biochemistry. For example, cytochrome oxidase has a K_m which is orders of magnitude below the typical K_m of intact fruit (1-3 kPa). This suggests an oxygen gradient inside the fruit in such a way that the local oxygen partial pressure in the center of the fruit is much lower than in the storage atmosphere. This observation inspired MANNAPPERUMA *et al.* (1991) and later on LAMMERTYN *et al.* (2003a) to develop a gas exchange model based on chemical reaction kinetics. The model is essentially a system of two coupled diffusion equations, one for O_2 and one for CO_2 which are coupled through the respiration kinetics

$$\frac{\partial}{\partial t}[O_2] = D_{O_2}\nabla^2[O_2] - V_{O_2} \tag{2}$$

$$\frac{\partial}{\partial t}[CO_2] = D_{CO_2}\nabla^2[CO_2] + RQ_{cell} \quad V_{O_2} + \frac{V_{m,f,CO_2,cell}}{\left(1+\frac{[O_2]}{K_{m,f,O_2,cell}}\right)} \tag{3}$$

$$V_{O_2} = \frac{V_{m,O_2,cell} \quad [O_2]}{\left(K_{m,O_2,cell}+[O_2]\right)\left(1+\frac{[CO_2]}{K_{mn,CO_2,cell}}\right)} \tag{4}$$

with D_{O2}, the gas diffusivity of O_2 in pear tissue; V_{O2}, the O_2 consumption rate, ∇^2, the Laplace operator; $V_{m,O2,cell}$, the maximum cellular aerobic O_2 consumption rate; $K_{m,O2,cell}$, the tissue Michaelis-Menten constant and $K_{mn,CO2,cell}$, the tissue Michaelis-Menten constant for non-competitive inhibition of CO_2 on O_2 consumption; D_{CO2}, the CO_2 diffusivity in pear tissue; V_{CO2}, the CO_2 production, RQ_{cell}, the tissue respiration quotient; $V_{m,f,CO2,cell}$, the maximal tissue fermentative CO_2 production rate; and $K_{m,f,O2,cell}$, the inhibition constant of O_2 on the tissue fermentative CO_2 production. Appropriate boundary conditions need to be supplied as well (LAMMERTYN *et al.* 2003a and 2003b).

The couple (2)-(3) of nonlinear partial differential equations cannot be solved analytically, and numerical solution is required. Hereto the equations are discretised over a mesh of discretisation points – so-called nodes – to yield a large system of ODE couples (one

equation for O_2 and one for CO_2) which describe the evolution of O_2 and CO_2 in these nodes. The ODE couple in a particular node is also coupled with that in the neighbouring nodes, and, as a consequence, all ODEs must be integrated in the time domain simultaneously. Several discretisation methods exist, including the finite difference, finite element and finite volume method, and the reader is referred to the literature for details about them (e.g., NICOLAÏ *et al.* 2001). It is important to note that commercial software (e.g., Femlab, Comsol AB, Götebörg, Sweden) exists which simplifies the implementation of numerical discretisation considerably and brings it into reach of a postharvest engineer who only needs to have some affinity with engineering mathematics.

Based on this model LAMMERTYN *et al.* (2003a, 2003b) computed three-dimensional O_2 and CO_2 profiles in Conference pears for various storage conditions. They observed that the predicted contours of the simulated CO_2 and O_2 profiles corresponded very well with the contours of core breakdown – a CA related disorder characterised by brown areas and eventually tissue breakdown and cavities – as observed by means of Magnetic Resonance Imaging (MRI) and X-ray Computer Tomography (CT) scans of the pears. The authors also carried out a simulation study to evaluate the effect of cooling management. They were able to show that delaying the application of controlled atmosphere conditions until three weeks after the beginning of the cooling period was beneficial to reduce the incidence of core breakdown (LAMMERTYN *et al.* 2003b). HO *et al.* (2006) extended the model of LAMMERTYN *et al.* (2003a and 2003b) with a permeation term and an equation for N_2 transport. A very good correspondence between measured and predicted gas partial pressures was obtained. Typical contours of O_2 and CO_2 are shown in **Figure 2**.

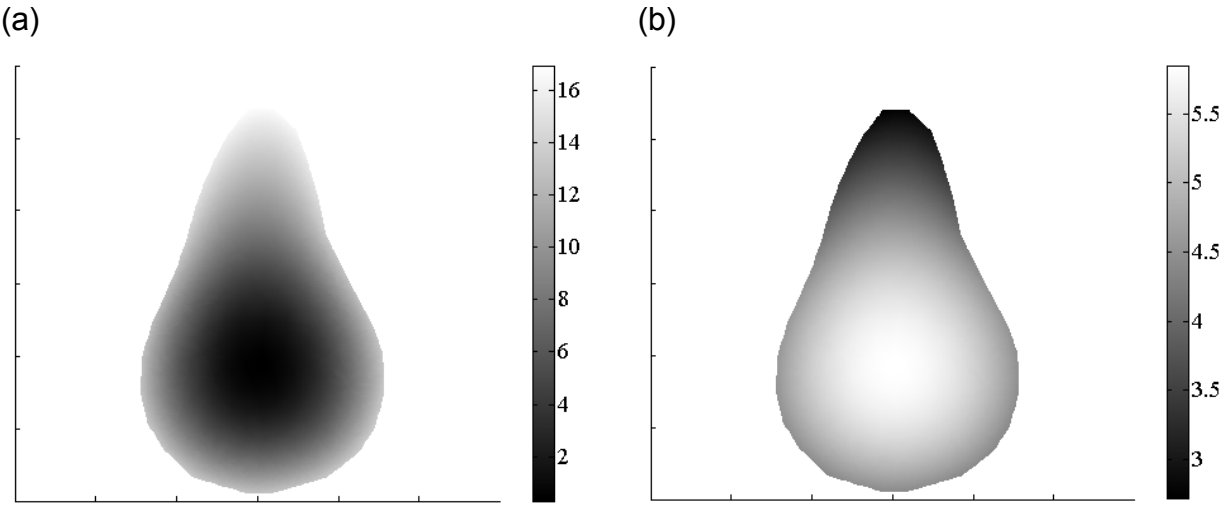

Figure 2: Contour plots of O_2 (a) and CO_2 (b) partial pressure in Conference pear stored at 20°C, 20 kPa O_2, 0 kPa CO_2 and 80 kPa N_2

Many problems remain, though. Diffusion coefficients have been shown to vary considerably inside the fruit tissue (SCHOTSMANS *et al.* 2003, HO *et al.* 2005). This variation is certainly linked to the histology of the tissue, but this relationship is not well understood.

Further, it would be beneficial to be able to evaluate the effect of the local gas conditions on metabolic fluxes through metabolic network models. Such models include much more details about the actual biochemistry than the currently used Michaëlis-Menten models and would be useful to understand the biochemical causes of disorders such as core breakdown. This disorder is associated with membrane degradation processes which are believed to be related to impaired metabolic fluxes (VELTMAN *et al.* 1999). Finally, the model of LAMMERTYN *et al.* (2003a) essentially describes the metabolic gas distribution in the intercellular space – the actual gas concentration inside the cells is most probably lower. This is indicated by the K_m value for respiration which was determined by the authors and which was still larger than typical K_m values for cells and certainly cytochrome oxidase. Multiscale models might be appropriate to study these effects.

4 Moisture Transport

Fruit always looses water during storage. This results in economic (mass) and quality (shrivel) losses. The cuticle which covers the fruit epiderms acts as a natural water impermeable barrier. Epidermal cells are similar to parenchyma cells but are smaller, have a larger aspect ratio and more tightly packed. The bulk of the fruit consists of parenchyma cells which are essentially semipermeable phospholipid membranes filled with cytoplasm and surrounded by a primary cell wall which is typically about 3 μm thick and which consists of cellulose fibrils embedded in a pectin matrix. In between the cells there is a pectin layer called middle lamella which glues the cells together. The most important plant cell organel is the vacuole which is surrounded by a phospholipid membrane and which typically covers almost the entire cell volume. The cytoplasm of neighbouring cells are connected through plasmodesmata - narrow channels that act as intercellular cytoplasmic bridges to facilitate communication and transport of nutrients between plant cells. The plasmatic membrane and also the membranes of all intracellular organels contain proteins – the so-called aquaporins – which serve as additional passive water transport channels. Vascular bundels connect the stem with the calyx. They consist of xylem, responsible for water translocation in the plant, and phloem, responsible for the movement of most of the organic compounds. The conducting cells of the phloem contain cytoplasm and are joined end-to-end, thus forming a low-resistant transport system through the plant. The conducting cells (or vessel members) of the xylem, however, have lost their protoplast and the remaining cell walls form a long vessel. The end walls of individual vessel members are perforated to facilitate water transport under a hydrostatic pressure gradient. The xylem also contains xylem fibers that are long thin dead cells with a strongly lignified cell wall. Because of these transport structures, the cytoplasm of the apple cells form a interconnected spatial region which is called the *symplast*. The cell walls and the intercellular space form another region through which water can be transported and which is called the *apoplast* (NOBEL 1991).

Moisture gradients in fruit (apple, pear) have been modelled by means of Fick's second law of diffusion and subsequently validated by means of MRI (NGUYEN *et al*. 2005). However, fruit shrink when they loose moisture, and the coupled hygromechanical problem is notably difficult to solve. Further, moisture in fruit is not free but entrapped in cells and its behaviour is determined by its thermodynamic state. The latter is affected by osmotic, turgor and capillary effects.

5 Multiscale Modelling

From the preceeding sections it is clear that, unlike traditional engineering materials, fruit tissue has a complex fine structure. Nature has designed cellular tissue in such a way as to facilitate transport of metabolic gases and water. As a consequence, the continuum hypothesis does not hold anymore and a new modelling paradigm is required to describe the mechanics of deformation of vegetative tissue. The availability of such models would lead to increased insight into gas and moisture transport processes in fruit during storage.

A *multiscale model consists of* a hierarchy of models, which describe the mechanical behaviour at different spatial scales in such a way that the submodels are interconnected. It is convenient to distinguish three length scales:

- The *macroscale* addresses the fruit as such (10^{-3} – 10^{-2} m). At this scale the fruit is considered as a continuum which consists of different materials – skin and flesh.
- At the *mesoscale,* the actual topology of the fruit tissue incorporating the topology of the intercellular space and cell arrangement is considered (10^{-5} – 10^{-3} m). This involves the different types of tissue inside the fruit but also microscopic features such a lenticells and cracks in the wax layer which may affect gas and moisture transport and mechanical behaviour.
- The *microscale* is the cellular scale (10^{-6} – 10^{-4} m). Cell features such as the cell wall, the middle lamella and the vacuole are important for both moisture transport as well as mechanical behaviour.

In the multiscale modelling paradigm, numerical experiments are carried out at the smallest scale under consideration to compute apparent parameters, which are then used in a model which operates at a coarser scale. This process is repeated until the largest scale – typically a continuum-type model – is reached. At this scale, the macroscopic response variables of interest – fruit deformation under loading, water loss – are computed using apparent properties derived from the smaller scale model by a mathematical procedure called *homogenisation* (PANASENKO 2005, HASSANI & HINTON 1999). The reverse downscaling procedure is called *localisation* and can be used to investigate how the calculated macroscopic response variables affect microscopic events such as failure of cells. The concept of multiscale modelling is entirely new in postharvest technology and even plant physiology.

The development of such models is, however, complicated because of several reasons. First, the characterisation of the structure at the cellular and subcellular scale is not trivial (SCHNEIDER *et al.* 2002). X-ray computer tomography (CT) has been used to visualise and model the internal pore space of a variety of vegetative materials with a resolution limited to about 10 micrometers (KUROKI *et al.* 2004). As an example, in **Figure 3**. the 3D pore space of apple parenchyma tissue is visualised by means of X-ray microfocus CT. Such models can readily be meshed for finite element analysis of gas or moisture transport.

Measurements of mechanical and transport properties at the microscale level are difficult to perform, and few experimental techniques are available. Turgor pressure measurements can be carried out on individual cells in a tissue using the pressure probe (HÜSKEN *et al.* 1978). However, application of the technique to higher plant tissue consisting of small cells requires high technical skills. Nano-indentation techniques seem promising to determine mechanical properties on cellular scale, but have not been explored on individual fruit cells.

Model validation at meso and microscale is challenging. Experiments with well-defined tissues with known internal turgor pressure have to be carried out to validate the predicted mechanical behaviour. Measurement on tissue level require a sufficiently detailed, three dimensional understanding of tissue structure and deformations, and hence advanced imaging techniques suitable for the testing of biological material in its native hydrated state (HEPWORTH & BRUCE 2000, DONALD *et al.* 2003, ZDUNEK *et al.* 2004).

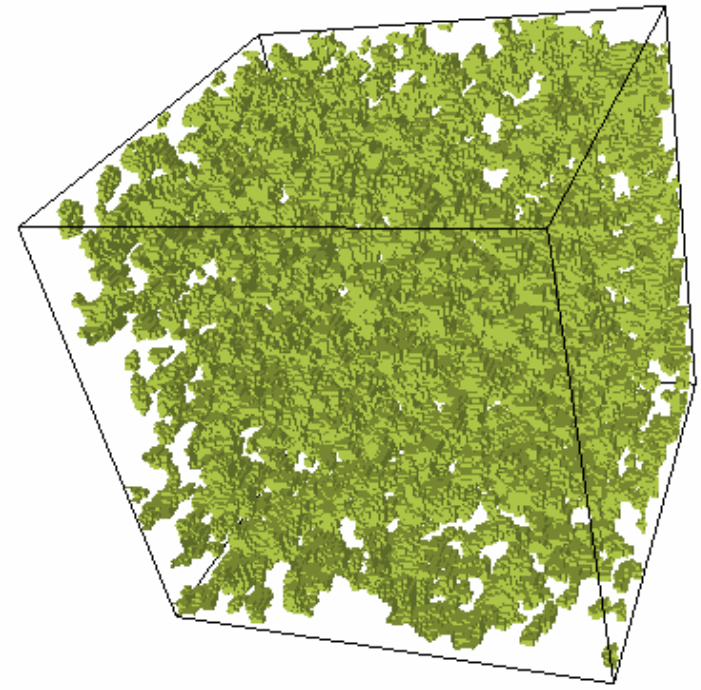

Figure 3: 3D pore-cellular material surface of apple parenchyma tissue (Victor Mendoza, unpublished) obtained by means of X-ray microfocus CT

Multiscale models were first introduced in postharvest engineering by VERAVERBEKE *et al.* (2003a and b) who used a multiscale approach to model moisture loss of apple. They

measured first moisture transport properties of the different materials (cutin, wax, parenchyma tissue) and incorporated them subsequently into a mesoscale continuum model which took into account the different components of the cuticle such as cutin and wax, and epidermal structures such as cracks and lenticels. The mesoscale model was used to estimate apparent diffusion properties of the skin which were then introduced in a macroscopic continuum model. This model was used successfully to understand the differences in moisture loss between Jonagold and Elstar apples which were shown to be related to the presence of cracks in the wax layer of Elstar which did not disappear during storage as was the case with Jonagold.

Current research focusses on gas transport in fruit tissue. As an example, in **Figure 4.** the O_2 concentration in apple parenchyma tissue during a numerical experiment is shown. It is clear that the oxygen concentration in the intercellular space is considerably larger than within the cells. Such information can be used to estimate apparent transport properties which can be inserted in a macroscale continuum model.

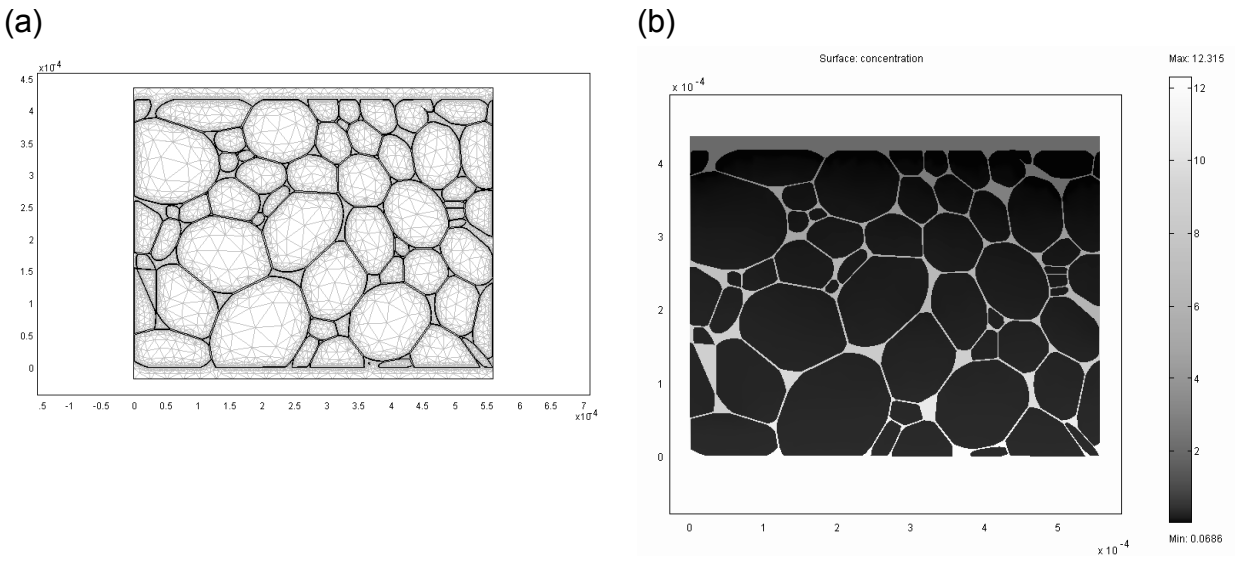

Figure 4: Finite element mesh (a) and simulation (b) of the O_2 concentration in pear parenchyma tissue (Quang Tri Ho, unpublished); concentrations in mol/m^3

6 Conclusions

Optimisation of controlled atmosphere storage requires a profound insight in the gas and moisture transport properties in the fruit during storage. While continuum type transport models in general describe the transport processes well, they involve apparent material properties which need to be obtained experimentally. Also, they do not lead to increased insight. Multiscale modelling addresses the transport processes at different spatial scales and integrates the models which each operate at a specific scale. While such an approach

clearly is advantageous, many problems still have to be solved such as obtaining the tissue topology at smaller scales and measuring the model parameters experimentally.

Acknowledgements

The authors would like to acknowledge the Flanders Fund for Scientific Research (FWO-Vlaanderen) (project G.0200.02) and the K.U.Leuven (projects IDO/00/008 and OT 04/31) for financial support. Author Pieter Verboven is Postdoctoral Fellow with the Flanders Fund for Scientific Research (FWO-Vlaanderen).

References

BEAUDRY R.M. (1999): Effect of O2 and CO2 partial pressure on selected phenomena affecting fruit and vegetable quality. *Postharvest Biology and Technology*. 15: 293-303

BURTON W.G. (1982): *Post-harvest physiology of food crops*. Longman, London and New York

DONALD A.M., BAKER F.S., SMITH A.C., WALDRON K.W. (2003): Fracture of plant tissues and walls as visualized by environmental scanning electron microscopy. *Annals of Botany*, 92: 73-77

HASSANI B., HINTON E. (1999): *Homogenization and Structural Topology Optimization: Theory, Practice, and Software*. Springer Verlag, New York

HEPWORTH D.G., BRUCE D.M. (2000): Measuring the deformation of cells within a piece of compressed potato tuber tissue. *Annals of Botany*. 86: 287-292

HO Q.T., VERLINDEN B.E., VERBOVEN P., VANDEWALLE S., NICOLAÏ B.M. (2006): Gas permeation in pear fruit. *Submitted*

HO Q.T., VERLINDEN B.M., VERBOVEN P., NICOLAÏ B.M. (2005): Measurement of space dependent gas diffusion properties of pear tissue using optical sensors. *Submitted*

HÜSKEN D., STEUDLE E., ZIMMERMAN U. (1978): Pressure probe technique for measuring water relations of cells in higher plants. *Plant Physiology*. 61: 158-163

KADER A., SEAVER D. (2001): Optimal Controlled Atmospheres for Horticultural Perishables. Davis. In: *Postharvest Technology Research and Information Center*, 2001, pp 153

KUROKI S., OSHITA S., SOTOME I., KAWAGOE Y., SEO Y. (2004): *Postharvest Biology and Technology* 33(3): 243-255

LAMMERTYN J., SCHEERLINCK N., JANCSÓK P., VERLINDEN B.E., NICOLAÏ B.M. (2003a): A respiration-diffusion model for 'Conference' pears I: model development and validation. *Postharvest Biology and Technology*. 30: 31-44

LAMMERTYN J., SCHEERLINCK N., JANCSÓK P., VERLINDEN B.E., NICOLAÏ B.M. (2003b): A respiration-diffusion model for 'Conference' pears: II. Simulations and relation to core breakdown. *Postharvest Biology and Technology*. 30: 45-57

MANNAPPERUMA J.D., SINGH R.P., MONTERO M.E. (1991): Simultaneous gas diffusion and chemical reaction in foods stored in modified atmospheres. *Journal of Food Engineering.* 14: 167-183

NGUYEN T.A., DRESSELAERS T., VERBOVEN P., D'HALLEWIN G., CULLEDU N., VAN HECKE P., NICOLAÏ B.M. (2005): Finite element modelling and MRI validation of 3D transient water profiles in pears during postharvest storage. *Journal of the Science of Food and Agriculture*. Accepted

NICOLAÏ B.M., VERBOVEN P., SCHEERLINCK N. (2001): The modelling of heat and mass transfer. In: *Food Process Modelling* (TIJSKENS L.M.M., HERTOG M.L.A.T.M., NICOLAÏ B.M. (Eds.)). Woodhead Publishing Limited and CRC Press LLC, Cambridge, UK and Boca Raton, FL, USA, pp. 60-86

NOBEL P.S. (1991): *Physicochemical and Environmental Plant Physiology*. Academic Press Inc. San Diego.

PANASENKO G. (2005): *Multi-scale Modelling for Structures and Composites*. Springer

SCHOTSMANS W., VERLINDEN B.E., LAMMERTYN J., NICOLAÏ B.M. (2003): The relationship between gas transport properties in apple and the histological properties of the apple tissue. *Journal of the Science of Food and Agriculture.* 84: 1131-1140

VELTMAN R.H., SANDERS M.G., PERSIJN S.T., PEPPELENBOS H.W., OOSTERHAVEN J. (1999): Decreased ascorbic acid levels and brown core development in pears (Pyrus communis cv. communis). *Physiologia Plantarum*. 107(1): 39-45

VERAVERBEKE E.A., VERBOVEN P., VAN OOSTVELDT P., NICOLAÏ B.M. (2003a): Prediction of moisture loss across the cuticle of apple (Malus sylvestris subsp. mitis (Wallr.)) during storage Part 1. Model development and determination of diffusion coefficients. *Postharvest Biology and Technology*. 30: 75-88

VERAVERBEKE E.A., VERBOVEN P., VAN OOSTVELDT P., NICOLAÏ B.M. (2003b): Prediction of moisture loss across the cuticle of apple (Malus sylvestris subsp. mitis (Wallr.)) during storage Part 2. Model validation and sensitivity analysis. *Postharvest Biology and Technology*. 30: 89-97

YEARSLEY C.W., BANKS N.H., GANESH S., CLELAND D.J. (1996): Determination of lower oxygen limits for apple fruit. *Postharvest Biology and Technology*. 8: 95-109

ZDUNEK A., UMEDA M., KONSTANKIEWICZ K. (2004): Method of parenchyma cells parametrisation using fluorescence images obtained by confocal scanning laser microscope. *Electronic Journal of Polish Agricultural Universities*. Agricultural Engineering, Vol. 7(1)

Artificial Intelligence as a Tool for Modelling of Post-Harvest Processes

I. Farkas
Department of Physics and Process Control, Szent István University, Gödöllő, Páter K. u. 1., H-2103 Hungary, E-Mail: Farkas.Istvan@gek.szie.hu

Abstract: *This paper deals with the opportunities of the use of artificial intelligence methods for the modelling of post-harvest processes. The main emphasize is given to the use of artificial neural network (NN) modelling especially for grain drying as a widely applied dehydration technology. The aim of the study was to set up a neural network in order to determine the relationship between the moisture distribution in the material bed to be dried and the physical parameters of the drying air temperature, humidity and air flow rate. An overview is given on the selection aspects of neural network structure and specifically to the influencing parameters as sampling time, randomised training, different training algorithms, number of hidden neurones, number of linked data series and type of validation data. As a conclusion it has been stated that a properly selected structure of neural network model can be used to determine the moisture distribution in a fixed-bed grain dryer. It can also be stated that besides other factors the selection of training and validation input data for NN model has a strong influence on the applicability. Copyright© 2006 IFAC*

Keywords: *drying, grain, neural network, training, validation, measurement*

1 Introduction

Concerning the post-harvest processes beside the energy consumption impacts the quality issues remain the most determining factor.

The main problem in the grain drying process is to determine the moisture content in the material bed. Overdrying requires excessive energy and even can damage the quality of the dried material, especially in case of seed. On the other hand the grain will be vulnerable to mildew if the moisture content remains high. There is an option to determine the moisture content in the drying bed by measurement but the accuracy of this approach is probably not satisfactory. Weather conditions and dust have a great effect on the accuracy, as well. Another way to determine the moisture distribution is to calculate the moisture content based on drying air parameters using physically based or black-box models. Physically based models give a moderately good result in most cases but it normally takes a great effort to identify their parameters and also to solve the model itself. Derivation of the classical black-box models seems to be an uncomplicated approach. However, the application of such models is mainly limited to process control.

The artificial neural network is a well-known tool for solving complex problems and it can give reasonable solutions even in extreme cases or in the event of technological faults (LIN & LEE, 1995). HUANG & MUJUMDAR (1993) created a neural network in order to predict the performance of an industrial paper dryer. The neural network model by JAY & OLIVER (1996) was used for predictive control. TRELEA *et al.* (1997) successfully used explicit time and recurrent neural networks for modelling the moisture content of thin-layer (5 cm) corn during the drying process and for wet-milling quality at constant air flow rate and absolute humidity and variable temperature. THYAGARAJAN *et al.* (1997) modelled an air heater plant for a dryer using a neural network. SREEKANTH *et al.* (1998) predicted psychometric parameters using various neural network models. KAMINSKI *et al.* (1998) used a neural network for data smoothing and for modelling material moisture content and temperature. The literature cited clearly encourages further study of the application of artificial neural networks to modelling of post-harvest and within that the drying process.

This paper describes an application to grain drying in which a particular neural network is used for studying the influence of sampling time, randomised training, different training algorithms, number of hidden neurones, number of linked data series and type of validation data. The structure of the NN was selected to include all the inputs and outputs of the drying system.

The work reported in this paper deals with the use of the neural network for modelling purposes, making comparison with the physically based thin-layer grain drying model. Given a well-fitting the model it becomes possible to extend it to different dryer arrangements. The ultimate target is to use the neural network for control of the entire drying process.

2 Modelling Approaches

As a classical way of modelling the physically-based models (PBM) are normally used for determine the performance evaluation of drying process. However the PHBs makes some difficulties in setting up the most appropriate equations, to determine the accurate values of their parameters and to find the most efficient methods for the solution. At the same time we are discussing the option of the use of NN for modelling purposes along with their uncertainties and difficulties in determination their optimal topology and parameters for the given problem, e.g. post-harvest technology this time. Sometimes, in order to provide input data for training the neural network a well identified physically based model are considered to use instead of full-scale or laboratory measurements. Furthermore we are discussing the above mentioned modelling approaches in the above mentioned context.

2.1 Physically-based model

The scheme of a fixed-bed grain dryer along with its space discretization is shown in **Figure 1.**

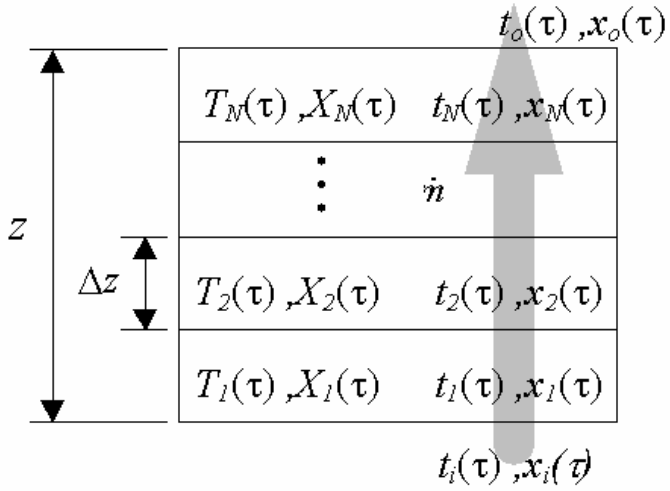

Figure 1: Schematic diagram of a fixed-bed grain dryer

The temperatures (*t*-air, *T*-material) and humidities (*x*-air, *X*-material) were calculated for each layer. The height of one layer is Δz. The air flow rate $\dot{m}$ was kept constant neglecting the leakage in the system. The physically based model of the dryer was set up based on O'CALLAGHAN (1971) and SUN *et al.* (1995) papers. The model input was the air flow rate, the inlet air temperature and humidity while the output were the moisture contents in the bottom, the middle and the top layers and the outlet air temperature and humidity for the whole drying period as a function of time.

The material to be dried was barley. The appropriate governing equations and the relevant parameters are described in the following.

Drying rate equation

$$-\frac{\partial X}{\partial \tau} = k(X - X_e) \qquad (1)$$

$$k = 139.3\, e^{\frac{-4426}{t+273}} \qquad (2)$$

$$X_e = 7040\frac{\sqrt{x}}{(1.8t+32)^2} + 0.06015 \quad (3)$$

Mass balance equation

$$A\partial z\rho\frac{\partial X}{\partial\tau} + A\dot{m}\partial\tau\left(x(z+\partial z) - x(z)\right) = 0 \quad (4)$$

Heat balance equation

$$A\dot{m}\partial\tau\left(h(z+\partial z) - h(z)\right) + A\partial z\rho\left((c+c_w X)\frac{\partial T}{\partial\tau} + \frac{\partial X}{\partial\tau}c_w T\right) = 0 \quad (5)$$

$$h = 1005t + x\left(1820t + 2501\,10^3\right) \quad (6)$$

Heat transfer equation

$$k_{vol}A\partial z\partial\tau\left(t-T\right) = A\partial z\rho\left((c+c_w X)\frac{\partial T}{\partial\tau} - \frac{\partial X}{\partial\tau}(h_v - c_w T)\right) \quad (7)$$

$$k_{vol} = 71441.67\left(\frac{0.6\dot{m}(t+273)}{1000}\right)^{0.6011} \quad (8)$$

$$h_v = 1820t + L_v \quad (9)$$

Using the abovementioned equations a layer by layer calculation was applied. During the calculation the first question was to decide about the appropriate size of space discretization, i.e. the number of layers. In order to determine the most appropriate thick-

ness of the grain layer the number of the layers in the calculations was varied in a way to provide the possibility of comparison in the middle layers, i.e.:

$$N_k = 3^k \ (k = 0, 1, \ldots) \qquad (10)$$

The drying time was set-up 300 minutes, the integral step was selected as 1 second. The inputs were generated accordingly and stored together with the outputs every second for later training and validation of NN.

The physically based model was implemented in C code and for the simulation study MATLAB software was used to generate input data for training.

Simulation trials with different number of layers were performed until the differences between the last two trials in temperature and moisture content of the middle layer were less than 1^{o}C and 1%, respectively. The moisture content comparison result can be seen in **Figure 2**. It can be seen that the difference between 9 and 27 layers are practically small.

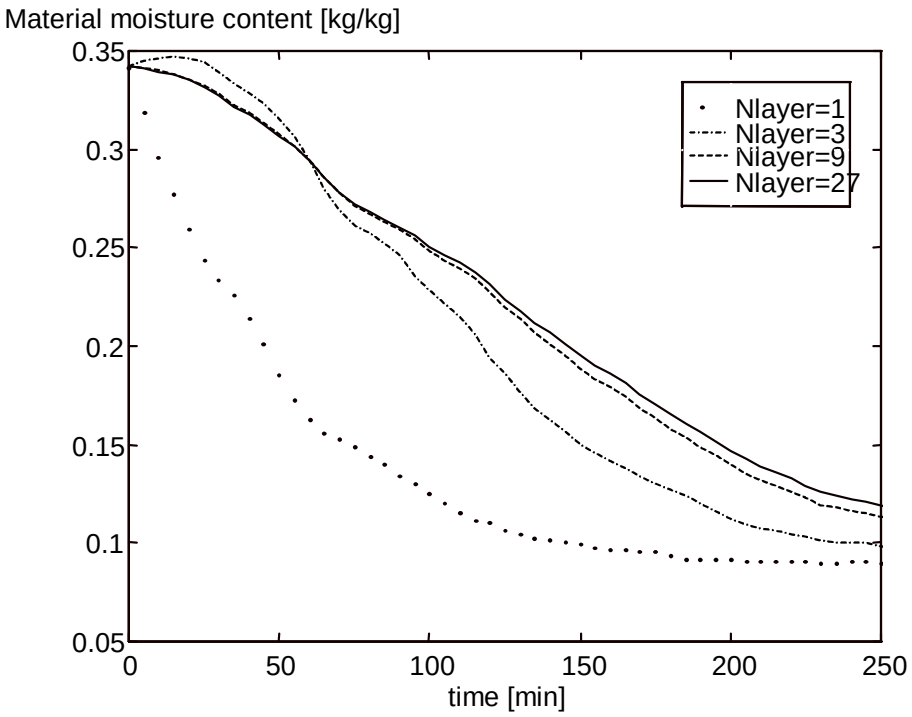

Figure 2: Temperature profile of the middle of the drying bed using different number of layer

In **Figure 3** a comparison of moisture contents in the bottom, the middle and the top layers of the drying bed is shown using 9 and 27 layers in the simulation.

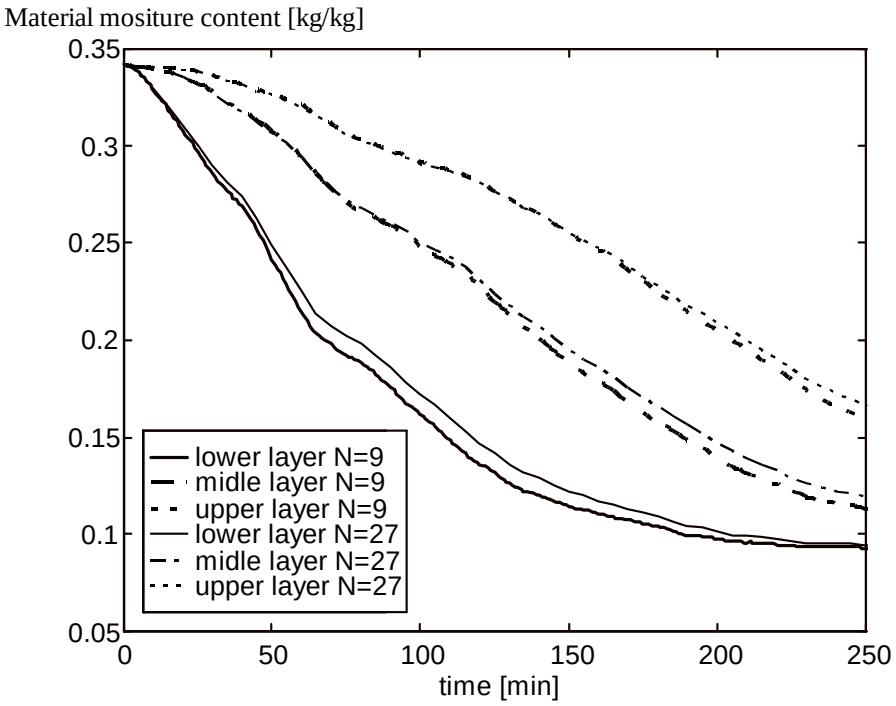

Figure 3: Temperature distribution in the drying bed using 9 and 27 layers

Maximum differences in moisture contents between the two simulations in the bottom, middle and the top layers were, 0.0063, 0.0076 and 0.011, respectively. On that basis it was desired to use 9 layers as the space discretization in further calculations. Since the height of the drying bed (*Z*) was 0.305 m, so the corresponding thickness of one layer was approximately 3.4 cm.

2.2 Neural network model

Several NN topologies were considered for the use of modelling the drying process as it was suggested by FARKAS *et al.* (2000a). The choice of a topology depends on careful selection of the input system variables and the controlled output variables e.g. moisture contents in the different layers of the material bed. Each case the neural network is three layer feed-forward structures with five hidden neurones. The layout of the networks applied can be seen on **Figures 4-8**.

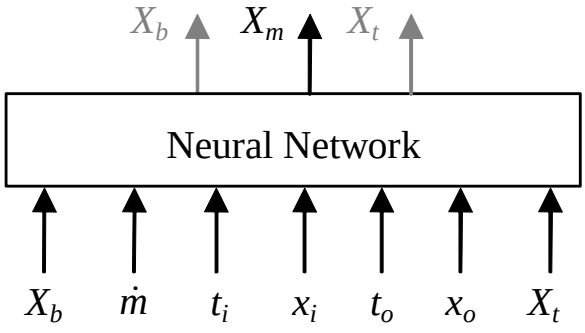

Figure 4: NN1-Middle layer estimator

Estimates the moisture content in the middle layer using air parameters and moisture content in the bottom and in the top layer.

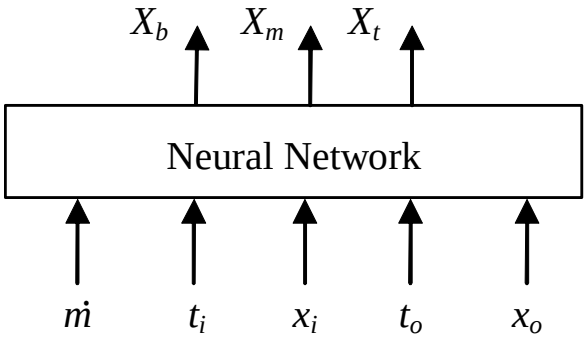

Figure 5: NN2-Moisture content calculator

Calculating moisture content in the bottom, middle and upper layer using air parameters.

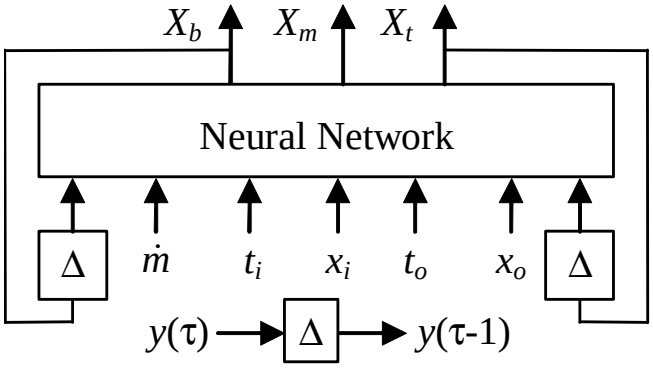

Figure 6: NN3-Modelling moisture content

Modelling moisture content in the bottom, middle and upper layer using air parameters and the delayed value of calculated moisture contents.

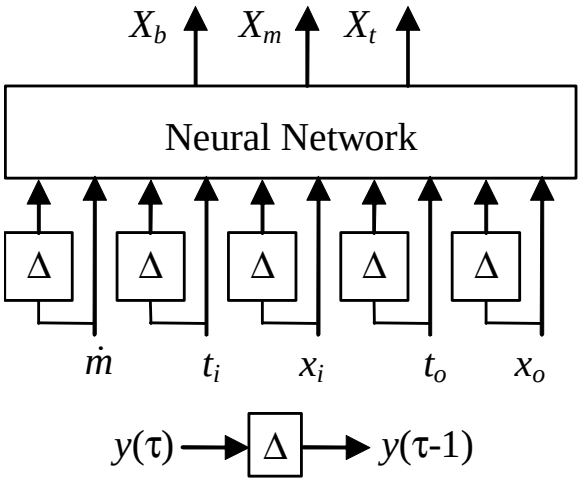

Figure 7: NN4-Modelling moisture content

Modelling moisture content in the bottom, middle and upper layer using air parameters and their delayed values.

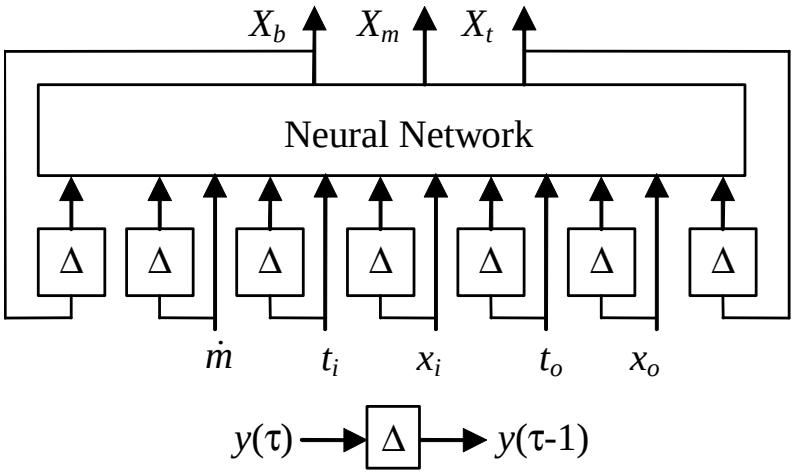

Figure 8: NN5-Modelling moisture content

Modelling moisture content in the bottom, middle and upper layer using the actual and the shifted air parameters and the delayed value of calculated moisture contents.

3 Training the Neutral Networks

Input data used for training the neural network of different structure was the same. The drying air temperature, air flow and absolute humidity were changed randomly to train higher order dynamics, as well. The applied input data along time are shown on **Figure 9**.

The outlet air temperature and absolute humidity in the layers were calculated based on physically based model described before. The data was transformed into [0,1] interval before training the neural network. The number of input data record was 250. In each training loop each data record was trained five times with back-propagation algorithm. One training step means to calculate the error between the network output and the desired output and to modify the weight of the neural network. The description of the algorithm can be found in the book of C.-T. LIN & C.S.G LEE (1995).

During the training process all the introduced neural network structures have different training speed e.g. the number of calculation loops in order to reach the required accuracy, as it can be seen on **Figure 10**. The cost function expresses the stop condition of the training.

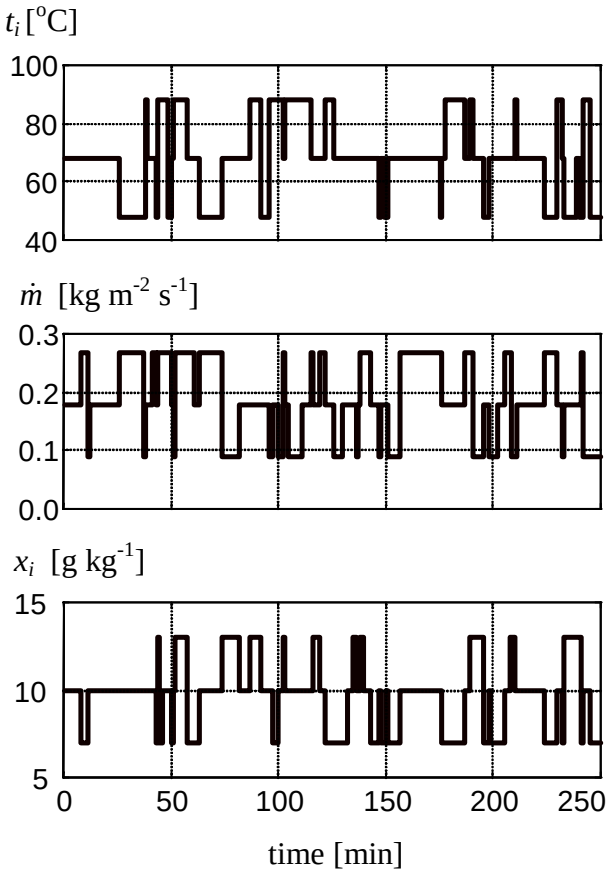

Figure 9: Input data for training the neural network

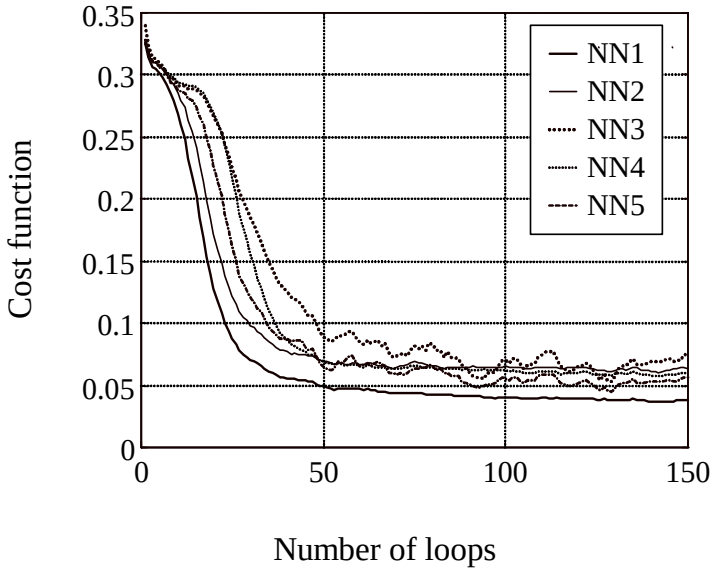

Figure 10: Cost function as a function of training loop

From the Figure it can be seen that the simplest model (NN1) has the best result e.g. the fastest convergence. This model has real moisture content in the bottom and in the top layer as input. The results shows, that the estimated moisture content is better in the top layer than in the middle or in the bottom layer, because the moisture content is determined based on outlet air parameters. The difference between PBM and neural network model is much larger between bottom and middle layer to middle layer and top layer.

4 Validation the Neutral Networks

For validation constant and multi-flow data were chosen the constant as because the real industrial drying processes (**Figure 11** and **12**).

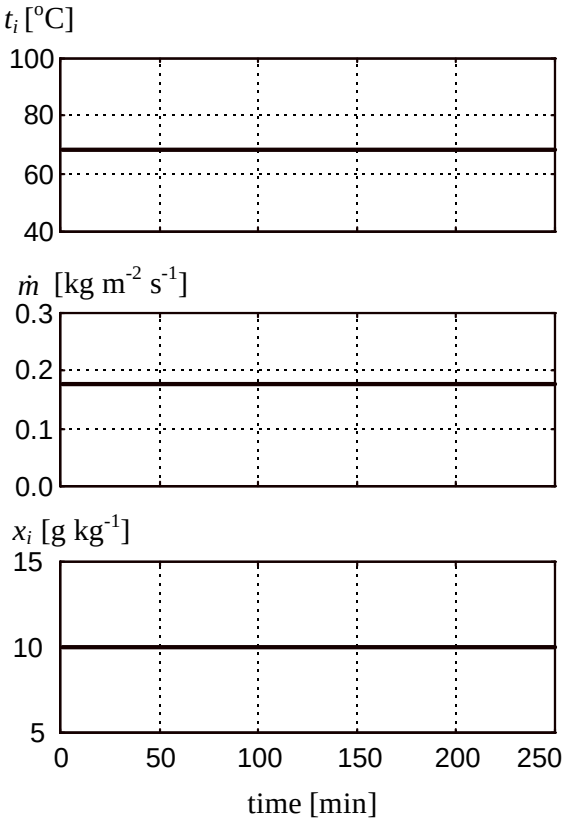

Figure 11: Constant input data used for validation

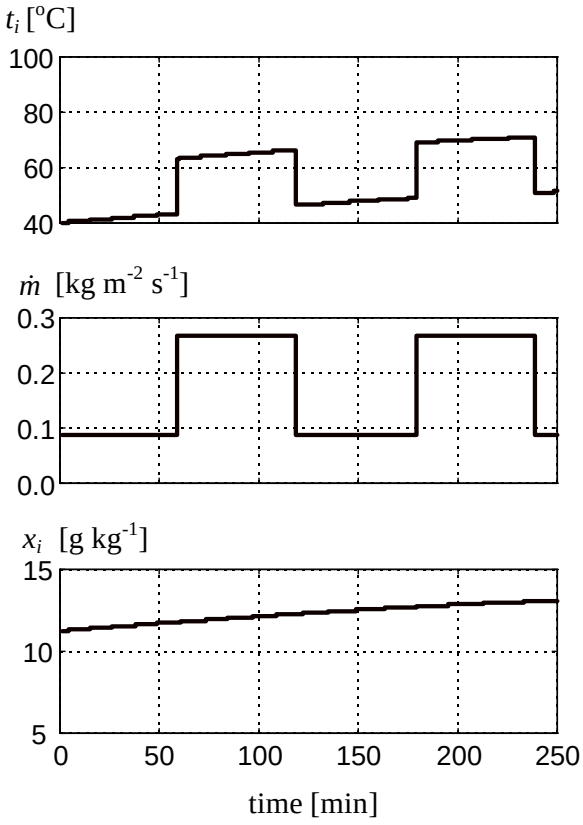

Figure 12: Input data for validation of multi-flow dryer

The validation data for multi-flow dryer were taken from outside weather parameters. The air flow was switched between two states to simulate intermittent drying, the air temperature and humidity was considered based on weather condition from 8:00 till 12:10.

From the validation results it can be stated that the networks NN3 and NN5 have the worst result in estimating the middle layer moisture content where the calculated network output was connected to the network input.

The NN3 and NN5 networks have feedback. It looks like that the simple feedback of the output sign on the input spoils the training speed, and also has worse results in training and during validation.

During the validation calculation correlation coefficients were used in order to make comparison between the different models. It has been somehow found unusable for the purpose of determination the correctness of the simulation compared to the measurements. In further work therefore average and maximal deviation will be introduced calculated.

5 Sensitivity of the Neural Nerwork

There has been carried out an extensive study on validation of the NN model along with the influences different parameters as the sampling time, the randomised training, the different training algorithms, the number of hidden neurones, the number of linked data series and the type of the data as it was suggested by FARKAS *et al.* (2000b). In this experiment a three layer feed-forward neural network with six hidden neurones was used. The NN contained also delayed feed-back from the output to the input.

5.1 Measures of model evaluation

Comparing the different training and validation results the average deviation and the maximum difference were applicable to use. The average deviation was defined as:

$$s_a = \sqrt{\frac{\sum_{i=1}^{n}\sum_{j=1}^{m}\left(X_{ij} - \hat{X}_{ij}\right)^2}{n\,m}} \qquad (11)$$

where n is the number of output variables which means three moisture contents (X_l, X_m, X_t) in our case. m is the number of training data pairs and X_{ij} and $\hat{X}_{ij}$ are the corresponding moisture contents of training and the NN outputs.

The maximum difference was defined as:

$$d_m = \max\left(\sum_{i=1}^{n}\sum_{j=1}^{m}\left|X_{ij} - \hat{X}_{ij}\right|\right) \qquad (12)$$

5.2 Selection of different sampling times

It was found that increasing the time step decreases the average deviation between the original training points and the outputs of the NN. For the given example discussed before, the average deviations were 0.0371, 0.00736 and 0.00284, respectively for the sampling times 5, 30 and 120 seconds. It can be observed that the fluctuations are larger at the beginning of the drying if small sampling time is selected, because of the large number of points. The explanation of this effect can be that the back-propagation algorithm minimises the difference between one input-output training pair in one step, and than it modifies the network weights based on the calculation point by point. In such a way, the neural network partly ‘forgets’ the behaviour of the process at the beginning. The more points are used the higher fluctuation will be at the beginning of the process. Randomised training can be used for reducing this effect when the points are randomly selected to train the neural network.

5.3 Influence of randomised training

In order to avoid high fluctuation at the beginning of the process the training pairs were randomly selected from the entire drying period. Using randomised training pairs for back-propagation algorithm it caused considerably improvement in the results even in case of a large number of training pairs. In case of randomised training of neural network with 5 second sampling time, the average deviation was dropped significantly from 0.0371 to 0.0046. The result shows furthermore that there is no fluctuation effect at the beginning of drying process, so using randomised training pairs is to be recommended for real applications.

5.4 Modification of the training algorithm

Preliminary studies showed that the original back-propagation algorithm could be slightly improved after some modifications. The first changing was to introduce an adaptive learning constant during the training. Another modification was changing the weights. After such experiments it can be concluded that there is almost no influence caused by the modifications, so it can be concluded that the original algorithm could be efficiently used without any modification.

5.5 Influence of the number of hidden neurones

A sensitivity study was performed in order to determine the influence of the number of hidden neurones in the NN. The sampling time was selected as 120 seconds along with randomised training pairs and the original back-propagation algorithm. From the results it can be concluded that the best approximation was achieved when the number of hidden neurones was between 3 and 5. The approximation was extremely bad in case of 1 hidden neuron. Increasing the number of hidden neurones caused even slightly worse result compared to the interval {3,4,5}. From these results, it is proposed to use four neurones in hidden layers in future work covering the fix-bed drying parameters.

5.6 Influence on the number of linked data series

As it was said before it has been realised that a single data series is not reasonably enough for training the NN. Training with one data series validation results can be unsatisfactorily in case of changing in input data. To achieve better performance in neural network modelling it seems a good idea to link together different number of data series as one virtual drying process.

For comparison purposes the overall average deviation ($\bar{s}_a$) was calculated on the base of the average deviations occurred in the validations:

$$\overline{s}_a = \sum_{i=1}^{n_v} \frac{s_{a,i}}{n_v} \tag{13}$$

where n_v is the number of the linked validation data series.

Figure 13 shows the influence on the number of linked data series for constant (c), slow random (s) and fast random (f) training processes.

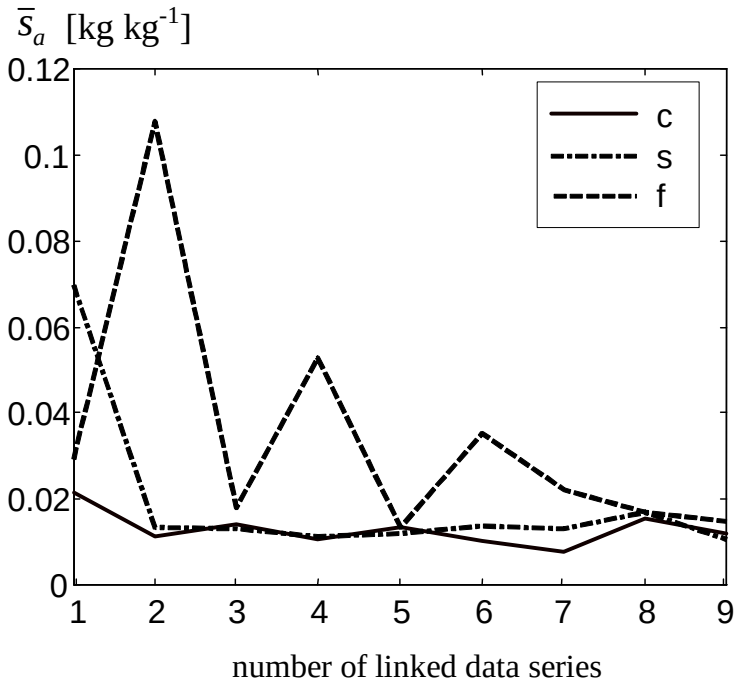

Figure 13: Influence on linked data series

The result shows that increasing the number of linked data series for training increases the accuracy of the NN model. Fast random signals caused the largest fluctuation at low number of linked data series. The overall average deviation in moisture content in all three cases was around 1% which seems to be a very reasonable result.

Figure 14a-c show an example of validation results for the case of constant, slow and fast random trainings and validations for the case of 9 linked data series.

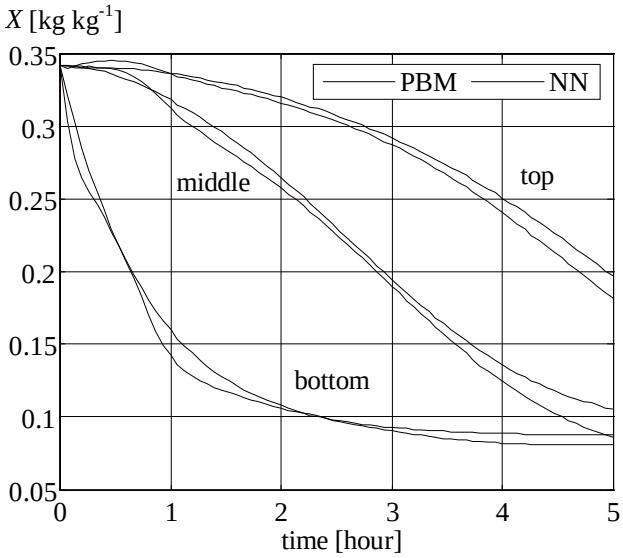

Figure 14 a: Result of constant training and validation (s_a=0.0083)

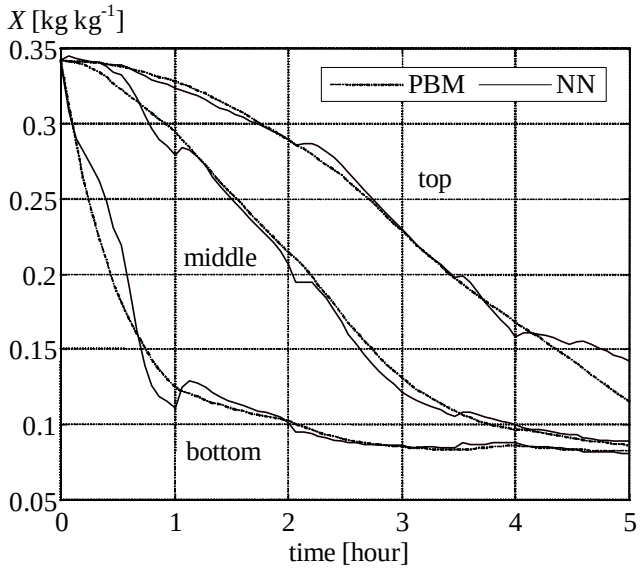

Figure 14 b: Result of slow random training and validation (s_a=0.0084)

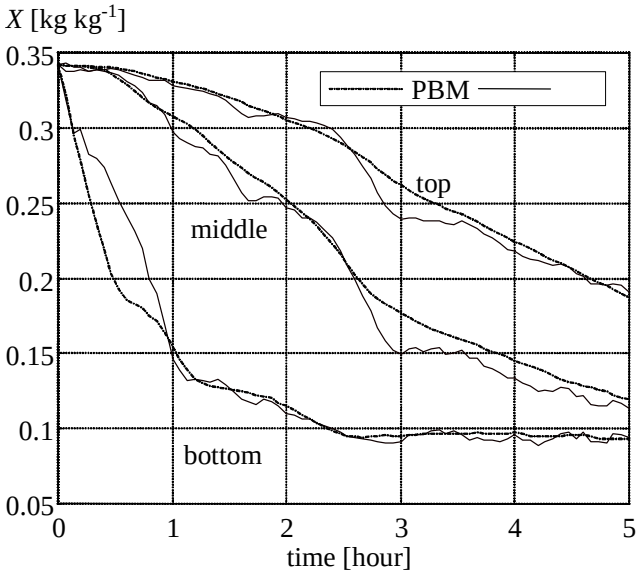

Figure 14 c: Result of fast random training and validation (s_a=0.0117)

5.7 Influence on different type of validation data

There were several trials to validate the NN with different (constant, slow and fast random) type of data. **Figure 15** shows the average deviations for the validations using different inputs.

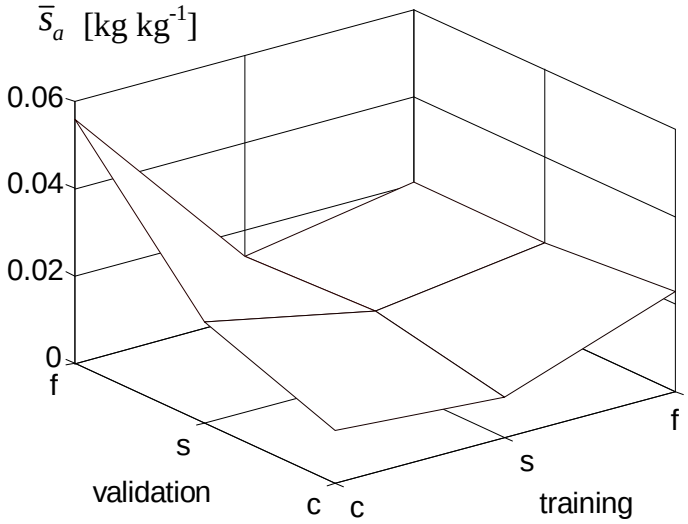

Figure 15: Validation results using different type of input data

Figure 16a-b show an example of validation results for the case of constant training and fast random validating, and slow random training and constant validating for the case of 9 linked data series.

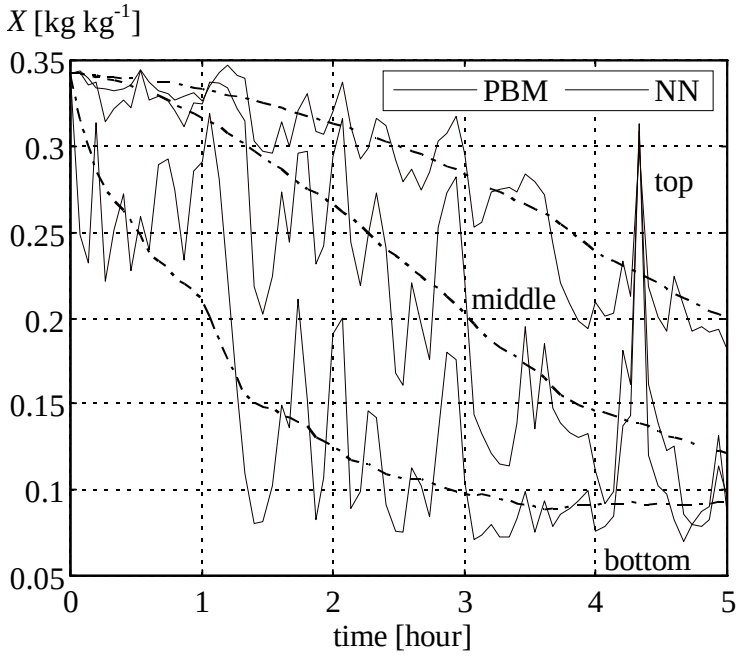

Figure 16a: Result of constant training and fast random validation (s_a=0.0359)

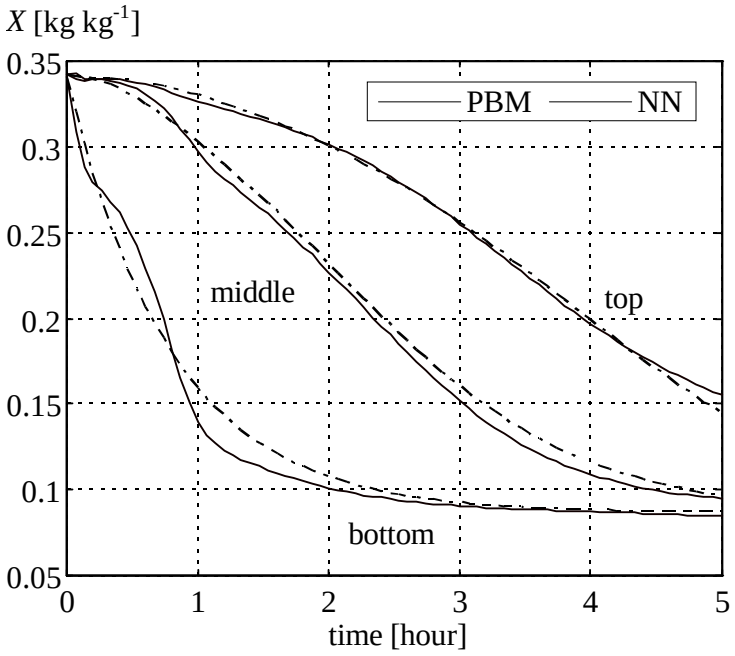

Figure 16b: Result of slow random training and constant validation (s_a=0.0064)

Table 1 shows the maximum differences in the validations using different type of input data.

It can be observed from the Table that the case of slow random training gives reasonable good result for both constant and fast random validations. Constant training gives the worse result for the case of fast validation signal.

Table 1: Maximum difference of cross validation using different type of input data

Training	Validation		
	c	*s*	*f*
c	0.0186	0.0355	0.0729
s	0.0122	0.0200	0.0216
r	0.0239	0.0222	0.0257

6 Identification of NN Based on Measurements

Small-scale laboratory drying set-up (**Figure 16**) was used to provide data for training and validating of neural network as it was suggested by FARKAS *et al.* (1999).

The diameter of drying tube was 0.1 m, the length was 0.6 m. Small-scale hot air jet provided preheated air for the dryer. The power of hot air jet was 2000 W while the air speed was 1.8 m/s in the empty dryer tube and 0.6 m/s with three times 300 g bag of corn. The

connection between the air heater and the drying tube was thin aluminium ring in order to reduce the disturbance of heater to the drying tube weight.

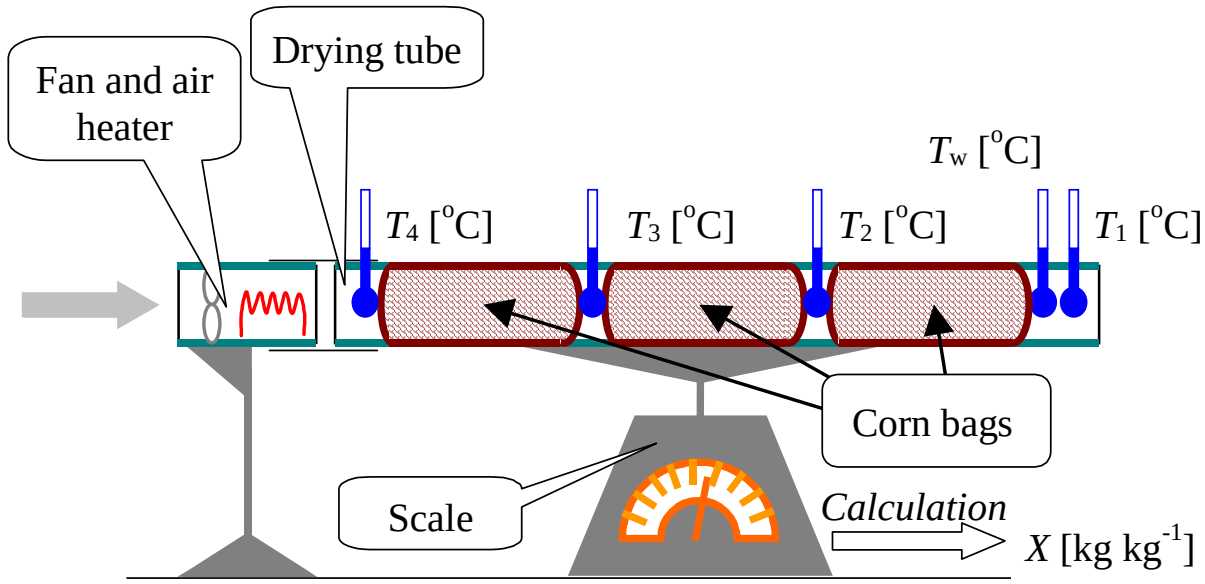

Figure 16: Layout of laboratory measurement

The weight of drying tube was continuously measured using Bosh EP2000 scale. Material moisture content was calculated based on the initial weight and the moisture content of corn and the difference of weights. The temperature was measured at three positions using LM 335 integrated temperature sensor calibrated at 60°C. The first position (T_1) was at the end of the drying tube while the other two positions (T_2, T_3) were inside the tube. Here another sensor was installed for measuring the wet bulb temperature for estimating the air humidity. The temperature at the inlet (T_4) was not continuously measured.

There were performed the measurement of several independent drying processes. The corn was rewetted before each experiment. The heat and fan were manually controlled. The fan was always at maximum power, while heat was switched between zero and maximal using different intervals from 30 minutes to 4 hours. The parameters were measured in each 2 seconds and stored the average in each 10 seconds.

The measured data were filtered using weighted moving average to get rid of disturbances. Two data series were selected for neural network application from the performed measurements. Most of the measurement contained significant error because of the sensor accuracy and model size. **Figure 17** shows a series of measurements.

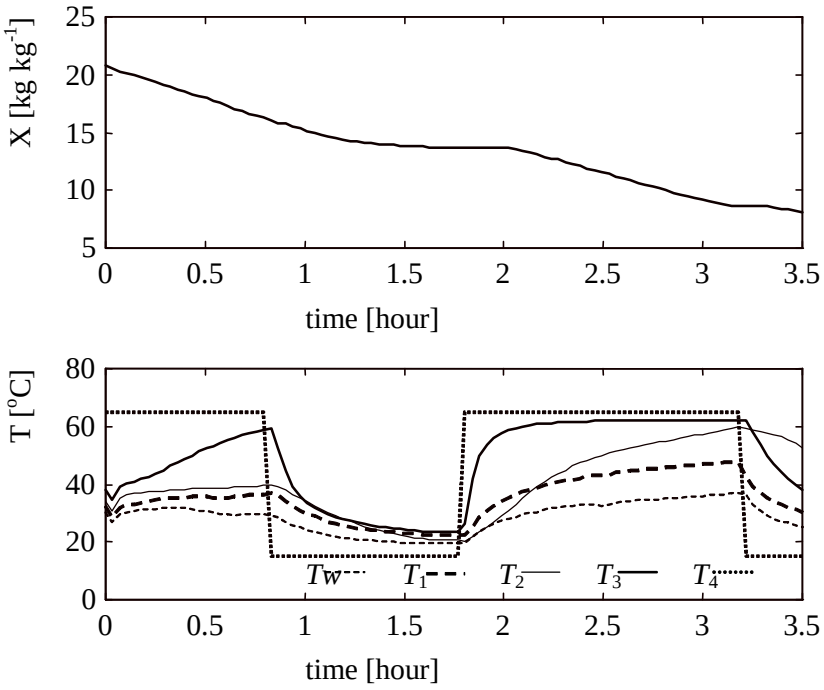

Figure 17: Calculated moisture content and measured temperatures

The wet bulb temperature (T_w) was always smaller than T_1, the difference was bigger at higher temperature, because the relative humidity was lower. Relation between temperature T_2 and T_3 depended on the temperature and the moisture of the corn, there is no clear relation between them. Temperature T_4 was determined based on the state of the heater and the preliminary measurements. The results of the comparison can be seen **Figure 18**.

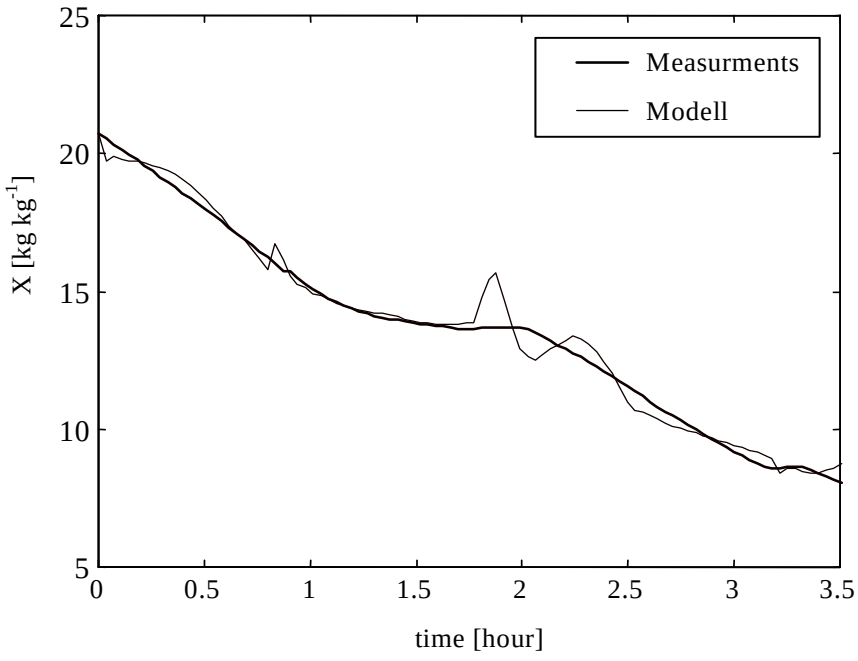

Figure 18: Measured and modelled moisture content

The results show that in some cases the neural network can precisely describe the moisture content in the drying bed. The neural network peeks occurred when the temperature changes was high, i.e. the heater was turned on or off. Due to the small size of the dryer and the measurement errors the validation of neural network was not hundred percentages successful.

7 Conclusions

On the basis of the study carried out in this paper it can be concluded that the neural network (NN) model can be used during post-harvest processes especially for estimation the moisture distribution along the depth in a fixed-bed dryer. The outputs of the neural network however are much more sensitive to the changes of the inputs than they are in the case of physically based model.

It should be stated that the selection of NN topology is essential step.

The sensitivity study of the NN method yielded the following main observations. Using a three layer feed-forward neural network a fairly large deviation can be observed between the cases using time increasing and randomised training pairs for the back-propagation algorithm. Especially, in the case of a large number of data pairs, randomised training pairs are strongly recommended.

Slight modifications in back-propagation algorithms do not improve the results significantly.

The number of neurones in the hidden layer could be optimised for four neurones.

It can be stated that besides other factors the selection of training and validation input data for NN model has a strong influence on the applicability.

Average deviation and maximum difference could be used to estimate the influence of the number of linked data series and the different training and validation input data.

It was realised that for satisfactorily number of training data series should be linked together and used as a virtual process in NN modelling. It can be concluded that the *slow* training signals yield reasonably good result even for *constant* and *fast* validation inputs. Training with *constant* signals provides quite a worse result for *fast* signal validation.

Further work was performed to study the use of laboratory scale measurements to validate the calculated of moisture distribution based on inlet and outlet air parameters using neural network and physically based model, as well.

The output results show that in some cases the neural network can precisely describe the measured moisture content in the drying bed. The neural network peeks occurred when the temperature changes was high, i.e. the heater was turned on or off.

Acknowledgements

The work was carried out within the Hungarian-German bilateral project No. D-5/03.

Nomenclature

A area of dryer (0.097 [m^{-2}])
c specific heat of barley (1300 [J kg^{-1} K^{-1}])
c_w specific heat of water (4186 [J kg^{-1} K^{-1}])
d_m maximum difference in moisture content (kg kg^{-1}])
h specific enthalpy of air [J kg^{-1}]
h_v specific enthalpy of water vapour [J kg^{-1}]
k_{vol} volumetric heat transfer coefficient [$Jm^{-3}s^{-1}K^{-1}$]
k drying rate [s^{-1}]
L_v specific heat of evaporation for water [2.501 10^6 J kg^{-1}]
m number of training data pairs [-]
$\dot{m}$ air flow rate, [kg m^{-2} s^{-1}]
n number of output variables [-]
N number of layers [-]
s_a average deviation in moisture content (kg kg^{-1}])
t air temperature [°C]
T material temperature [°C]
x air humidity [kg kg^{-1}]
X material moisture content [kg kg^{-1}]
X_e equilibrium material moisture content [kg kg^{-1}]
z height of dryer (0.305 [m])
$\partial\tau$ calculation time step (10 [s])
∂z height of one layer (z/N [m])
φ relative humidity of air [%]
ρ bulk density of barley (500 [kg m^{-3}])
τ time, s

Subcripts

l air and material parameters in lth layer (1...N)
i air parameters inlet to dryer
o air parameters outlet from dryer

References

FARKAS I., REMÉNYI P., BIRÓ A. (1999): Modelling of a small scale agricultural grain dryer by the use of neural network method, Proceedings of IMACS/IFAC Second International Symposium on Mathematical Modelling and Simulation in Agriculture and Bio-Industries, June 7-9, 1999, Uppsala, Sweden, pp. 59-64

FARKAS I., REMÉNYI P., BIRÓ A. (2000a): A neural network topology for modelling grain drying, *Computers and Electronics in Agriculture*, Vol. 26, pp. 147-158

FARKAS I., REMÉNYI P., BIRÓ A. (2000b): Modelling aspects of grain drying with a neural network, *Computers and Electronics in Agriculture*, Vol. 29, pp. 99-113

HUANG B., MUJUMDAR A.S. (1993): Use of neural network to predict industrial dryer performance, *Drying Technology*, 11 (3), pp. 525-541

JAY S., OLIVER T.N. (1996): Modelling and control of drying processes using neural networks, Proceedings of the 10th International Drying Symposium (IDS'96), Kraków, Poland, 30 July - 2 August, 1996, Vol B, pp. 1393-1400

KAMINSKI W., STRUMILLO P., TOMCZAK E. (1998): Neurocomputing approaches to modelling of drying process dynamics, *Drying Technology*, 16 (6), pp. 967-992

LIN C.-T., LEE C.S.G. (1995): Neural fuzzy systems, Prentice Hall Inc

O'CALLAGHAN J.R., MENZIES D.J., BAILEY P.H. (1971): Digital simulation of agricultural dryer performance, *Journal of Agricultural Engineering Research*, 16 (3), pp. 223-244

SREEKANTH S., RAMASWAMY H.S., SABLANI S. (1998): Prediction of psychrometric parameters using neural networks, *Drying Technology*, 16 (3-5), pp. 825-837

SUN Y., PANTELIDES C.C., CHALABI Z.S. (1995): Mathematical modelling and simulation of near-ambient grain drying, *Computers and Electronics in Agriculture,* 13, pp. 243-271

THYAGARAJAN T., PANDA R.C., SHANMUGAM J., RAO P.G., PONNAVAIKKO M. (1997): Development of ANN model for non-linear drying process, *Drying Technology*, 15 (10), pp. 2527-2540

TRELEA I.C., COURTOIS F., TRYSTRAM G. (1997): Dynamic models for drying and wet-milling quality degradation of corn using neural networks, *Drying Technology*, 15 (3&4), pp. 1905-1102

„New Palace“
at the western end of the main promenade in Sanssouci Park.

“Sanssouci Palace“ and the „Vineyard Terraces“

Weather Generator a Tool for Supporting Agricultural Modelling

L. Kuchar
Department of Applied Mathematics, Agricultural University Wroclaw
ul. Grunwaldzka 53, PL-50357 Wroclaw, Poland

Abstract: *In the paper the modified weather generator WGENK producing synthetic daily data of solar radiation, maximum and minimum temperature, and total precipitation is presented. A modified WGENK model, introduces annual courses of transition probability, α parameter of Γ distribution, and correlation's between solar radiation and temperatures described by trigonometric polynomials, as well set of parameters calibrating monthly rainfall variance. The method was tested by comparing statistics of 100-years of generated data with 20 years of observed weather data for Legnica Meteorological Station (Southwest Poland). The main result of model modification – monthly average rainfall variance was reduced about four times compared to original WGEN Richardson model.*

Keywords: *Mathematical model, Weather generator, Meteorological data.*

1 Introduction

For the needs of agronomic and environmental models, particularly simulation models daily data of solar radiation, maximum and minimum temperature, and total precipitation are most often required (RICHARDSON 1985, HUNT *et al*. 1998). If there are no required data or they are missing, applications of models are very limited. The situation mentioned occurs if there is a lack of a meteorological station or new environmental conditions or when new records of data are not available. First methods generating data for the needs of agricultural modelling were constructed in the beginning of eighties, mainly for crop simulations for a new climate scenarios (BRUHN *et al*. 1980, RICHARDSON 1985). Daily records of data were simulated by means of general climate information. Weather generators like many environmental statistical models, use Markov chains to determine occurrence of wet/dry days, and gamma or exponential probability distribution for amount of rainfall. Daily values of solar radiation, temperature maximum and minimum are considered as a weakly stationary process and generated by general linear model (GLM). Depending on location of future application more studies were related to choosing an appropriate probability distribution for each climate variable (HAYHOE 2000).

Generated data series are required to have the same statistics as climatology data including means, variations and cross, lag and lag-cross correlations of solar radiation

and temperature. The amount of precipitation and its variation is also expected to be the same as from observed data (HAYHOE 1998, LARSEN & PENSE 1982). While means and variations of generated data (except variation of precipitation) sufficiently estimate moments of theoretical distribution, there are still poor fitting in precipitation variation, precipitation extremes and correlations between variables (KUCHAR 2004).

In Richardson's weather generator, the cross, the lag and the cross-lag correlation illustrate seasonal and spatial relation between variables, are constant through locations and over the year (RICHARDSON 1985). Recently, spatial and monthly course of correlation are introduced to the models by staircase function. Correlations differ from month to month and location, however constant within the given month (SCHOOF & ROBESON 2002). Transition probabilities and parameters of rainfall probability distribution are fixed monthly or biweekly as a set of 12 or 26 values (RICHARDSON 1985) or estimated by strait function (HAYHOE 2000).

In this paper parametrization of serial correlation, transition probability, and α parameter of Γ probability distribution is studied. Daily values of correlation, transition probability, and α parameter of Γ probability distribution are fitted by a trigonometric polynomial function and then used for data generation. The idea of using continuous function versus staircase or strait function is to preserve continuous changes of generated data and their climatology statistics.

Also, new idea of calibration of β parameter of Γ probability distribution for monthly precipitation to better fit rainfall variation is introduced.

2 Data

Evaluation of WGENK model and particularly estimation of seasonally correlation and variation of total rainfall were done based on the data obtained for first order Institute of Meteorology and Water Management (IMGW) station located in Southwest of Poland (Legnica Meteorological Station, 51°13'N, 16°14'E). Daily data of SR solar radiation ($MJm^{-2}day^{-1}$), maximum and minimum temperature (°C), and total precipitation (mm) was collected for the twenty years period. Legnica Station was selected so that there would be no data gaps. In a few cases of missing solar radiation data were estimated based on values of minimum and maximum air temperature and precipitation together with calculated values for clear sky radiation according to HUNT *et al*. (1998).

3 Methodology

A WGENK model - modification of the well-known WGEN, weather generator of RICHARDSON (1985) generates daily values of precipitation (P), solar radiation (SR),

maximum (T_{max}) and minimum temperature (T_{min}). The occurrence of precipitation has an influence on the solar radiation and the temperature for a day by determining a status (wet or dry day) and independently generating solar radiation and temperature for a given status day. The model preserves the dependence in time, and the seasonal characteristics for locations (RICHARDSON 1985).

Precipitation is generated by means of the first-order Markov chain to determine occurrence of wet/dry days, and then two-parameter gamma distribution for the amount of rainfall (BRUHN *et al*. 1980, LARSON & PENSE 1982). The transition probabilities and α parameter of Γ distribution are continuous during the year for a given location owing to the application a trigonometric polynomial function in the form (KUCHAR 2004):

$$W_n(t)=\sum_{k=1}^{n}(a_k \sin(kt)+ b_k \cos(kt)) \qquad (1)$$

which describes seasonal changes (t defines a day of the year $1 \leq t \leq 365$, n - the degree of the polynomial, and a_k, b_k - coefficients).

Estimation of a_k, b_k coefficients is made by the method of least square. Selection of the polynomial degree n is halted when the proportion of the total variation in the response variable is explained by the fitted model in 90%, or n arbitrary exceed number of months. Functions $W_n(t)$ are fitted by non linear approximation using NLIN procedure given by SAS Institute Inc.(1988).

Daily values of solar radiation (SR), temperature maximum (T_{max}) and minimum (T_{min}) are considered as a weakly stationary process includes seasonal changes of correlation's (cross, lag and lag-cross) between factors in the form:

$$d_i = \mathbf{A} \cdot d_{i-1} + \mathbf{B} \cdot e_i \qquad (2)$$

where d_i is a vector (3x1) of normalized residuals for all three variables for day i; e_i is a vector (3x1) of independent random components normally distributed with mean zero and variance one; **A** and **B** are matrices (3x3) obtained from equations: $\mathbf{A}=\mathbf{M}_1\mathbf{M}_o^{-1}$, $\mathbf{B}\mathbf{B}^T= \mathbf{M}_o^{-1} \mathbf{A}\mathbf{M}^T$, and $\mathbf{M}_o$, $\mathbf{M}_1$ are matrices (3x3) of cross correlations ($\mathbf{M}_o$) and lag-correlation, lag-cross correlations ($\mathbf{M}_1$) of variables SR, T_{max}, T_{min} (RICHARDSON 1985). Seasonally correlation (for each correlation i.e. components of $\mathbf{M}_o$, $\mathbf{M}_1$ matrices) is described by trigonometric polynomial function (1) in the same manner as transition probability and α parameter of Γ distribution. Solar radiation and temperature are generated by eq. (2) which use daily values of correlation estimated by function (1). To prevent poor estimation of transition probabilities, α parameter and correlations smoothing them by 11-day moving window be-

fore function fitting and Richardson's suggestion of twenty-years observation (RICHARDSON 1985) are applied.

New approach, presented in this paper, determines better fitting of rainfall variance by the model. Set of coefficients k_i (i=1,2,...,12) for month i, reshapes Γ probability distribution for a given day t ($1 \leq t \leq 365$). Parameters β determines shape of $\Gamma(\alpha_t, \beta_t)$ probability distribution are obtained using formula: $\beta_t = \mu_t/(w_t \cdot \alpha_t)$, for a given scale - α_t, average total rainfall - μ_t and weights - w_t, where $w_t = k_1$ for $t \in [1,31]$, $w_t = k_2$ for $t \in [32,59]$, . . . , $w_t = k_{12}$ for $t \in [334,365]$. In other words, shape parameters β (estimated based on data sample) of Gamma distribution (applied for data generation) are multiplied by coefficients k_i to minimize difference between observed and generated variance of total precipitation.

4 Results

The WGENK weather generator was examined by parallel comparison: observed climatology vs. WGEN, and observed climatology vs. WGENK. The above evaluation was made by means of the data from meteorological stations and generated by both models 200-year data series. For all data, the values of means, variances and correlations in different time period as annual, vegetative period (March - October), bimonthly and monthly, were computed and evaluated by absolute differences between observed and generated parameters as well as relative differences in form: abs(observed - estimated)·100% /observed.

Data generated by WGEN method has shown low errors for all means, and variances of solar radiation and both temperatures (these results are not shown in a table). Only the variance of precipitation and correlations like the lag, cross and cross-lag proofed a poor estimation and not acceptable errors (**Tables 1** and **2**). To improve the above estimation WGENK procedure introduces to the model annual courses of transition probabilities, α parameter of Γ distribution, variables correlation described by trigonometric polynomial approximation and β parameter calibration. First, to make a better rainfall variance approximation, time series of transitions probability and α parameter are smoothed by moving average (five points on either side of the target) and fitted by trigonometric polynomial, and calibrated by w_t weights.

The new approach compared to previous results (KUCHAR 2004) has reduced absolute errors of variances for precipitation (generated vs. observed) about two/three times, and relative error to 6% compared to the original method (Table 1), depending on considered period. Annual absolute error of standard deviation was reduced from 7.0 mm to 3.0 mm and relative error from 8.2% to 3.0%, respectively. The best results were obtained for monthly periods: absolute error of standard deviation was reduced from 5.6

mm to 1.6 mm while relative error from 24.0% to 6.2%. No significant differences were noted for precipitation sums (Table 1).

As expected, there were no significant improvements in fitting of means and variances for solar radiation, maximum and minimum temperature.

Table 1: Average absolute and relative error for sums and standard deviations of precipitation, WGEN and WGENK method, and different time period /Legnica meteorological station/

	WGEN			
Time	**Absolute Error [mm]**		**Relative Error [%]***	
Period	**Sum**	**SD**	**Sum**	**SD**
Annual	1.0	7.0	0.2	8.2
Season	1.0	5.0	0.2	6.0
Month	2.5	5.6	5.6	24.0
	WGENK			
Annual	1.0	3.0	0.1	3.0
Season	1.0	1.6	0.1	1.6
Month	1.2	1.6	2.1	6.2

(*) (abs(observed - estimated)/observed)·100%

The same trigonometric approach was used to fit a seasonal correlation (KUCHAR 2004). Each correlation given by $\mathbf{M}_o$, $\mathbf{M}_1$ matrices was smoothed by 11-day moving window before function fitting. Approach used for annual course of correlations reduced errors of correlations about three times (comparing to WGEN model); new correlations were statistically examined (at 0.05 level) and accepted in 95% for all 240 computed tests while for original method accepted in 52.7%. For the annual period, highest average reduction error was observed for cross correlations (from 0.07 to 0.02). In these cases the number of significant different correlations between observed and generated data was 4.6% while for original WGEN 49.6%.

There is a significant reduction of errors for vegetative and bimonthly periods. This fact is well shown by absolute difference between models, but first of all shown by percentage of statistically different (at alpha 0.05) tests. The evidence of method improvement is observed for monthly correlations.

For this period the biggest error reduction for absolute differences was observed for cross correlation (error reduction from 0.19 to 0.05). Percentage of significant different correlations were reduced from 18.8% to 0.8% (lag correlation), 40.0% to 0% (cross correlation), and from 63.1% to 0.9% (lag-cross correlation).

Table 2: Average absolute error for cross, lag and cross-lag correlation between solar radiation, maximum and minimum temperature, and percentage of significant different correlation from climatology at α=0.05 for specified period /Legnica meteorological station/

Correlation Type	Time Period	Average Absolute Error	
		WGEN	WGENK
Lag	Annual	0.04	0.02
	Vegetative	0.04	0.01
	Bimonthly	0.06	0.02
	Monthly	0.10	0.04
Cross	Annual	0.07	0.02
	Vegetative	0.07	0.02
	Bimonthly	0.12	0.04
	Monthly	0.19	0.05
Lag-Cross	Annual	0.05	0.03
	Vegetative	0.06	0.02
	Bimonthly	0.10	0.03
	Monthly	0.16	0.04
		Percentage of Significant Differences at α = 0.05	
		WGEN	WGENK
Lag	Annual	36.7	0.0
	Vegetative	71.7	0.0
	Bimonthly	24.6	1.2
	Monthly	18.8	0.8
Cross	Annual	49.6	4.6
	Vegetative	83.3	0.4
	Bimonthly	42.1	1.3
	Monthly	40.0	0.0
Lag-Cross	Annual	79.2	5.0
	Vegetative	78.3	5.4
	Bimonthly	49.6	1.7
	Monthly	58.8	0.8

From the point of view of type of correlation the best improvement was obtained for cross, while most deficient for lag correlations. The structure of errors depends on type of correlation, time and duration of period and method is shown in Table 2.

4 Conclusions

A new WGENK weather generator, tested for weather data from Legnica Meteorological Station (Southwest Poland) showed low errors for means and variances of generated data, and accepted errors for lag, cross, and cross-lag correlation. Computed tests have shown significant improvement in the method fitting of annual seasonality of transition probability, α parameter of Gamma probability distribution and correlation course of variables by application of the trigonometric polynomial function. In addition, application of β parameter calibration reduced standard deviation relative error of precipitation three/four times compared to original WGEN model.

References

BRUHN J.A., FRY W.E., FICK G.W. (1980): Simulation of Daily Weather Data Using Theoretical Probability Distributions. *J. Appl. Meteorol.*, 19: 1029-1036

HAYHOE H.N. (1998): Relationship between weather variables in observed and WXGEN generated time series. *Agric. For. Meteorol*., 90: 203-214

HAYHOE H.N. (2000): Improvements of stochastic weather data generators for diverse climates. *Climate Res.,* 14:75-87

HUNT L.A., KUCHAR L., SWANTON C.J. (1998): Estimation of solar radiation for use in crop modelling. *Agric. For. Meteorol.*, 91: 293-300

KUCHAR L. (2004): Using WGENK to generate synthetic daily weather data for modelling of agricultural processes. *Math. Comput. Symul*., 65: 69-75

LARSEN G., PENSE R. (1982): Stochastic Simulation of Daily Climatic Data for Agronomic Models. *Agron. J.,* 74: 510-514

RICHARDSON C.W. (1985): Weather simulation for crop management models. *Trans. ASAE.,* 28, 1602-1606. SAS Institute Inc. (1988). *SAS/STAT User's Guide. Release 6.03 Edition.* Cary, North Carolina

SCHOOF J.T., ROBESON S.M. (2002): Seasonal and spatial variation of serial and cross-correlation matrices used by stochastic weather generators. In: *Preprint 13th Conf. on Applied Climatology, Portland, Oregon 13-16 May*.: 142-145

Impact of Weather Forecast Uncertainty in Optimal Climate Control of Storehouses

T.G. Doeswijk, K.J. Keesman and G. van Straten
Systems and Control Group, Wageningen University, P.O. Box 17, 6700 AA Wageningen, Netherlands, E-Mail: timo.doeswijk@wur.nl

Abstract: *Indoor climates of storehouses can be controlled by using outdoor weather conditions. For indoor climate predictions in, for instance, optimal control strategies weather forecasts are needed. As weather forecasts are uncertain, predicted model states and related costs become uncertain. Usually, the medium-range weather forecast consists of an ensemble of forecasts. Hence, the uncertainty of the weather forecast is known a priori. Furthermore, the model itself is subject to uncertainties. The objective of this paper is to evaluate the uncertainty of the costs related to both weather and model uncertainty given the controls. The worst-case scenarios show that if closed loop optimal control strategies are used the costs are more sensitive for model uncertainty than for weather uncertainty. Copyright © 2006 IFAC*

Keywords: *Optimal control, uncertainty, post harvest, storage, weather forecast*

1 Introduction

Indoor climate in greenhouses, office buildings and storage facilities for agricultural produce are generally related to outdoor weather conditions (CRAWLEY *et al*. 2001, LUKASSE *et al*. 2006a, TAP 2000). The indoor climate is affected by for instance heat transfer through walls, radiation, respiration and evapotranspiration of organisms, ventilation with outdoor air and by active heating or cooling. If anticipating control strategies such as receding horizon optimal control are to be used for controlling the indoor climate using outdoor climate, weather forecasts become important. Uncertainties in weather forecasts then lead to uncertain predicted indoor climates. Moreover, the cost function relating to any kind of optimal control strategy is subject to errors in the weather forecasts. The sensitivity of the model outputs and the related cost function therefore needs to be investigated. For both air conditioned buildings (HENZE *et al*. 2004) and a potato storage facility (KEESMAN *et al.* 2003, LUKASSE *et al.* 2006B) it was shown that a good weather forecast reduces the cost function almost as much as a perfect weather forecast. In these studies short term weather forecasts (1 to 2 days ahead) were used. In this study which focuses on effect of the uncertainty in weather forecasts, medium range weather forecasts (up to 10 days ahead) are used.

The medium range weather forecast (PALMER *et al*. 1997) consists of an ensemble of 50 different weather forecasts. All 50 ensemble members have an equal probability of occurring. Hence, the uncertainty of the weather forecasts is known a priori. This knowledge can be used to evaluate a calculated optimal control solution by calculating the costs of each of the ensemble members. Next to this, the optimal control solution can be evaluated a posteriori with the observed weather.

In general, a model is an approximation and not an exact representation of the system investigated. Hence, not only uncertainties in the inputs (*i.e.* weather forecasts) but also uncertainties of the model effect the outcome of an optimal control algorithm.

The objective of this paper is to evaluate the effect of uncertainty in the weather forecast on the costs of the calculated optimal control problem of a potato storage facility. Furthermore, the effect of model uncertainty on the costs is investigated. Finally, a time criterion for which the optimal control problem is to be recalculated (*i.e.* feedback is applied) based on model and input uncertainties is proposed.

The paper is structured as follows: first a brief description of the storage model and the cost function are given. Next, the type of weather forecasts used is explained. Then, the open loop and closed loop evaluations using weather forecasts and observations are given in subsequent sections. Finally, results are discussed and conclusions are drawn.

2 Preliminaries

2.1 Storage model

The model used to simulate a potato storage facility is based on the work of (LUKASSE *et al.* 2006a). The original model was simplified to make it suitable for use in a receding horizon optimal control algorithm (LUKASSE *et al.* 2006b). A brief description of this discrete-time model is:

$$x_{T,k+1} = x_{T,k} + p_1 + \left(d_{T_{wb,ext},k} - x_{T,k}\right)\left(p_3 + \left(p_2 p_5 u_{mix,k}\left(p_7 + \left(1 - p_7\right) u_{vent,k}\right)\right.\right. \tag{1}$$

$$x_{CO_2,k+1} = x_{CO_2,k} + p_1 p_4 + \left(d_{CO_2,ext,k} - x_{CO_2,k}\right)\left(p_2 u_{mix,k}\left(p_7 + \left(1 - p_7\right) u_{vent,k}\right) + p_6\right) \tag{2}$$

where x_T represents the product temperature, x_{CO2} the CO_2 concentration in the bulk, $d_{Twb,ext,k}$ the ambient wet bulb temperature, $d_{CO2,ext,k}$ the ambient CO_2 concentration, u_{vent} the fraction of maximum possible internal ventilation, u_{mix} the fraction of ambient air in the air flow, and p a vector of parameters containing physical and design parameters. Hence, the control input is defined by: $u=[u_{mix}, u_{vent}]^T$. The sample time used for this model is one hour.

The temperature of the bulk can be measured. The CO_2-concentration, however, is difficult to measure in practice. The storehouse therefore is controlled on the product temperature. The CO_2-concentration is simulated to avoid too high concentrations that lead to damage of the product (see section 2.3). This is possible because the CO_2-concentration reduces very fast during ventilation, *i.e.* the CO_2-concentration reaches equilibrium fast.

2.2 Weather forecasts

The weather forecasts used in this paper are the so-called medium range weather forecasts provided by Weathernews Benelux. This means that the forecast up to 10 days ahead is given. Due to the chaotic nature of the atmosphere, the weather forecast is sensitive to the initial conditions. Therefore, an ensemble prediction system (PALMER *et al.* 1997) is introduced to improve the forecast quality and to get more insight into the uncertainty of the forecast. The weather forecast used in this paper consists of 50 ensemble members. Each of the members have an equal chance of occurring. The ensemble mean is used as the nominal weather forecast.

A new weather forecast becomes available every 24 hours. Short term weather forecasts (up to 36 hours ahead) can be improved by using local observations (DOESWIJK & KEESMAN 2005). A similar method is used here to correct the medium range weather forecast.

2.3 Cost function

To give a little more insight into the control objectives of the potato storehouse, the elements of the cost function are mentioned below. How the weighting factors are chosen is beyond the scope of this paper. The following control objectives are to be fulfilled:

- The temperature of the bulk must be kept as close as possible to a pre-specified reference temperature ($\min_u \|x_{T,k} - T_{ref}\|$).
- The temperature must always be kept above a specified minimum temperature (inequality constraint $x_{T,k} > T_{min}$)
- The temperature may not decrease faster than a specified limit within 24 hours (inequality constraint) ($x_{T,k} - x_{T,k-24} < T_{\Delta}$).
- The weight loss of the product due to evaporation must be minimized ($\min_u \sum_{k=0}^{H} f_1(x_{T,k}, d_{Twb,k}, u_k)$) with H the control horizon.
- The CO_2-concentration must always be kept below a specified maximum (inequality constraint $x_{CO2} < CO_{2,max}$)
- The energy costs related to ventilation must be minimized ($\min_u \sum_{k=0}^{H} f_2(u_{vent,k})$).

2.4 Receding horizon optimal control

Given the model -, a weather forecast (containing $d_{Twb,ext,k}$) and assuming $d_{CO2,ext,k}$=0.0314 to be constant, a control trajectory can be calculated that minimizes a cost function according to:

$$\min_{u_k} J = \min_{u_k} E\left[\phi[x_{k+H}] + \sum_{k=0}^{H} L[x_k, u_k, d_k]\right] \tag{3}$$

where the expected value is taken because the weather forecast is a stochastic variable (STENGEL 1994). In the investigated case there are no final costs *i.e.* $\phi[x_{k+H}]$=0. If this open-loop control problem is solved repeatedly every I hours (I < H) given the updated (or measured) states and weather conditions the control loop is closed. This control strategy is called receding horizon optimal control (RHOC).

The RHOC solution with the nominal weather forecast is taken as the reference point for the uncertainty evaluation. The RHOC was started at 13 April 2005 and ended at 2 June 2005 using medium-range weather forecasts for location 'De Bilt, The Netherlands'. The forecast horizon of the weather forecast also determines the horizon of the RHOC (H=217 hours). During this period every six hours a new optimal control trajectory was calculated (*i.e.* I=6) with a new external weather forecast. The initial conditions of each optimal control run was taken equal to the measurements. In addition, the newly calculated controls were implemented. A total of 203 optimal control trajectories are calculated (4 times a day, almost 51 days). An example of a calculated control trajectory with the accompanying predicted state and cost evolution is presented in **Figure 1**.

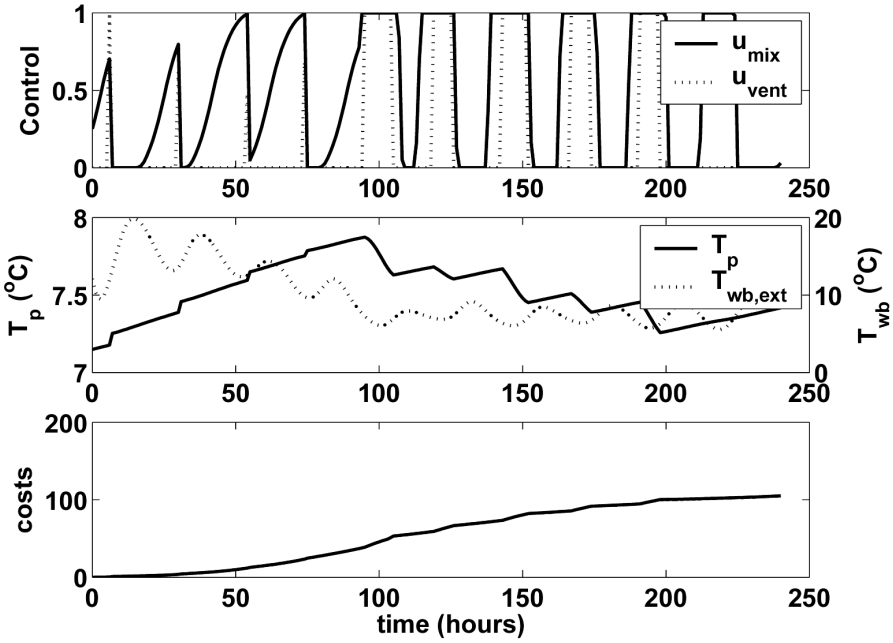

Figure 1: Optimal control output of 1 May 2005. The subfigures show respectively: calculated optimal controls; predicted product temperature and external wet bulb temperature; predicted cumulative costs

The reference temperature (T_{ref}) in this case was 7^{o}C. With the increasing temperature also the costs increase. Therefore, long periods of ventilation occurs if the external wet bulb temperature is lower than the product temperature.

3 Weather uncertainty

There are several possibilities to evaluate the uncertainties in the cost function. First the change in cost function is investigated when observations of the weather are used instead of the forecast. Second, the effect of ensemble members on the cost function is investigated. It should be noted that no new RHOC calculations are performed based on different weather forecasts or parameter values. The calculated costs based on the nominal weather forecast are compared with other weather forecasts or parameter sets with the same calculated control trajectories of u_{mix} and u_{vent}.

3.1 Open loop evaluation

If the model is run again but now with the observed weather instead of the forecasted weather, a change in costs is observed. In **Figure 2** the difference between calculated and realized running costs are given with the running costs defined by:

$$R = \sum_{k=0}^{r} \mathcal{L}\left(x_k, u_k, d_k\right) \tag{4}$$

If r=H then R=J.

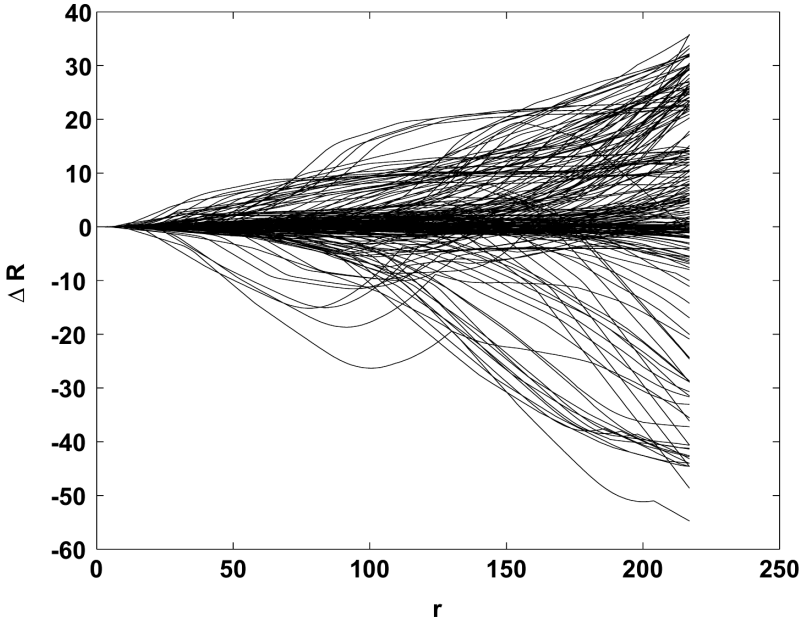

Figure 2: Difference in calculated absolute costs and realized costs of 203 optimal control runs

All 203 cost function trajectories are recalculated with the observed weather and the given control trajectories. It can be seen that the total cost difference can be both positive and negative. This means that, given the control trajectory, the realized weather can reduce the total costs more than was expected from the forecasted weather. It does not mean that the calculated control trajectory is also related to the minimum if the observed weather was used in the RHOC.

Because the total absolute costs J change for every optimal control run, because of changing initial states and changing weather forecasts, the relative change in the cost function, *i.e.* $\Delta R^{rel}=[(R_{obs}\tilde{R}_{fct})/(J_{obs})]$, is given in **Figure 3**.

The absolute costs can change dramatically (not shown here) over the researched period because the outside temperature increases. Especially, the cost criterion $||x_{k,\tilde{T}}T_{ref}||$ then increases. Relatively to the costs at t_k+H, however, the change in costs do not seem to change that dramatically.

Using the observed weather to calculate the costs is a useful a posteriori tool. To evaluate the uncertainty of the costs a priori, however, other information about the uncertainty of the weather forecast is needed. The uncertainty of the weather forecast is embedded within the ensemble (see section 2.2). By calculating the costs related to each of the ensemble members the worst case scenario can be evaluated, *i.e.* the ensemble member for which the costs are highest of all. In **Figure 4** the worst-case cost differences are presented.

It can be seen here that the worst-case scenarios always lead to increased costs and these costs are considerably larger than the realized costs (figure 2).

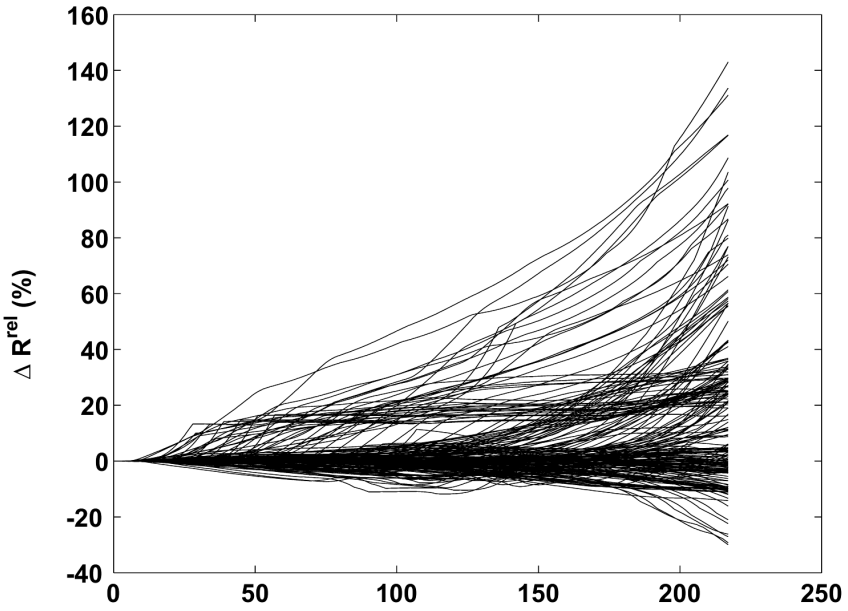

Figure 3: Difference in calculated relative costs and realized costs of 203 optimal control runs

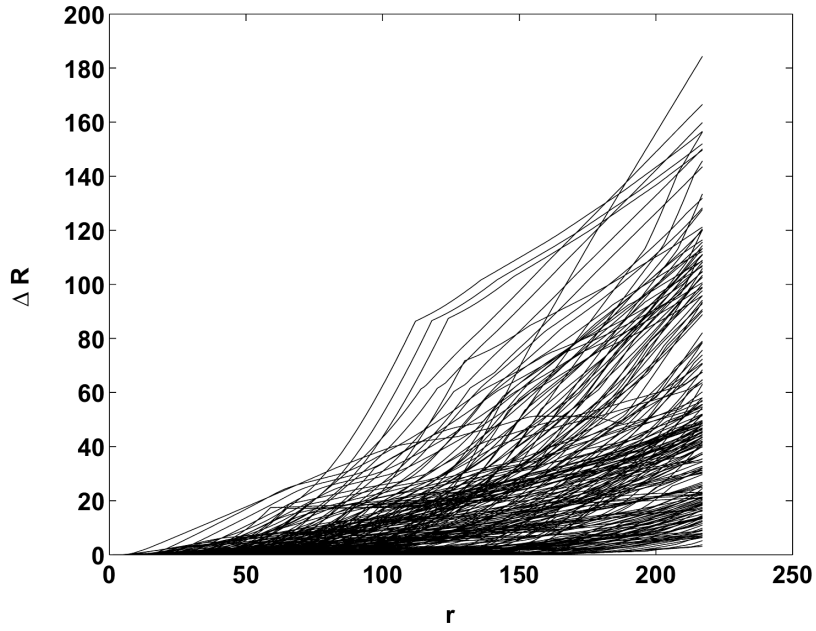

Figure 4: Difference in calculated absolute costs and maximum costs based on the ensemble of the 203 optimal control runs

3.2 Closed loop evaluation

In the specific RHOC implementation every six hours the newly calculated controls are implemented. This means that the uncertainty in the cost function after six hours needs to be evaluated. In **Figure 5** the differences between calculated costs using nominal weather and actual costs based on observed weather are presented for each control run at k=6.

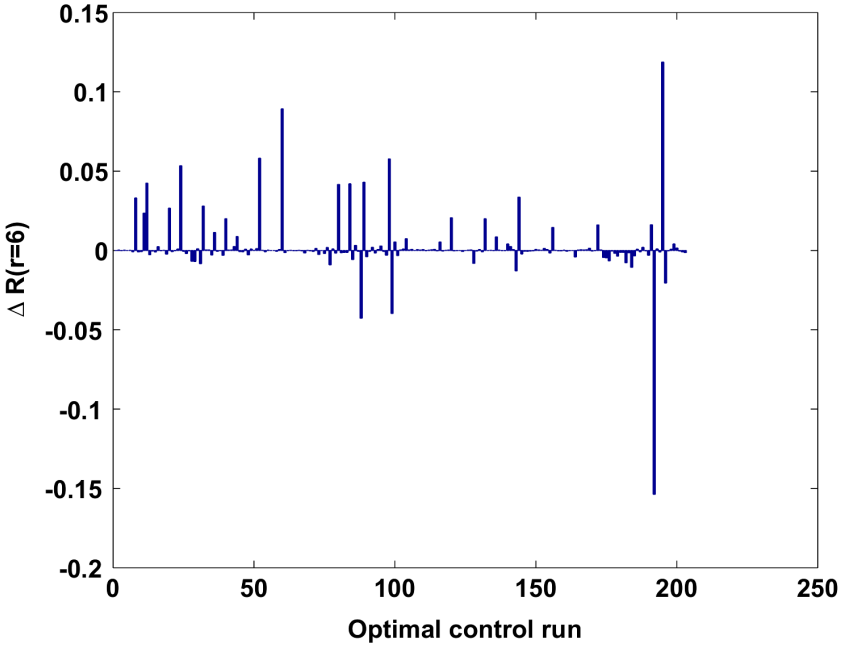

Figure 5: Difference in calculated costs and realized costs of each of the 203 optimal control runs after six hours

The increased and decreased costs can be clearly seen from this figure. If all the costs shown in this figure are summed the additional costs are known for the given period. These costs as well as the relative contribution to the total costs at the final time are given in **Table 1**.

Table 1: Additional costs of the realized costs and the worst-case scenarios for model and weather forecast uncertainty

	$\Sigma(\Delta J)$	$\Sigma(\Delta J)/J_{tot}$
observations	0.47	0.10 %
weather ensemble	1.72	0.37 %
parameter ensemble	15.4	3.29 %

From the a priori known weather forecast uncertainty from the ensemble the worst-case scenario can be calculated. The additional worst-case costs at the moment that a new optimal control trajectory was calculated, *i.e.* six hours, are presented in **Figure 6** for each of the calculated RHOC runs.

Again, the figure shows that the costs always increase. The total additional costs (see table 1) in this case, however are still very low.

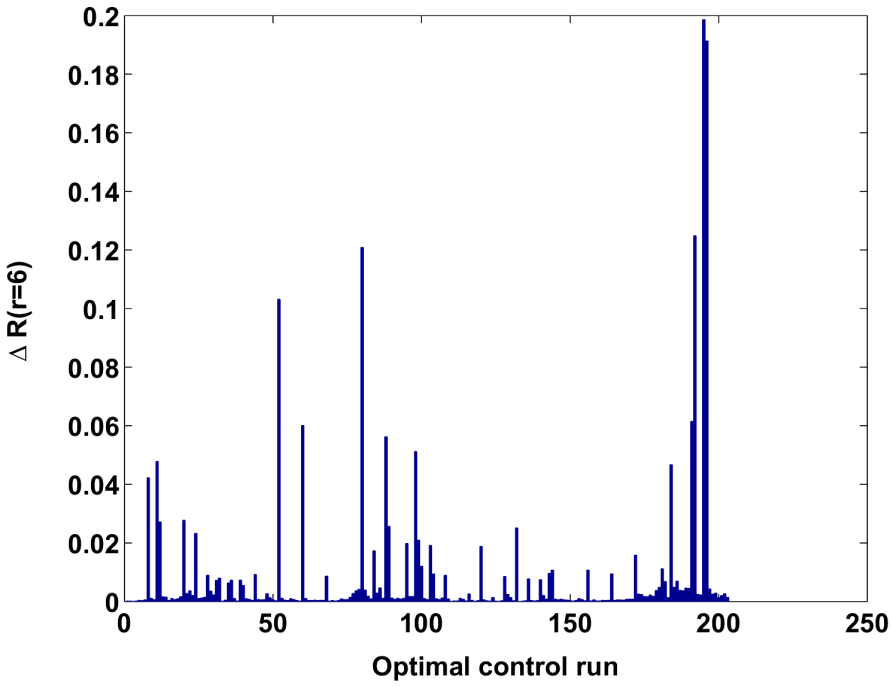

Figure 6: Difference in calculated costs and maximum costs based on the ensemble of each of the 203 optimal control runs after six hours

4 Model Uncertainty

The model was calibrated with available data from a storehouse. A perfect fit, however, is not a realistic assumption because of modeling deficiencies, changing internal conditions and so on. From the calibration it results that the model lacks information to be a precise predictor. In general, the model fits quite well but at some instances misfits occur.

To evaluate the effect of an imperfect model, model parameters are varied and this modified model is assumed to be the actual system. The model is changed by changing the parameters p_1, p_2 and p_3 of eqn. The changes may vary between 50% and 150% of the nominal value. The selected parameter variability is chosen quite arbitrarily but are within range with the estimated parameters of several different storehouse compartments. Fifty parameter sets are obtained with Latin hypercube sampling, assuming that the parameters are uncorrelated. The worst-case scenarios for all 203 optimal control runs are given in **Figure 7**.

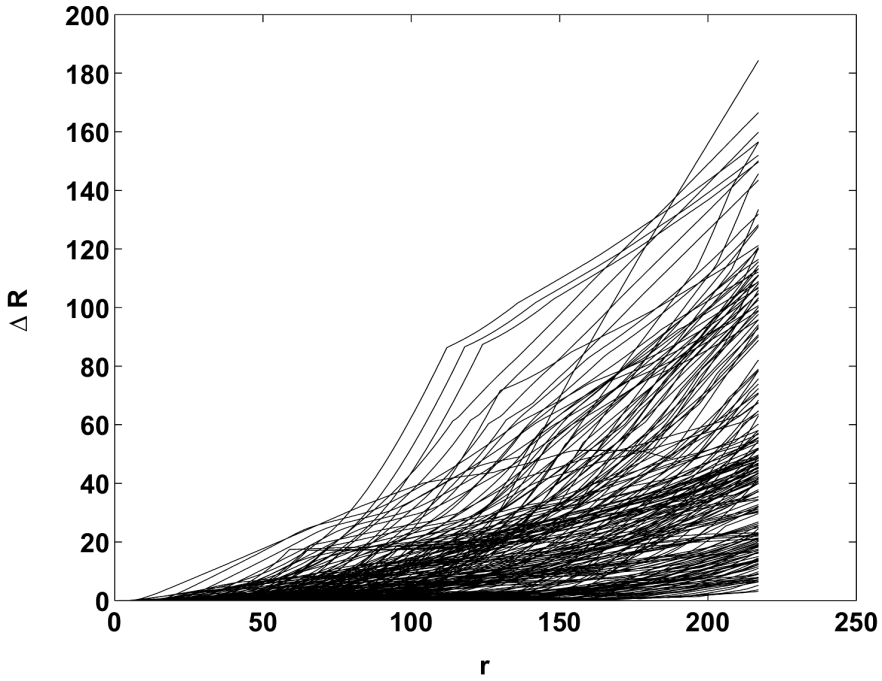

Figure 7: Difference in calculated nominal costs and upper bound of costs based on the parameter ensemble of each of the 203 optimal control runs

For the given parameter sets the costs increase considerably. To get more insight in the closed-loop uncertainty, the maximum cost differences at the 6 hour forecast for each of the subsequent control runs are given in **Figure 8**.

At this specific horizon the cost increase is within reasonable limits as can be seen in table 1.

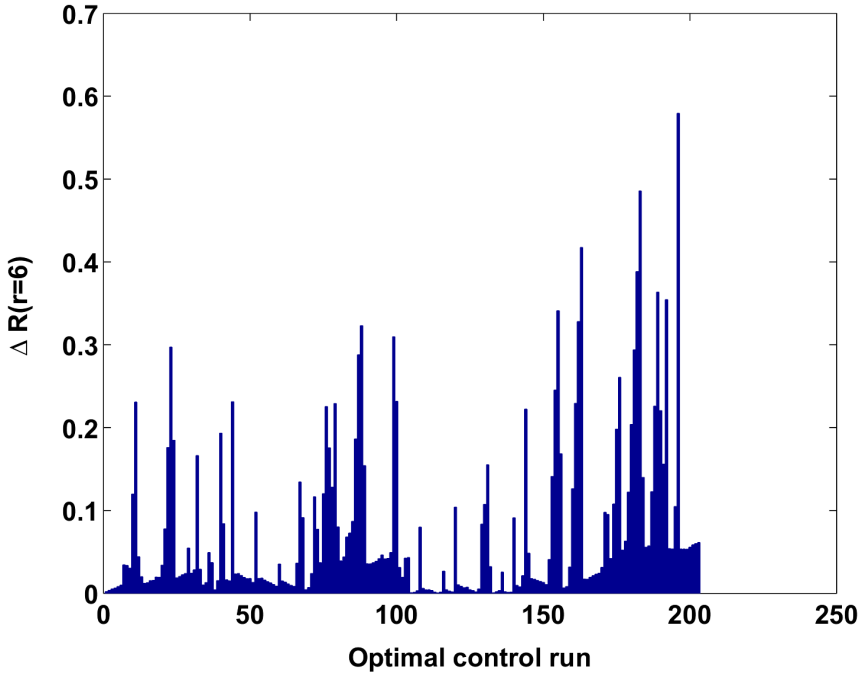

Figure 8: Difference in calculated nominal costs and upper bound of costs based on the parameter ensemble of each of the 203 optimal control runs after six hours

5 Discussion

If in open loop the calculated costs based on the weather forecast and the *actual* costs given observed weather and realized controls are compared, it is evident that the costs can both increase and decrease. Not only the total costs are of importance but also the relative costs. During a long warm period the optimal calculated costs will increase significantly. The absolute increase or decrease due to uncertain weather forecasts can then be quite large whereas the relative change may be reasonable. The opposite may also occur, *i.e.* large relative change versus a low absolute change.

Prior knowledge about the uncertainty of the forthcoming weather is very useful to study uncertainties in the near-future costs. From figures 2 and 4 it can be calculated that for this specific case the cost-increase is in general much larger for the worst-case scenario than for the observed weather. The same can be seen in the closed loop control in figures 5 and 6. From these figures it can be seen that the ensemble, indeed, is a useful tool to evaluate the uncertainty of the cost function a priori.

From the chosen parameter variability it can be seen that the worst-case scenario generally has a larger effect on the cost function than the worst-case weather uncertainty. The actual uncertainty based on the true parameters, however, could not be evaluated as these were not available. It is expected that, in analogy to the weather forecast uncertainty, the actual cost increase is lower and in some optimal control runs even decreases.

It has been shown in this case study that applying feedback every six hours reduces the uncertainty of the calculated costs tremendously. Given an uncertainty interval the maximum feedback time can be calculated as well. In **Table 2** the maximum deviation in the cost function from the weather forecast uncertainty is given for different time-intervals between two subsequent optimal control runs (I).

It can be seen that the difference in costs up to 24 hours is relatively small. Hence, in case of a communication failure between optimization algorithm and control computer of less than *e.g.* one day no manual intervenience is required.

Table 2: Additional costs of the realized costs and the worst-case scenarios for model and weather forecast uncertainty.

	6	12	18	24	48	72
$\Sigma(\Delta J)/J_{tot}$	0.37 %	1.15 %	2.05 %	3.17 %	8.0 %	14.2 %

6 Concluding Remarks

In post-harvest storage of agricultural produce, optimal control strategies can be used to anticipate on future weather conditions. In the simulation case-study with real weather forecasts and observed weather it appeared that there are only slight cost increases due to uncertainty in weather forecasts if the optimal control problem is calculated every 6 hours in a RHOC context. Furthermore, even the a priori known worst-case scenario from the weather forecast ensemble leads to a satisfactory result with a 6 hour interval RHOC. The interval between two subsequent optimal control runs can be increased given a user defined uncertainty limit. In the shown case an increase up 24 hours leads to a maximum increase of less then 5%.

If the model is known to be inaccurate it is expected that the uncertainty of the total costs are more subjected to model uncertainty then to weather forecast uncertainty. For the investigated case, the worst-case scenario still showed an increase of the total cost of less than 5% which seems to be acceptable. The effect of the actual model uncertainty, however, can only be calculated a posteriori.

Acknowledgements

We are indebted to Weathernews Benelux for providing the weather forecasts and Agrotechnology and Food Innovations for providing the storage model and the accompanying RHOC solutions. This research is part of the WIC2 project, which is carried out in cooperation with PRIVA Hortimation, Tolsma, WNI and Agrotechnology and Food Innovations.

References

CRAWLEY D.B., LAWRIE L.K., WINKELMANN F.C., BUHL W.F., HUANG Y.J., PEDERSEN C.O., STRAND R.K., LIESEN R.J., FISHER D.E., WITTE M.J.,GLAZER J. (2001): Energyplus: creating a new-generation building energy simulation program. *Energy and Buildings*, 33 (4): 319-331, Sp. Iss. SI

DOESWIJK T.G., KEESMAN K.J. (2005): Adaptive weather forecasting using local meteorological information. *Biosystems Engineering*, 91 (4): 421-431

HENZE G.P., KALZ D.E., FELSMANN C., KNABE G. (2004): Impact of forecasting accuracy on predictive optimal control of active and passive building thermal storage inventory. *Hvac & R Research*, 10 (2): 153-178

KEESMAN K.J., PETERS D., LUKASSE L.J.S. (2003): Optimal climate control of a storage facility using local weather forecasts. *Control Engineering Practice*, 11 (5): 505-516

LUKASSE L.J.S., DE KRAMER-CUPPEN J.E., VAN DER VOORT A.J. (2006a): A physical model to predict climate dynamics in ventilated bulk-storage of agricultural produce. *International Journal of Refrigeration*. Accepted for publication

LUKASSE L.J.S., VAN DER VOORT A.J., DE KRAMER-CUPPEN J.E. (2006b): Optimal climate control to anticipate future weather tnd energy tariffs. In *Proceedings of Control Applications in Post-Harvest and Processing Technology*, Potsdam, Germany. Bornimer Agrartechnische Berichte. Accepted for publication.

PALMER T.N., BARKMEIJER J., BUIZZA R., PETROLIAGIS T. (1997): The ecmwf ensemble prediction system. *Meteorological Applications*, 4 (4): 301-304

STENGEL R.F. (1994): *Optimal Control and Estimation*. Dover publications, New York

TAP F. (2000): Economics-based optimal control of greenhouse tomato crop production. PhD thesis, Wageningen University

Optimal Control of a Finite-Capacity Fresh-Food Distribution Network

F. Dabbene[1], P. Gay[2] and N. Sacco[3]
[1] IEIIT-CNR, Politecnico di Torino, 10129 Torino, Italy
[2] DEIAFA, Facoltà di Agraria, Università degli Studi di Torino, Grugliasco (TO), Italy
[3] DAUIN, Politecnico di Torino, 10129 Torino, Italy

Abstract: *In this paper we present a novel approach for the optimization of fresh-food supply chain by managing a trade-off between logistics and some index measuring the quality of the food itself.*

We propose an hybrid model of the chain, with a part constituted by event-driven dynamics (the supply chain itself) and a part with time-driven dynamics (the dynamics of some parameters characterizing the jobs in the supply chain). The proposed optimization method has been implemented taking into account finite-capacity constraints of the nodes of the supply-chain. Copyright © 2006 IFAC

Keywords: *Food Supply Chains, Hybrid systems, Optimisation*

1 Introduction

The distribution of fresh food products such as meat, vegetables, fruits and dairy from producer to vendor is in general a complex process, owing to the perishable nature of these agricultural products.

A distribution (or supply) chain is constituted by a sequence of activities performed in order to deliver a product to a destination with the highest possible quality. Any activity has a potential impact on the product due to the interaction between the action environment and the product.

In some cases, e.g. when a product is stored into a cell together with other products, not only the interaction between the product and the surrounding environment is important, but also the interactions between the various products. In this context each product can be seen as an “object” described by a dynamical model which takes into account the physiological processes occurring in the product.

These processes are generally affected by the conditions in the immediate environment of the product itself.

The nature of these interactions is largely defined by means of fundamental physical laws and the generally accepted rules in a particular discipline.

The first step in the design of a node of a supply chain (e.g. a chiller or a storage cell) is for the user to draw up specifications. In fact, in many cases, poor design in existing networks is mainly due to a mismatch between the purpose the nodes were originally designed for and how they are actually used. A proper sizing of network throughput and node loads could be in fact a difficult task without the aide of ad-hoc simulation tools.

In this paper we present a novel approach for the optimization of fresh-food supply chains by managing a trade-off between the logistics of the food treatment, for instance the food delivery date against the quality of the food itself.

Some preliminary results have been proposed in (DABBENE *et al*. 2005) where it was assumed that the single node constituting the network can process more than one job at a time and that it has infinite capacity. Therefore we did not consider queues before the single nodes. In this paper we deal with the more realistic case in which the node have a finite capacity and can process a maximum number of jobs at a time. This fact will highly influence the optimization of the logistics.

2 Problem Description and Notation

In this section, we present the problem of optimizing a food supply chain. The first step consists of constructing a mathematical model of the chain. The model we propose is a hybrid model, with a part constituted by time-driven dynamics and one by event-driven dynamics.

We consider a supply-chain configuration consisting in a network formed by n successive nodes in which the different jobs are processed in a sequential way.

To keep the formalism at a general level, we will use the term “job” to refer to the generic portion of food to be treated (which can be for example a pallet of fresh-fruits, a meat carcass, etc.), and the term “nodes" to refer to the different servers in which different activities are performed on the product (e.g. refrigeration or storage cells, transportation, etc.).

The total number of jobs that enter the chain is m. The jobs enter in the first cell at different time instants (and with possibly different initial conditions of the parameters describing them) and are processed sequentially from node 1 to node n. Every node has the possibility to process more than one job at a time. The number of processed jobs in a node at a specific instant is realistically bounded (finite process capacities).

To the generic i^{th} job we associate a measure of goodness $y_i(t)$, that we call *attribute*, and which represents some characteristics (e.g. internal temperature, firmness, ripening, microbial charge, etc.) that we choose as representative of the goodness of the product.

The attributes $y_i(t)$ of the different jobs vary in time according to a differential equation which depends on the operating conditions of the network and on the different j^{th} node where the job is currently processed. Analogously the supply-chain is characterized by a

vector of parameters $\chi \in \mathrm{R}^{\mathrm{q}}$ that represents the operating conditions under which the network is running. Some of these parameters may be directly imposed by the network manager, and can therefore be considered as *control variables*, while other parameters are instead not directly accessible. In a general setting, these uncontrollable parameters may be either fixed (deterministic) and possibly not perfectly known, or stochastic subject to random variations. Examples of such parameters may be transportation times, power of already existing plants, etc.. Hence, we partition the parameter vector $\chi \in \mathrm{R}^{\mathrm{q}}$ into two vectors, i.e.

$$\chi = \begin{bmatrix} \chi_C \\ \chi_{NC} \end{bmatrix},\ \chi_C \in \mathrm{R}^{\mathrm{qC}},\ \chi_{NC} \in \mathrm{R}^{\mathrm{qNC}} \tag{1}$$

with $q = q_{NC} + q_C$, and where χ_C contains all the controllable parameters, while χ_{NC} contains the remaining (uncontrollable) ones.

Moreover, taking into account the physical meaning of the parameters, the vectors χ_C and χ_{NC} can be partitioned again as

$$\chi_C = \begin{bmatrix} \theta_C \\ \Delta T_C \end{bmatrix} \text{ and } \chi_{NC} = \begin{bmatrix} \theta_{NC} \\ \Delta T_{NC} \end{bmatrix} \tag{2}$$

being θ_C and θ_{NC} the vectors which gather the controllable and uncontrollable physical parameters of the supply chain, such as for instance the power of the cells, whereas ΔT_C and ΔT_{NC} are the are the vectors which gather the times spent by the jobs in the cells.

Finally with the aim of simplifying the notation, we also introduce the vectors

$$\theta = \begin{bmatrix} \theta_C \\ \theta_{NC} \end{bmatrix} \text{ and } \Delta T = \begin{bmatrix} \Delta T_C \\ \Delta T_{NC} \end{bmatrix} \tag{3}$$

that gather the physical and time variables, respectively.

In the following sections we will describe the discrete-event dynamics of the supply chain and the time-driven dynamics of the attributes $y_i(t)$.

2.1 Discrete-event dynamics

If we denote by τ_i^j the time instant in which the i^{th} job departs from the j^{th} node and we suppose that each node can contain infinite jobs, then we can formalize the discrete-event dynamics by means of the following recursive equation, for $i=1,\ldots,m$ and $j=1,\ldots,n$

$$\tau_i^j = \tau_i^{j-1} + s_i^j(\Delta\mathrm{T}), \quad \tau_i^0 = a_i \tag{4}$$

where a_i denotes the arrival time of the i^{th} job in the first node. The function $s_i^j(\Delta\mathrm{T})$ gives the time the i^{th} job spends in the j^{th} node; this time is a function of the parameters ΔT and, therefore, of χ.

Hence, the vectors $\tau_i = \left[\tau_i^0 \quad \tau_i^1 \quad \ldots \quad \tau_i^n\right]^T$, $i=1,\ldots,m$, gather the times when the i^{th} job switches between nodes. With this notation the generic element $\delta\tau_i^j$ of the vector $\Delta\mathrm{T}$, which represents the time spent by the i^{th} job in the j^{th} cell, can be written as

$$\delta\tau_i^j = \tau_i^j - \tau_i^{j-1} \tag{5}$$

and belongs to $\Delta\mathrm{T}_C$ or $\Delta\mathrm{T}_{NC}$. Hence, equation (4) can be stated as

$$\tau_i^j = \tau_i^{j-1} + \delta\tau_i^j, \quad \tau_i^0 = a_i \tag{6}$$

being $s_i^j(\Delta\mathrm{T}) = \delta\tau_i^j$. Finally, for notation ease, we also define the composite vector $\tau = \left[\tau_1^T \quad \tau_2^T \quad \ldots \quad \tau_m^T\right]^T$ that we call the *vector of events occurrence time*.

The position (node) $p_i(t)$ in which the i^{th} job is at time *t* can be therefore obtained as a function of τ_i. In particular, we may represent the evolution of

the variables $p_i(t)$, $i=1,\ldots,m$, using a simple differential equation

$$\dot{p}_i(t) = \sum_{j=0}^{n-1} \delta\left(t - \tau_i^j\right), \quad p_i(0) = 0 \tag{7}$$

where $\delta(\cdot)$ is the Dirac delta function.

Clearly, the variable p_i can assume only the discrete values $0,1,2,\ldots,n$ and is a monotonically

nondecreasing function of time.

Analogously, at each time instant *t*, the number of jobs $m^j(t)$ in the j^{th} node can be computed noticing that

$$\begin{aligned} \dot{m}^j(t) &= \sum_{i=1}^{m} \delta\left(t-\tau_i^{j-1}\right) - \sum_{h=1}^{m} \delta\left(t-\tau_h^{j}\right) \\ m^j(0) &= 0. \end{aligned} \tag{8}$$

Equations (8) indicates that the number of jobs in the j^{th} node increases when a generic job *i* leaves the $(j-1)^{th}$ node at τ_i^{j-1} and enters the j^{th} node and decreases when a generic job *h* (not necessarily the i^{th} one) leaves the node j^{th} at τ_h^j.

Equations (7) and (8) fully describe the dynamic behaviour of the network, giving at each time instant, the number of the jobs present in each node. These equations were derived in the ideal case of infinite capacity nodes. In the next section, we specify these equations to the case when the nodes have finite capacity.

2.2 Finite capacity constraints

As previously mentioned, a more realistic description of the systems should take into account the case of finite capacity of the nodes of the supply chain. To this end, if we define the capacity $C_j \in N$ for the j^{th} node $j=1,\ldots,n$, it descends that a generic job *i* can enter such a node at the time τ_i^{j-1} only if $m^j\left(\tau_i^{j-1}\right) < C_j$ that is, only if at time τ_i^{j-1} there is at least one free slot in the j^{th} node.

Taking into account such capacity constraints, the event-driven dynamics described by (6) becomes

$$\tau_i^j = \begin{cases} \tau_i^{j-1} + \delta\tau_i^j & \text{if } m^{j+1}\left(\tau_i^{j-1} + \delta\tau_i^j\right) < C_{j+1} \\ \min\limits_h \left\{ \tau_h^{j+1} \mid \tau_h^{j+1} > \tau_i^{j-1} + \delta\tau_i^j \right\} & \text{if } m^{j+1}\left(\tau_i^{j-1} + \delta\tau_i^j\right) = C_{j+1} \end{cases} \tag{9}$$

$$\tau_i^0 = a_i$$

with $\tau_i^j = \tau\left(\Delta T, C_{j+1}\right)$.

The above system gives the time instant in which the i^{th} job departs from the j^{th} node in both the cases when the $(j-1)^{th}$ node has at least a free slot or not.

In particular, the first of the (9) coincides with the first of the (6) and gives the time instants in which the i^{th} job can departs from the j^{th} node when free space is available in the node *j*+1. As in the non-constrained case, the term $s_i^j(\Delta T)$ in the equation represents the time spent by the job *i* in the node *j* and it is a function of the variables ΔT. On the other hand, the second equation of the (9) says that the i^{th} job can depart from the j^{th} node as soon as another job departs from the $(j+1)^{th}$ node. In particular, the first job leaving the $(j+1)^{th}$ node is given by $\bar{h} = \arg\min_h \left\{ \tau_h^{j+1} \mid \tau_h^{j+1} > \tau_i^{j-1} + \delta\tau_i^j \right\}$. In this case, the actual times δ_i^j and δ_i^{j+1} the i^{th} job spends in the j^{th} and $(j+1)^{th}$ node depend on the time instant $\tau_{\bar{h}}^{j+1}$ the $\bar{h}^{th}$ job departs from the node *j* +1, and may be obtained using the following relations:

$$\begin{aligned} \delta_i^j &= \tau_{\bar{h}}^{j+1} - \tau_i^{j-1} > \delta\tau_i^j \\ \delta_i^{j+1} &= \tau_i^{j+1} - \tau_{\bar{h}}^{j+1} > 0 \end{aligned} \qquad (10)$$

In particular, the first relation in (10) gives the time spent by the i^{th} job in the j^{th} node whereas the second one gives the time spent by the i^{th} job in the $(j+1)^{th}$ node. Note that $\delta_i^j > \delta\tau_i^j$ and that $\delta_i^{j+1} > 0$ since $\tau_i^{j+1} > \tau_{\bar{h}}^{j+1}$.

In the formulation here described, due to the second of the (10), the time instants τ_i^k, $k > j+1$, at which the i^{th} job departs from the k^{th} node, does not change (we refer to this case, as *case a*). An alternative solution may be found by imposing that $\delta_i^{j+1} = \delta\tau_i^{j+1}$, that is by delaying all the i^{th} jobs departures from the node *k*, $k > j+1$. In this second formulation, we define the delay $\Delta_i^j = \delta_i^j - \delta\tau_i^j = \tau_{\bar{h}}^{j+1} - \tau_i^j$, that is the time spent by the i^{th} job in the j^{th} node waiting for a free slot in the $(j+1)^{th}$ node. Then we define the new time instants when the job i^{th} job departs from the k^{th} node, for $k > j$, by means of the relation

$$\bar{\tau}_i^k = \tau_i^k + \Delta_i^j, \quad k > j \qquad (11)$$

and we refer to this case, as *case b*.

It is worth noting that the two cases above described represent two alternative ways to manage the event-driven dynamics of the jobs in a finite capacity environment.

Summarizing, the event-driven dynamics in equation (9) can be stated as the single equation

$$\begin{aligned}\tau_i^j &= \left[\tau_i^{j-1} + \delta\tau_i^j\right]\left[1 - \delta_K\left(m^{j+1}\left(\tau_i^{j-1} + \delta\tau_i^j\right), C_j\right)\right] \\ &\quad + \delta_K\left(m^{j+1}\left(\tau_i^{j-1} + \delta\tau_i^j\right), C_j\right)\min_h\left\{\tau_h^{j+1} \mid \tau_h^{j+1} > \tau_i^{j-1} + \delta\tau_i^j\right\} \\ \tau_i^0 &= a_i\end{aligned} \tag{12}$$

where δ_K is the above introduced Kronecher function

$$\delta_K(i,j) = \begin{cases} 1 & \text{if } i = j \\ 0 & \text{otherwise.} \end{cases} \tag{13}$$

Note that, due to the condition expressed by the equation (8), it descends that equation (14) is an equivalent, more compact, formulation of (12) where the condition expressed by the "if" statement are managed by the Kronecker delta functions.

2.3 Time driven dynamics

We denote with $y = [y_1 \quad y_2 \quad \dots \quad y_m]^T$ the vector of attributes. As already mentioned, the attribute $y_i(t)$ relative to the i^{th} job evolves in time according to a differential equation. More precisely, $y(t)$ can be seen as the output of a system of differential equations

$$\begin{aligned}\dot{x}(t) &= f(x(t), \tau, \chi) \\ y(t) &= g(x(t), \tau, \chi)\end{aligned} \tag{14}$$

with initial conditions $x(0) = \varsigma_0$, being *x* a vector gathering the state variables of the different products and the states variables that describe the interaction with the surrounding environment. Notice that equations (12) and (14) define in all aspects a hybrid system, where the time-driven dynamics of (14) depend on the vector of events τ, whose dynamics are expressed by the recursion (12). We remark also that, looking at the problem from a different point of view, (14) is in effect a switching system in which the switching times are regulated by the recursion (12).

3 Optimization

The model described in the above section discriminates all the possible behaviour that the system can exhibit acting on the controllable parameters χ_C. The role of the network manager consist of choosing the best operating conditions considering different aspects as operating

expenses, product and process conditions and final product quality.

Goal of the optimization algorithm is to choose the controllable parameters χ_C in order to minimize a performance function that measures the performance of the supply chain we propose in this section. In particular, we introduce a performance function *J* constituted by the sum of three terms

$$J(\chi) = J(\chi_C, \chi_{NC}) = C(\chi_C, \chi_{NC}) + P(\chi_C, \chi_{NC}) + D(\chi_C, \chi_{NC})$$

The first term takes into account the cost related to the particular operating condition χ_C (e.g. power consumption, transport costs, etc.). The second term contains the performance requirement relative to the product attributes, that could be expressed in different ways depending on the specific product. For instance, we may consider:

- trajectory tracking: we desire that $y_i(t)$ follows a given reference $\tilde{y}(t)$; therefore $P(\chi_C, \chi_{NC}) = \|y_i(t) - \tilde{y}(t)\|$, being $\|\cdot\|$ a norm (for instance $\|\cdot\|_2$, $\|\cdot\|_\infty$, etc.)
- final value objective: $y_i(t)$ should achieve, leaving the last node at τ_i^n, the desired value $\bar{y}_i$; this corresponds to imposing $P(\chi_C, \chi_{NC}) = \left\| y_i\left(\tau_i^n\right) - \bar{y}_i \right\|$.

Since the behaviour of $y(t)$ depends on the operating conditions χ, requirements 1. and 2. are traduced in a cost term $P(\chi_C, \chi_{NC})$.

The third term $D(\chi_C, \chi_{NC})$ is related to the logistic aspects of the chain, such as due date d_i (which measures the difference between the actual final time τ_i^n and the desired one $\bar{\tau}_i$ or deadlines, by means of costs of earliness $C_E(\chi) = \sum_{i=1}^{m} \left(\max\left\{0, d_i - \tau_i^n\right\} \right)^\alpha$ or tardiness $C_T(\chi) = \sum_{i=1}^{m} \left(\max\left\{0, \tau_i^n - d_i\right\} \right)^\beta$, where $\alpha \in \mathrm{N}$ and $\beta \in \mathrm{N}$ are suitable coefficients which allows to consider linear, quadratic, etc., earliness and tardiness costs.

From a practical point of view, the operating conditions in general are constrained and bounded in specific intervals. Moreover, there are other constraints due to the finite capacity of the nodes, as described in Section 2.2, and which yield to unfeasible values of the controllable parameters.

This corresponds to assume the variable χ_C to belong to a compact set X_C, e.g. $\chi_C \in \mathrm{X}_C$.

The optimization problem simply writes

$$\min_{\chi_C \in \mathrm{X}} J(\chi_C, \chi_{NC}). \tag{15}$$

We remark that $J(\chi)$ is not an algebraic function, but involves differential terms. In order to solve the problem (15), in the next section we have to discuss how to manage the non controllable parameters $\chi_C \in \mathrm{X}_C$ in both the cases of infinite and finite capacity.

Thus, in the next sections, we will first describe the optimization procedure in the nominal case and with uncertainty in the case of infinite capacity. Then, we describe a way to build feasible solutions for the more complicate finite capacity case.

3.1 Uncertainty

In a real supply chain there are many factors that can introduce uncertainty in the network. First of all the natural variance of biological products that may render the behaviour (time driven dynamics) of each job slightly different. In many applications, this kind of variability cannot be neglected and could have a high influence on the observed system (see examples in e.g. HERTOG 2002, HERTOG 2004, and PEIRS *et al*. 2002). Second, process conditions in each node that can vary and, third, discrete events dynamics could be perturbed by external and unmodelled factors or disturbances.

The role and the way to manage uncertainty in post-harvest and food engineering processes has been recently considered in many works (see e.g. VAN IMPE *et al*. 2001 and references therein).

In the so-called second-order modelling approach (NAUTA 2000), for example, the perturbations affecting empirical data and/or model parameters are subdivided in uncertainty and/or variability.

Uncertainty represents the lack of perfect knowledge of a parameter value, which may be reduced by additional measurements, further improvement of a measurement method (e.g. detection limit, precision), or, if applicable, model structure improvement.

Variability, on the other hand, represents a true heterogeneity of the population that is a consequence of the physical system and is irreducible by additional measurements. However, since in a quantitative study it is often difficult to separate variability and uncertainty, especially when both have the same order of magnitude, an alternative is to globally characterize them by associating a probability function to each quantitative parameter.

Different methods have been proposed to quantify the effects of the propagation of the uncertainty affecting model parameters on the output of the studied system. One of the widely used is the Monte Carlo method. The main drawback of this technique may be the large number of repetitive simulation necessary to obtain an acceptable level of accuracy

and the fact that the distribution over the data points must be completely specified in a probabilistic sense.

Other methods have therefore been suggested to provide computationally attractive alternatives for specific applications, like, for example, for distributed parameter systems with parameter fluctuations in space (e.g. the first-order perturbation algorithm, see NICOLAÏ *et al*. 2000) or simultaneously in space and time (e.g. the variance propagation algorithms.

Since the objective of this research is methodology oriented, only the (overall) perturbation on parameters is considered without attempting to distinguish between uncertainty and variability.

In the specific, the vector of non controllable parameters χ_{NC} may be affected by random uncertainty, that is $\chi_{NC} = \overline{\chi}_{NC} + \nu_{\chi}$

where χ_{NC} is the nominal value of the non-controllable variables, and ν_{χ} is a random variable with zero mean and associated probability measure Ψ. With this assumption the cost function $J(\chi_C, \chi_{NC})$ results to be a random variable. Hence, the problem needs to be formulated in a stochastic framework.

A frequently used requirement in this context is to optimize an “average” instance of the problem: in other words, one asks to minimize the expected value of the objective function taken with respect to the random uncertain parameters χ_{NC} (see for instance KUSHNER & YIN 1997), that is

$$\min_{\chi_C \in \mathrm{X}} E(\chi_C), \qquad E(\chi_C) \doteq E_{\chi_{NC}} \{ J(\chi_C, \chi_{NC}) \} \tag{16}$$

where $E(\chi_C) = \hat{E}(\chi_C) + \upsilon$ is the expectation of $J(\chi_C, \chi_{NC})$ taken with respect to the probability measure Ψ. The above stochastic optimization problem is in general very hard to solve, since the mere evaluation of the expected value $E(\chi_C)$ (even if an analytical expression of the cost function were available, which is not our case), would require the solution of a multiple integral.

Here, following a similar philosophy, we consider an *empirical* version of the expectation

$$\hat{E}(\chi_C) \doteq \frac{1}{N} \sum_{i=1}^{N} J\left(\chi_C, \overline{\chi}_{NC} + \nu_{\chi}^{(i)}\right) \tag{17}$$

where $\nu_{\chi}^{(i)}$ are uncertainty samples drawn according to the probability measure Ψ, and make use of this approximation for the solution of the optimization problem. In principle $\hat{E}(\chi_C)$ could be evaluated using Monte Carlo analysis with a large enough number of samples *N*, but this solution generally leads to excessive computational loads. To overcame this problem, we follow the solution approach proposed by Spall (see e.g. SPALL 1992, SPALL 2003) and tackle the problem via a Simultaneous-Perturbations Stochastic Approximation (SPSA) approach. This method allows to reduce the computation complexity of the problem by introducing, at each iteration, an approximation on the gradient which requires only two evaluation of the cost function.

In details, the SPSA algorithm is based on a recursive algorithm in which successive approximations of the optimal value

$$\chi_C^* \doteq \arg \min_{\chi_C \in \mathrm{X}} E(\chi_C) \tag{18}$$

are recursively constructed based on noisy observations of the cost function. In other words, we assume to have *noisy measurements* of our cost function $E(\chi_C)$, e.g. $E(\chi_C) = \hat{E}(\chi_C) + \upsilon$, where υ is a random variable with zero mean.

The recursion mimics a classical gradient descent method, in which the gradient w.r.t. χ_C of the functional $E(\chi_C)$ is not available but approximated at each step using only two (possibly noisy) evaluations of the cost function.

Formally, let $\chi_C^{(k)}$ denote the k^{th} estimate of the optimal solution, and let $\left\{\eta^{(k)}\right\}$ be a random sequence of column random vectors where $\eta^{(k)} = \left[\eta_1^{(k)} \quad \eta_2^{(k)} \quad \ldots \quad \eta_{NC}^{(k)}\right]$ are not necessary identically distributed. The two-sided SPSA algorithm to update $\chi_C^{(k)}$ is constructed as follows

$$\chi_C^{(k+1)} = \Pi_{\mathrm{X}}\left[\chi_C^{(k)} - \alpha^{(k)}\left[\eta^{(k)^{-1}}\right]\frac{\hat{E}_+^{(k)} - \hat{E}_-^{(k)}}{c^{(k)}}\right] \tag{19}$$

where $\Pi_{\mathrm{X}}[\cdot]$ is the projection operator on the set X, $c^{(k)}$ is a positive sequence converging to zero, $\alpha^{(k)}$ is the step-size multiplier, and $\left[\eta^{(k)^{-1}}\right]$ is defined as the vector containing the inverses of the elements of $\eta^{(k)}$. The values $\hat{E}_{\pm}^{(k)}$ represent the empirical cost function taken at parameter values $\chi_C^{(k)} \pm c^{(k)}\eta^{(k)}$, i.e.

$$\hat{E}_{\pm}^{(k)} \doteq \hat{E}\left(\chi_C^{(k)} \pm c^{(k)} \eta^{(k)} \right)$$

Various convergence results of this algorithm have been proven under different hypothesis, see for instance SPALL 2003, GERENCSER *et al.* 2001, HE *et al.* 2003 and references therein. In particular, it can be shown that the algorithm still converges when the empirical mean is constructed with a very small number of samples. Indeed, even a single sample is sufficient, i.e. *N*=1 in (17), thus allowing to significantly simplify the algorithm, generating at each step a single instance $\nu_{\chi}^{(k)}$ of the uncertainty and letting

$$\hat{E}_{\pm}^{(k)} \doteq J\left(\chi_C^{(k)} \pm c^{(k)} \eta^{(k)}, \overline{\chi}_{NC} + \nu_{\chi}^{(k)} \right)$$

3.2 Building feasible solutions

The optimization algorithm introduced above provides solutions which may be not feasible when the finite capacity constraints are taken into account or when some physical parameters do not belong to their admissible set Θ_C. In this section we describe the optimization procedure which manages such unfeasibility. To this aim it is worth noting that any feasible solution $\chi_C^{(k+1)} = \left[\chi_C^{(k+1)} \quad \Delta \mathrm{T}_C^{(k+1)} \right]$ can be built by means of a projection step, performed by the operator $\Pi_{\mathrm{X}}[\cdot]$ in (19), which operate in different ways for the physical parameters and the time vector, giving

$$\begin{aligned} \chi_C^{k+1} &= \Pi_{\mathrm{X}_C}\left[\hat{\theta}_C^{k+1} \right] \\ \Delta \mathrm{T}_C^{k+1} &= \Pi_{\Delta \mathrm{T}}\left[\Delta \hat{\mathrm{T}}_C^{k+1} \right] \end{aligned} \qquad (20)$$

where $\hat{\chi}_C^{k+1}$ and $\Delta \hat{\mathrm{T}}_C^{k+1}$ are the unfeasible solution provided, at the k^{th}, step by the SPSA algorithm and χ_C^{k+1} and $\Delta \mathrm{T}_C^{k+1}$ are the projected, feasible, solution provided by equations (26).

As regarding the operator $\Pi_{\mathrm{X}_C}[\cdot]$, it simply computes the orthogonal projection of $\hat{\chi}_C^{k+1}$ into X_C whereas $\Pi_{\Delta \mathrm{T}}[\cdot]$ needs a non-trivial implementation. In effect, in order to respect finite capacity requirements, given the vector $\Delta \hat{\mathrm{T}}_C^{k+1}$ the actual switching times τ_i^j have to be computed by means of equation (14). Then, each single element of the feasible vector can be easily computed by means of the (12) and, then, by inverting the function $s_i^j(\Delta \mathrm{T})$.

3.3 The optimization algorithm

We are now in the position of explicitly state the optimization algorithm for the approximate solution of the optimization problem (20):

The modified SPSA algorithm

- *Select initial point* χ_0*, number of steps K, and set k=0*
- *While* $k \le K$
  - $k = k+1$
  - *Generate a sample of uncertainty* $\chi_C^{(k)} = \overline{\chi}_{NC} + \nu_\chi^{(k)}$
  - *Generate a vector* $\eta^{(k)}$ *according to a Bernoulli processes*
  - *Build* $\hat{E}_\pm^{(k)} \doteq J\left(\chi_C^{(k)} \pm c^{(k)}\eta^{(k)}, \overline{\chi}_{NC} + \nu_\chi^{(k)}\right)$
  - *Construct the next point as* $\chi_C^{(k+1)} = \Pi_{\mathrm{X}}\left[\chi_C^{(k)} - \alpha^{(k)}\left[\eta^{(k)^{-1}}\right]\frac{\hat{E}_+^{(k)} - \hat{E}_-^{(k)}}{c^{(k)}}\right]$
- *end while*

Details on the implementation of this algorithm with case studies can be found in DABBENE *et al.* (2006)

4 Conclusions

We introduced a general framework for describing a fresh-food supply chain, and proposed an optimization methodology to improve the performances of the network preserving the quality of the product. More precisely we introduced an optimization procedure which gives the optimal values of the parameters describing the nodes of the supply-chain and the optimal time each job must spend in any node. The proposed method is able to handle finite--capacity constraints of the nodes.

References

DABBENE F., GAY P., SACCO N., TORTIA C. (2005): Optimization of Fresh-Food Supply Chains in Uncertain Environments: an Application to the Meat Refrigeration Process, *Proc. of the Control Decision Conference*, 2077-2082, Seville, Spain

GERENCSÉR L., HILL S.D., VÀGÒ Z. (2001): Discrete Optimization via SPSA, *Proceedings of the American Control Conference*, 1503-1504, Arlington, VA, 2001

HE Y., FU M.C., MARCUS S.I. (2003): Convergence of Simultaneous Perturbation Stochastic Approximation for Nondifferentiable Optimization. *IEEE Transactions on Automatic Control*, AC 48: 1459-1463

HERTOG M.L.A.T.M. (2002): The impact of biological variation on postharvest population dynamics. *Postharvest Biol. and Technol.*, 26: 253-263

HERTOG M.L.A.T.M., LAMMERTYN J., DESMET M., SCHEERLINCK N., NICOLAÏ B.M. (2004): The impact of biological variation on postharvest behaviour of tomato fruit. *Postharvest Biol. and Technol.*, 34: 271-284

KUSHNER H.J., YIN G. G. (1997): *Stochastic Approximation Algorithms and Applications*. Springer, New York

PEIRS A., SCHEERLINCK N., BERNA PEREZ A., JANCSÓK P., NICOLAÏ B.M. (2002): Uncertainty analysis and modelling of the starch index during apple fruit maturation. *Postharvest Biol. and Technol.*, 26: 199-207

SPALL J.C. (2003): *Introduction to Stochastic Search and Optimization: Estimation, Simulation, and Control*. Wiley, New York

VAN IMPE J.F., BERNAERTS K., GEERAERD A.H., POSCHET F., VERSYCK K.J. (2001): Modelling and prediction in an uncertain environment, In: *Food Process Modelling* (TIJSKENS, L.M.M., HERTOG, M.L.A.T.M., NICOLAÏ, B.M. (Eds.)), 156-179. Woodhead Publishing Limited, Cambridge

Robust Control of Thermal Treatments in Can Industry

Alfonso Baños[1], P. García[2] and Lucía Checa[2]
[1] Dpto. Informática y Sistemas, Univ. Murcia, 30071 Murcia, Spain
[2] Centro Tecnológico Nacional de la Conserva y la Alimentación, Molina de Segura, Murcia, Spain

Abstract: *Thermal treatments for a variety of products in can industry result in a control problem with large uncertainty. Single design methods usually fail, being necessary the use of more advanced robust control techniques. In this work, the QFT technique has been used to design the control system of a heat exchanger as a central part of the CTC pilot plant. The experimental results show that the control system performs efficiently for a variety of usual products in can industry, and for different types of thermal treatments.*

Keywords: *can industry, process control, termal treatment, robust control.*

1 Introduction

The problem of temperature control for a wide variety of products and at different operation points (depending on the specific thermal treatment) is hard to solve by conventional means, for example using PID controllers with simple rules for tuning, or even autotuning. The reason is simple: the controller has to be designed for a proper treatment of the product in the presence of potentially large uncertainty with respect to the product. In addition, typically a product can be processed at different temperatures depending on the specific thermal treatment. Since the dynamic is highly non-linear and uncertain, a PID simply designed to work efficiently for a operation point and a particular product, usually degrades considerably its performance when the product and/or the operation point is changed.

In this work, QFT (Quantitative Feedback Theory), a robust control technique, is used for the control of an industrial heat exchanger. The followed approach is based on (BAÑOS *et al.* 2003). The basic idea consists of obtaining a family of linear time invariant (LTI) plants that describe the dynamic of the heat exchanger for different products and at different operation points. Once this family of LTI plants is obtained, modelled as a set of frequency responses, QFT is then applied to obtained a robust controller. The goal is ambitious, to get a stable control system with a specified performance in terms of allowed (narrow) tolerances over the closed loop frequency response.

In Section 2 a brief description of the CTC pilot plant and the thermal treatments that are the purpuse of this work is given. Section 3 develops the different identification strategies that will be used to obtain realistic plant model from a control point of view. In Section 4,

the QFT robust control technique is used to design a control system of CTC pilot plant heat exchanger. Basically, two designs are performed based on two sets of plant models. Finally, in Section 5, experimental results will be discussed.

2 The CTC Pilot Plant

CTC stands for “Centro Tecnológico Nacional de la Conserva y la Alimentación”. It is a national R+D centre that was founded in 1997 to serve the agriculture and food industry in improving its production process. CTC has a pilot plant designed to experiment new techniques and process before its transference to the industry. Can industry is a clear target of the centre, being important the application of advanced control techniques that may impact the (automatic) thermal treatment of different types of products before its packaging to a can. To this purpose, the CTC pilot plant (**Figure 1**) is equipped with two heat exchangers, for warming up and for cooling the product before its packaging.

Figure 1: The CTC Pilot Plant

In general, the thermal treatment is based on three goals (DOWNING 1996): i) to destroy microorganisms that are dangerous to health, ii) to destroy microorganisms and enzymes that may deteriorate the food, and iii) to optimise food quality factors with a minimum economical cost. From a control point of view, the main difficulties arise in the control of the warming up heat exchanger, since a good thermal treatment need to be done with very precise high temperature control in order to obtain an sterile product with good enough tasting properties. In addition, this has to be efficiently done for a variety of products, and at different operation points.

3 System Identification

Systems identification is a specialized and mature discipline and there are well established techniques (LANDAU 1990). Two single methods are used in this work: one parametric method based on the estimation of the step response (a first order with delay model has been used), and a non parametric model based on the estimation of the frequency response.

3.1 First order with delay models

A classic technique is to estimate low order models that fits with the (experimental) step response. Usually, this gives single models, e.g. a first order with delay is typical used in heat exchangers

$$P_\theta(s) = k \cdot \frac{e^{-sT_0}}{1 + T_P\, s} \qquad (1)$$

where the plant dynamic for a particular product and around an operation point is parameterised by the gain k, the time constant T_p and the delay T_0. Iteration of the method for different products and operation points (given by the specific thermal treatment) results in a single first method for obtaining the family of LTI plants that will serve as a model of the (warming up) heat exchanger for control purposes.

A large number of experiments have been done over the heat exchanger. The step response is then used to compute the parameters k, T_p, and T_0. For control purposes, the model needs to be expressed as a transfer function with parametric uncertainty. The results expressed as parametric uncertainty is given by the following intervals:

(2)

3.2 Frequency Response models

QFT is a frequency domain control technique. Thus, a family of frequency response is a good model for utilization of the method. In addition, frequency response gives richer information than the step response, and a superior control system design may be expected in terms of performance.

A widely used method for estimating the frequency response of a system is based on the used PRBS signals (LANDAU 1990). A PRBS signal is used as input, since it can be design to have a spectrum with significative components in some region of interest. A detailed exposition of how to properly select the PRBS parameters is for example given in (LANDAU 1990). It is worthwhile to note that the previous step response works need to be done for a proper selection of that parameters. An example of experiment with PRBSs is given in **Figure 2**, where variations over the steady state of the temperature and the control valve are shown (for a given vapour pressure).

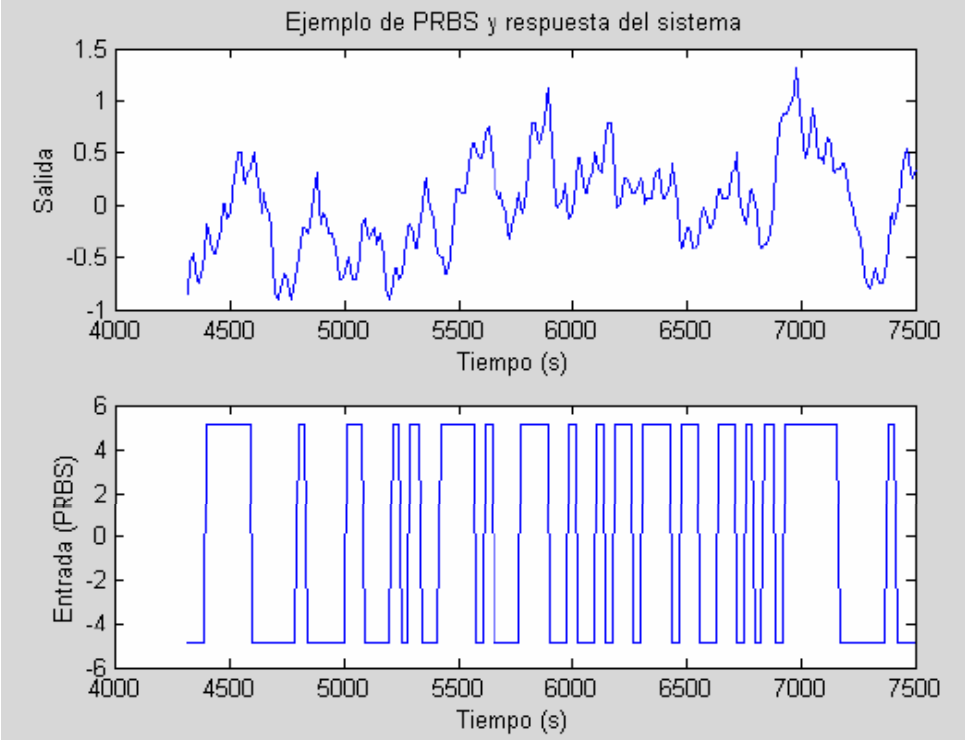

Figure 2: PRBS experiment

A number of identification experiments have been mader with different products and at several operation points of interest. In Fig. 3 some of the frequency responses obtained are shown. The working frequency interval is from 0.01 to 0.03 rad/s. The behaviour at high frequencies is a combination of the delay and sampling. Since all the experiments has been performed with a sampling frequency of ω_s = 0.63 rad/s (or a sampling time T_s = 10 s), the maximum visible frequency with these techniques is theoretically $\omega_s/2$ = 0.31 rad/s. However, a realistic practical bound is always lesser, usually $\omega_s/10$ or even below. This simply means that of the information given in Fig.3 over 0.06 rad/s can be neglected.

Note that **Figure 3** can be considered as the frequency response of a uncertain LTI system, the uncertainty being represented as the set of frequency responses. All these responses have been computed by using the MATLAB *Identification Toolbox*.

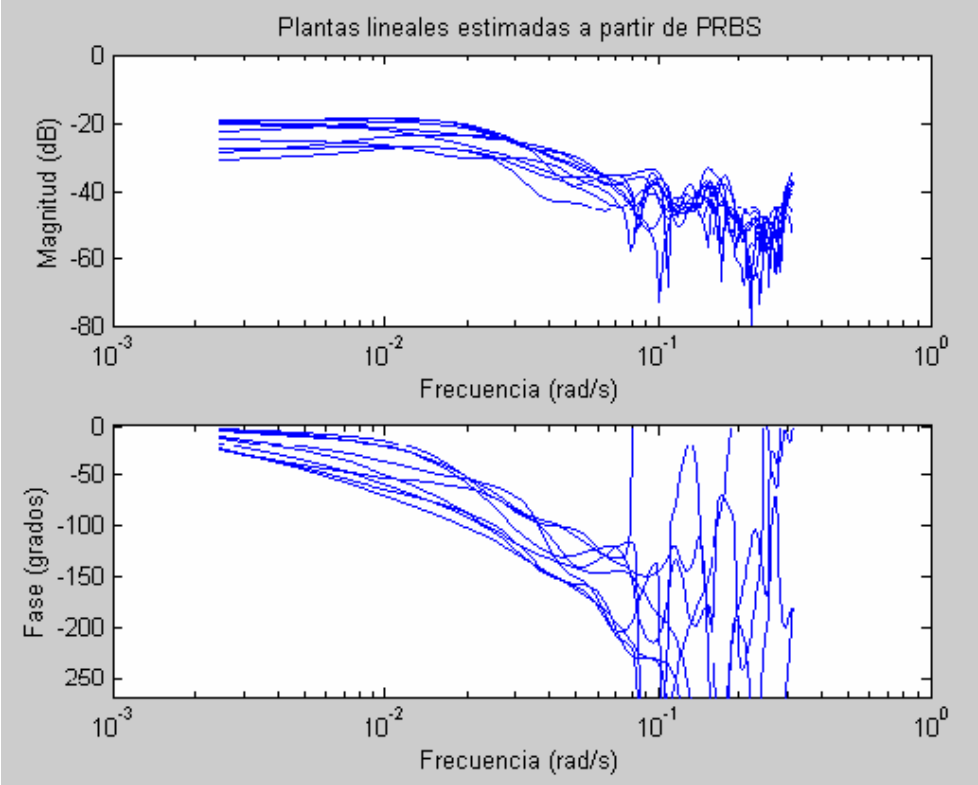

Figure 3: PRBS experiment

4 Robust Control Using QFT

Here the goal is to design a robust control system that guarantees both an stable and optimal operation for all the products and temperatures (operation points) considered in Section 3.

The chosen design method has been QFT (Quantitative Feedback Theory). Two designs has been performed, using as basis the two models obtained in Section 3, the time domain model and the frequency domain model. The design specifications are closed loop stability and disturbance rejection. More specifically a robust stability margin of 45º and the maximum disturbance rejection will be the main design specifications. For tracking a precompensator will be designed in addition to obtain a smooth transition in the case that a change of operation point is given in the process.

In both designs, a PID structure will be used to shape the loop gain to the design restrictions

4.1 A brief introduction to QFT

QFT stands for Quantitative Feedback Theory. It is a robust control technique that is especially well suited for control problems with large plant uncertainty. It has been developed since the early 60's by Prof. Horowitz and his collaborators (HOROWITZ 1992), and it

has been applied to scalar/multivariable, LTI/nonlinear and time varying, single loop/multiloop systems.

QFT works in the frequency domain, thus plant models can be derived from transfer functions (usually with parametric uncertainty) or directly by sets of frequency responses. QFT basically consists of several design steps:

1. Computation of *templates*. A template represents, at a given frequency, the uncertainty of the plant. It is a region of the Nichols Plane corresponding, being each point given by the phase and magnitude of a plants set element (see Figures 4 and 7). For a set of working frequencies, the first design step consists of computing the templates set.
2. Computation of *boundaries.* Given (robust) stability and performance specifications, each template generates a boundary. If the nominal open loop gain avoids the boundaries, one boundary at every working frequency, then closed loop specifications are satisfied for all the plants considered in the template (see Figures 5 and 8).
3. Nominal *open loop shaping*. Once the boundaries are computed, the next design step is to compute (*shape*) the open loop gain that fits them in some optimal way. In general, this is a hard computational problem that usually has been solved heuristically. Once the open loop gain is obtained, the feedback compensator is directly computed. In addition, a precompensator must be added to the feedback structure to satisfy tracking specifications.

For application of QFT, two types of plant models will be considered, as indicated in Section 3.1. In first place, first order models with delay have been identified based on step responses. Secondly, frequency response model have been computed using the systems response to pseudo random binary sequences (PRBSs). In both cases, the heat exchanger have been manually operated to different operations points, and the corresponding input (step/PRBS) has been added to analyze the dynamic behaviour in that operation points. Both types of experiments have been performed for different types of products.

4.2 First QFT design based on the first order with delay mode

The information collected from the identification experiments is processes as indicated in Section 3.1, given as result the parametric model (1)-(2).

The QTF design procedure outlined in Section 4.1 will be applied. The uncertain parametric model (1)-(2) result is the set of templates given in **Figure 4**.

In addition, **Figure 5** gives robust stability boundaries that guaranty a phase margin of 45º for all the plants in the model set.

Finally the feedback compensator is shaped in the Nichols Chart to avoid the QFT boundaries (Figure 5), with the largest possible gain to additionally meet the disturbance rejection specification. A PID compensator has been obtained with the Bode diagram given in **Figure 6** (the Bode plot corresponds to the open loop gain for a nominal plant).

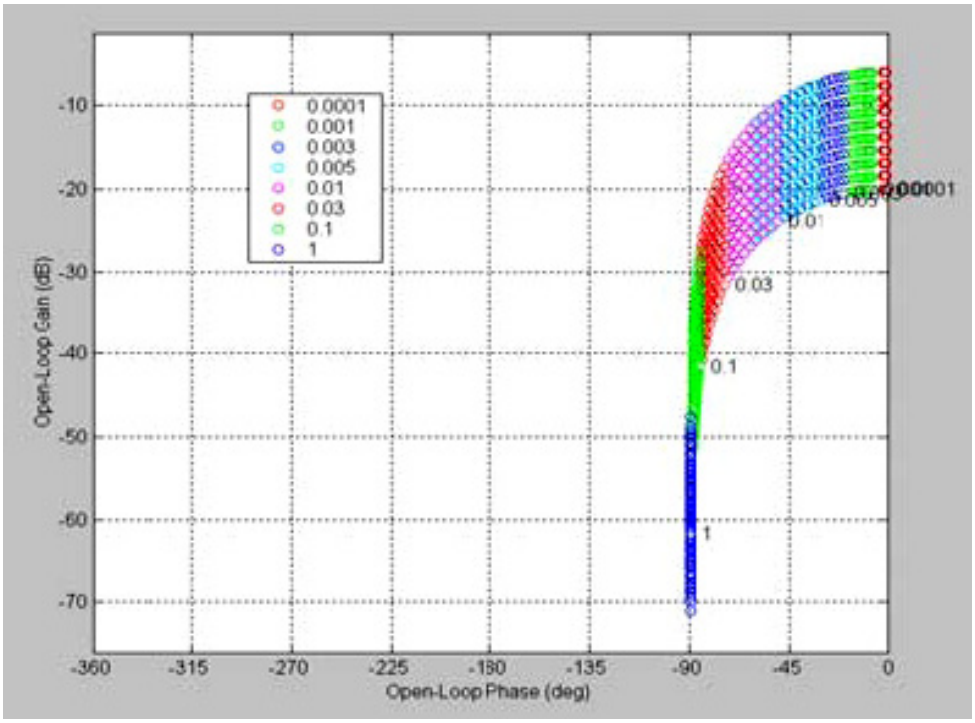

Figure 4: Plant templates of the first oder with delay models

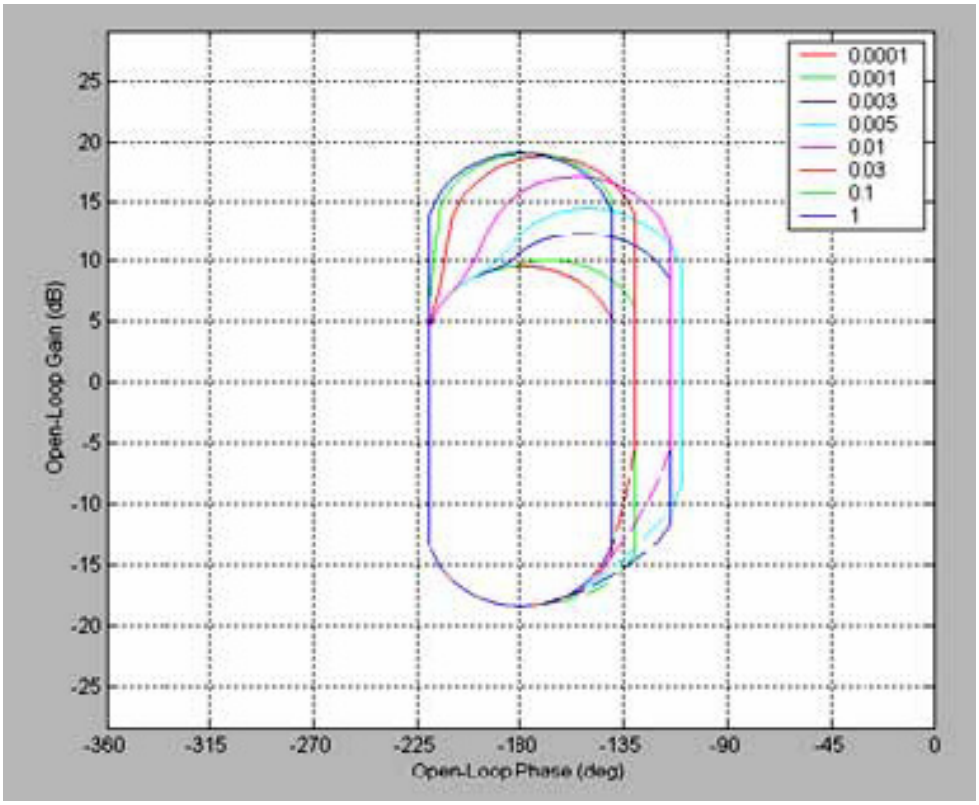

Figure 5: QFT robust stability boundaries

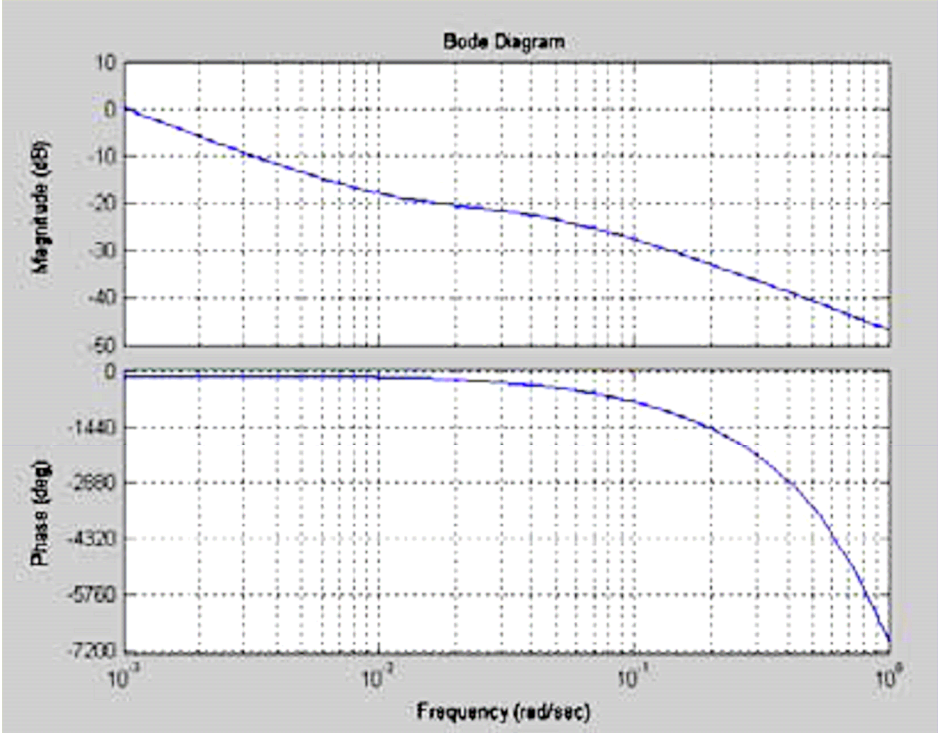

Figure 6: Bode plot of the loop gain

4.3 Second QFT design based on the frequency response models

A second design has been performed by using the frequency response models derived in Section 3.2. The firs step in QFT design is template computation. In this case the templates, given in **Figure 7**, are less structured that the used in the first QFT design, specially in medium/high frequencies. As commented above, this is basically due to the lack of precision for frequencies higher that 0.06 rad/s.

These templates has been used in combination with the robust stability specification to derive the boundaries shown in **Figure 8**.

Again, if the open loop gain is properly shaped to avoid the these boundaries the closed loop system is guarranteed to have a phase margin of at least 45º, for every considered product and operation point for the heat exchanger. To satisfy the disturbance rejection specification, the loop mush be shaped to has the maximum possible gain at each working frequency.

A second PID compensator has been shaped to these boundaries. Note that in this case, exhibing the frequency response models a richer behavior, it is possible to shape a more energic compensator, being the open loop Bode diagram shown in **Figure 9**. Also a comparison between both PID designs is made. Since the modelling given in the frequency domain is less conservative, it is possible to obtain a loop with higher gain in the operational bandwith of the heat exchanger whitout making the system unstable. As a result, the secon design is much more efficient in rejecting disturbances.

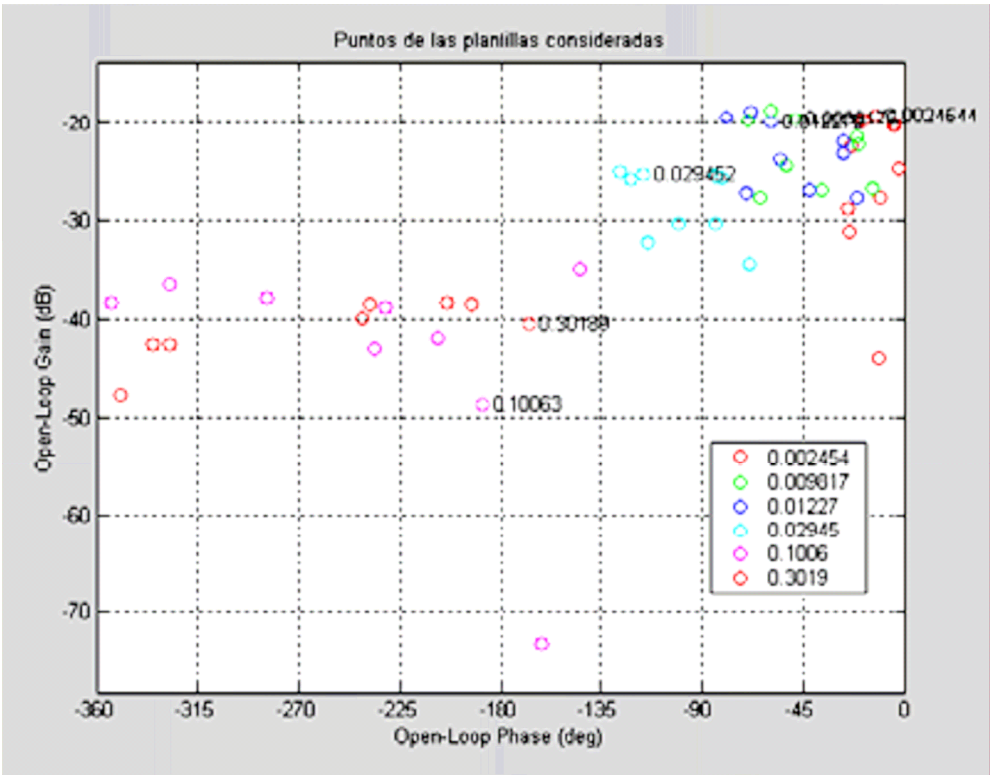

Figure 7: Plant templantes (frequency response models)

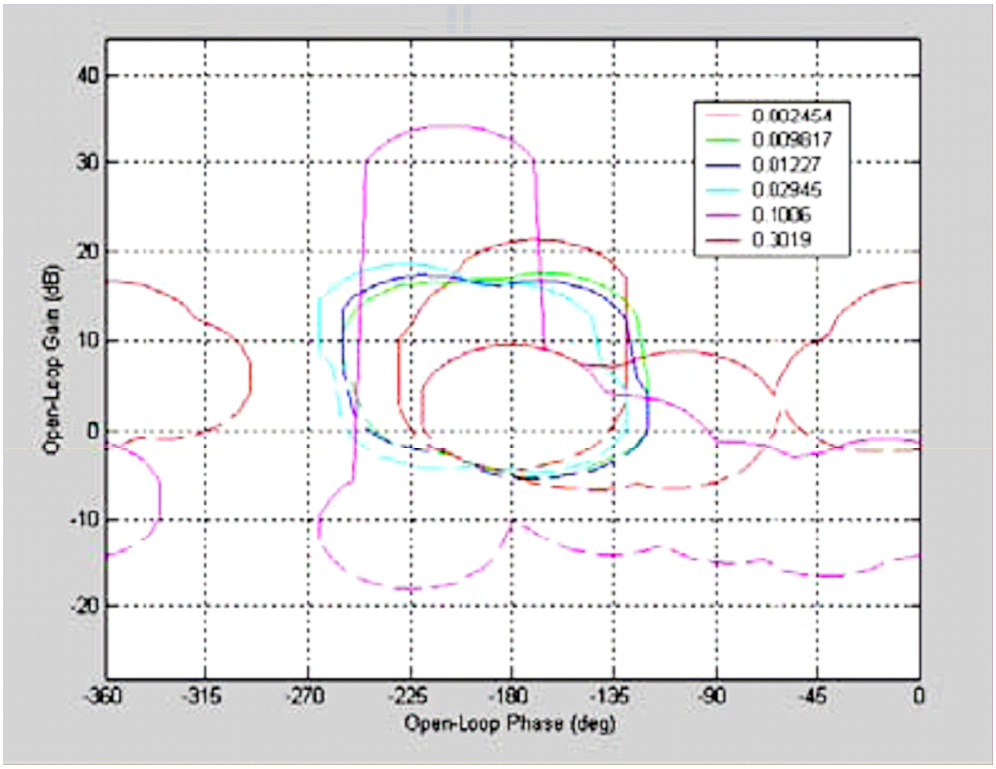

Figure 8: QFT stability boundaries

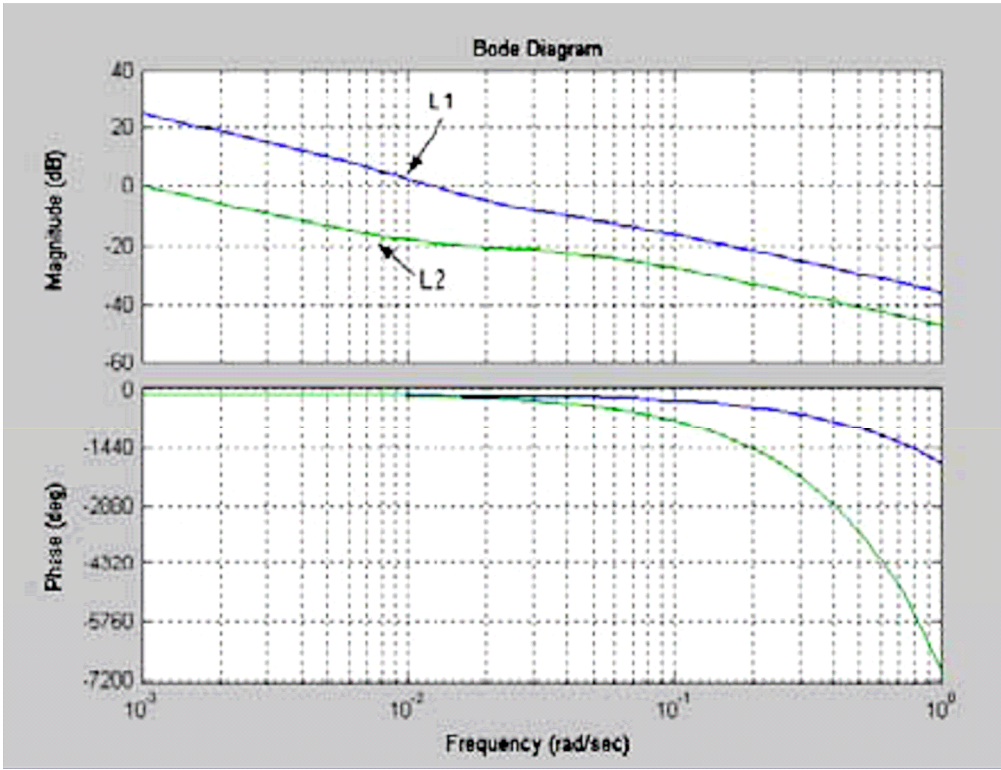

Figure 9: Bode plots of the nominal open loop gain for QFT designs #1 and #2

5 Experimental Results

A number of experiments has been performed in the CTC pilot plant. Although the first QFT design has been used in some cases and it has been proven to be robust enough, its has performed very slow and sometimes inefficient to reject common disturbances. The second QFT design has been adopted with some additional changes. For example, the derivative term has been filtered to avoid sensor noise effects, and also an precompensator has been added to produce a smooth transition in reaction to abrupt setpoint changes.

In **Figure 10**, some experimental data are shown, corresponding in this case to the pasteurisation of a fruit juice. The reference of temperature is 96.5 Celsius degrees. As a result, the real pasteurisation temperature has been controlled between 95.2 and 97. 6, a very good result in which the error is less than 1.4 %. Similar results have been obtained for other products.

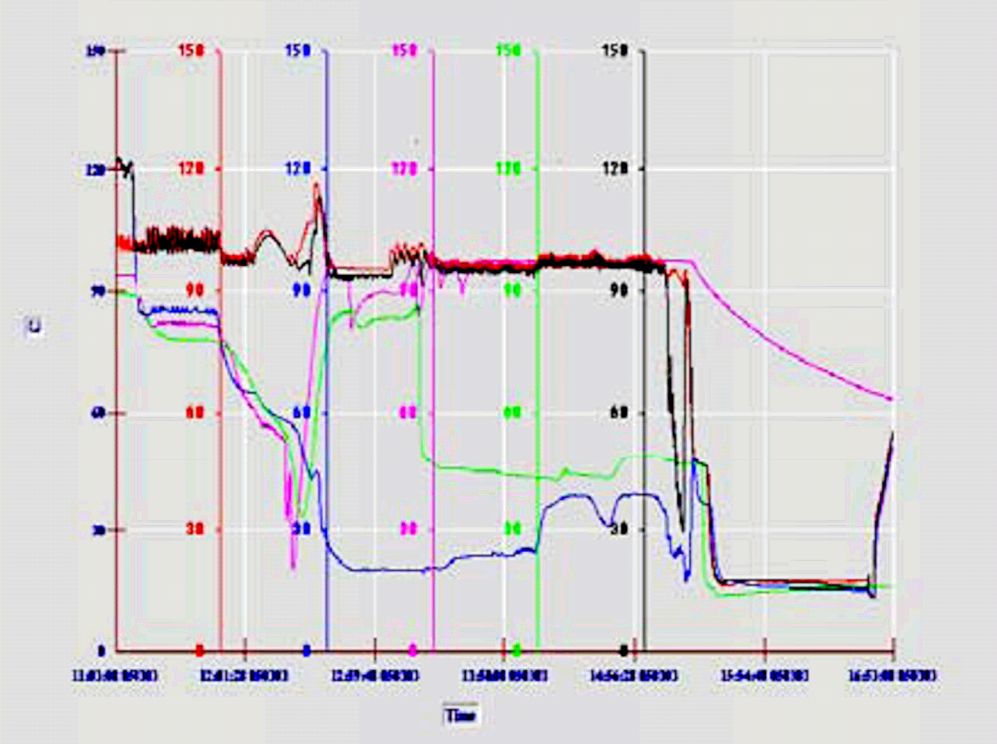

Figure 10: Control experiment in the CTC pilot plant

Conclusions

The control problem of different thermal treatments to different products has been approach from a robust control perspective. Using the information about step response and the frequency response of the (linearized) LTI plants, QFT has been used to design a feedback compensator. Due to the fact that a PID structure is already available in the control hardware of the heat exchanger, a PID controller (with a filtered derivative term) has been designed with the goal of obtaining a stable operation with maximum disturbances rejection, working for all the members of the family of LTI plants, that is for the set of considered products and at different operation points. The QFT design based on frequency response models has performed very efficiently in practice, and in fact it has been adopted in the pilot CTC plant.

Acknowledgements

Authors thanks Prof. Franciso J. Montoya for his help in the implementation of some identification experiments. This work has been supported in part by Ministerio de Ciencia y Tecnología under project DPI2004-07670-C02-02 and Comunidad Autónoma de la Región de Murcia under project 00507/PI/4.

References

BAÑOS A., LAMNABHI-LAGARRIGUE F., MONTOYA F.J. (2001): Advances in the Control of Nonlinear Systems. Lectures Notes in Control and Information Science #264, Springer-Verlag, London

BAÑOS A., YANIV O., MONTOYA F.J. (2003): "Nonlinear QFT synthesis by local linearization", Int. Journal of Control, vol.76, No. 5, pp. 429-436

LANDAU I.D. (1990): System Identification and control design. Prentice Hall

CASP A., ABRIL J. (1998): Procesos de conservación de alimentos. Mundi-Prensa, Madrid.

DOWNING, D. (1996): A Complete Course in Canning. Vol. 3, Chap. 3 and 12. CTI Publications, Maryland

HOROWITZ I.M. (1992): Quantitative Feedback Theory, QFT Press

LENNART L. (2001): System Identification TOOLBOX. The Math Works Inc, Natick

PREUB K., LE LANN M., RICHALET J., CABASSUD M., CASAMATTA G. (1998): Thermal control of chemical batch reactors with predictive functional control. Journal A, 39: 13-20.

REUTER H. (1988): Aseptic Packaging of Food. Technomic Publishing Company Inc, Pennsylvania

TE BRAAKE H., VAN CAN E., SCHERPEN J.M., VERBRUGGEN H. (1998): Control of nonlinear chemical processes using neural models and feedback linearization. Comput. Chem. Engng, 22: 1113-1127

A Monitoring and Distributed Control System for Wins Fermentation Via Ethernet/IP

M. Gil-Martínez, R. Martín and C. Elvira
System Engineering and Automation Group, Electrical Engineering Department.
University of La Rioja. Luis de Ulloa, 20, 26004 Logroño, SPAIN.
E-mail:[montse.gil, ricardo.martin, carlos.elvira]@die.unirioja.es

Abstract: *A monitoring and distributed control system oriented towards the vinification process in a winery is presented in this paper. Using a SCADA application in the master PC station, the winemaker has access to the controlled fermentation variables in a remote way and in real-time. Distributed input/output interfaces drive the data from/to the sensors-actuators into the industrial network, where the master PC manages the information flow. The communications follow the Ethernet/IP and CIP industrial protocols. The goal is to provide winemakers with a tool to make timely decisions when fermentation readings fall outside of the specified ranges, to perform an automatic control of the vinification operations, and to build exhaustive data bases for further studies on the fermentation conditions and the wine quality. Copyright © 2006 IFAC.*

Keywords: *Wine fermentation, Distributed control, SCADA Monitoring, Communication networks, Automation.*

1 Introduction

Rioja wines are embraced by one of the oldest Designation of Origin in Spain. The technical development experienced by Riojan viticulture and winemaking for hundred of years constitutes the ultimate foundation of the great quality, prestige and character of Rioja wines around the world. Nowadays, wine making is an important worldwide industry, where wines from different regions compete in a very selective market. Wine quality is mainly affected by two factors: viticulture know-how and the art of winemaking. This paper focuses on the latter, applying the latest technologies in automatic control, monitoring, and industrial communications to the winery, and specifically to the fermentation process.

According to the experience of oenologists, this paper suggests integrating basic and advanced sensors into the winery vinification section so that the fermentation stage can be monitored and storaged in real-time. This would enable winemakers to make timely decisions when fermentation readings fall outside of specified ranges, to perform an automatic control of the vinification operations, and to build exhaustive data bases for further studies on the fermentation conditions and the wine quality. To execute these control tasks, a

SCADA software application will be developed, providing a flexible and user-friendly software environment.

Nowadays, industrial automation depends on industrial communications. However, there is not a unique standard among manufacturers of hardware and software solutions for connecting real-world devices with computer networks for remote monitoring and control. The goal of this paper is to propose a flexible solution, based on widely used standards, supported by the main manufactures of industrial automation equipment, and according to the latest technologies, while being open to future trends. With this premises, the network topology presented in this paper will be distributed. CIP will be the standard industrial networking protocol used for the application layer and Ethernet/IP for the underlying network layers. In the hardware area, commercial input/output digital/analogue interfaces, distributed throughout the vinification section, will collect the sensor-actuator information and encapsulate it in messages following the specified network protocol. A master processor will be connected to the same physical net, and it will manage the client-server communications using the same protocol. The flexibility of the industrial network will allow a controlled access from a remote station, e.g. in the network of the winery management, to any sensor or actuator located in the vinification production plant.

In order to validate the monitoring and distributed control strategies proposed, a small-scale vinification system is being built in the laboratories of the Electrical Engineering Department in the University of La Rioja (Spain).

The paper is organized as follows. Section 2 introduces the goals under the perspective of the winery and the fermentation process. Section 3 describes the distributed control system proposed: the sensors and actuators to be incorporated, the physical structure of the distributed network, and the industrial communication protocols. Section 4 presents the SCADA interface, from which the winemaker performs the monitoring and control tasks. The main conclusions are in Section 5.

2 Winery and wine-making

From a vertical perspective, the winery is divided into two sections: management and production. Winery management deals with the wine tracking, from the grape reception, through the wine production and storage to its selling and marketing. Afterwards, in a horizontal perspective, the wine production section attends to the wine-making process including pre-processing, vinification and post-processing; (RUIZ 2004). The pre-processing for making red wine involves tasks such as: the removal of seeds and stalks and clarification if necessary, grape crushing, the addition of sulphur compounds, and mash cooling/heating among others. Another wine-making approaches, such as the carbonic maceration, follow different procedures (RUIZ 2004). Post-processing includes operations such as: stabilization, clarification, aged, bottled, and so on. These vary depending on the kind of red wine: young, *reserva*, *crianza* and *gran-reserva*.

Then, the vinification process is only under the scope of this work, including the supervision and control of the two fermentations: the alcoholic and the malolactic reactions; (RUIZ 2004). Between both, the marcs and any solid components are separated from the wine, which is then subject to decantation and clarification operations.

The solution proposed provides the hardware and software infrastructure to interchange information related to the vinification process between the management and the production area in the winery, and also inside the production section.

Depending on the winery capacity and the annual production scheduling, the active vinification section may contain a variable number of fermentation vessels (see **Figure 1**). These can be grouped in basic units of two vats (for alcoholic and malolactic fermentations). Sensor and actuators will be incorporated (see Section 3.1). The analysis of some variables requires high cost sensors or specific fluid conditions to perform reliable essays. Then, a specific tank of reduced dimensions, labelled as analytical station, is proposed to incorporate special purpose sensors. While sensors on the vats must be duplicated along the *n* basic units in a section, the analytical station can be shared. Other sensors and actuators are integrated into the pipe network for fluid transport and recirculating operations.

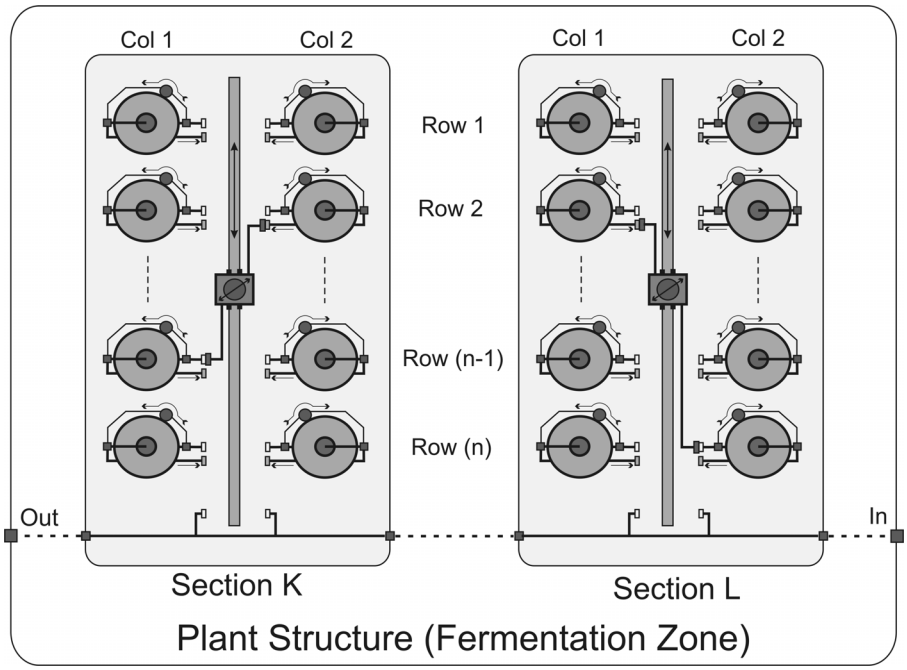

Figure 1: Fermentation sections in the winery

3 Distributed Control System

3.1 Sensors, Actuators and Transmitters

In consonance with the winemaker's experience (RUIZ 2004), basic and advanced actuators and sensors have been incorporated into the fermentation vats, the analytical station, or the network of pipes that interconnect the tanks in the production section. The automa-

tion system provides: on-line periodic analysis following the oenologist scheduling implemented on the SCADA supervisor, and adopting corrective actions as part of automatic control loops or attending to specific orders (manual mode). If the sensor performing the required analysis is located in the analytic station vat, the must-wine sample must be transferred to it from the selected fermenter from a certain section of the winery. Subsequently, the tools provided by the automatic system are described.

A precise tracking and control of the temperature is crucial to drive and moderate the alcoholic and malolactic fermentation reactions. Two PT100 electrodes of different length are located at different heights of each tank to show spatially distributed temperature variations. As a temperature actuator, a cooling/heating system provides the necessary energy required by the temperature control strategy implemented in the SCADA supervisor.

Density variations are also relevant indicators of the fermentation evolution. A precise measurement of the must-wine density is provided through periodic experiments in the analytic station where the solid phase has been removed. A bridge of load-cells, disposed under the fermentation vessels, indicates the weight of the wine-storage, and its variations during the fermentation evolution or transferring operations.

Other important parameters are pH and Redox. These indexes are measured by the same sensor, which can be fixed to the transferring pipes or incorporated in the analytical-station tank.

Following oenologist criteria, other sensors can be incorporated into the vessels, and mainly into the analytical station, for example, to quantify the total polyphenol index, the acidity levels, the grade of alcohol, the total sugar concentration, and so on. Using the analytical vat, certain additives, such as yeasts, can be dosed and pumped to the main fermentation tanks.

The CO_2 production rate is measured based on the differential pressure principle that detects a device incorporated at the top of the alcoholic fermentation vat.

The main vats are provided with a mechanism to recirculate the wine must from their base to the top, and to sprinkle it on the marc-hat, at the same time that this marc-hat is crumbled in a controlled way. The goal of the mechanical actuated system is to promote the interchange of organoleptic properties between the solid and the liquid phases.

Transfer operations are performed in the reception of the wine must, in its transportation from the alcoholic to the malolactic fermenters, and in the wine expedition for post-processing. These control operations require a pump, a flow-meter, and a set of electro-valves inside the appropriated geometry of pipes.

The signals from the sensors and to the actuators are conditioned to analogue 0-4-20mA industrial standard. The sensor-actuator devices, transmitters, pump regulators, solid-state relays, power supplies and other control and electronic devices are in boards, distributed throughout the production section that command.

3.2 Distributed control network

The global control structure is shown in **Figure 2**. The final-end devices (sensors and actuators, and their additional electronics) are distributed throughout the winery. Attending to previously described vinification operations, the final-end devices can be associated in two main groups: (a) those devices associated to a specific tank in a section (e.g. a PT100 sensor, or the recirculating system), and (b) those located in the analytical station (e.g. pH sensor) or in the network pipe-net (e.g. pump), which all the tanks in a section share. According to the type of variable, the signal can be analogue (e.g. load cell weight) or digital (e.g. electrovalve commands). Besides, the signals can be inputs (I) from the sensors (e.g. PT100) or outputs (O) to the actuators (e.g. pump). Overall, analogue/digital I/O signals from/to a section or its tanks enter the industrial network bus via commercial Acromag® modules, that use Ethernet/IP industrial protocol (ACROMAG 2004a). There are: digital modules configurable as inputs or outputs, analogue input and analogue output modules. An Acromag switch device concentrates and commands up to four I/O modules. The Acromag devices and some of their controlled variables are depicted in **Figure 3**. Switches and I/O cards are distributed near the commanding sensors/actuators. The whole system is flexible and the necessary number of I/O analogue/digital modules can be added, for example, to attend a larger vinification area or to include the control of the pre- and post-processing operations.

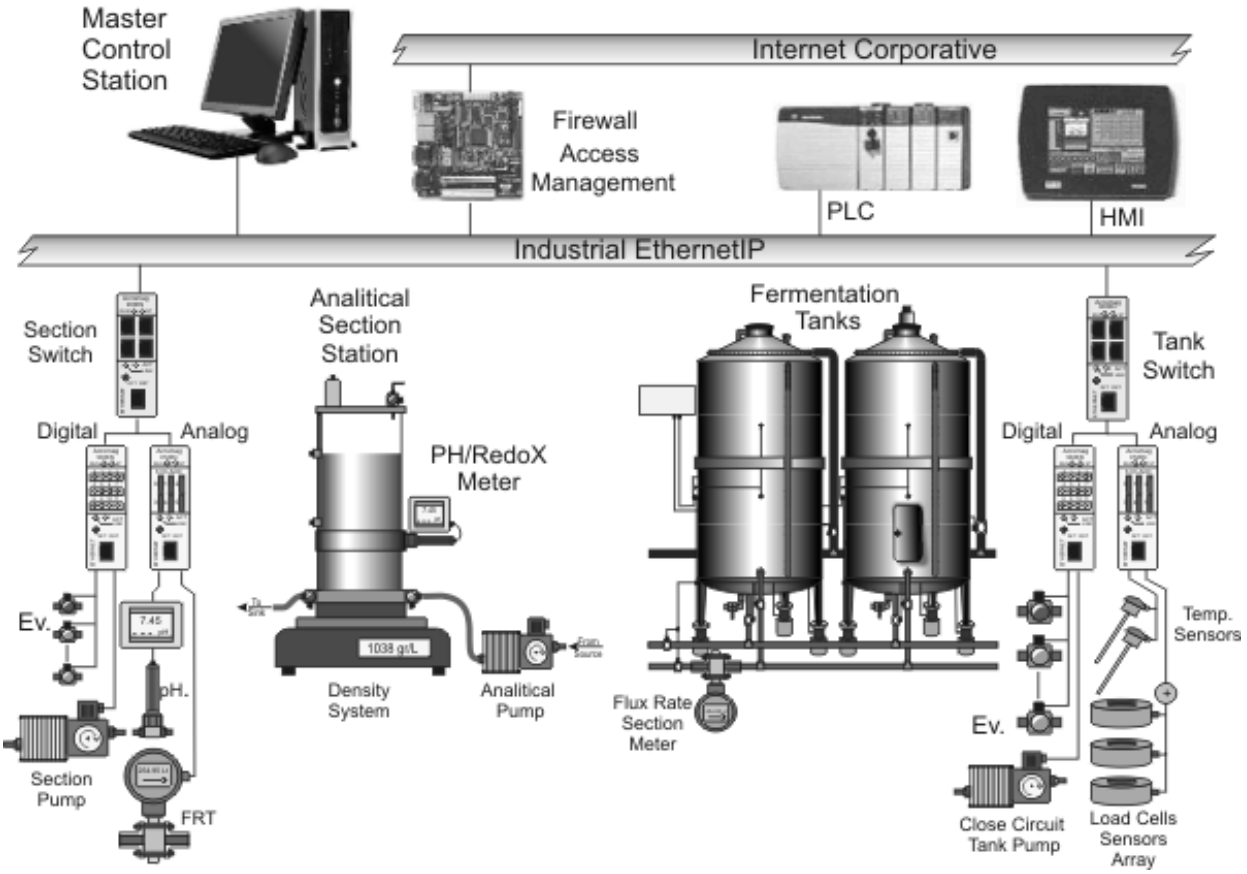

Figure 2: Distributed control network

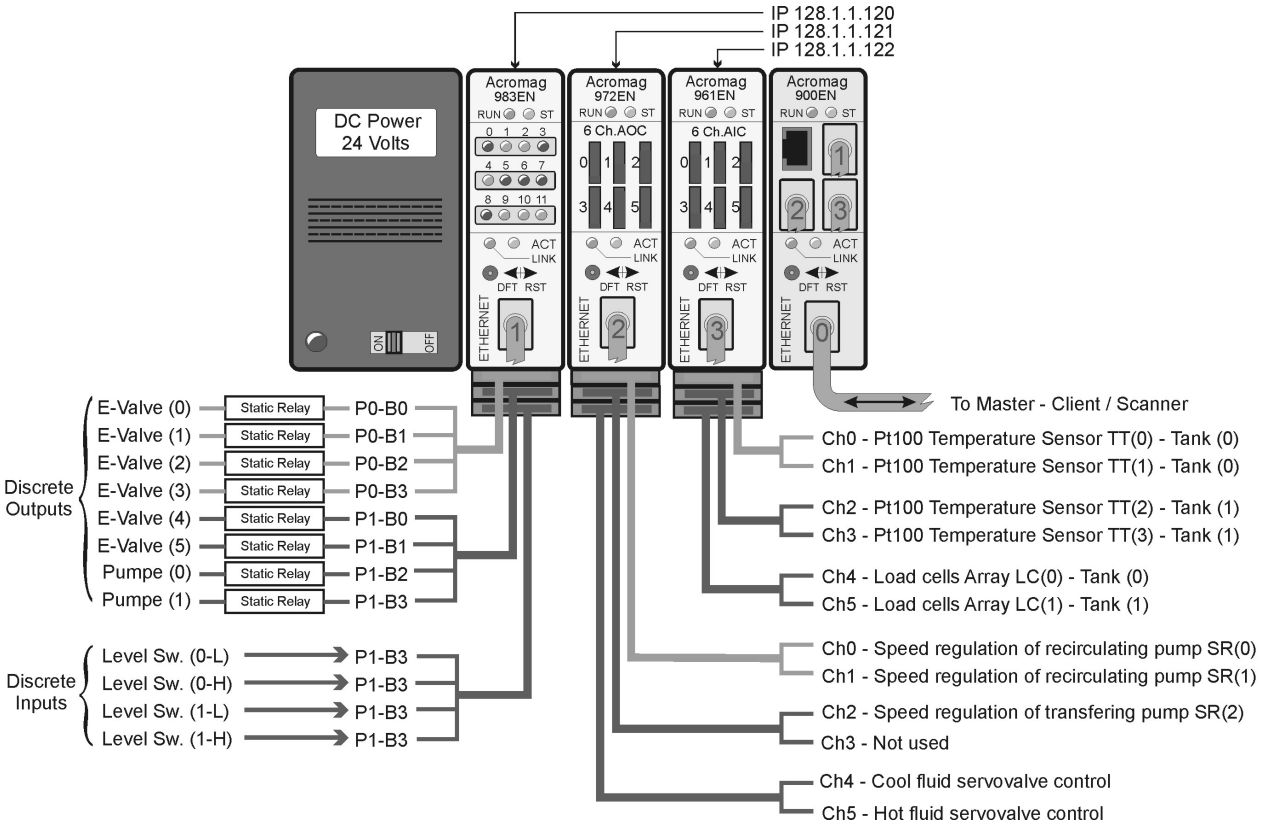

Figure 3: Digital/Analogue I/O and Switch Acromag modules

In consonance with Figure 2, a master control station (usually a personal computer, PC) concentrates the information from the distributed I/O modules. It manages the entire communication system. Programmable logic controllers (PLC) and other peripheral devices (HMI) can be incorporated to the network to accomplish specific intelligent control tasks. In the master PC, a SCADA software application provides a flexible and user-friendly software environment to monitor and control the wine fermentation (see Section 4).

Apart from the industrial network previously described, there is the corporative or enterprise network in an upper level. Both nets can interchange information related to the vinification process. Hardware and software resources must be provided to assure controlled accesses and protective firewalls.

3.3 Industrial communications protocols

On industrial communications, there is no unique standard among manufacturers of hardware and software solutions for connecting real-world devices with computer networks for remote monitoring and control. World-wide acceptance of Ethernet products shows that the ultimate and future tendencies point to Industrial Ethernet solutions (Ethernet/IP, EtherCAT, Profinet, Modbus/TCP,…). In this work, Ethernet/IP (E/IP[1]) has been adopted since it is considered an open network standard because (a) its physical and data link lay-

ers use standard IEEE 802.3 Ethernet, (b) its network layer uses the TCP/IP suite of protocols, (c) its supported by four independent networking organizations, (d) E/IP technology is also available free of charge for developers and vendors; (ACROMAG 2004b). E/IP was born in the year 2000 as a combination of the traditional Ethernet with a specific layer protocol targeted to the process control and automation (CIP: control and information protocol). Originally used in the office environment, Ethernet detractors argue that it lacks of enough determinism and reliability in the harsh industrial area. However, nowadays new industrial net technology (connectors, shielded cables, …) has resolved this durability issue. And the use of fast switches and routers enlarges the determinism and bandwidth by sub-dividing the large network, avoiding collisions and providing a direct connection only between the sender and the receiver. Besides that, recent advances in communications point to 10/100 Gbits Ethernet networks versus the actual speed of 10/100 Mbits.

The OSI[2] model in **Figure 4** (ACROMAG 2004b) represents the basic network architecture adopted in this work. It combines a physical network (Ethernet), with a networking standard (TCP[3]/IP or UDP[4]/IP), and a standard method of representing and interpreting the data (CIP[5]). According to E/IP and CIP protocols in the OSI model, the networking messages in this work have been encapsulated as **Figure 5** shows.

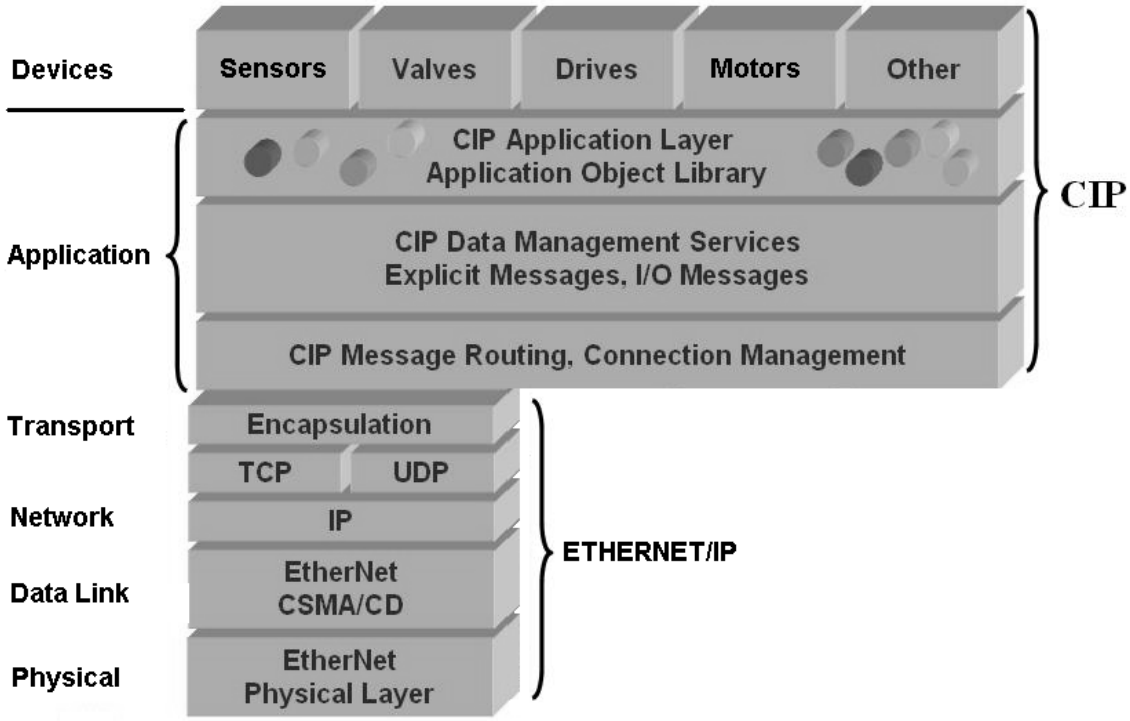

Figure 4: OSI Reduced Network Model with protocols: EthernetIP on CIP

[1] E/IP: Ethernet Industrial Protocol (http://www.ethernet-ip.org/)
[2] OSI: Open System Interconnect.
[3] TCP: Transmisión Control Protocol
[4] UDP: User Datagram Protocol
[5] CIP: Communications Industrial Protocol

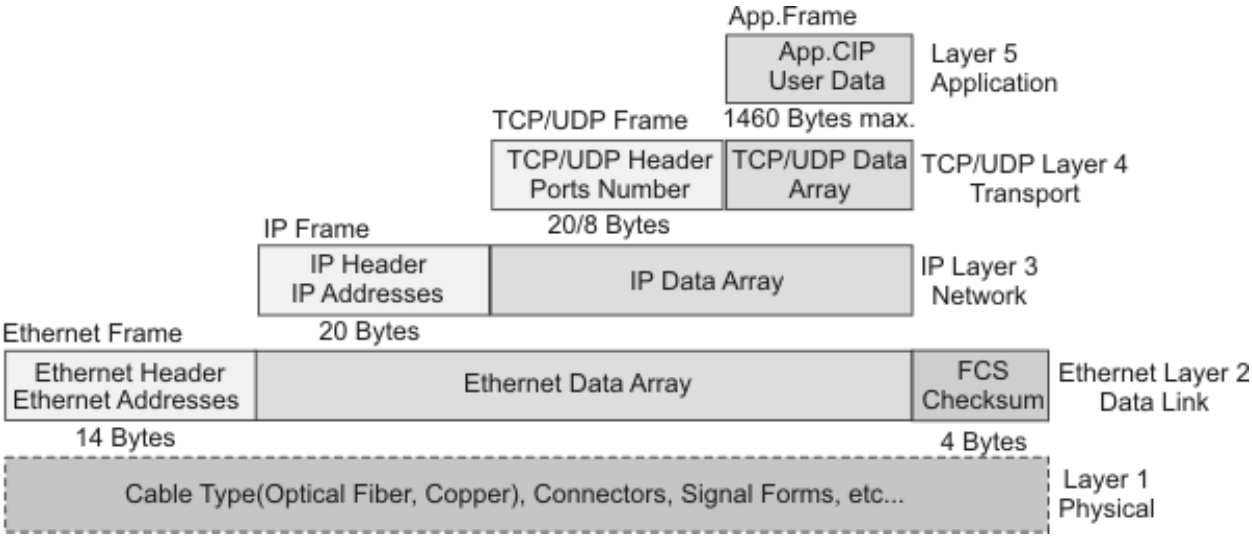

Figure 5: Encapsulation of messages

Ethernet/IP shares the same lower four layers of the OSI model common to all Ethernet devices. This makes it fully compatible with existing Ethernet hardware. TCP ensures that all the packets of data are received correctly (bi-directional communication) and, the other option, UDP guarantees prompt delivery of data packet (unidirectional flow). IP makes sure that messages are correctly addressed and routed. Hence, UDP/IP has been the protocol used for critical time tasks, such as the control and monitoring of the vinification process, while TCP/IP has been used only for configuration commissions. Mainly two types of *implicit* I/O messages following UDP/IP have been used for 'real-time' monitoring and control: (a) *polled*: the master station (PC) sequentially requires the slaves (Acromag I/O channels) to send the information, that is interpreted further; (b) *strobed*: the master PC sends a message to the net in a broadcast mode, and after that, the I/O slave modules reply. (ODVA, 2001b)

CIP is an open available protocol that is widely supported by many manufacturers of industrial equipment (see ODVA[6] group). It can be implemented in conventional PC platforms, in industrial control workstations based on Linux or Windows, or in embedded design proprietary systems (DeviceNet™ or ControlNet™). For future technology advances, CIP is independent from the underlying network layers, meanwhile other protocols develop on proprietary EIP, e.g. Modbus/TCP™ of the Schneider Group, Profinet™ of Siemens or HFE Fieldbus™ of FieldBus Foundation.

The CIP application layer defines rules for organizing and interpreting the data. Each node or device in the net is modeled as a *collection* of *objects* that meets the *encapsulation*, *polymorphism*, and *heritance* principles, and that are characterized by *attributes*, *methods* and *events*. Then, each network object is characterized by the parameters: Class ID, Instance ID, Attribute ID, Service Code, MAC ID. (ODVA, 2001a; ACROMAG 2001a).

[6] ODVA. Open Devicenet Vendor Association, that joins together more than 300 manufactures of automation and control devices.

This particularizes in the winery automation as follows. The network structure in Figure 2 is now represented hierarchically in **Figure 6**. Then, the conversation between the master PC and the slave Channel 0, connected to a specific PT100 sensor, is based on activating certain *methods* of the *objects* emitter-receiver using encapsulated messages whose structure follows Figure 5. The SCADA software application for control and monitoring in the master station has also been developed under the principles of OOP[7]. The following example sequence illustrates the methodology used. The vinification process defines a *class* that includes a collection of *objects*: the sections. The class section includes a collection of objects: tanks, analytical station, and pipe-network. The class tank includes a collection of tanks, and each one has a collection of objects, such as the cooling/heating system or the temperature sensors. And, so on. All these objects or instances have their own

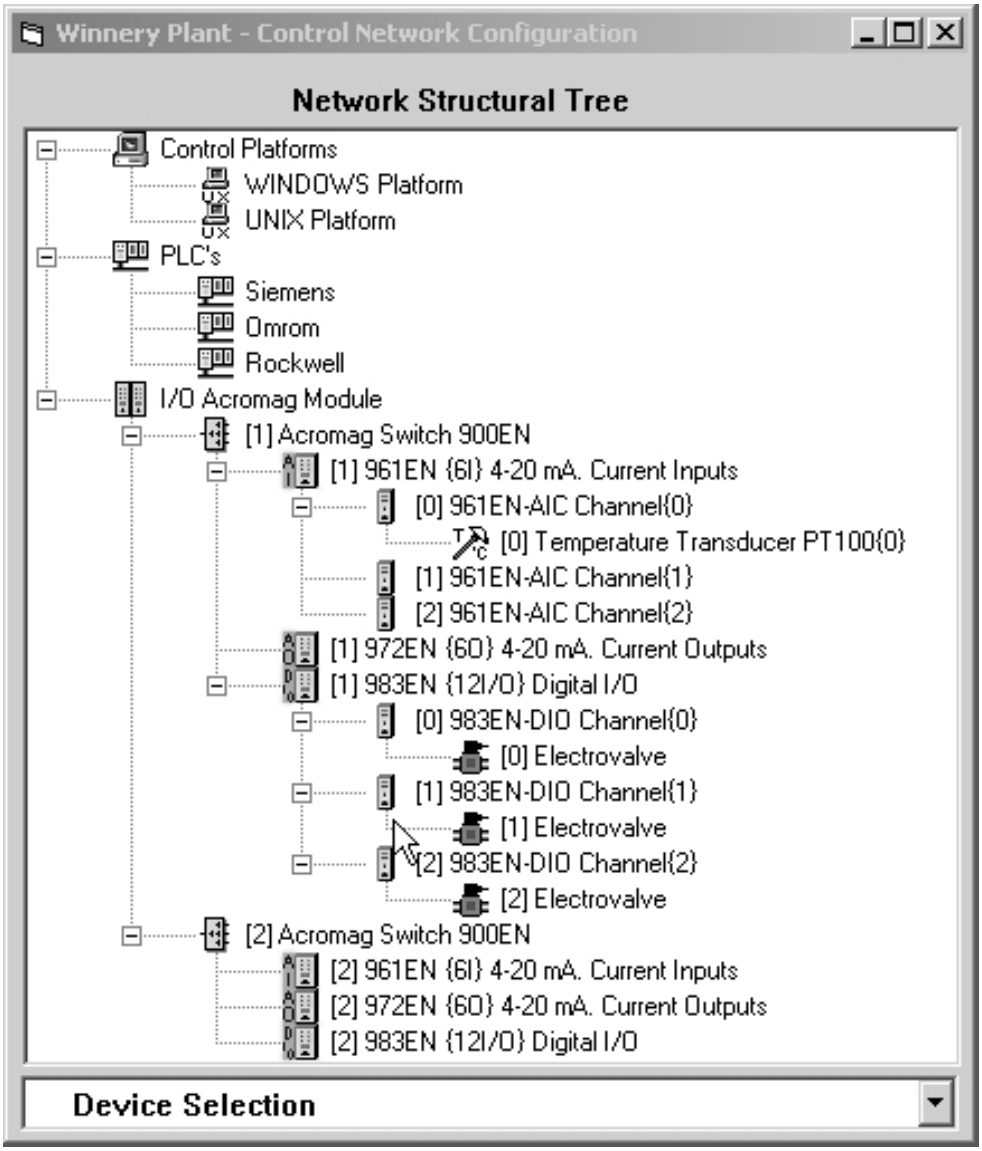

Figure 6: Network Hierarchical Tree Structure

[7] OOP. Object Oriented Programming.

attributes, methods and events, and others inherited by its belonging to a class. Equally, the winemaker actions on the SCADA graphical interface imply the activation of methods of the objects. Some of these methods carry on I/O operations that put the object 'master PC' in contact with the object 'slave I/O channel'. According to Figure 6, the object 'input channel 0' belongs to a collection of objects 'channels' in the class 'Acromag analogue input module (961EN)'. This class includes a collection of objects that are all the analogue input modules. As long as, four Acromag modules are connected to one switch, a specific analogue input module is also an object in the class 'Acromag switches modules'. The lowest elements in the tree inherit the object 'identifier (ID)' of their superiors. The ID object distinguishes the devices in the network.

To perform the communications according to CIP standard, Acromag devices are defined by *required objects*, *application objects* and *device specific objects*. The *required objects* used are: the 'Identity Object*'* (distinguishes the device in the net), the 'Message Router Object', the 'Connection Manager Object*',* the 'TCP/IP Interface Object' (with the data for the IP layer configuration: IP address, IP mask, gateway, server domain and name,…), the 'Ethernet Link Object' (with the configuration data for the Ethernet Layer: interface speed, flags, MAC ID). The *device specific objects* are: the 'Discrete Input Data Object' (whose attributes contain the input data-array sent towards the net, data-array that comes from an input module or goes to and output module) and the 'Discrete Output Data Object' (whose attributes enclose: the data-array that comes out from the net, the Watchdog Timeout by Port, and the Watchdog Timeout State, amongst others). Both specific objects take part of the 983EN-6012 Acromag® device, with configurable discrete Input or Output channels that are used to control and monitoring digital variables (electrovalves, pumps,…). Another *device specific object* of the Acromag modules is the 'Analog Input Data Object'. Some of its attributes include the vector of analogue values that comes into the net (a) from the input analogue modules (Acromag® 961EN-6006 device for monitoring temperature, flow rate, pH, redox,...) or (b) towards the output analogue modules (Acromag® 972EN-6006 devices for analogue control variables). See Figure 3 and Reference (ACROMAG 2004a).

4 SCADA Software

A SCADA (Supervisory Control And Data Acquisition) software has been developed as the interface between the winemaker and the automatic controlled vinification process. Consequently with the OOP principles, the tool has been developed using Visual Basic language (SILER & SPOTTS 2001, 2004), and it runs in the master PC station of Figure 2.

The SCADA structure and its main utilities are shown in **Figure 7**. The information management refers to schedule the data acquisition: variables to measure, timetables to perform the essays, procedures (e.g. volume of fluid to transfer from tank A to analytic station), and so on. Captured information is organized in files and data-bases for post-processing. Statistics and reports can be emitted. Based on the captured information, con-

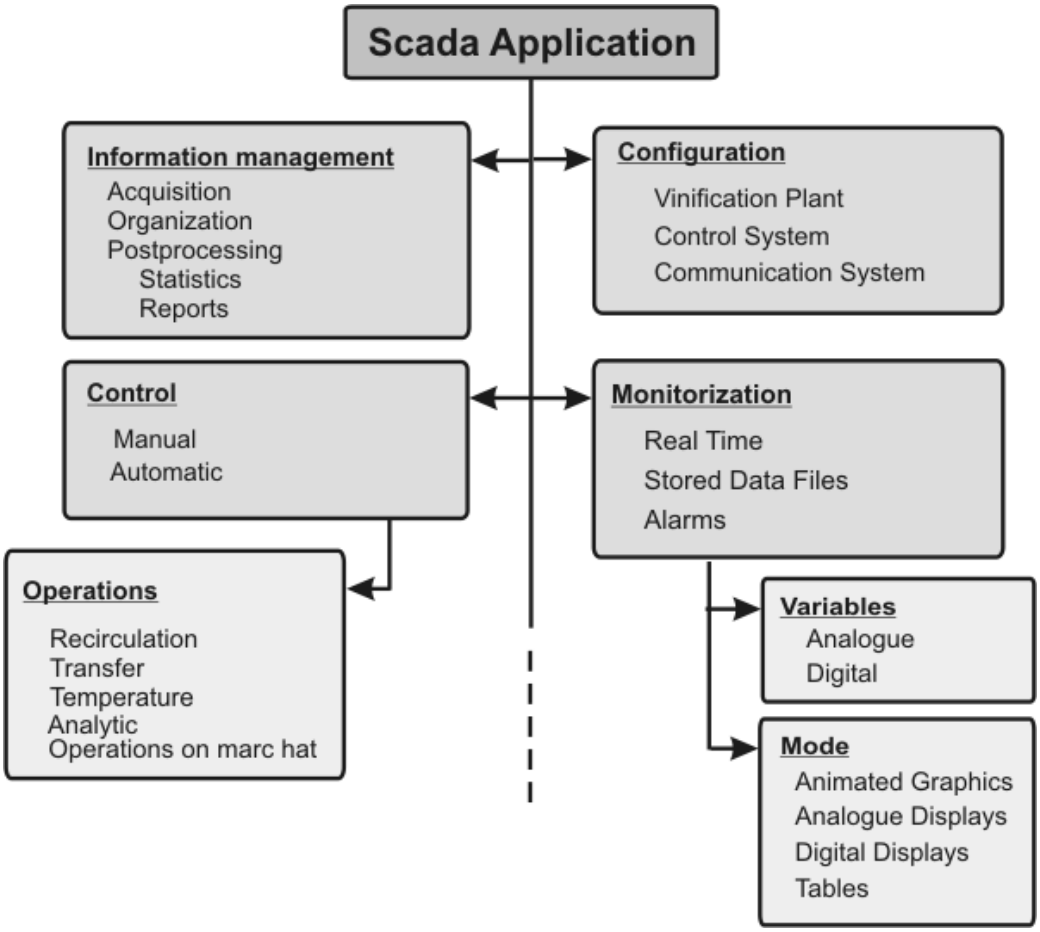

Figure 7: SCADA software

trol operations or monitoring tasks can be executed. The process variables can be monitored in real-time, or the user may require the load of past records. Out-of-range fermentation variables, or simply, dysfunctions of the devices in the automatic system are registered and visualized as alarms. The software provides a variety of graphical modes. Digital variables, such as pumps or electrovalves states, are shown by leds. Wine flow along the pipes or the level reached in the tanks are illustrated with animated graphs. The evolution of main fermentation variables requires of analogue graphics or tables. **Figure 8** illustrates a monitoring screen. Automatic and manual control of main vinification operations (Figure 7) are supported. An SCADA screen for control and monitoring is shown in **Figure 9**.

5 Conclusions

A monitoring and distributed control system oriented towards the vinification process in a winery has been presented in this paper. Using a SCADA application in the master PC station, the winemaker has access to the controlled fermentation variables in a remote way and in real-time. Distributed input/output interfaces drive the data from/to the sensor-actuators into the industrial network, where the master PC manages the information flow.

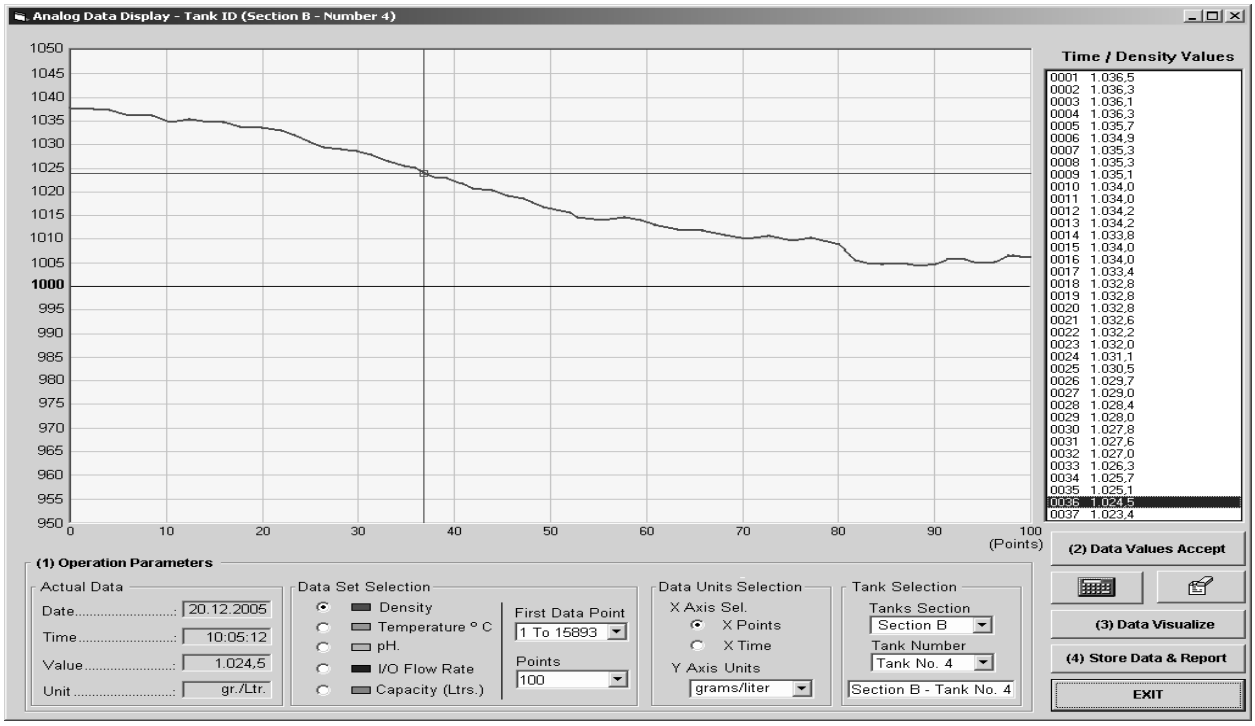

Figure 8: Monitoring SCADA menu

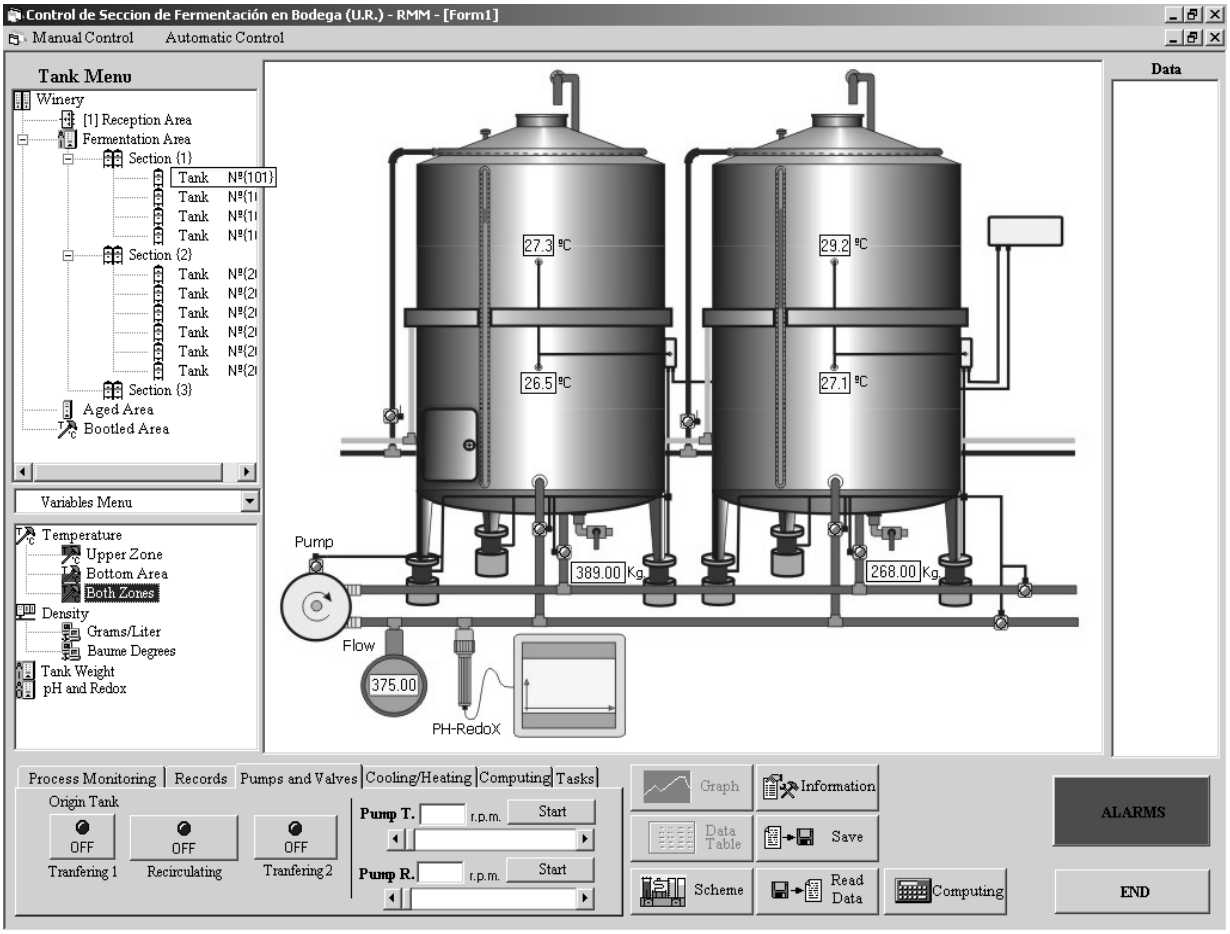

Figure 9: Control and monitoring SCADA menu

The communications follows the Ethernet/IP and CIP industrial protocols. The solution offered is flexible in terms of the winery capacity and the level of automatization desired, while being adapted to the latest technologies and open to futures advances in communication networks and automation devices. Fermentation data, collected during several seasons, will be organized in data bases in future works. The objective will be the synthesis and validation of dynamic complex models that interrelate the fermentation conditions and the wine quality.

Acknowledgements

The authors gratefully appreciate the support of the Government of La Rioja through the ANGI 2004/13 grant, and of Spanish 'Comisión Interministerial de Ciencia y Tecnología (CICYT)' through the DPI'2003-08580 grant.

References

ACROMAG INC. (2004a): User Manual Ethernet Devices 961EN, 972EN, 983EN. http://www.acromag.com/

ACROMAG STAFF. (2004b): Technical Reference – Ethernet/IP. http://www.ethernet-ip.org/

ODVA STAFF (2001a): CIP Common Specification. Vol.1, Release 1.0. Open DeviceNet Vendor Association

ODVA STAFF (2001b): Ethernet/IP Adaptation of CIP Specification. Vol. 2, Release 1.0. Open DeviceNet Vendor Association

RUIZ HERNANDEZ M. (2004): Tratado de Vinificación en Tinto. AMV Ediciones. Spain

SILER B., SPOTTS J. (2001): Visual Basic 6. Prentice Hall. (2004) Visual Basic.Net. Pearson Education

„Green Trellises“
close to Sanssouci Palace.

„Orangery Palace“
in the Sanssouci Park, including greenhouses, sculptures, fountains, arcades and terraces.

Nondestructive Quality Assessment of Pickling Cucumbers Using Visible and Near Infrared Spectroscopy

I. Kavdir[1], R. Lu[2], D. Ariana[2], M. Ngouajio[3]

[1] Department of Agricultural Machinery, College of Agriculture, Canakkale Onsekiz Mart University 17020 Canakkale, Turkey

[2] USDA Agricultural Research Service, 224 Farrall Hall, Michigan State University, East Lansing, MI 48824, USA

[3] Department of Horticulture, A428 Plant and Soil Sciences, Michigan State University, East Lansing, MI 48824, USA

Abstract: *This study was aimed at developing a nondestructive method for measuring the firmness, skin and flesh color, and dry matter content of pickling cucumbers by means of visible and near-infrared spectroscopy. Two cucumber varieties were tested in the study. Spectroscopic measurements were made from each intact cucumber in interactance mode. Standard methods were used to measure skin and flesh color, firmness, and dry matter content of the pickling cucumbers. Calibration models were developed using the partial least squares method. Good correlations were obtained in predicting firmness values measured by the slope of the Magness-Taylor force/deformation curve for the pooled data with the coefficient of determination (R^2) of 0.75 for calibration and 0.67 for validation. Better correlations were obtained in predicting skin chroma values (R^2 = 0.89 for calibration and 0.83 for validation). Results for predicting dry matter content of the cucumbers were not satisfactory partly due to the narrow dry matter content distribution in the samples. Copyright © 2006 IFAC*

Keywords: *Near-infrared spectroscopy, pickling cucumber, firmness, color, dry matter content.*

1 Introduction

Nondestructive quality measurement of fruits and vegetables has been becoming more important with the increasing demands for better food quality and faster and more efficient post harvest quality evaluation. These demands force the food producers to assess their products more vigorously. Near-infrared (NIR) spectroscopy has good potential in assessing the high moisture crops as it is accurate, fast, economical and, most importantly, nondestructive (KAYS 2000).

Pickling cucumbers received at the processing plant usually come from different growing, storage or handling backgrounds. Therefore, a rapid and effective quality evaluation of pickling cucumbers before processing would be valuable for controlling and assuring the quality and consistency of final products. Firmness, skin and flesh color, and dry matter

content are important quality parameters for pickling cucumbers. Firmness is one of the most important factors determining fruit quality (DAN *et al.* 2003). A pickling cucumber is expected to be firm in all its transversely cut sections including mesocarp (fruit wall) and carpel (seed cavity). Firmness values of fresh cucumbers are highly correlated with those of cucumbers in salt stock (SNEED & BOWERS 1970). Cucumbers with superior textural qualities are preferred for both pickling and fresh consumption (GOFFINET 1977). Hence, measuring the firmness of fresh cucumbers before brining for pickling or before fresh consumption would help to produce quality fresh cucumbers or pickles. MILLER & KELLEY (1995) evaluated pickling cucumbers using visible/near-infrared (Vis/NIR) light transmission; they reported that pickling cucumbers may vary in firmness in mesocarp and carpel areas. Therefore, pickling cucumbers should also be tested for carpel firmness, which is especially important for speared pickled cucumbers. Random destructive firmness test on selected cucumbers during sorting operations cannot provide a reliable quality assessment for pickling products.

Various works have been reported on nondestructive determination of fruit or vegetable flesh qualities such as firmness and sugar content using NIR reflectance spectroscopy. NIR spectroscopy was used in assessing soluble solids and/or firmness in tomatoes (SLAUGHTER *et al.* 1996, not listed in the Ref. list), bulbs or tubers (PEIRIS *et al.* 1999), sweet cherries (LU 2001), apples (LU *et al.* 2000), and melon and pineapples (GUTHRIE & WEDDING 1998). NIR spectroscopy has also been used for determining the maturity of fresh dates (SCHMILOVITCH *et al.* 1999) and constituents in potatoes (HARTMANN & BÜNING-PRAUE 1998, not listed in the Ref. list.).

This study was aimed at nondestructive determination of pickling cucumber quality using visible/NIR spectroscopy. Specific objectives were to determine correlations between spectral reflectance and firmness, skin and flesh color, and dry matter content, respectively, for the purpose of predicting the overall fruit quality nondestructively.

2 Materials and Methods

'Journey' and 'Vlaspik' pickling cucumbers were used in this study. Journey cucumbers were hand harvested from an experimental field at Michigan State University (MSU) Horticultural Teaching and Research Center (East Lansing, MI, USA) on August 1st of 2005. Vlaspik cucumbers were hand harvested from a commercial field in Ravenna, Michigan on August 24th of 2005. Presorted cucumbers (in the diameter range of 40-47 mm diameter) were used in the experiment.

Three hundred twenty five cucumbers harvested from MSU were stored at 10°C and 95% relative humidity for up to 18 days. About 50 cucumbers were tested at three day intervals during the two-and-half week storage period. The same procedure was followed for 294 cucumbers from the second group of cucumbers (harvested on August 24th). A total of 619 cucumbers from the two varieties were tested in the study.

2.1 Spectroscopic measurements

A miniaturized CCD-based Vis/NIR spectrometer (Model S2000, Ocean Optics Inc., Florida, USA) which had a spectral range between 550 nm and 1100 nm was used in interactance mode (**Figure 1**). Light from the light source (Oriel Instruments, Connecticut, USA) was carried to the sample via a fiber optic ring light guide of 26 mm diameter. Cucumbers were placed with the longitudinal middle section of their flat surface against the ring light guide (Fig. 1). There was a separating distance of approximately 8 mm between the illuminating ring and the detecting area so that only light that has entered the sample tissue and then existed onto the detecting area would be detected. The integration time for the spectrometer was 500 ms.

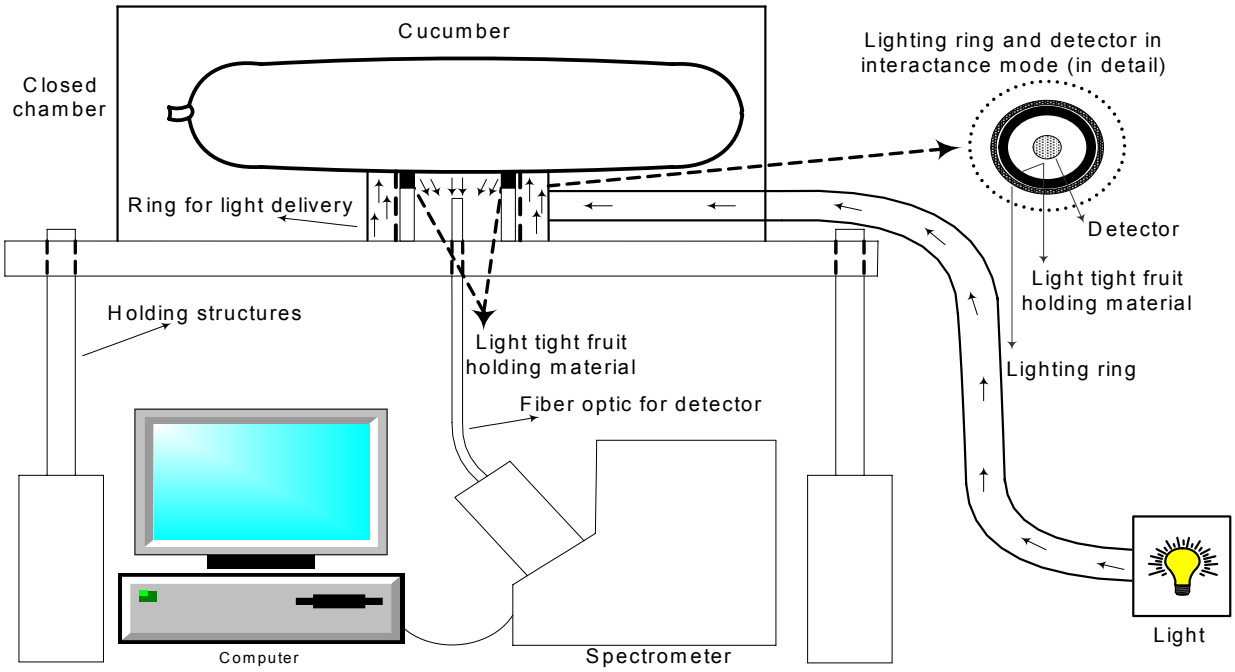

Figure 1: Reflectance measurement in interactance mode

Dark and reference spectra were collected and saved for every ten samples. A white Teflon disk of 25 mm high was used as a reference. Spectral measurements were performed in a closed chamber painted black to exclude ambient light. Cucumbers were held at room temperature (~22°C) for about 14 h before spectroscopic and standard physical measurements were made.

2.2 Color measurements

Skin and flesh color was measured from the intact (for skin color) and peeled cucumber areas (for flesh color), where spectrometer readings were made, using a digital colorimeter (Model CR-400, Minolta-Konica Sensing Inc., Osaka, Japan)., Skin color was first meas-

ured followed by flesh color measurements after a 2-3 mm thick peel was removed from the same area where spectral measurements had been performed. Prior to color measurements, the colorimeter was calibrated with a standard white calibration plate. Color readings were recorded in the format of CIE XYZ color space (also known as CIE 1931 color space). It was then converted into Lab color space (CIE L*a*b*) which is an absolute color space. Chroma ($\sqrt{a^{*2}+b^{*2}}$) and hue (arc tan [*b**/*a**]) were derived from Lab color space.

2.3 Magness-Taylor (MT) firmness measurement

Fruit firmness was tested using a texture analyzer (Model TA.XT2, Stable Micro Systems, Goldalming, Surrey, UK) with a 6-mm diameter probe for 10 mm penetration into the peeled section of each fruit. The loading speed of the probe was 2 mm/sec. The probe first passed through the mesocarp and then into the endocarp of the fruit. Slope, maximum force and strain energy (i.e., the area under force/deformation curve from 0 to 6 mm of deformation) recorded were considered to be measures of fruit firmness. Slope values were calculated from the line connecting the two points at 0 mm and 2 mm on the MT force/deformation curve (**Figure 2**). This portion of the MT force/deformation curve was highly linear, reflecting the elastic response of the cucumbers.

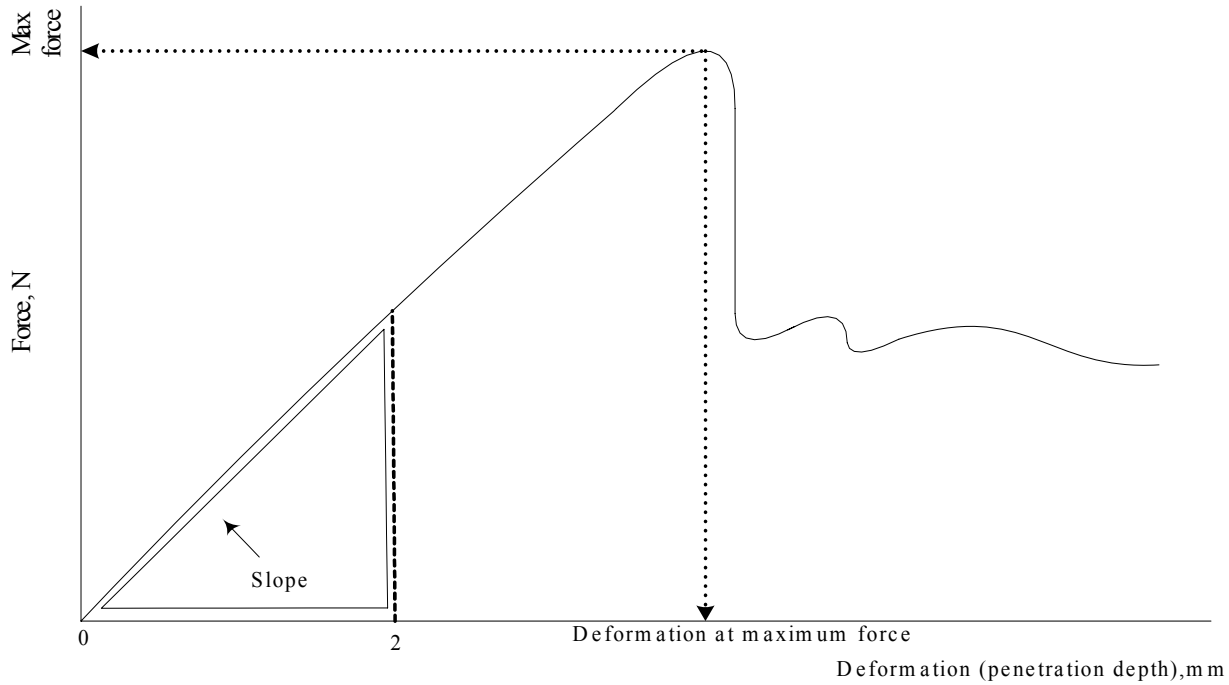

Figure 2: Force/deformation curve from the Magness -Taylor penetration test for a sample

2.4 Dry matter content

A cucumber slice of 0.7-1.0 cm thick was taken adjacent to the firmness measurement area on the side of the blossom end. Cucumber slices were dried in a convection oven at 80°C for 24 h. Dry matter content, expressed on a wet basis, was determined by taking the difference between the weights of the slice before and after the oven drying.

2.5 Data processing

Relative reflectance spectra were calculated from the raw reflectance spectra of cucumber samples using the following equation:

$$\text{Relative reflectance} = \frac{\left|sample - dark\right|}{\left|reference - dark\right|} \qquad (1)$$

The relative reflectance spectra were then preprocessed using the Savitzky-Golay smoothing method (with the gap size of 19 data points and a second order polynomial fitting function) and mean centering. Logarithm and first and second derivatives of the relative reflectance data were taken following the preprocessing. The partial least squares (PLS) method was used to develop calibration models from 2/3 of the cucumber samples for predicting firmness, skin and flesh chroma, and dry matter content. The models were validated with the remaining samples.

Cucumbers from the two varieties were evaluated separately and also together as one data group (all). Log and first and second derivative of the relative reflectance spectra were applied to each of the three data groups (Journey, Vlaspik and pooled) in order to find the optimal calibration models.

3 Results and Discussion

For different data treatments, the best results were obtained by taking the natural logarithm of the spectra and using all the cucumbers (Journey and Vlaspik), as measured by the correlation between NIR predictions and the quality parameters. Also, superior results were obtained for Journey variety compared to Vlaspik variety (results were not given). However, the paper only reports results for the pooled data (Journey and Vlaspik).

3.1 Measurements of cucumber quality

Table 1 shows the mean and standard deviation of firmness measurements in terms of MT area, slope and maximum force, skin and flesh color measurements and dry matter content of the two cucumber varieties and the pooled data from both varieties. Firmness measurements for Vlaspik cucumbers were significantly higher compared to those for

Table 1: Summary of the means and standard deviations (S.D.) of Magness-Taylor area, slope and maximum force (firmness), skin and flesh color values and dry matter content for two cucumber varieties

Variety (Number of samples)		Firmness			Skin color		Flesh color		Dry matter
		Area[+]	Slope[‡]	Max Force	Chroma	Hue	Chroma	Hue	(%)
Journey (325)	Mean	67.02	4.29	23.31	27.97	-0.96	26.48	-1.09	3.88
	S.D.	13.94	1.24	4.73	6.08	0.05	4.28	0.02	0.38
Vlaspik (294)	Mean	101.09	6.75	31.36	25.91	-0.96	22.90	-1.11	4.03
	S.D.	15.15	1.26	4.36	5.89	0.05	4.45	0.03	0.33
Pooled (619)	Mean	83.20	5.46	27.37	26.99	-0.96	24.78	-1.10	3.95
	S.D.	22.38	1.75	6.25	6.07	0.05	4.71	0.03	0.36

[+] Area under the Magness-Taylor force/deformation curve (from 0 to 6 mm of deformation, Fig. 2).
[‡] Slope was obtained from the line connecting the two points at 0 mm and 2 mm on the MT force/deformation curve.

Journey cucumbers. Similar differences for skin and flesh chroma between the two varieties were also observed. However, the dry matter contents for the two varieties were about the same.

Firmness of the cucumbers increased during the first three days after harvest and then decreased steadily with time for the rest of the storage period (**Figure 3**). The three firmness indexes, i.e., MT area, slope and maximum force, displayed a similar change pattern over the storage period.

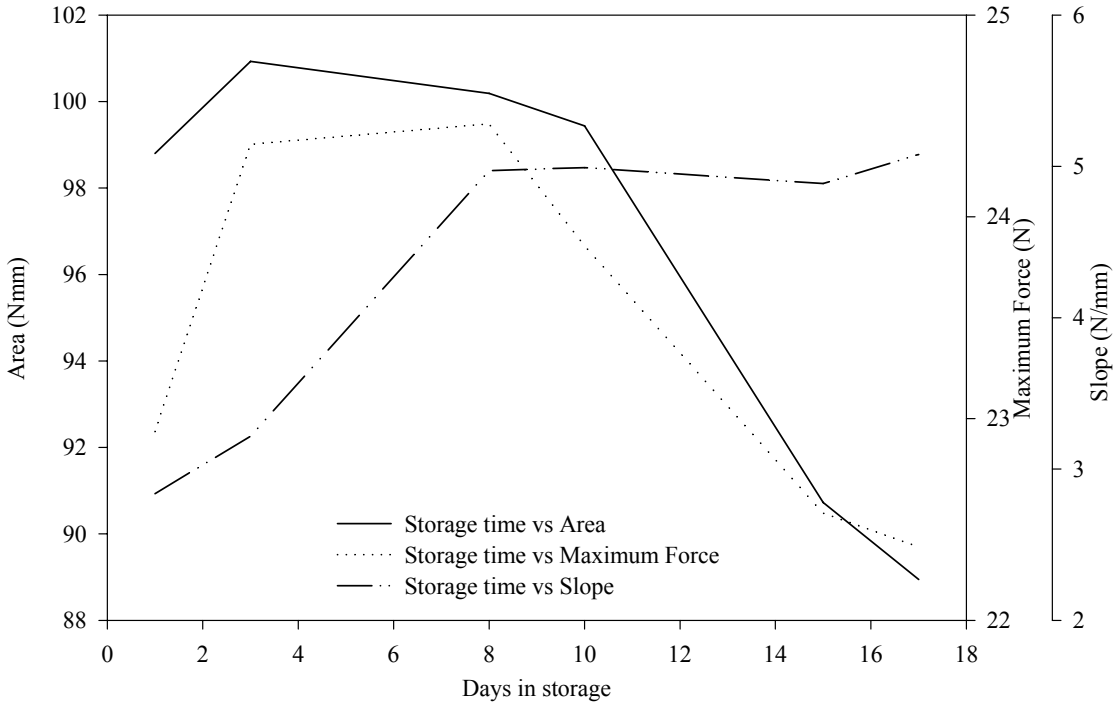

Figure 3: Change of firmness (as measured by the area and force) with storage time for Journey cucumbers

3.2 Relative reflectance spectra of cucumbers

Figure 4 shows average relative reflectance curves of the cucumbers obtained by the Vis/NIR spectrometer at the first, middle and last day of the storage period. The relative spectra had one broad reflectance peak starting at 680 nm and ending around 930 nm. Throughout the entire spectral range (550 nm-1100 nm) cucumbers at the end of their storage period showed consistently higher reflectance values while the cucumbers at the beginning of the storage period showed lower reflectance values. Cucumbers in the middle of their storage period had reflectance (absorption) values in between the other two cucumber groups (Fig. 4).

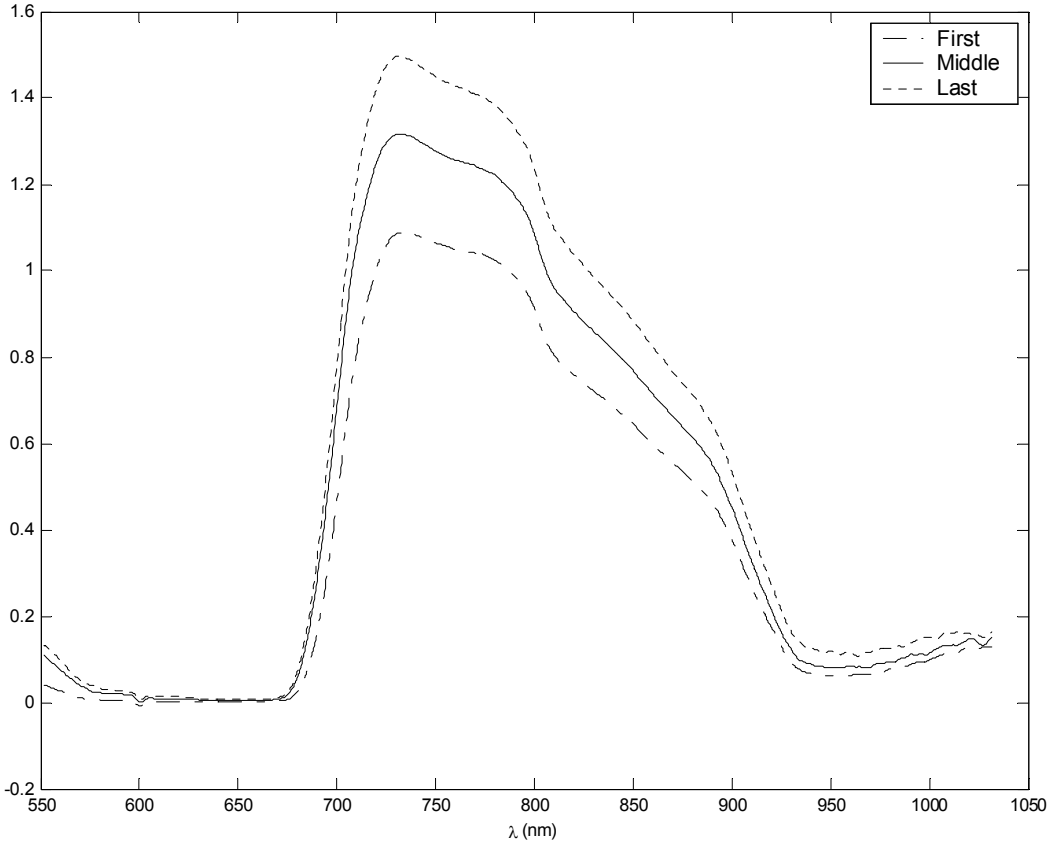

Figure 4: Average relative reflectance spectra of Journey cucumbers obtained by the Vis/NIR spectrometer at the first, middle and last day of the storage period

3.3 Firmness prediction

Table 2 summarizes firmness prediction results from PLS analyses. Best results were obtained from the natural logarithm of the relative reflectance of spectra (only these results are given in Table 2). Among the three firmness indexes, MT slope had the best correlation with spectral measurements. MT area under the force-deformation curve (from 0 to 6 mm of deformation) provided the second highest firmness prediction while MT maximum force produced the lowest R^2 value. The correlations of NIR reflectance with firmness (MT

area, slope and maximum force) for the pooled data in calibration ranged from 0.41 to 0.75 (Table 2). The SECs (standard errors in calibration) were 16 for MT area, 0.90 for slope and 4.84 for maximum force. When the models were used to predict firmness, the R^2 values ranged between 0.36 and 0.67 while SEPs (standard errors in prediction) were 15, 1 and 4.93 for MT area, slope and maximum force, respectively.

Table 2: Summary of the calibration and prediction results from partial least squares analysis for visible and near-infrared determination of firmness and skin and flesh color for the pooled data of Journey and Vlaspik cucumbers (Results were obtained by taking the natural logarithm of the relative reflectance spectra)

Property measured		Factors	Calibration		Validation	
			R^2	SEC	R^2	SEP
Firmness	Area[+]	7	0.54	16.00	0.52	15.00
	Slope[‡]	11	0.75	0.90	0.67	0.99
	Maximum Force	7	0.41	4.84	0.36	4.93
Skin color	Skin Chroma	11	0.89	1.90	0.83	2.70
	Skin Hue	5	0.76	0.02	0.76	0.03
Flesh color	Flesh Chroma	6	0.32	3.90	0.27	4.00
	Flesh Hue	11	0.70	0.01	0.65	0.02

[+] Area under the Magness-Taylor force/deformation curve (from 0 to 6 mm of deformation, Fig. 2).
[‡] Slope was obtained from the line connecting the two points at 0 mm and 2 mm on the MT force/deformation curve.
R^2: coefficient of determination; SEC (or SEP) = standard error of calibration (or prediction)

Less firm cucumbers tended to reflect more light in interactance mode than firmer cucumbers (Fig. 4). This observation seems justifiable since the reflected light measured in interactance mode had traveled in the cucumber flesh for at least 8 mm distance before it re-emerged from the fruit. Firm cucumbers generally have denser cells or stronger cellular structures and hence it is more difficult for light to propagate in the fruit. On the other hand, it is also possible that the physiological change accompanied with the fruit softening process could also affect light absorption or reflectance.

MT slope is more closely related to the elastic properties of the cucumber fruit while MT maximum force and area are a better measure of the mechanical strength or the combined elastic properties and failure strength of the fruit. Hence better correlation for MT slope (**Figure 5**) may suggest that NIR spectroscopic measurements were better related to the elasticity of cucumbers than with the mechanical strength of the fruit (Table 2).

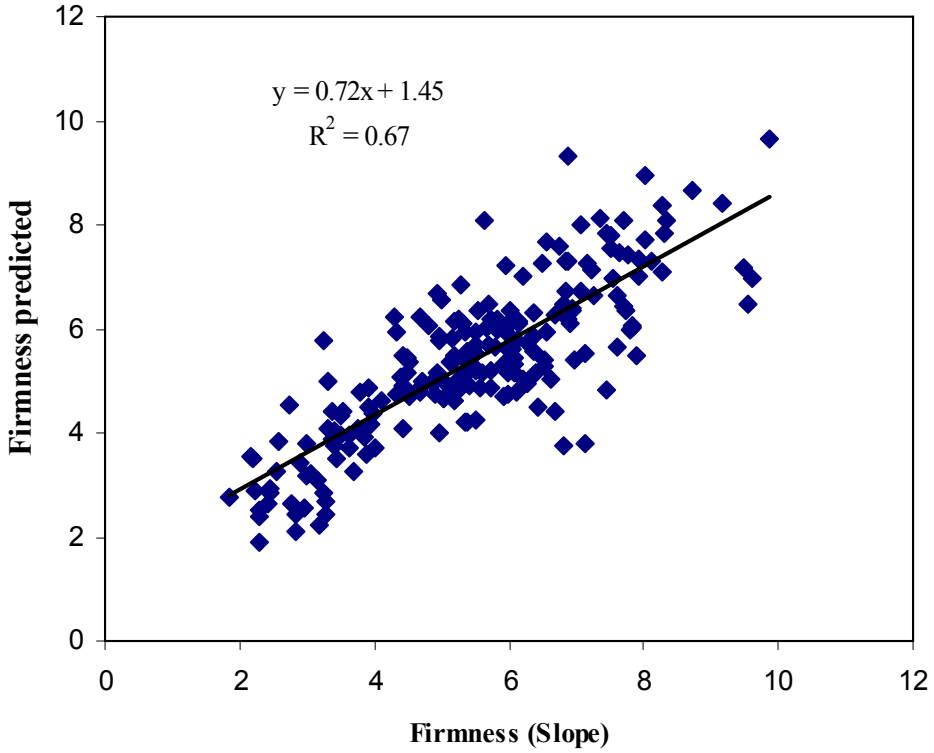

Figure 5: Visible/near-infrared predictions of cucumber firmness (slope) for the pooled data

3.4 Color prediction

High values for the coefficient of determination were obtained for skin chroma (R^2 = 0.89 for calibration and 0.83 for prediction) as the visible region was covered by the spectrometer (**Figure 6**). Good correlation results (R^2 = 0.76 for both calibration and prediction) were also obtained for skin hue (Table 2).

Values of the coefficient of determination obtained for flesh color in calibration or validation were lower compared to the correlation results for skin color; this was especially true for flesh chroma (Table 2). Values of the coefficient of determination for flesh hue were much higher than those obtained for flesh chroma (Table 2 and **Figure 7**). These results may imply that the change in both skin and flesh colors could be detected by the Vis/NIR spectrometer.

3.5 Dry matter prediction

Low R^2 values for calibration and prediction of dry matter content were obtained for all the data treatments (Journey, Vlaspik and pooled) although correlation values for predicting the dry matter content for Journey variety (R^2= 0.64 in prediction) was better than Vlaspik variety (R^2=0.13). This may be due to the narrow range of the dry matter content among the cucumbers in the data groups studied (Table 1).

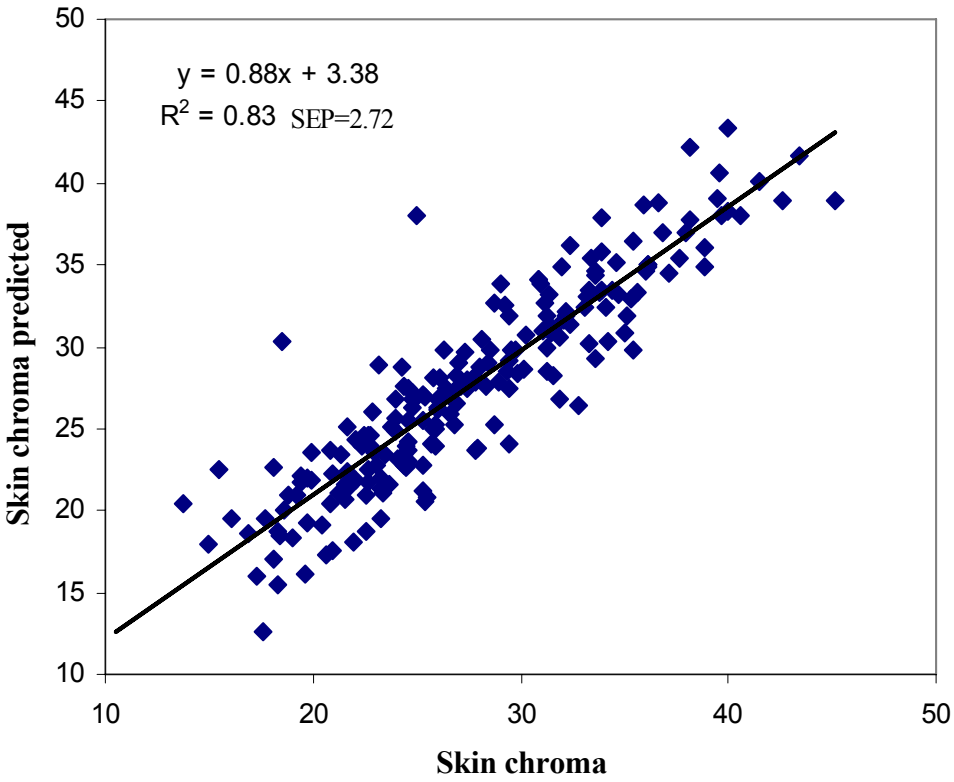

Figure 6: Visible/near-infrared spectroscopic predictions of skin chroma for the pooled cucumbers from two varieties

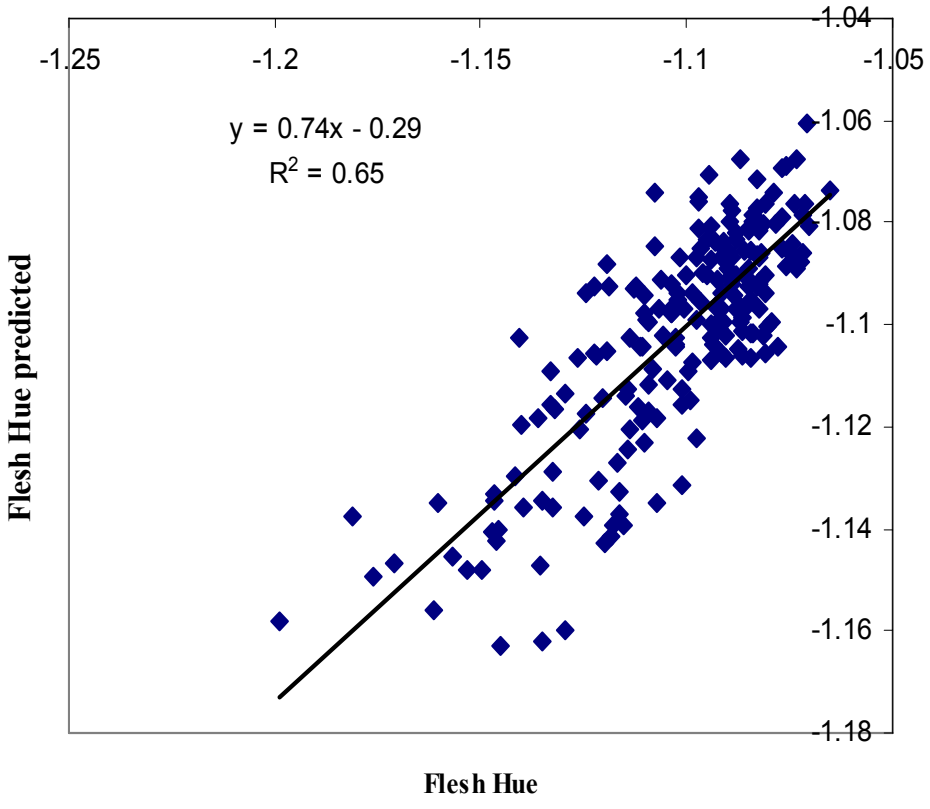

Figure 7: Visible/near-infrared spectroscopic predictions of flesh color for the pooled data of two cucumber varieties

4 Conclusions

Among different spectra treatments, the natural logarithm of the relative reflectance spectra had best results for predicting cucumber quality parameters.

Near-infrared measurement had a good correlation with the Magness-Tayor (MT) slope (R^2 = 0.67 for validation). Predicting firmness using the area under the MT force/deformation curve produced lower correlation values (R^2 = 0.52) while using maximum force resulted in the lowest correlation.

High correlation between visible/near-infrared measurements and skin color chroma values was obtained (R^2 = 0.89 for calibration and 0.83 for prediction). Although flesh color predictions were not as good as the skin color predictions, promising results were obtained for flesh hue.

Correlation relations in predicting dry matter content were not good.

This research demonstrated the potential usefulness of visible and near infrared spectroscopy for measuring quality of pickling cucumbers. However, further studies are needed on different light illumination/sensing modes in order to improve the performance of Vis/NIR spectroscopy in predicting quality of pickling cucumbers.

Acknowledgements

The authors thank Mr. Benjamin Bailey, Engineering Technician for USDA Agricultural Research Service, for his technical support for this research and Dr. Daniel E. Guyer for his support and help. This work was funded in part by TUBITAK-BAYG (The Scientific and Technological Research Council of Turkey).

References

DAN H., OKUHARA K., KOHYAMA K. (2003): Discrimination of cucumber cultivars using a multiple-point sheet sensor to measure biting force. J. Sci. Food Agric. 83: 1320-1326

GOFFINET M.C. (1977): Some anatomical considerations in the study of cucumber fruit texture. J. Amer. Soc. Hort. Sci. 102(4): 474-478

GUTHRIE J., WEDDING B. (1998): Robustness of NIR calibrations for soluble solids in intact melon and pineapple. J. Near Infrared Spectrosc. 6: 259-265

HARTMANN R., BÜNİNG-PFAUE H. (1998): NIR determination of potato. Potato Research. 41: 327-334

KAYS S.J. (2000): On-line near infrared quality assessment of high moisture plant products. pp. 119-127. In: Integrated View of Fruit & Vegetable Quality. W.J. Florkowski, S.E. Prussia, R.L. Shewfelt (eds.), Technomic Pub., Lancaster, PA

LU R., GUYER D.E., BEAUDRY R.M. (2000): Determination of firmness and sugar content apples using near-infrared diffuse reflectance. Journal of texture studies 31: 615-630

LU R. (2001): Predicting firmness and sugar content of sweet cherries using near-infrared diffuse reflectance spectroscopy. Trans ASAE. 44(5): 1265-1271

MILLER A.R., KELLEY T.J. (1995): Nondestructive evaluation of pickling cucumbers using visible-infrared light transmission. J. Amer. Soc. Hort. Sci. 120(6): 1063-1068

PEIRIS K.H.S., DULL G.G., LEFFLER R.G., KAYS S.J. (1999): Spatial variability of soluble solids or dry-matter content within individual fruits, bulbs, or tubers: Implications for the development and use of NIR spectrometric techniques. Hortscience. 34(1): 114-118

SNEED F.D., BOWERS J.L. (1970): Green fruit characters of cucumber as related to quality factors in brine stock. J. Amer. Soc. Hort. Sci. 95(4): 489-491

SCHMILOVITCH Z., HOFFMAN A., EGOZI H., BEN-ZVI R., BERNSTEIN Z., ALCHANATIS V. (1999): Maturity determination of fresh dates by near infrared spectrometry. J. Science Food and Agric 79: 86-90

SLAUGHTER D.C., BARRETT D., BEORSIG M. (1996): Nondestructive determination of soluble solids in tomatoes using near infrared spectroscopy. J. Food Science 61(4): 695-697

Optimal Climate Control to Anticipate Future Weather and Energy Tariffs

Leo Lukasse, Aart-Jan van der Voort, Janneke de Kramer-Cuppen
Agrotechnology & Food Innovations B.V., Wageningen University and Research
P.O. Box 17, 6700 AA Wageningen, Netherland

Abstract: *The objective of this research is to develop a methodology to augment classical climate controllers with a means to anticipate future external disturbances, esp. ambient temperature and electricity tariffs. Receding horizon optimal control (RHOC) is used as the methodology to augment the classical feedback controllers. The algorithm used to solve the RHOC problem is presented. In simulation the technology is applied to the case of ventilated potato storage, indicating a large added value. Therefore the control algorithm is currently being tested in full-scale storage facilities. Copyright © 2006 IFAC.*

Keywords: *cold storage, potato storage, ventilation, refrigeration, energy*

1 Introduction

Climate control in storage facilities for agricultural produce is usually just a matter of feedback temperature control with the sole objective to reduce the temperature to its setpoint. The feedback controller responds to elevations of the measured product temperature T_{pr} above setpoint T_{ref} by withdrawing heat, sometimes by means of ventilating with ambient air of sufficiently low temperature T_{amb}, often by means of activating a refrigeration plant.

The impossibility to anticipate future external inputs causes suboptimalities. For example feedback control lacks the ability to:

- Utilize cheap ventilation to cool down below T_{ref} if today $T_{amb} < T_{ref}$ while it is forecasted that tomorrow $T_{amb} > T_{ref}$.
- Postpone refrigeration if the energy price is now high while it is expected that it will be low in a few hours/days. Fluctuating energy prices have been common practice in terms of fixed day/night tariffs, but more fluctuations due to liberalisation of the European energy markets are to be expected.

The objective of this research is to develop a methodology to augment the classical climate controllers with a means to anticipate future external disturbances, esp. ambient temperature and electricity tariffs.

2 Methodology: Optimal Control

It was decided to use receding horizon optimal control (RHOC) as the methodology to augment the classical feedback controllers. RHOC has the capability to (optimally) anticipate future disturbances. Moreover the RHOC framework naturally handles system non-linearities.

Figure 1 schematically depicts how a RHOC simulation is performed. At initial time t_0 the current state $x(t_0)$ is measured/estimated and put in to an optimal control (OC) problem with time window $[t_0, t_0+H]$. Output of the OC problem is the computed optimal control sequence $[u(t_0), .., u(t_0+H)]$. Only the first few controls $[u(t_0), .., u(t_0+t_c-1)]$ are implemented. Each time when a control interval t_c has gone by the above cycle is repeated.

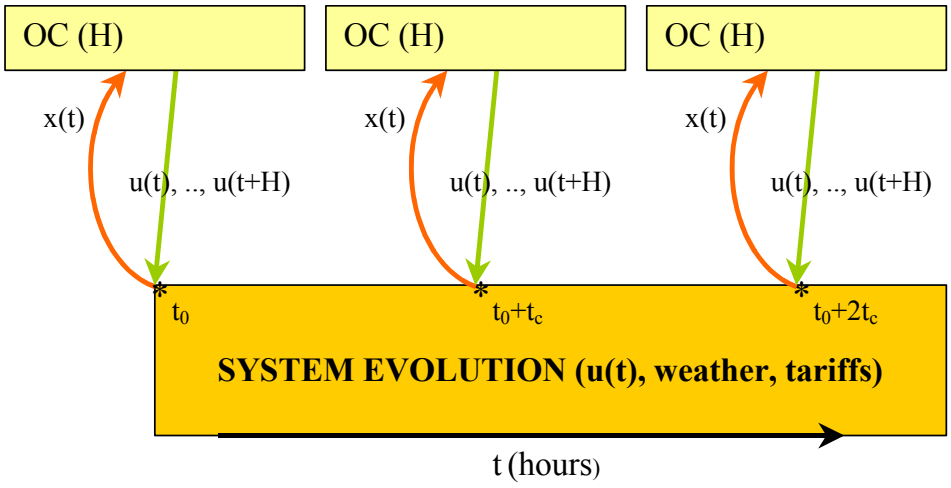

Figure 1: RHOC simulation scheme

Figure 2 illustrates how the RHOC components interact. Inputs to the OC in Figure 2 are: objective function, weather forecasts, expected tariffs and x(t). In an OC two main components are distinguished: a physical model of the controlled system and an optimizer. The output of the OC is: optimal control $u^*(t)$. By calling OC on a regular interval OC becomes RHOC.

The generic OC problem is given by

$$\min_{u(0),..,u(N-1)} J(u) = \phi(x(N)) + \sum_{k=0}^{N-1} L[x(k), u(k), k] \qquad (1)$$

subject to

$$x(k+1) = f[x(k), u(k), k] \qquad (2)$$

and

$$u_{\min}(k) < u(k) < u_{\max}(k) \qquad (3)$$

After defining the Hamiltonian H

$$H(x,u,k) = L(x,u,k) + \lambda(k+1)^T f(x,u,k) \quad (4)$$

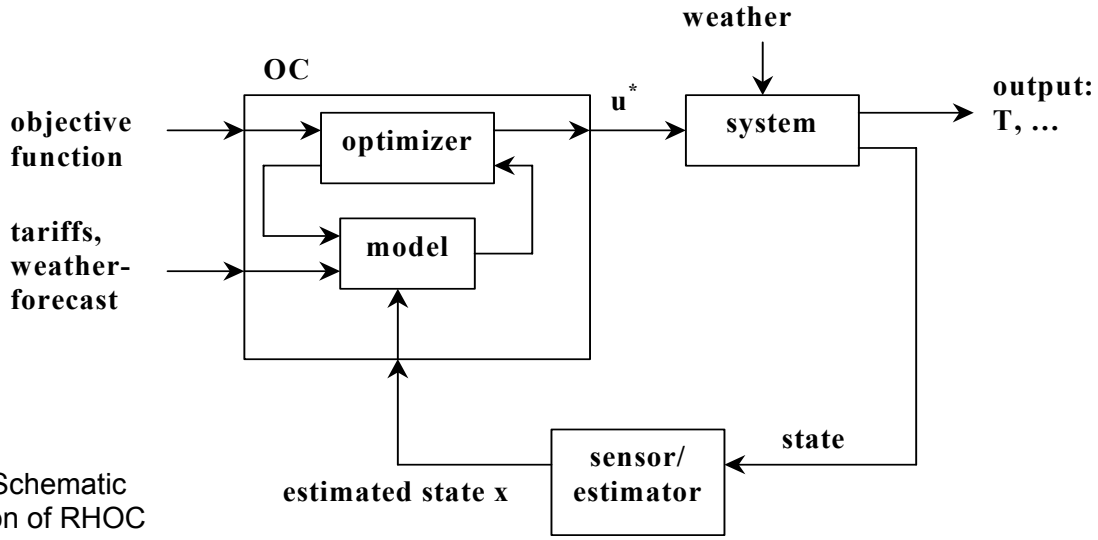

Figure 2: Schematic presentation of RHOC

Pontryagin's Minimum Principle (*e.g.* LEWIS 1995) states:

A control sequence $u^*(k)$ and the resulting state trajectory $x^*(k)$ are optimal, i.e. minimize J(u) in eqn. 1, if the 4 conditions below are met:

state equations (condition 1):

$$x(k+1) = f[x(k),u(k),k] \quad (5)$$

costate equations for 0 ≤ k ≤ N-1 (condition 2):

$$\lambda^T(k) = \frac{\partial L}{\partial x} + \lambda^T(k+1) \cdot \frac{\partial f}{\partial x}^T \quad (6)$$

Minimum condition for 0 ≤ k ≤ N-1 (condition 3):

$$H(x,u^*,k) \le H(x,u,k) \quad (7)$$

Boundary conditions (condition 4):

$$x(0) = x_0$$

$$\lambda^T(N) = \frac{\partial \phi(x(N))}{\partial x} \quad (8)$$

The optimizer in Figure 2 solves the OC problem formulated above by means of an iterative non-linear optimization procedure:

1. Choose an initial control sequence *u(k), k=0,1, .., N-1.*
2. Simulate the state equations (eqn. 2) forward in time for given *x(0)* and *u(k)*.
3. Evaluate *J(u)* and terminal costate $\lambda^T(N)$ (eqn. 8).
4. Simulate the costate equations (eqn. 6) backward in time from N to 0, using $\lambda(N)$ and *u(k):*
5. Compute $\partial H(x,u,\lambda,k)/\partial u$ (=$\partial J(u)/\partial u$) for k = *0, 1, .., N-1*:

$$\frac{\partial H(x,u,\lambda,k)}{\partial u} = \frac{\partial L(x,u,k)}{\partial u} + \lambda(t)^T \frac{\partial f(x,u,k)}{\partial u} \qquad (9)$$

6. Determine the conjugate gradiet search direction SD_i for iteration *i* from the gradient $\partial H(x,u,\lambda,k)/\partial u$ and the search direction SD_{i-1} used in the previous iteration.
7. Perform a line search, cq. compute the changes $\delta u(k)$ of *u(k)* based on SD_i such that the minimum condition (eqn. 7) is closer met. This boils down to optimizing the stepsize *s*>0 in:

$$\delta u(t) = -s \cdot SD_i \qquad (10)$$

   Optimizing *s* is a one-dimensional optimization problem, in de code this is solved by a call to the standard matlab-function *fminsearch*.
8. Compute new *u(k)* according to

$$u_{i+1}(k) := u_i(k) + \delta u_i(k) \qquad (11)$$

9. Stop if (max. no. of iterations is exceeded) or ($\delta u(t)^T \cdot \delta u(t) < tol_1$) or (improvement in $J(u) < tol_2$)
10. Go to step 2 for next iteration.

The above algorithm exhibits a guaranteed convergence to a local minimum if f, L, f_x, L_x, f_u and L_u are continuous functions of both x and u. (In)equality constraints on combinations of x(k) and u(k) may also be handled by the above algorithm after reformulating the OC problem. See *e.g.* PIERRE (1969) and VAN HENTEN (1994).

3 Case: Ventilated Potato Storage

Developing RHOC for potato stores (**Figure 3**) involves several steps:

1. model development
2. formulating the OC problem
3. feeding the RHOC with weather forecasts
4. (RH)OC simulation
5. analysis of added value

Figure 3: A Dutch potato store

In chapter 3.1 through 3.5 each of the above steps is described.

3.1 Model Development

First a detailed physical model of the climate distribution in potato stores was formulated.

Figure 4 shows the common outline of ventilated storage facilities. The two control inputs are the position of the hatches for mixing inlet and return air u_{mix} (u_1) and the fraction of fan capacity used for air circulation u_{fan} (u_2). The ambient temperature T_{amb} acts as a disturbance on the system.

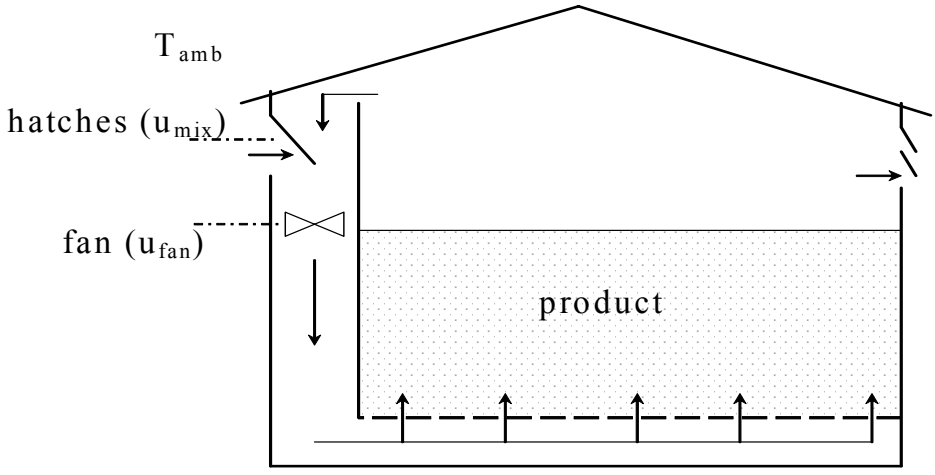

Figure 4: Common outline of potato storage facilities

After parameter calibration the model fits well to extensive data collected from three different potato stores. The good fit for all three cases is achieved with the calibration parameters calibrated on the basis of data from one case only (**Figure 5**). For more information on the detailed climate model see LUKASSE *et al.* (2006).

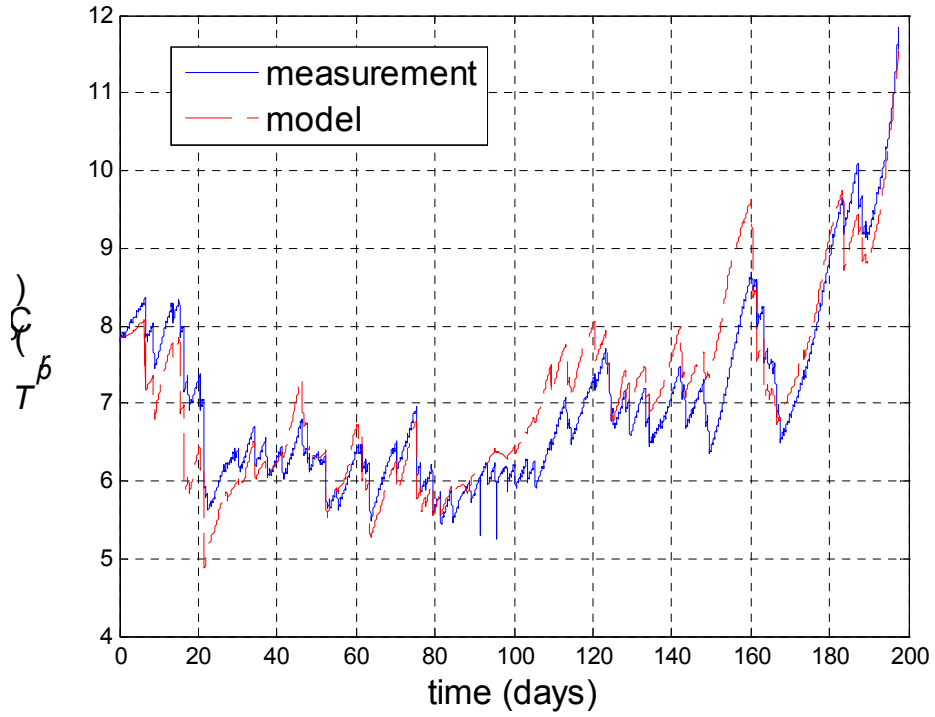

Figure 5: Model fit to measurements (validation data)

The validated detailed model is a perfect tool to analyze the effect of design and control parameters, but requires too much computation time to take the role of the model in Figure 2. Therefore the model has been reduced to

$$x_T(k+1) = x_T(k) + t_s * (p(1) + (p(2) + p(3) * u_1(k) * u_2(k)) * (T_{amb}(k) - x_T(k))) \quad (12)$$

$$x_e(k+1) = x_e(k) + t_s * p(4) * u_2(k) \quad (13)$$

where p(1) till p(4) are model parameters, t_s is the sampling interval (1 hour), and

x_T = average produce temperature [°C].

x_e = consumed electricity [kWh].

The above model reduction slashes the computation time by a factor 15 at the expense of a slightly larger prediction error. Note the non-linearity in eqn. 12 caused by the product of x and u.

3.2 Formulating the OC Problem

For OC the reduced model of chapter 3.1 is augmented with two running cost states and an objective function J(u):

$$x_{L,T}(k+1) = x_{L,T}(k) + t_s * (x_T(k) - T_{ref}(k))^2 \quad (14)$$

$$x_{L,e}(k+1) = x_{L,e}(k) + t_s * e(k) * p(4) * u_2(k) \quad (15)$$

$$J(u) = x_{L,T}(N) + p_w(1) * x_{L,e}(N) \quad (16)$$

The 4-dimensional state thus becomes

$$x = [x_T \quad x_e \quad x_{L,T} \quad x_{L,e}] \quad (17)$$

where e(k) is the energy tariff at time k (€/kWh), $p_w(1)$ is a weight parameter in objective function J(u), and

$x_{L,T}$ = penalty costs for deviations between x_T and temperature setpoint T_{ref}.

x_e = costs of consumed electricity [€].

The above formulated OC problem merely is a *climate* control issue without explicitly taking into account the issue of produce quality. The choice to focus on this lower level optimization problem is motivated by the wish to develop a technology which is broadly applicable. Incorporating produce quality in J(u) would require produce quality measurements and produce quality evolution models for each specific species and cultivars of stored produce. Now the produce-independence allows for straightforward generalization to other storage facilities.

3.3 Feeding the RHOC With Weather Forecasts

As illustrated in Figure 2 the OC requires input information with respect to energy tariffs and expected weather. For the case of potato storage there is no uncertainty in the expected energy tariffs: it is a simple high/low tariff-structure, where the low tariff applies during night and in the weekends.

Defining the expected weather is less trivial. In this project the OC is fed with the 10 days ahead weather forecasts provided by project partner WNI. Due to the instable nature of the atmosphere the weather forecast is sensitive to initial conditions. Therefore WNI uses an EPS ensemble prediction system (PALMER *et al.* 1997) to gain insight in the uncertainty of the forecast. Each day the EPS provides an ensemble consisting of 50 members. Each of the members contains a temperature prediction for 10 days ahead at 6-hour intervals ('50 EPS members' in **Figure 6**). All members have an equal chance of realization. In pre-

paring the weather forecast input to OC the mean of all 50 members is taken. This mean prediction is first interpolated to hourly values, then improved using the current local $T_{amb}(0)$ measured outside the storage facility ('$T_{amb}(0)$' in Figure 6), and finally put in to the OC ('OC input' in Figure 6).

Figure 6 depicts just an arbitrary example of a 10-days EPS forecast and the temperature forecast put in to the OC. In this case the temperature spread between the 50 EPS members is small during the first two days, and then gradually increases till over 10°C for the 10 days ahead prediction. This is a common phenomenon in the EPS predictions, although the exact pattern varies. Incidentally the temperature spread between the members reduces temporarily for further ahead predictions. To a minor extend this occurs in Figure 6: from day 3 to day 4 the spread in predicted temperatures reduces. In this application these prediction uncertainties hardly hamper the optimality of the RHOC control scheme, for more details see DOESWIJK *et al.* (2006).

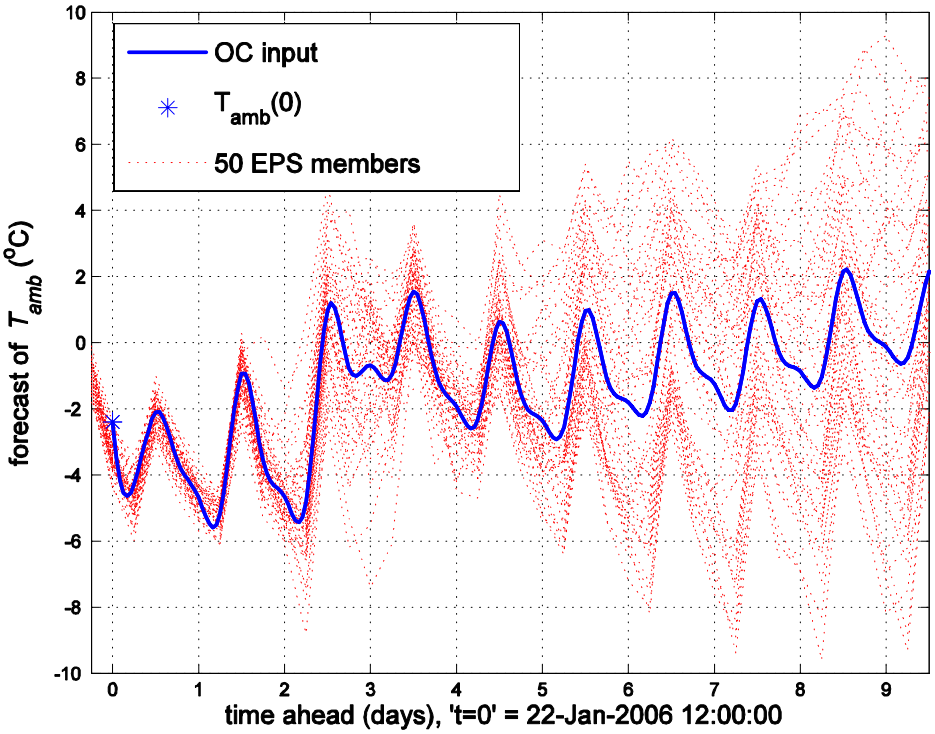

Figure 6: used weather forecasts

3.4 (RH)OC simulation

In the MATLAB® simulation environment the above OC problem was combined with a self-programmed optimizer according to chapter 2 to solve the OC problem. In the software development optimizer and model are strictly separate modules. This reduces the development time when moving on to other application, and facilitates the testing of modifications in the optimizer on multiple cases. The correct functioning of the OC was verified by testing the optimality of its solution. This check is done by re-simulating the

model over the time interval [t, t+H] many times with slightly perturbed control inputs. In each simulation run one element of the optimal control sequence $u^*(t)$, ..,$u^*(t+H)$ is perturbed by +5% or –5% of the control span [0, 1], yielding a perturbed objective function value J_{pert}. Altogether this requires 4*H runs: 2 control inputs * H time instants * (a positive and a negative perturbation). If in all of the 4*H runs $J_{pert} \geq J^*$ then the computed solution u^* is accepted as the optimal solution. After verification of the correct functioning of OC a complete RHOC scheme is simulated, in which model and system in Figure 2 are identical and the state estimator yields perfect knowledge of the true state.

The RHOC simulation study exhibits attractive behaviour, especially in periods of unsteady weather. Here 'unsteady weather' means weather in which the diurnal 24h temperature cycle exhibits significant variations over two consecutive days. **Figure 7** depicts some of the RHOC results.

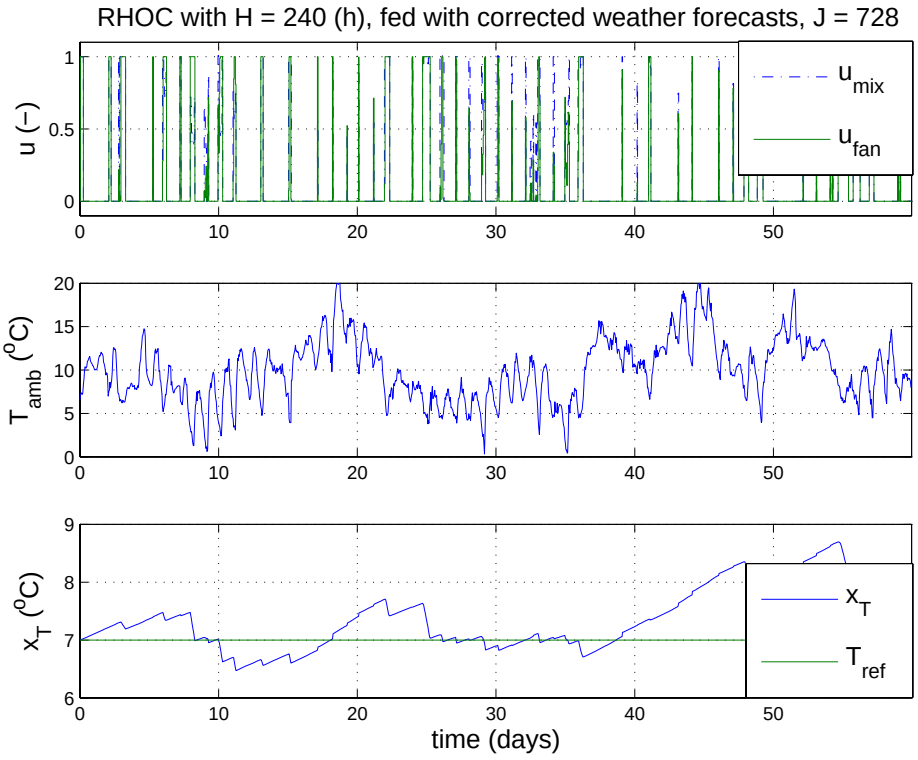

Figure 7: example of an optimization result

A warm period occurs for 16<t<20 (Figure 7 b). In the days before the RHOC anticipates this period by reducing x_T below T_{ref} by ventilation (u_{fan}) with cold ambient air (T_{amb}). The consequence of this anticipation is that x_T around t = 22 remains closer to T_{ref} than would have happened without this anticipation.

3.5 Analysis of added value

Figure 7 is just one example, but how would an implementation of RHOC in potato stores perform on average? To answer that question numerous simulations have been run over 2 months periods for various combinations of 1) model and system, 2) weather and weather forecast, and 3) tunings of the objective function. Even for large deviations between model and system (prediction errors) it turns out that it is worthwhile to use RHOC to plan the control of fans and hatches in ventilated potato stores. For many different cases so-called (J,H)-plots have been made. **Figure 8** is just one characteristic example of a (J,H)-plot.

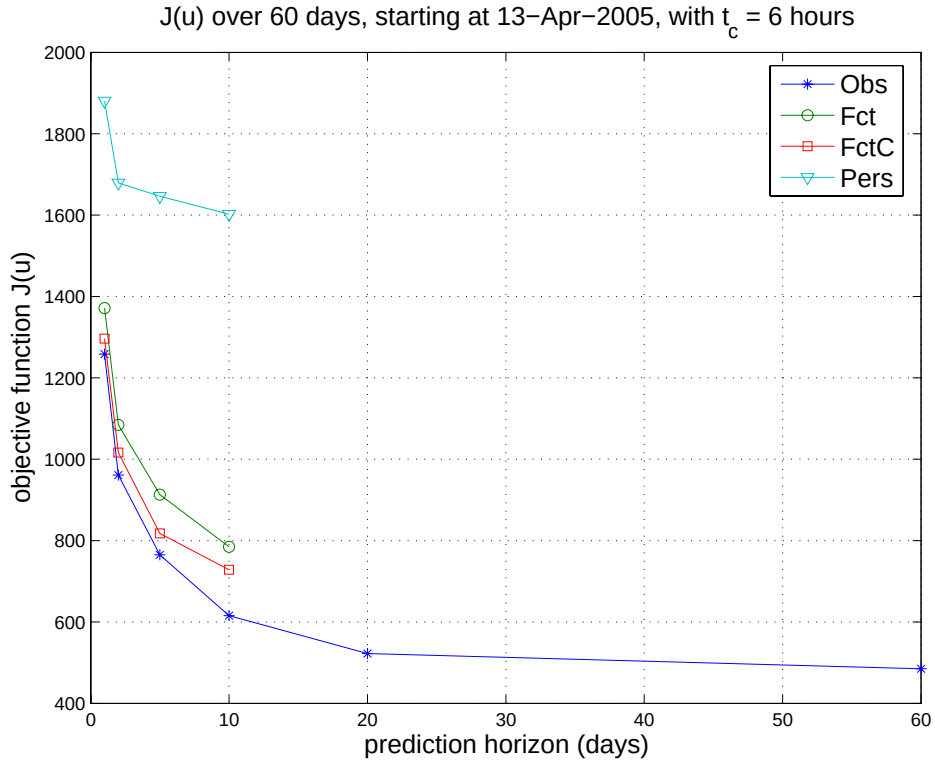

Figure 8: (J,H)-plot for mid April '05 till mid June '05

In Figure 8 the curve 'Obs' shows the realization of J(u) as a function of prediction horizon H when the control scheme of Figure 2 is simulated over the 60 days from mid April '05 till mid June '05 using the observations of T_{amb} as input to 'system' and 'model'. Obviously this is a theoretical exercise gaining insight in the feasible J(u) as a function of H for perfect weather forecasts. The best feasible J(u) is the case where H=60 (anticipate the full simulation horizon) combined with perfect prior knowledge of T_{amb} ('Obs'-curve for H=60). The 'Obs'-curve shows that anticipating more than 20 days ahead makes hardly any sense for this case.

The other three curves are cases where ‘model’ in Figure 2 is fed with three different types of weather forecasts, while ‘system’ in Figure 2 is always fed with observations. ‘FctC’ is the mean EPS ForeCasT Corrected with current locally measured T_{amb} (Figure 6). ‘Fct’ is just the mean EPS ForeCasT without any further correction. ‘Pers’ assumes that the cycle of T_{amb} observed over the last 24 hours persists over the prediction horizon.

Is it wise to use H=10 or would a smaller H establish a better J(u) by less anticipation on errors in predicted T_{amb}? The fact that J(u) is negatively correlated with H for any kind of forecast is sufficient reason to use H=10. Apparently the possible negative effect of anticipating prediction errors is outperformed by the positive effect(s) of increasing H.

Why does H=10 yield more optimal results than smaller H, even for the simple ‘Pers’ weather forecast? This has to do with a combination of system dynamics and objective function. The objective function (eqn. 16) penalizes 1) deviations of x_T from T_{ref} and 2) the electricity costs of u_2 (running the fans). In this case the costs precede the benefits: first invest in electricty of running the fans and only later reap the benefit of reduced storage temperatures. $u_2(k)>0$ increases $x_{L,e}(k+1)$ (eqn. 15) on the one hand, but if $x_T(k)>T_{ref}$ and $T_{amb}(k)<x_T(k)$ then on the other hand it decreases $x_{L,T}(k+i)$ for i=2, 3, .., i_{max} (eqn. 14). The total benefit of decreased $x_{L,T}(k+i)$ for i=2, 3, .., i_{max} has to do with the impulse response of $x_{L,T}$ on u_2. The closer k approaches H the larger the part of the impulse response that disappears behind the horizon H and the less likely it is that the OC will decide to invest in $u_2(k)$. In RHOC with a small H this ‘terminal effect’ will affect even $u_2(0)$ and hence the overall J(u) in Figure 8 after simulation over a 60 days period will deteriorate due to smaller H.

Are more accurate 10 days forecast worthwhile? Yes, for H=10 ‘Fct’ outperforms ‘Pers’ (J=800 vs. J=1500). Improving ‘Fct’ with the current locally measured T_{amb} reduces J even further till J=730 (‘FctC’ for H=10 in Figure 8). There remains space for further improvement as for H=10 the best feasible J is ± 610 (‘Obs’).

Figure 9 depicts the distribution of the costs J(u) over the individual terms in J(u) (eqn. 14-16) for the realization in Figure 7. This realization is achieved with H=10 and weather forecast type ‘FctC’, causing costs J=730 in Figure 8. In Figure 9 the costs of temperature deviations from setpoint ($x_{L,T}$) exceed the costs of electricity consumption ($p_w(1)*x_{L,e}$). After tuning $p_w(1)$ such that the trade-off between temperature control and electricity costs looks acceptable, this ratio is a characteristic phenomenon over many simulations. Figure 9 nicely illustrates that the costs of $x_{L,T}$ rise esp. in periods where x_T is far off from T_{ref}.

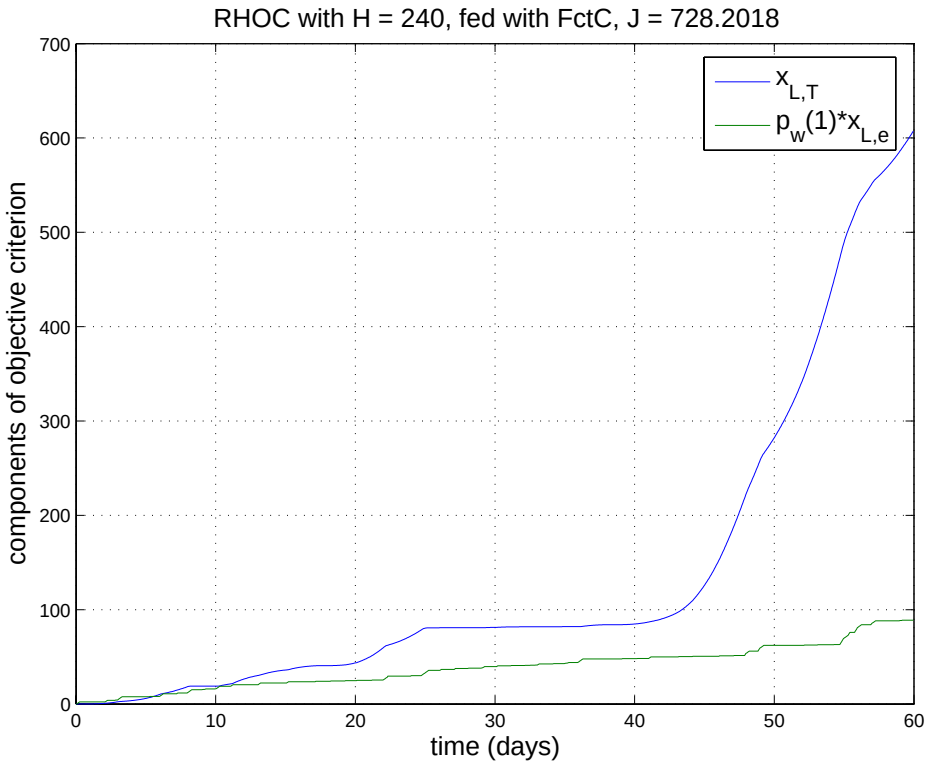

Figure 9: components of J(u) for realization in Figure

How do the above simulation results relate to current practice? To answer this question the above simulations were done with a model calibrated on a real storage facility. In the 60 days after 13 April '05 power consumption and temperature in that real facility were measured. Those measurements were input to eqns. 14-16 to evaluate the practically realized J(u) by the current controller. This yielded an objective function value of 3500, which is far worse than the values achieved by RHOC (Figure 8). Yet it would be premature to conclude that RHOC performs far better than current practice for a number of reasons, *e.g.*:

1. despite calibration there remains a mismatch between model and the real storage facility.
2. Does a scientist's appreciation expressed in a formula J(u) really match the farmer's appreciation?
3. How do the costs of making and maintaining this control technology operational compare to the current costs?
4. How robust is the new technology to all sorts of possible hard- and software failures, and how does that compare to current practice?

4 Discussion

This paper's case study demonstrates that the RHOC technology has the potential to improve current day climate control in potato storage facilities. That is why project partner Tolsma Techniek is currently testing the technology in experiments on fullscale storage facilities. In this stage it is too early to conclude on the outcome of those experiments. Moreover for the time being the commercial viability remains uncertain.

Of course the technology has been developed with a broader scope than 'just' potato storage in Northwest Europe. The question arises which other applications are potentially worthwhile. This is any climate control application meeting the following requirements:

1. heat/cold buffering is technically possible,
2. varying external disturbances (weather, energy tariffs) affect the climate control, and these variations are to some extend predictable.

Heat/cold buffering is possible in either 1) the controlled process itself by allowing process temperature fluctuations (like T_{pr} in the above case of potato storage) or in 2) a special purpose heat/cold buffer attached to the process like the hot water tanks commonly seen in Dutch greenhouses or *e.g.* eutectic plates at cold stores.

5 Concluding Remarks

Receding Horizon Optimal Control seems to have an added value for ventilated potato stores. Because of the promising simulation results project partner Tolsma Techniek is currently testing the implementation in full-scale storage facilities.

Of course the thoughts of the project team go beyond the 'limited' scope of potato storage in Northwest Europe.

Acknowledgements

This research is part of the Weather In Control 2 project (wic2). Wic2 is supported with a grant of the Dutch Programme EET (Economoy, Ecology, Technology) a joint initiative of the Dutch Ministries of Economic Affairs, Education, Culture, Sciences; and of Housing, Spatial Planning, and Environment. Wic2 (www.afsg.nl/wic2) is a cooperation between Wageningen UR, PRIVA BV, Tolsma Techniek Emmeloord BV and WNI BV.

References

BRYSON A.E. JR. (1999): *Dynamic Optimization.* Addison-Wesley, Menlo Park (California)

DOESWIJK T.G., KEESMAN K.J., VAN STRATEN G. (2006): Impact of weather forecast uncertainty in optimal climate control of storehouses. *Proc. of 4th IFAC/CIGR workshop on Control Applications in Post-Harvest and Processing Technology (CAPPT 2006), Potsdam, Germany*

GILL P.E., MURRAY W., WRIGHT M.H. (8th print, 1989): *Practical Optimization*. Academic Press, San Diego

LEWIS F.L. (1995): *Optimal Control*. 2nd edition, Wiley-Interscience Publications

LUKASSE L.J.S., DE KRAMER-CUPPEN J.E., VAN DER VOORT A.J. (2006): A physical model to predict climate dynamics in ventilated bulk-storage of agricultural produce. *Accepted for publication in International Journal of Refrigeration*

PALMER T.N., BARKMEIJER J., BUIZZA R., PETROLIAGIS T. (1997): The ECMWF ensemble prediction system. *Meteorological Applications*, **4**, pp. 301-304

PIERRE D.A. (1969): *Optimization theory with applications.* Wiley, New York

VAN HENTEN E.J. (1994): *Greenhouse climate management: an optimal control approach*. PhD-thesis

Measuring Possibilities of Low Range Air Speed in Dryers and Storehouses

I. Seres[1], L. Kocsis[2], A. Wójcicki[1], K. Gottschalk[3] and I. Farkas[1]

[1] Department of Physics and Process Control, Szent István University
Gödöllő, Páter K. u. 1., H-2103 Hungary
Tel.:+36 28 522055, E-Mail: Farkas.Istvan@gek.szie.hu

[2] Hungarian Academy of Sciences, Process Control Research Group
Gödöllő, Páter K. u. 1., H-2103 Hungary

[3] Leibniz-Institut für Agrartechnik Potsdam-Bornim,
Max-Eyth-Allee 100, D-14469 Potsdam
Tel.: +49 331 5699 0314, E-Mail: kgottschalk@atb-potsdam.de

Abstract: *The use of the solar energy in various fields, for example for drying is a very actual problem. In the Department of Physics and Process Control, Szent István University, Gödöllő, Hungary a solar dryer was developed. In this paper the development of a low range air speed sensor for measuring the air pattern of the natural convection inside the dryer is presented. After choosing the working principle, it was modeled by numerical software, and a one-dimensional prototype was set up. Calibrations were carried out together with the sensitivity analysis of the important parameters. One the base of the calibration a two-dimensional horizontal prototype was developed, as well. In the presentation the modeling and the measurement results of the two-dimensional case are presented together with the further plans. Copyright© 2006 IFAC*

Keywords: *flow rate, sensor, solar dryer, modeling, measurement, calibration*

1 Introduction

Concerning the post-harvest processes beside the energy going impacts the quality issues remain the most determining factor.

For most of the agricultural products the quality control means post-harvest treatments (cleaning, drying, conservation) and proper storage. The air ventilation for a part of these techniques (drying, storage) is essential. In some cases artificial ventilation is used for the higher airflow, but for some cases the natural ventilation is enough to provide enough fresh air. Such kind of conditions is occurring for example during solar drying or for long time storing of given products. But to achieve the proper natural airflow pattern, the measurement of the flow is very important. The accurate measurement of a low range (0,01-0,2 m/s) air speed is not a simple task, but there are a few solutions for it. In the next chapter the used methods and equipment will be considered, but as it will be shown, all of the commercially available equipment has some disadvantages for the desired conditions.

This is the background why the Department of Physics and Process Control, Szent István University Gödöllö, Hungary and the Department of Post-harvest Technology, Institute of Agricultural Engineering Bornim (ATB), Potsdam, Germany has started a common research on developing a low range (natural convection) air speed sensor.

The aim is to develop a sensor, which can be load to a pile of the agricultural products together with the product. The commercially available low range sensors are not fit to this need because of the mechanical impact during the load. Another important aspect if the sensor can be used with a normal data logging system (which does not need a special individual meter), what is not general for the law range sensors. This reason is important if we want to use bigger number of sensors for measuring the air flow distribution inside a pile.

2 Sensor Survey

The different air flow meters can be categorized from different aspects, now it is done on the basement of the physical principle they use. The measurements generally mean energy transformation from one form of energy to another one. In case of flow measurement it means, that we convert the kinetic energy of the flowing medium to another kind of energy. (UPP & LANASA 2002).

Categorization (and short analysis) of the used flow meters:

Mechanical meters. The mechanical meters can not fulfil the requirements of the aim, as generally they are not sensitive enough.

Meters based on the Bernoulli law. (Sensors rely on the pressure drop or head occurring as a fluid flows by a resistance) This kind of meters give an important class of the velocity measurements, but considering the low air density and low air speed, the pressure difference is too small to detect accurately.

Magnetic meters. A nice principle, but the magnetic properties of the air are not good for it.

Meters based on acoustical or optical waves. These type of meters measure very precisely, but they can not be used to measure inside the pile. However during the calibration of the developed sensor, a laser Doppler anemometer is planned to use.

Meters based on thermal effects. Hot wire anemometer: The hot wire anemometer working well for low range air speed measurement, but it has a special measuring head, what is very sensitive for the mechanical impacts, so it can not be loaded to a pile. Another disadvantage is that the sensor can not be connected directly to a data logging system, it needs a special meter. (BENEDICT 1984).

3 The Selected Measuring Principle

As there was no ideal sensor for the purpose, the development of a new sensor was decided, with the principle (we call it thermal principle) as follows:

There is a heating element with a power of few watts in the air and a temperature sensor (e.g. a PT100 temperature dependent resistance) is fixed around it. With now flow through the system the sensor gets some heat from the heat source what can be measured by measuring the temperature of the sensor. But if there is airflow from the direction of the heating element, then the absorbed heat and the temperature of the sensor will be changed. This idea proper for measuring only one direction component of the air flow, but building a symmetrical setup with two PT100 sensor it can measure the all the flow direction in one dimension. The setup of the sensor for one dimension can be seen in **Figure 1**.

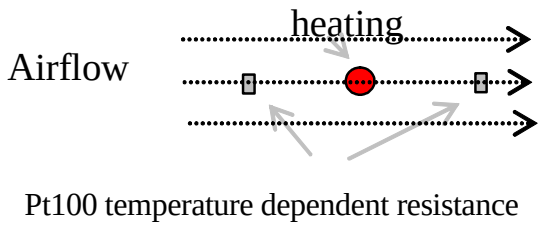

Figure 1: Schematic figure of the developed sensor

4 Modelling

After the defining of the proposed setup a modeling was started to simulate the behaviour of the sensor, and to determine some basic quantities. The simulation was done with the ANSYS software, which has a special unit for dealing with fluid dynamics. This Computational Fluid Dynamics (CFD) package can handle laminar and turbulent flow, compressible mediums with heat transfer, and can be used for steady state and transient models as well (ANSYS CFD FLOTRAN 1994).

First the model of a wind channel was set up with a steady state 2 dimensional model. In the model a constant (time independent, but changeable) inlet air speed was used on the left side of the channel, the boundary conditions on the side of the channel were to set to zero air velocity for each coordinate, and the pressure at the right side of the channel was set to equal to the surrounding pressure (ANSYS OPERATION GUIDE 1996). The flow pattern in case of 0,1 m/s inlet airspeed for this model can be seen in **Figure 2**.

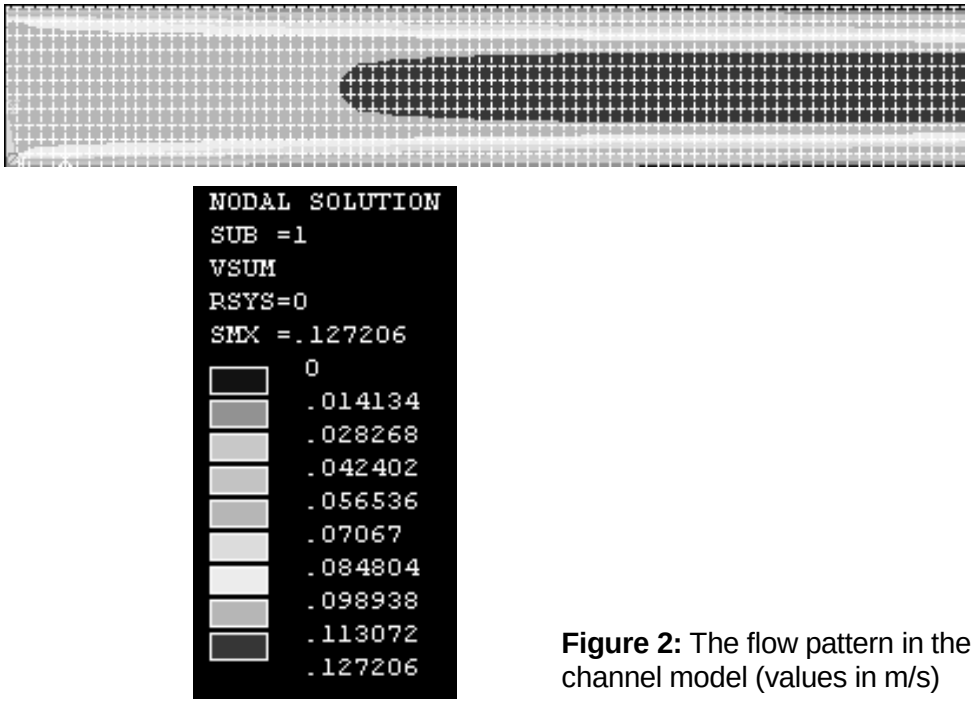

Figure 2: The flow pattern in the wind channel model (values in m/s)

This model was developed by installing a heating element in the middle of the wind channel. For this model the temperature field of a 0,1 m/s inlet velocity air is graphed in **Figure 3**.

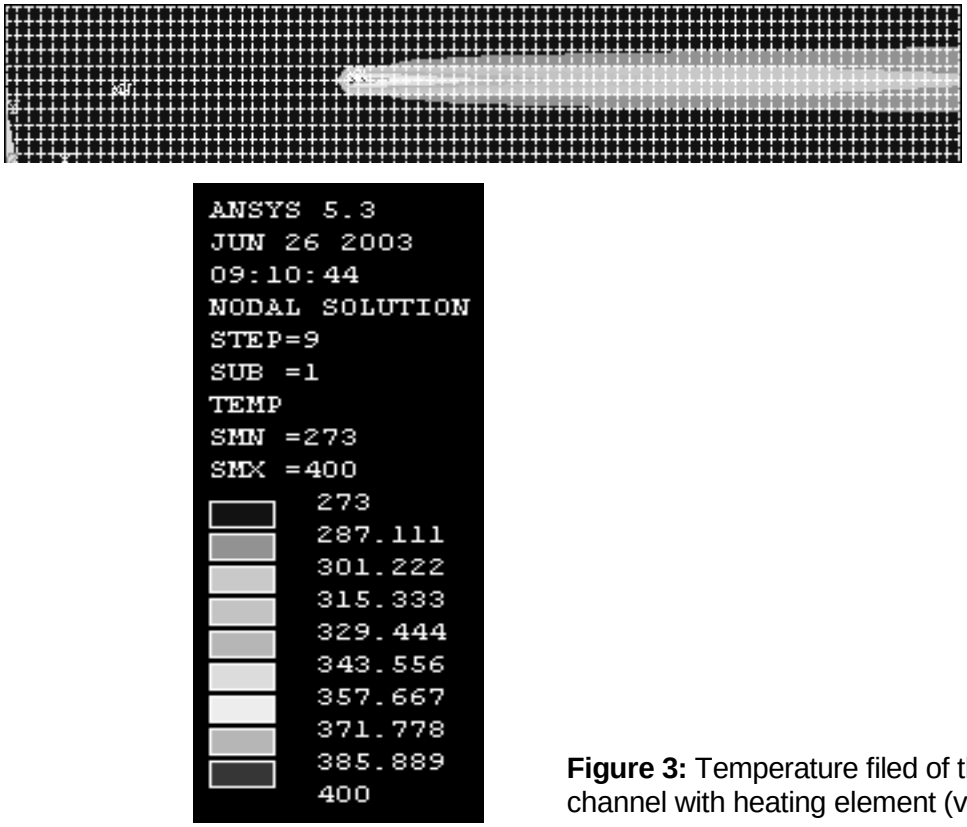

Figure 3: Temperature filed of the wind channel with heating element (values in K)

For lower air speeds the effect of the buoyancy is stronger, as it is graphed as a result of the model with 0.01 m/s inlet air speed in **Figure 4**.

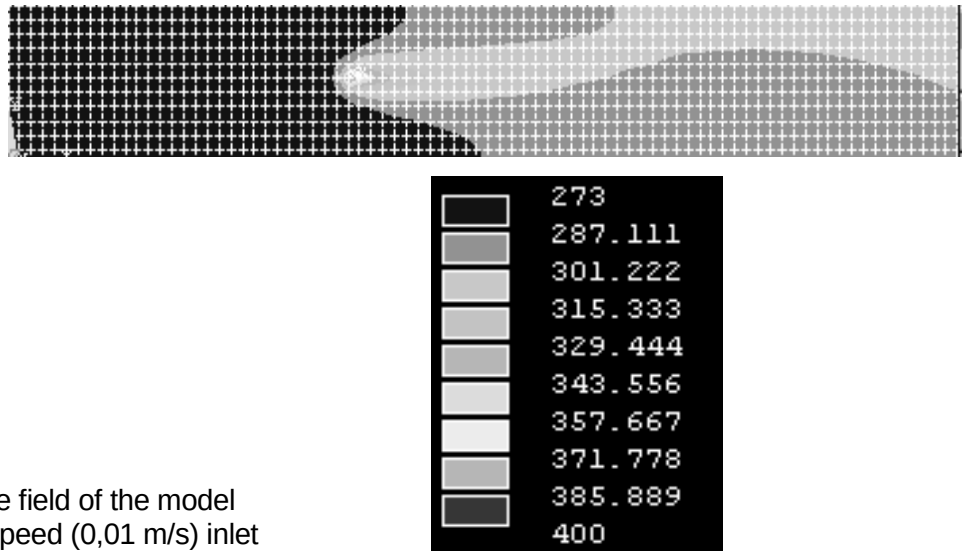

Figure 4: Temperature field of the model wind channel for low speed (0,01 m/s) inlet

As the principle of the developed sensor is based on the changing of the temperature in the middle of the wind channel, a special graph for that is shown in **Figure 5**. The figure shows that the principle was considered can work, as installing two Pt100 sensors for the two sides of the heating element, represented by the peak in the temperature distribution graph, there are different air temperatures (273 K and 300K in our case) which cause so big difference in the resistance that it can be measured accurately. (SERES *et al.* 2003)

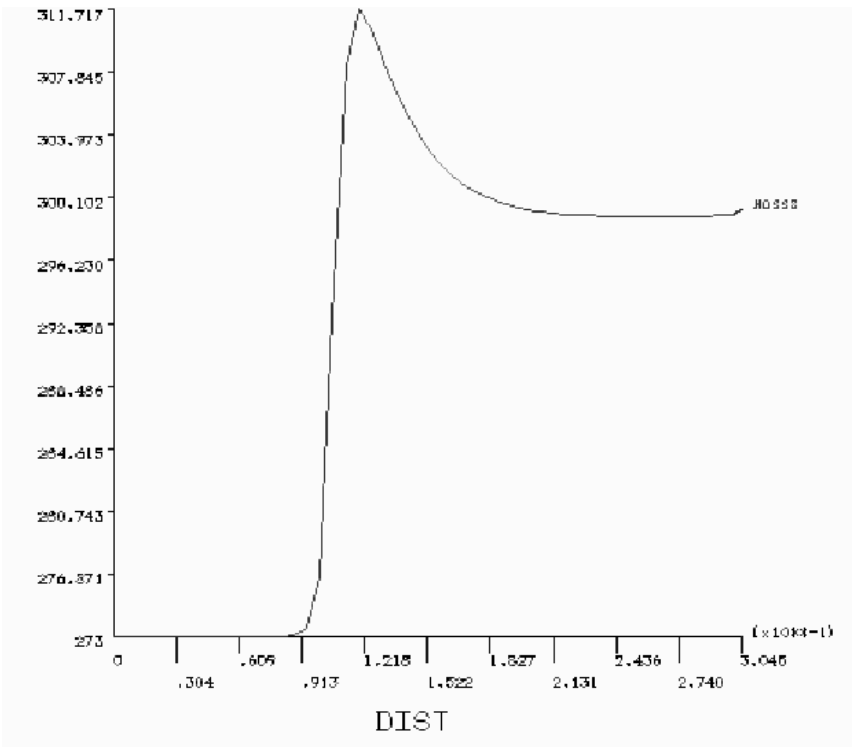

Figure 5: Temperature changing along the axis of the wind channel

5 Prototype Sensor and Calibration

Parallel with the modeling construction of a prototype of the proposed sensor was started. The prototype consists of a maximum 10W/12V heating element and two Pt100 temperature sensors symmetrically to the heating. The picture of the prototype can be seen in **Figure 6**.

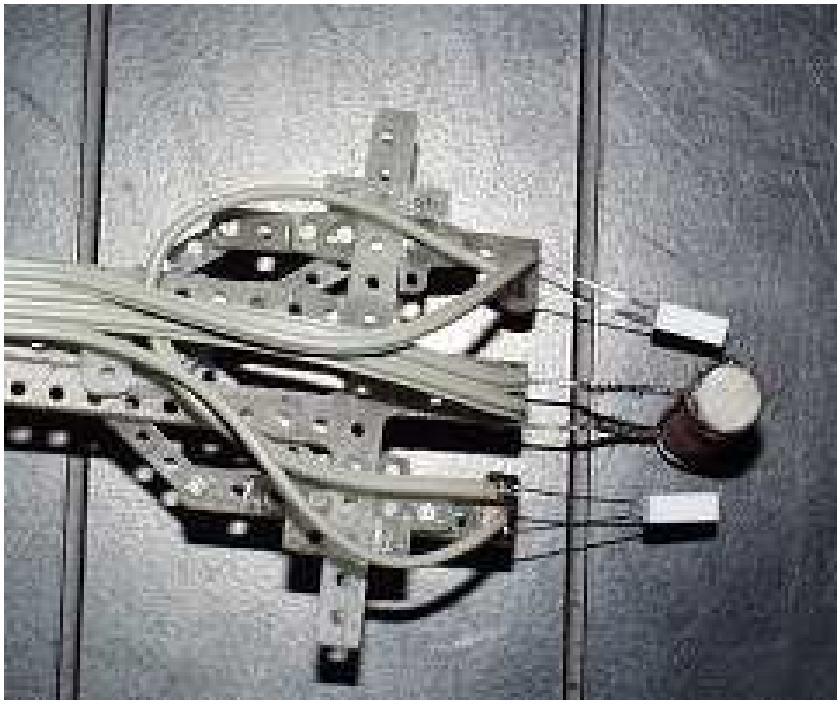

Figure 6: The prototype of the developed sensor

As this prototype is planned to test the principle under different circumstances, the distance of the sensors from the heating can be changed by a mechanical equipment, where the common distance can be regulated by a screw.

The sensor prototype was tested in a wind channel. The sensitivity of the sensor was measured by measuring the time constant of the Pt100 resistance in resting air. (In flowing air the time constant should be smaller).

From the results 31 s time constant was considered for the used Pt100 resistance in resting air environment as can be seen in **Figure 7**. This means a relatively slow sensor, but it is enough for the proposed aim, as fast changes are not usual in the storehouses and dryers.

The symmetrically installed Pt100 sensors were connected to a Wheatstone bridge to convert the resistance sign to voltage, and to make the device direction dependent. The scheme of the connection is shown in **Figure 8**.

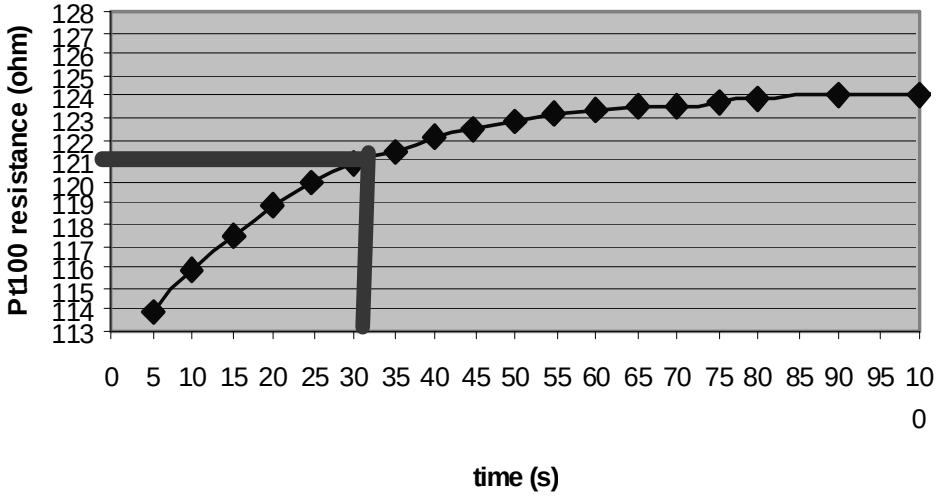

Figure 7: Determination of time constant for Pt100 sensors in air

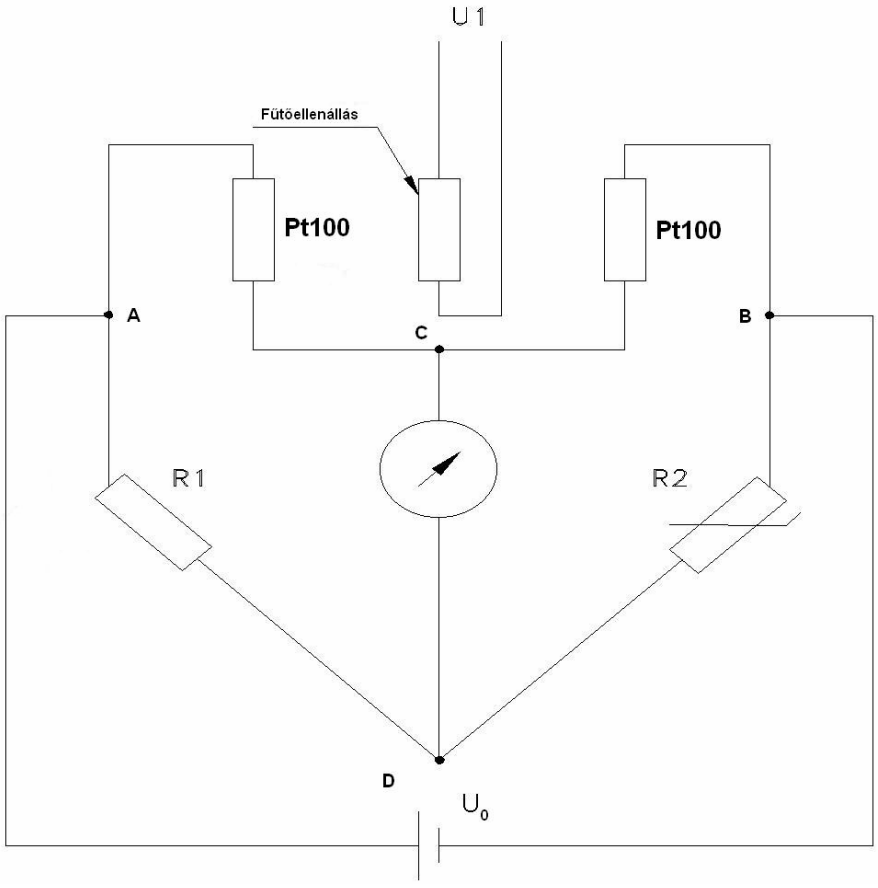

Figure 8: The Wheatstone bridge connection of the sensor

With the Wheatstone bridge the sensor was tested in wind channel. The first results are graphed in **Figure 9**. In the figure the output voltage of the Wheatstone bridge is graphed against the air velocity in the middle of the channel (where the sensor was fixed) with different Pt100-heater distances (SERES *et al.* 2004).

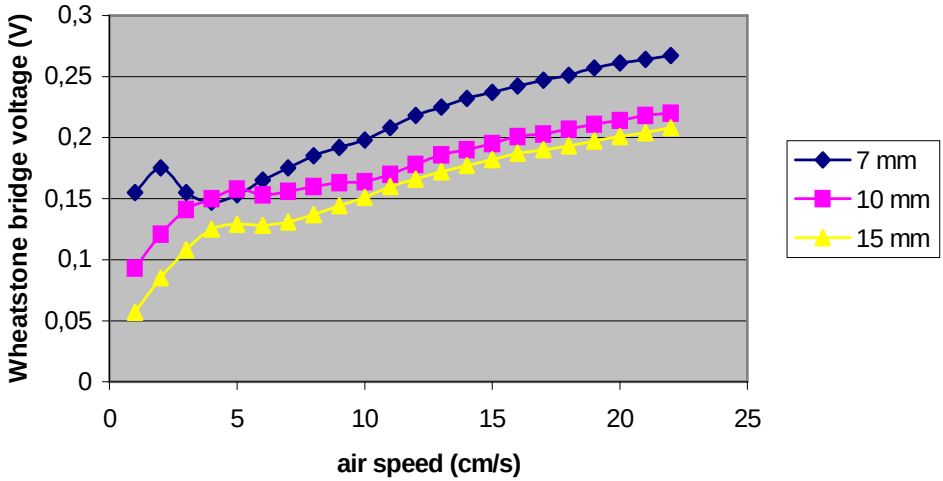

Figure 9: Calibration results for the prototype with different Pt100-heater distances

The calibration of the sensor was performed in the Department of Post-harvest Technology, Institute of Agricultural Engineering Bornim (ATB), Potsdam, Germany, where a sophisticated wind channel is available.

6 Two dimensional Sensor Design

After the prototype of the one dimensional sensor was developed and calibrated, as a continuation of the work, development of a two dimensional sensor was initiated. As because the air flow in the vertical direction is much more complicated as in the other two directions, first a horizontal two dimensional model was developed.

For the measurement of this temperature distribution, a two dimensional (horizontal planar) measuring equipment was developed and constructed. During the measurements the parameters of the heat flow generated by the heating element was examined with a planar grid constructed from Pt100 thermo sensors. The platinum thermometers were situated in the grid-points of a 1 cm division set for which the resistances of the Pt100 sensors, such as the temperature distribution, were measured in case of different air-flow velocities. In the middle of the Pt100 grid-points a heating elements was operated, whose superficial temperature was measured by an infrared sensor.

The picture of the planar grid arrangements developed for measuring purposes can be seen in **Figure 10**.

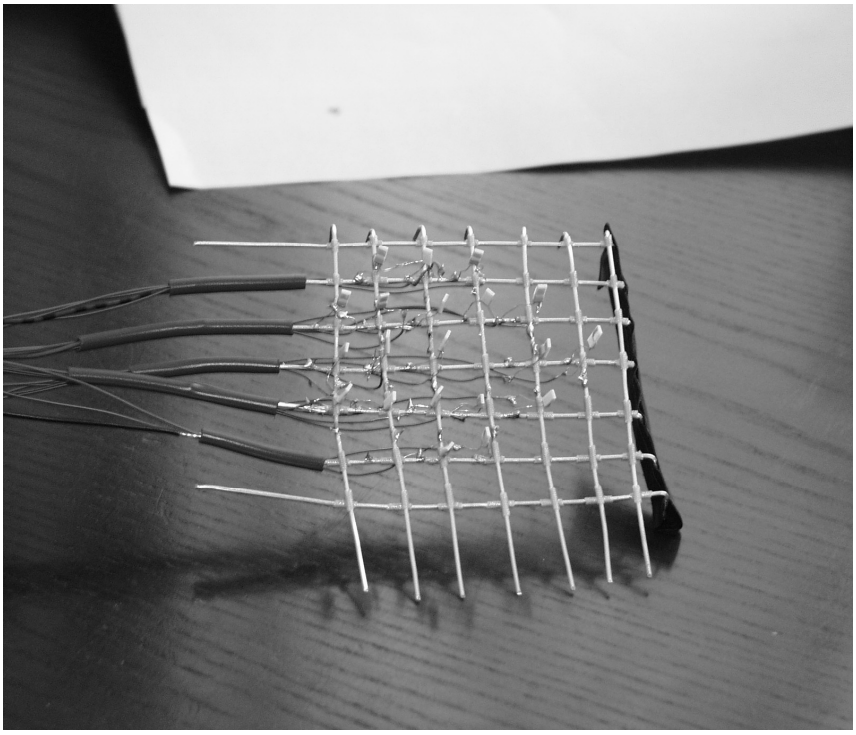

Figure 10: The developed planar grid with Pt100 sensors

From the measured data the temperature distribution can be get along the grid. The temperature distribution depends on the heat convection from the heating element to the measured points. The distribution can be obtained from the measured resistance data, but it can be read from the thermo-camera photos, as well.

From the camera photos a bit harder to get beck exact measurement data as the results are coded in colours. This method is very useful for visualizing the result, but much harder to get back exact numbers for the modelling. Because of this reason the modelling was based in the Pt100 resistance data.

In spite of its un-exactness the camera photos were used for demonstrating the working principle of the sensor. In the following a photo set (**Figure 11**a-d) will be presented, from which the changing of the temperature distribution around the heating element can be seen as the air speed was changed.

These kinds of thermo photo sets were taken not only as a function of air speed, but as a function of different heating power as well. The photo set of temperature pattern shown in Figure 10a-d were taken with the power of 10 W.

From the photos it can be seen, that with the growing air speed the temperature values are going down (the cooling effect of the airflow) and that the temperature distribution is changing.

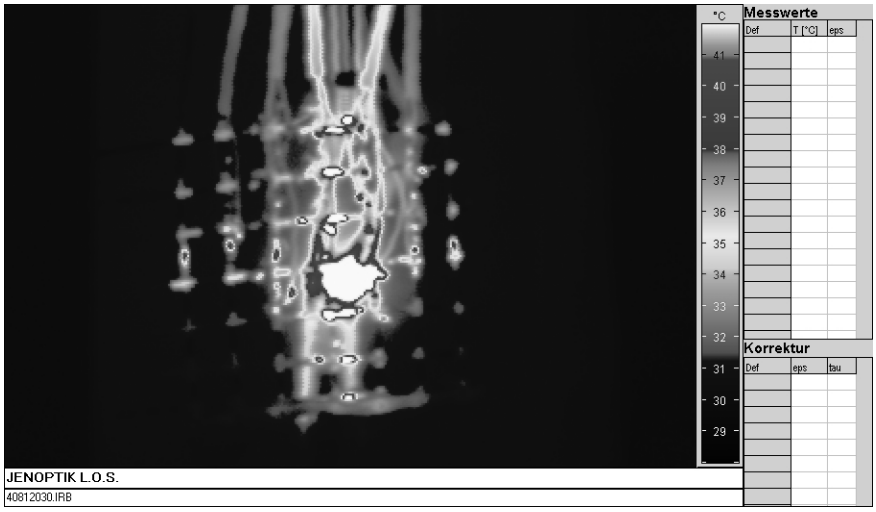

Figure 11a: Temperature patter at airspeed of 0,1 m/s

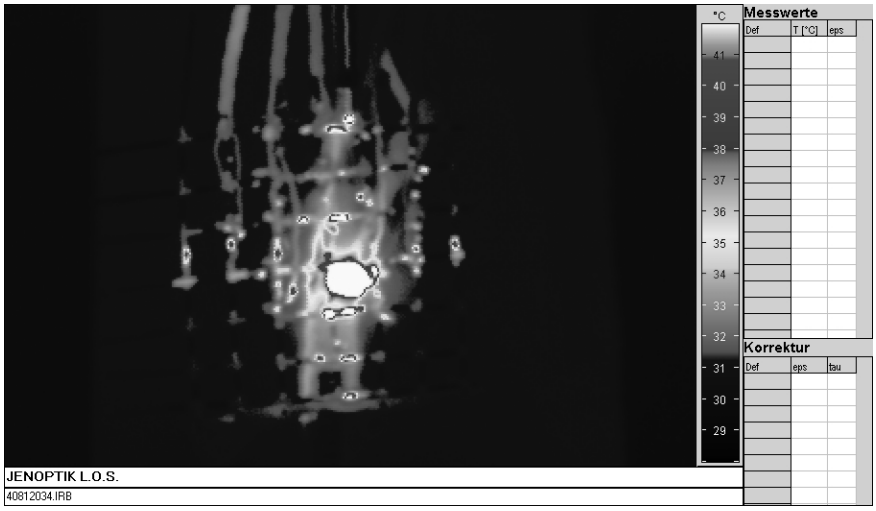

Figure 11b: Temperature patter at airspeed of 0,3 m/s

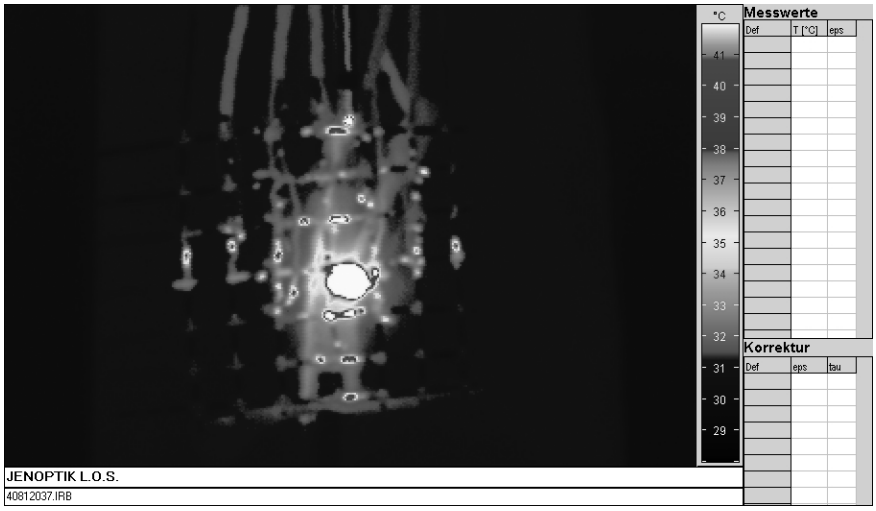

Figure 11c: Temperature patter at airspeed of 0,5 m/s

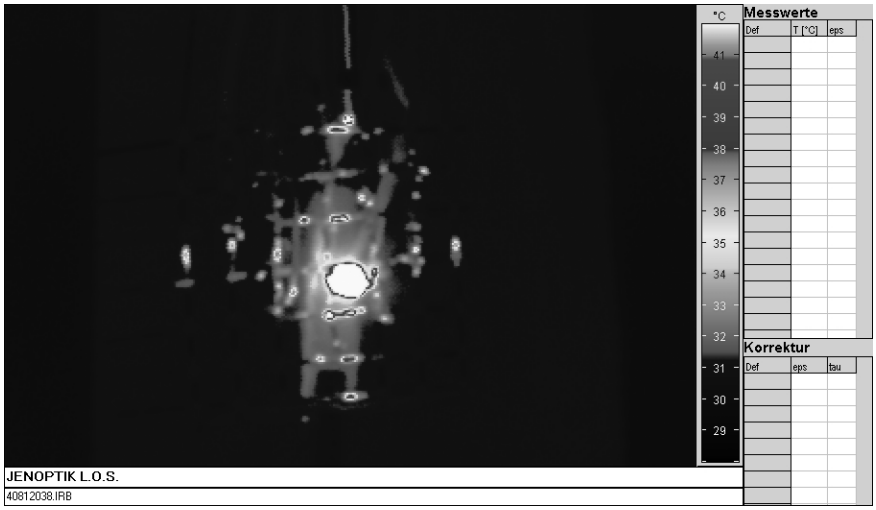

Figure 11d: Temperature patter at airspeed of 0,8 m/s

7 Modeling of the Modified Two Dimensional Sensor

From the measurements of the above described planar prototype, a simpler setup can be offered.

One prototype is to measure two perpendicular (horizontal) directions separately. In this case four Pt100s are necessary to measure an arbitrary air direction.

A control dataset for this case can be seen in **Figure 12**. From the graph the changing of the two dimensions Pt100 resistances, and so the velocity components can be got as it

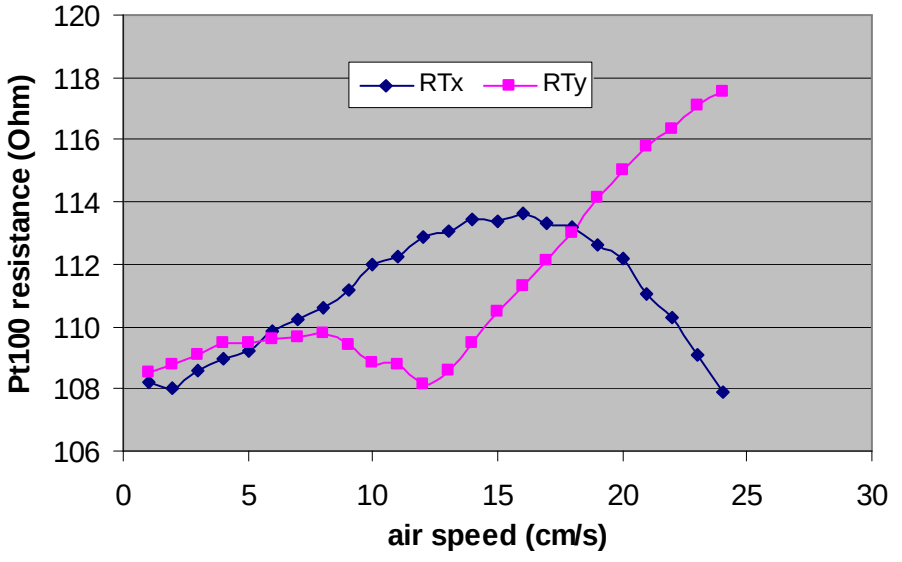

Figure12: Changing of the Pt100 resistances of two perpendicular Pt100 because of the air speed direction change

was described for the one dimensional prototype. From the velocity components (coordinates) the magnitude of the air speed can be get from Phytagora's theorem and the direction of the air speed form the

$$\varphi = arctg\left(\frac{v_y}{v_x}\right)$$

equation.

From the graph it can be analyze, that during the air speed growing up from 2 cm/s to 25 cm/s, that direction is changing from the y direction to the x, and back.

For some practical reasons a new setup is analyzed, as well. In this case three Pt100 sensor are around the heater symmetrically, and from the velocities of three measured direction the original velocity can be calculated.

8 Conclusions

- The natural ventilation range air speed measurement is not solved inside a pile of agricultural product, what was the initiation to develop a new sensor.
- After analyzing the used method the thermal principle was chosen, where the airflow has effect on the convective heat transfer from a heating element to the Pt100 resistance.
- The modeling of the process was carried out by the CFD unit of ANSYS software.
- A prototype of the one dimensional sensor was built, and for experimental purposes a wind channel was set-up.
- For the two dimensional modeling a planar grid was developed, where Pt100 thermo sensors were used to measure the temperature distribution in special grid points.
- From the results of the measurements for two dimension, two different geometry was developed for the horizontal airspeed measurement.

Acknowledgements

The work was carried out within the Hungarian-German bilateral project No D-5/03.

References

ANSYS CFD FLOTRAN, ANALYSIS GUIDE (1994): ANSYS Inc., Houston

ANSYS OPERATION GUIDE (1996): ANSYS Inc., Houston

BENEDICT R. (1984): *Fundamentals of Temperature, Pressure and Flow Measurement*, Wiley, New York

SERES I., FARKAS I., KOCSIS L., GOTTSCHALK K. (2003): Development of a low range sensor for the use of natural air flow measurement, Advances in Drying Technology, Proceedings of the Symposium EUDrying 03, /ed. by G.D. Saravacos, Z.B. Maroulis, M. Krokida, V.T. Karathanos/, Heraklion, Crete, September 4-5, p. 40-48

SERES I., FARKAS I., GOTTSCHALK K. (2004): Development of a low range air speed sensor for natural convection in solar dryer CD-ROM Proceedings, 14th International Drying Symposium, Sao Paulo City, Brazil, August 22-25, pp. 932-940

UPP E.L., LANASA P.J. (2002): Fluid Flow Measurement, A Practical Guide to Accurate Flow Measurement, Golf Professional Publishing, Boston

A Hybrid Model for Coupled Transport Processes Through Porous Media

Cs. Mészáros[1], Á.Bálint[2], I. Kirschner[3], K. Gottschalk[4] and I. Farkas[1]

[1] Department of Physics and Process Control, Szent István University
Páter K.u.1., H-2103 Gödöllő, Hungary
Tel.: +36 28 522055, Fax: +36 28 410804
E-Mail: Meszaros.Csaba@gek.szie.hu

[2] Department of Chemistry and Biochemistry, Szent István University
H-2103 Gödöllő, Páter K.u.1., Hungary

[3] Institute of Physics, Roland Eötvös University
Pázmány Péter sétány 1.A, H-1117 Budapest, Hungary

[4] Leibniz-Institut für Agrartechnik Potsdam-Bornim e.V. (ATB)
Max-Eyth-Allee 100, 14469 Potsdam, Germany, E-Mail: kgottschalk@atb-potsdam.de

Abstract: *A new method based on the common application of irreversible thermodynamics and fluctuation theory of phase transitions in porous media is proposed for calculating the moisture level and temperature in drying processes. Instead of parabolic partial differential equations, hyperbolic type partial differential equations are used for the basic mathematical model. The relaxation time constants, whose percolative state-dependence is also explicitly taken into account, are incorporated into this formalism. Some possible new research domains from the point of view of the mathematical and statistical physics are also indicated. Copyright© 2006 IFAC*

Keywords: *drying, extended irreversible thermodynamics, percolation theory, scaling relations*

1 Introduction

The basic relationships necessary for modelling are the balance equations expressing conservation laws (written here in substantial form for a quantity *A*, which in general case may be interpreted as a component of a tensor) (LANDAU & LIFSHITZ 1987, LUIKOV & MIKHAILOV 1965):

$$\frac{d}{dt}\int_V \rho A dV = -\int_\Omega \vec{J}_A \cdot d\vec{\Omega} + \int_V \sigma_A dV, \qquad (1)$$

where ρ denotes the density of this quantity, $\vec{J}_A$ is its flux, while σ_A denotes the source density of the same quantity *A* inside volume *V* separated by boundary surface Ω from the surrounding and the constitutive equations establishing links between fluxes of dif-

ferent quantities and thermodynamic forces X_i (e.g. temperature gradient) driving them, i.e.

$$J_i = \sum_{k=1}^{f} L_{ik} X_k, \left(i = 1, ..., f\right), \tag{2}$$

where *f* denotes the number of thermodynamic degrees of freedom and the conductivity matrix elements obey the crucial Onsager reciprocity relations, i.e. $L_{ik} = L_{ki}, \left(i, k = 1, ..., f\right)$ (LANDAU & LIFSHITZ 1987). The Onsager relations are particularly important and useful at studies of cross-effects (e.g. thermodiffusion process) in different dissipative systems. Moreover, nowadays there is an urgent need for extension (JOU *et al.* 2001, SOBOLEV 1997) of the Classical Irreversible Thermodynamics (CIT) operating on the base of the local equilibrium hypothesis, since many experimental results (including those relevant for the engineering problems) indicate, that instead of CIT, a more general formalism, based on the so-called Extended Irreversible Thermodynamics (EIT) must be applied at solving of such problems. Despite these obvious facts, which justify development and possible widespread applications of the EIT in various research fields, it seems to us, that this novel and successful physical theory has not been applied on large scale in drying engineering, i.e. exactly in this field which was one of the most important motivations for its elaboration (LUIKOV & MIKHAILOV 1965). In order to illustrate here its relevance in this field of engineering, we mention only one example, which essentially contains all the problems caused by applications of CIT in mathematical modelling of drying processes. The usually applied system of partial differential equations (PDE-s) of parabolic type is the following one (applied by common application of balance-, and constitutive equations discussed above):

$$\frac{\partial \Gamma}{\partial t} - L_{11}\nabla^2\Gamma - L_{12}\nabla^2 a = 0, \tag{3}$$

$$\frac{\partial a}{\partial t} - L_{21}\nabla^2\Gamma - L_{22}\nabla^2 a = 0, \tag{4}$$

i.e. it is written down for an intensive thermodynamic quantity *Γ* (e.g. temperature) and an extensive thermodynamic quantity *a* (e.g. moisture content in the porous matter) and can be solved relatively easily by use of the usual tools of the operation calculus. This approach has been studied in detail by various effective tools of the mathematical physics and applied on large scale in various engineering and fundamental research problems (LUIKOV & MIKHAILOV 1965, JOU *et al.* 2001). Among its most advanced applications we mention here those (KIRSCHNER 1971, KIRSCHNER *et al*. 1992-94) related to detailed analysis of stability properties of stationary thermodynamic states by variational princi-

ples, which have not been translated completely to the language of the numerical mathematics, although there are some very illustrative works (STARK 1974), indicating that continuation of this translation may provide further new and valuable numerical methods for transport processes. Despite their frequent applications, parabolic type PDE-s lead to a serious problem at mathematical modelling of transport processes: they imply, that propagation of disturbances through the system considered is always executed by infinitely large velocities see e.g. (JOU *et al.* 2001). In order to remove this internal paradox of the classical theory, the relevant tools of the EIT must be applied. Some of the methods elaborated with such purpose are presented in the next section.

2 Wave Approach of the Irreversible Thermodynamics

In order to use as realistic drying models as possible, the wave approach of the irreversible thermodynamics (WAT) will be applied here, because it leads to such descriptions of the realistic transport phenomena, which imply finite propagation velocities during these processes, i.e. it does not contradict to the basic principles of the contemporary physics – e.g. theory of relativity. The basic assumption of the WAT is, that appearance of thermal and/or diffusional waves is related to breaking down of the local thermodynamical equilibrium. Then, the entropy function will be extended by a kinetic contribution depending on thermodynamic current densities (fluxes). Therefore, the crucial relation of this theory is the following one:

$$s = s\left(a_1,...,a_f;\vec{J}_1,...,\vec{J}_f\right) = s_{eq}\left(a_1,...,a_f\right) + \\ + s_{kin}\left(\vec{J}_1,...,\vec{J}_f\right) \equiv \sum_{i=1}^{f}\Gamma_i\vec{J}_i + \frac{1}{2}\sum_{i,k=1}^{f} m_{ik}\vec{J}_i\cdot\vec{J}_k, \tag{5}$$

where m_{ik} is a non-positive symmetric matrix (GYARMATI 1977), allowing introduction of the relaxation time constants in a quite general way, i.e.

$$\tau_{ik} = -\sum_{l=1}^{f} L_{il}m_{lk}, \left(1 \le i,k \le f\right), \tag{6}$$

and leads to the following modification of the generalized constitutive equations:

$$\vec{J}_i = \sum_{k=1}^{f} L_{ik}\nabla\Gamma_k - \sum_{k=1}^{f}\tau_{ik}\frac{\partial\vec{J}_k}{\partial t}, \left(1 \le i \le f\right). \tag{7}$$

Furthermore, if we neglect the couplings between the dissipative transport properties and inductional behaviours of the system (GYARMATI 1977), the relaxation time matrix takes diagonal form and results in the following form of (hyperbolic type) coupled transport equations:

$$\tau_i \frac{\partial^2 \Gamma_i}{\partial t^2} + \frac{\partial \Gamma_i}{\partial t} - \sum_{k=1}^{f} \kappa_{ik} \nabla^2 \Gamma_k = 0, \left(1 \le i \le f\right), \tag{8}$$

$$\tau_i^* \frac{\partial^2 a_i}{\partial t^2} + \frac{\partial a_i}{\partial t} - \sum_{k=1}^{f} D_{ik} \nabla^2 a_k = 0, \left(1 \le i \le f\right). \tag{9}$$

A simplified version of this system (after detailed studies of possibilities for establishing hybrid mathematical models based on both stochastics and non-equilibrium thermodynamics - relevant for drying processes (FARKAS *et al.* 2000, MÉSZÁROS *et al.* 2001) was used (MÉSZÁROS *et al.* 2004) as a frame unifying techniques borrowed from both *EIT* and stochastics. It also contains couplings between spatial changes of intensive and extensive thermodynamic variables, i.e.:

$$\tau \frac{\partial^2 \Gamma}{\partial t^2} + \frac{\partial \Gamma}{\partial t} - L_{11} \nabla^2 \Gamma - L_{12} \nabla^2 a = 0, \tag{10}$$

$$\tau^* \frac{\partial^2 a}{\partial t^2} + \frac{\partial a}{\partial t} - L_{21} \nabla^2 \Gamma - L_{22} \nabla^2 a = 0 \tag{11}$$

This system has not been used in refined mathematical modelling methods of drying processes, although there are justifications for such applications, since at coupled heat and mass transfer processes through certain systems with complex structure (e.g. polymer solutions and capillary-porous bodies) there is a significant difference between relaxation time constants. Namely, after establishing of local- equilibrium values of the temperature (requiring time intervals of the order of magnitude of relaxation time constant of temperature τ_T), the relevant local-equilibrium values of the concentration (or moisture level) will be established after longer time intervals since in such systems $\tau_D >> \tau_T$ (SOBOLEV 1997)). Therefore, due to such differences between values of the different relaxation time constants, treatment of drying processes (as highly dissipative transport phenomena) in general case should be based on the application of hyperbolic type PDE-s instead of parabolic type ones.

3 A New Application of the Theory of Lommel-Functions

In order to solve the problem set up, we use a functional form for the temperature (and mass-) functions, which had been used for solving of problems related to both thermal equilibration of finite bodies heated in inhomogeneous manner (while their surfaces are maintained at given conditions) (LANDAU & LIFSHITZ 1987) and translation of variational principles of thermodynamics into direct numerical variational methods (STARK 1974). According to these procedures, the functions we are searching for are given by the following series expansion form:

$$T\left(\vec{r};t\right)\equiv T\left(x,y,z;t\right)=\sum_{n}c_{n}T_{n}\left(x,y,z\right)\cdot e^{-\lambda_{n}t}, \tag{12}$$

i.e. spatial-, and time-dependence are presented in the form of separated functions, and c_n are the series expansion coefficients of constant values. Obviously, the relaxation time interval necessary for establishing of thermal equilibrium is $\tau=1/\lambda_1$, and this time constant will dominate the whole process. Using the same separated form for time-, and space-dependence (11) for both temperature-, and moisture level functions and substituting them into basic system (2) we will get (the upper indices in the symbols λ_m^T,λ_m^M denote the reciprocal values of relaxation time constants for the temperature, and moisture level functions, respectively):

$$\begin{aligned}&\sum_{m}c_{m}^{T}\left[\left(E-K\right)\frac{d^{2}T_{m}\left(x\right)}{dx^{2}}+\lambda_{m}^{T}\cdot T_{m}\left(x\right)\right]\cdot e^{-\lambda_{m}^{T}t}=\\&=\sum_{m}c_{m}^{M}\left[\left(D-L\right)\frac{d^{2}M_{m}\left(x\right)}{dx^{2}}+\lambda_{m}^{M}\cdot M_{m}\left(x\right)\right]\cdot e^{-\lambda_{m}^{M}t}.\end{aligned} \tag{13}$$

Due to symmetry of the initial parabolic type coupled PDE system, it is plausible to assume, that the appropriate spatial harmonics of the solution functions have similar form, i.e.

$$\begin{aligned}&\frac{d^{2}T_{m}\left(x\right)}{dx^{2}}+\frac{\lambda_{m}^{T}}{E-K}T_{m}\left(x\right)=\frac{d^{2}M_{m}\left(x\right)}{dx^{2}}+\\&+\frac{\lambda_{m}^{M}}{D-L}M_{m}\left(x\right)=\psi_{m}\left(x\right).\end{aligned} \tag{14}$$

Then, the solutions for the same order spatial harmonics will be equal up to an (unimportant) numerical constant. In order to present the general solution for these spatial parts of

the solution functions in as concise form as possible, the following abbreviation system for the coefficients will be applied:

$$y(x) \equiv T_m(x), \left(M_m(x)\right) \Rightarrow c \equiv \frac{\lambda_m^T}{E-K}, \left(\frac{\lambda_m^M}{D-L}\right). \qquad (15)$$

For the sake of simplicity we identify the function $\psi_m(x)$ with the simplest polynomial of the *m*-th order, i.e. we take $\psi_m(x) \propto x^m$. Naturally, in general case, the functions $\psi_m(x)$ will be presented as linear combinations of such elementary polynomials with coefficients to be determined from the experimental data (e.g. by application of the powerful methods developed for coefficient identification of differential equations developed within framework of the theory of inverse problems (BITTERLICH & KNABNER 2003)). The general solution of this ordinary differential equation can be explained by use of a particular type of special functions, the so-called Lommel-function e.g. (LOMMEL 1884-86, LUKE 1969). Although examination of differential equations from the point of view of continuous groups represents active research area in engineering problems for decades e.g. (AMES 1967, OLVER 2000), the application of Lommel-type functions presented here may open a new research area related to studies of possible links between parabolic-, and hyperbolic-type formalisms. These functions ensure oscillatorial behaviour for the separated spatial parts and can be given by the following rather complicated expression (derived by use of the MAPLE 8 software package (MAPLE 8, 2002)):

$$y(x) = a \cdot \cos\left(\sqrt{c}x\right) + b \cdot \sin\left(\sqrt{c}x\right) - \frac{x^{1+n}}{\sqrt{x\sqrt{c}}\,c\left(3n+n^2+2\right)}$$

$$\left(-\frac{1}{(x\sqrt{c})^n}(n++2)(n+1)\cos(x\sqrt{c}) \quad (x^{1+n}\sqrt{c}\cos(x\sqrt{c}) - x^n \sin(x\sqrt{c})\right.$$

$$LommelS1(n+1/2,1/2,x\sqrt{c}) + \frac{1}{\left(x\sqrt{c}\right)^n}(n+2)LommelS\left(n+3/2,1/2,x\sqrt{c}\right)\cdot(x^{1+n}\sqrt{c}\sin\left(x\sqrt{c}\right)$$

$$\cos\left(x\sqrt{c}\right) - x^n + x^n\cos^2\left(x\sqrt{c}\right)) + x^{1+n}\sqrt{c}\left(\frac{n}{\left(x\sqrt{c}\right)^n}(n+2)(\cos(x\sqrt{c})-1)\right. \qquad (16)$$

$$(\cos(x\sqrt{c}--1)LommelS1(n+1/2,3/2,x\sqrt{c}) - \cos\left(x\sqrt{c}\right)\sin\left(x\sqrt{c}\right)(\sqrt{x\sqrt{c}} +$$

$$\left.+LommelS1(n+3/2,3/2,x\sqrt{c})(1+n)\frac{1+n}{\left(x\sqrt{c}\right)^n})\right)$$

and is illustrated for a low-order of these special functions (as well as temperature distribution calculated on its base) on the **Figures 1** and **2**.

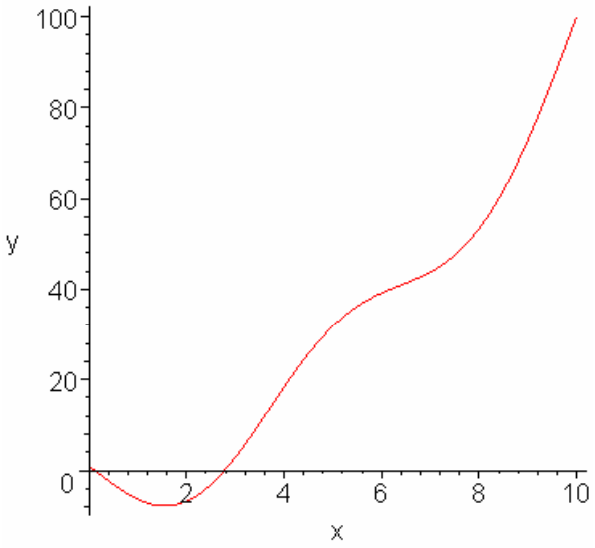

Figure 1: Low-order Lommel-function

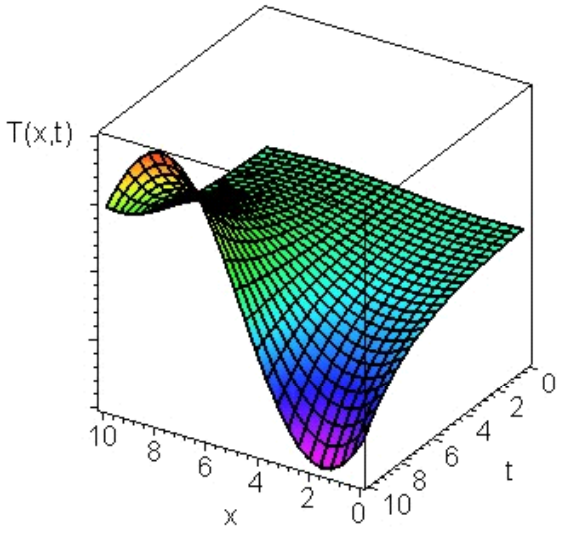

Figure 2: Temperature function

According to our knowledge, this application of the Lommel-type special functions is completely new in the theory of coupled transport processes. Therefore, it is obvious, that the procedure explained is able to produce physically realistic computational results without explicit use of the hyperbolic formalism. Moreover, these results justify the choice of the particular form of solution functions of the reaction-diffusion problem studied in this paper.

4 A New Application of the Percolation Theory of Phase Transitions

In order to introduce effective new methods for accurate mathematical modelling of leakage of water through capillary-porous bodies during drying processes, we have proposed (FARKAS *et al.* 2000, MÉSZÁROS *et al.* 2001, MÉSZÁROS *et al.* 2004) application of the exact theory of random media, the so-called percolation theory, because this well-developed branch of mathematics and statistical physics has shown (STAUFFER & AHARONY 1994) its efficiency at solving of many practical problems. The combination of the methods of non-equilibrium thermodynamics and percolation theory will be performed here in a restricted way: only certain quantities from the conductivity/coupling coefficients will be assumed as percolation-sensitive ones. This approach is justified by some very accurate experimental results from drying engineering practice (HUININK *et al.* 2002). The percolation probability p is the probability that a given conducting edge (or nodes determining it) belongs (belong) to an infinite open cluster. The quantity, which plays a crucial role in this theory is the critical percolation probability, usually denoted by p_c. According to the mathematically strict definitions of the topic, there are two phases in the case of percolation processes (taking place in systems with two or more dimensions). In the so-called subcritical phase (for which $p<p_c$) it is very probable, that every node (or edge) is in a finite open cluster, while

in the case of the supercritical phase (i.e. when $p > p_c$), each node (or edge) almost surely belongs to an infinite open cluster.

Then, the most important scaling relationships, necessary for this modelling, are explained by the probability difference $\Delta p = p - p_c$, (STAUFFER & AHARONY 1994). The mean value of the squared distance from an initial position of a particle executing random motion can be approximated respectively for the states below (***L***) and above (***H***) the critical percolation point as follows:

$$\left\langle R^2(t)\right\rangle \approx R_\infty^2\left[1-a\cdot e^{-\frac{t}{\tau_L}}\right], p_c \succ p;$$
$$\left\langle R^2(t)\right\rangle \approx Dt\left[1+b\cdot e^{-\frac{t}{\tau_H}}\right], p_c \prec p. \qquad (17)$$

The parameters relevant for description of the phase transition obey the following scaling relations:

$$R_\infty^2(p)\propto \Delta p^{-2\nu+\beta}, \tau_L(p)\propto \Delta p^{-2\nu-t+\beta},$$
$$D(p)\propto \Delta p^{t}, \tau_H(p)\propto \Delta p^{-2\upsilon-t-\beta}, \qquad (18)$$

where the critical indices β, v and *t* correspond to the order parameter of the phase transition, to the correlation length and to the specific conductivity, respectively. The critical index *t* has values between 1.1 and 1.6. The crucial relation we take over from this general formalism of the theory of percolative phase transitions is the following one:

$$D(p)\propto \Delta p^{t}, \qquad (19)$$

i.e. the mathematical modelling of the percolative behaviour of the system can be performed in a subtle way for the complete set of quantities characterizing the coupled heat and mass transfer through porous medium in random medium picture. Since (in the sense of relation (5)) the relaxation time constants depend on the actual values of the diffusion coefficient, too, it becomes possible to set up completely new modelling strategies able to follow dependence of the relaxation time constants on the percolative state of the system.

Following arguments explained in the introductory section, we write down here and apply hyperbolic type partial differential equations usually describing wave phenomena in dissipative systems. By application of the relevant relaxation time constants and within frame of the approach relevant for *coupled* transport processes (i.e. when the convection-free processes are treated) and later developed by many authors into a theory ap-

plicable on a large scale see e.g. (JOU *et al.* 2001), the actual system of transport equations takes the following form:

$$\tau_1 \frac{\partial^2 M}{\partial t^2} + \frac{\partial M}{\partial t} - D\nabla^2 M - K\nabla^2 T = 0,$$
$$\tau_2 \frac{\partial^2 T}{\partial t^2} + \frac{\partial T}{\partial t} - E\nabla^2 T - L\nabla^2 M = 0, \qquad (20)$$

where *M(x,t)* and *T(x,t)* denote the moisture level and temperature function, respectively, while τ_1 and τ_2 are the relaxation time constants characterizing time dependence of the same quantities. *D* is the ordinary- *E* is the termodiffusion coefficient, while *K* and *L* are symbols of the coupling coefficients. Although the relaxation time constants are in general case built up from conductivity and coupling coefficients (and are therefore thermodynamically state-dependent quantities (GYARMATI 1977)), their state-dependence will not be discussed here, because it would lead to research topics belonging to dynamic scaling theory (FARKAS *et al.* 2000). According to the usual, well-established descriptions of the coupled transport processes taking place in porous media (LUIKOV & MIKHAILOV 1965), these coefficients have the following meaning

$$D \equiv a_m, K \equiv a_m \delta,$$
$$E \equiv \varepsilon l \frac{c_m}{c_q} a_m \delta + a_q, L \equiv \varepsilon l \frac{c_m}{c_q} a_m \delta. \qquad (21)$$

Since according to our assumption the diffusion coefficient is taken as a percolatively state-dependent quantity, it is obvious that adequate state dependence is also valid (via relationship $a_m \equiv D \propto \Delta p^t$ from (18)) for other coefficients in (20), too.

Application of the above-described hyperbolic type *PDE* system (19) instead of the usually applied parabolic types is by all means justified, since this choice ensures correct description (in accordance with the wave approach of the irreversible thermodynamics) of the finite propagation velocity of disturbances. As we have mentioned earlier, the relaxation time constant relevant for moisture level changes is much more significant, than the one corresponding to the temperature function (SOBOLEV 1997). In that case, the PDE relevant for temperature simplifies into the usually applied parabolic type and leads (via direct combination of the PDE-s of (19)) to the following general formula (MÉSZÁROS *et al*. 2004), whose solution describes the spatial and temporal behaviour of the moisture level:

$$\tau_1 \frac{\partial^2 M(x,t)}{\partial t^2} + \frac{\partial M(x,t)}{\partial t} - D\frac{\partial M(x,t)}{\partial x^2} + \\ + \frac{1}{4\sqrt{\pi}t^{3/2}} \cdot \frac{K}{E^{3/2}} \int_\Omega T_0(\xi)\left[1 - \frac{(x-\xi)^2}{2Et}\right] \\ e^{-\frac{(x-\xi)^2}{4Et}} d\xi + \frac{1}{4\sqrt{\pi}t} \cdot \frac{KL}{E^{3/2}} \\ \int_0^t \frac{1}{\sqrt{t-\tau}} \int_\Omega \frac{\partial^2 M(\xi,\tau)}{\partial \xi^2}\left[1 - \frac{(x-\xi)^2}{2Et}\right] \\ e^{-\frac{(x-\xi)^2}{4Et}} d\xi d\tau = 0. \qquad (22)$$

Here, $T_0(\xi)$ is the initial temperature distribution of the porous matter being dried, while Ω denotes the spatial integration domain, i.e. the volume filled with this matter. It is obvious from (22), that percolative state dependence strongly influences the moisture level distribution through the coefficients:

$$D \equiv a_m, \frac{K}{E^{3/2}} \equiv \frac{a_m \delta}{\left(\varepsilon l \frac{c_m}{c_q} a_m \delta + a_q\right)^{3/2}}, \\ \frac{KL}{E^{3/2}} \equiv \frac{\varepsilon l \frac{c_m}{c_q} a_m^2 \delta^2}{\left(\varepsilon l \frac{c_m}{c_q} a_m \delta + a_q\right)^{3/2}}, \qquad (23)$$

while the conductivity coefficient E (in (21)) entering the general formula of the moisture level function in the product form Et, i.e.

$$E \equiv \varepsilon l \frac{c_m}{c_q} a_m \delta + a_q, \qquad (24)$$

in the critical region of the percolative phase transition (i.e. when the value of Δp is very small) may be well-approximated by the constant coefficient a_q. This simplification is also justified by the possible values of the phase transition criterion ε (i.e. the quantity determining the ratio of the liquid water (and therefore of the water vapour also) with respect to the

whole water content inside porous matter) is always smaller than one or at most equal to value one (LUIKOV & MIKHAILOV 1965). Therefore, at calculating of the moisture level distribution function in the case of percolative phase transitions, the crossover phenomena can be modelled accurately and incorporated into the general solution of the problem within frame of the approach applied here. Dependence of the coefficients playing role in the general solution (21) on the percolation probability difference and liquid-water vapour phase change criterion can be calculated directly and are presented on the **Figures 3** and **4**.

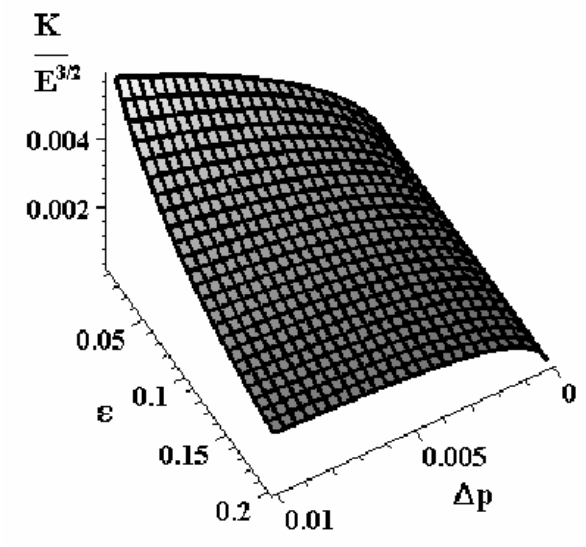

Figure 3: Dependence of the first coefficient on the phase change criterion and percolation probability difference

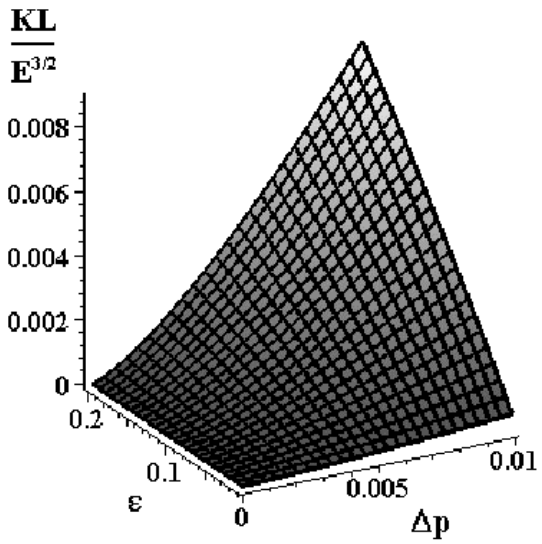

Figure 4: Dependence of the second coefficient on the phase change criterion and percolation probability difference

The figures were drawn by use of the MAPLE 8 software package (MAPLE 8 2002) and values of the coefficients are given in relative units for value 0.65 of the critical exponent *t*.

As a promising continuation of this work the statistical averaging (with respect to the possible successive percolation phase transitions from insulating states into completely conducting one and vice versa) of the coupled heat and mass transfer through porous medium can be performed leading to even more realistic drying models. Furthermore, the newest advanced transport models based on the common application of the fractal-, and percolation theory e.g. (ZELENYI & MILOVANOV 2004) may lead to even more refined descriptions of genuine drying processes. Their incorporation into mathematical models of drying processes is still absent in the literature.

5 Conclusions

In the present work foundation of a new, hybrid mathematical model for describing coupled heat and mass transport through porous media is presented. Requirements of both extended irreversible thermodynamics and contemporary percolation theory are taken into account, i.e. the finite propagation velocity of thermal disturbances and concentration inhomogeneities as well as the actual percolative state-dependence (due to the porous microstructure of the wet matter) are incorporated into model from the beginning. Although solution of the coupled system of hyperbolic type partial differential equations usually represents a serious difficulty, by neglecting the relaxation time constant relevant for temperature with respect to the time constant corresponding to the moisture level a simplified system can be obtained, whose solution can be obtained by direct application of software packages designed for symbolic computation. Finally, the percolative behaviour enters the solution functions via scaling relation describing percolative behaviour of the diffusion constant. Following this new strategy we were able to construct a completely new mathematical model for drying processes and to calculate and draw new, refined moisture level distribution functions. Moreover, our result indicates some possibilities for introducing of the concept of fractals into drying theory in a novel manner.

Nomenclature

A	numerical constant (-)
a_m	coefficient of mass transfer (m^2/s)
a_q	coefficient of temperature conductivity (m^2/s)
b	numerical constant (-)
c_m	specific mass coefficient of moist body (K/m^4)
c_q	specific heat capacity of moist body (J/kgK)
l	specific heat of evaporation (J/kg)
$M(x, t)$	moisture level function of the porous material (kg/kg)
p	percolation (occupation) probability (-)
Δp	percolation probability difference (-)
p_c	critical percolation probability (-)
$P(p)$	order parameter (-)
R	distance of a particle executing random motion in a percolative system from an initial position (m)
$R_\infty(p)$	scaling parameter (m^2)
t	time, critical exponent of the specific conductivity (s),(-)
$T(x, t)$	temperature function of the porous material (K)
x	spatial coordinate (m)

Greek Symbols

β critical exponent of the order parameter (-)

δ thermo-gradient (Soret) coefficient (m^2/K)

ε criterion of phase transition (-)

ν critical exponent of the correlation length (-)

Θ time constant of the lattice percolation in the ordered phase (s)

τ time constant of the lattice percolation in the disordered phase (s)

τ_1 macroscopic relaxation time constant of the moisture level (s)

τ_2 macroscopic relaxation time constant of temperature (s)

Acknowledgements

The authors gratefully acknowledge financial support of the German-Hungarian TÉT D-5/03 project and it is also acknowledged the support of the Bolyai Fellowship BO/00192/05-2005 given to Dr. Mészáros. Thanks to Hungarian Ministry of Education for awarding Széchenyi István Fellowship No 245/2003 to Dr. Bálint.

References

AMES W.F. (1967): *Nonlinear Ordinary Differential Equations in Transport Processes*, New York and London: Academic Press

BITTERLICH S., KNABNER P. (2003): *Experimental design for outflow experiments based on a multi-level identification method for material laws*, Inverse Problems 19, pp. 1011-1030

FARKAS I., MÉSZÁROS CS., BÁLINT Á. (2000): *Mathematical and Physical Foundations of Drying Theories*, Drying Technol. 18(3), pp. 541-559

GYARMATI I. (1977): *On the Wave Approach of Thermodynamics and some Problems of Non-Linear Theories*, J. Non-Equilib. Thermodyn. 2(4), pp. 233-260

HUININK H.P., PEL L., MICHELS M.A.J., PRAT M. (2002): *Drying processes in the presence of temperature gradients- Pore-scale modelling*, Eur. Phys. J. E 56, pp. 487-498

JOU D., CASAS-VAZQUEZ J., LEBON G. (2001): *Extended Irreversible Thermodynamics (3rd ,rev. and ext. Ed.)*, Berlin-Heidelberg-NewYork: Springer-Verlag

KIRSCHNER I. (1971): *Stability of Stationary Thermodynamic States* Acta Phys.Hung. 30, pp. 61-69

KIRSCHNER I., LEPPÄVUORI S. (1992): *Non-equilibrium, irreversibility, non-linearity and instability in the operation of sensors* Sensors and Actuators. A 31, pp. 275-282

KIRSCHNER I. (1994): *Stability of the Operation of Sensors* Sensors and Actuators. A 41, pp. 622-629

LANDAU L.D., LIFSHITZ E.M. (1987): *Fluid Mechanics*, London: Pergamon Press

LUIKOV A.V., MIKHAILOV YU.A. (1965): *Theory of Energy and Mass Transfer*, London: Pergamon Press

LUKE, Y.L. (1969): *The Special Functions and Their Approximations* Vol.1., New York: Academic Press

MAPLE 8 (2002): *A Symbolic Computation System*; Waterloo Maple Inc.

MÉSZÁROS CS., FARKAS I., BÁLINT Á. (2001): *A new application of percolation theory for coupled transport phenomena through porous media*, Math. Comp. Sim. 56, pp. 395-404

MÉSZÁROS CS., FARKAS I., BÁLINT Á., BUZÁS J. (2004): *Modeling of the coupled heat and mass transfer through porous media on the base of the wave approach*, Drying Technol. 22 (1-2), pp. 71-80

OLVER P.J. (1993): *Applications of Lie Groups to Differential Equations*, 2nd Ed., 3rd printing, Berlin-Heidelberg-New York: Springer-Verlag

SOBOLEV S.L. (1997): *Local Non-Equilibrium Transport Models* (in Russian), UFN 167(10), pp. 1095-1106

STARK A. (1974): *Approximation Methods for the Solution of Heat Conduction Problem using Gyarmati's Principle*, Ann. Phys. (Leipzig) 7(31), pp. 53-75

STAUFFER D., AHARONY A. (1994): *Introduction to Percolation Theory (2nd Rev. Ed.)*, London: Taylor & Francis

VON LOMMEL E.C.J. (1884-1886a): Die Beugungerscheinungen einer kreisrunden Öffnung und eines kreisrunden Schirmchens theoretisch und experimentell bearbeitet, Abh. der Mat. Phys. Klasse k.b. Akademie der Wissenschaften (München), 15, 229-328

VON LOMMEL E.C.J. (1884-1886b): Die Beugungerscheinungen geradlinig begrenzter Schirme, Abh. der Mat. Phys. Klasse k.b. Akademie der Wissenschaften (München), 15, 529-664

ZELENYI L.M., MILOVANOV A.V. (2004): *Fractal topology and strange kinetics: from percolation theory to problems in cosmic electrodynamics* (in Russian), UFN 174(8), pp. 809-852

Bruise Detection on Apples Using Hyperspectral Imaging System

Juan Xing and Josse De Baerdemaeker
Division of Mechatronics, Biostatistics and Sensors, Department of Biosystems, Faculty of Bioscience Engineering, CatholicUniversity of Leuven,
Kasteelpark Arenberg 30, B-3001, Leuven, Belgium.
E-Mail of corresponding author: juan.xing@biw.kuleuven.be

Abstract: *In this paper, the experiments carried out on 'Golden Delicious' apples with a hyperspectral imaging system have been reported. Chemometric tools such as Principal Components Analysis (PCA) and Partial Least Squares Discriminant Analysis (PLSDA) were used to extract and summarize the spectral information from the hyperspectral images. The results obtained from the chemometric techniques were used to construct virtual images. Afterwards, some image processing methods were applied on these artificial images to aid in classifying samples. This combination of image processing techniques and chemometric tools provides a very promising approach for bruise detection on apples.*

Keywords: *Bruise, Apple, Hyperspectral imaging, PCA, PLSDA*

1 Introduction

Appearance is an important quality index for apple fruits. Bruising is a most common surface injury occurring on apples. It is clear from literature that bruising is an important problem that reduces quality to the consumer and income to fruit and vegetable industries. Bruising is usually recognized as brown spots on apples. Moreover, bruising seems to be almost unavoidable in postharvest handling. BARITELLE & HYDE (2001) stated that an annual payback to fruit and vegetable industries in reducing bruising can be in billions of dollars worldwide.

For the non-destructive bruise detection on apples, in some cases, simple visual inspection may suffice. Human inspection and manual removal has been used in the fruit industry for a long time. However, the availability of fewer workers and increasing employment costs during the peak harvesting seasons have been identified as the significant factors demanding automation in the fruit industry.

In the light of providing a more consistent and objective evaluation of fruit quality, optical approaches, such as machine vision and spectroscopy, are considered as the most potential methods complementary to the human inspectors on the automatic fruit sorting line. Machine vision has succeededs in categorizing fruits with respect to the size, colour and

other appearance indices. However, its capacity for detecting surface defects is still limited and not reliable (LU 2003, LEEMANS & DESTAIN 2004).

Spectroscopy has a longer history than machine vision in food research. The spectroscopy, especially the near-infrared (NIR) spectroscopy, is mainly used for the prediction of constituents. In addition, spectroscopy measures an aggregate amount of light reflected or transmitted from a specific area of a sample (point measurement); it does not contain spatial information about the product.

Hyperspectral imaging is a technique that combines conventional imaging and spectroscopy to acquire both spatial and spectral information from an object. Because of this combined feature of imaging and spectroscopy, hyperspectral imaging can enhance and/or expand our capability of detecting some chemical constituents in an object as well as their spatial distributions. The data collection and processing is still time-consuming, which makes it at this moment impractical for being used on line as such. VOGT e*t al.* (2004) suggested wavelet transforms to shorten the computation time and reduce the storage space required. Another approach to make this technique feasible is to establish a multi-spectral imaging system based on the analysis of hyperspectral images. That means selecting several optimal filters for the camera, which are the wavebands sensitive to the property changes of fruits.

Notwithstanding its limitations, the hyperspectral imaging setup has been favoured as a starting point by researchers in a wide range of scientific and industrial fields (SCHULTZ *et al.* 2001, YANG *et al*. 2001, SCHUT *et al*. 2002). Hyperspectral imaging has also found its application for food quality evaluation and safety inspection: chicken carcasses (CHAO *et al*. 2001, YANG *et al*. 2005), poultry carcasses (PARK *et al.* 2002, LAWRENCE *et al*. 2003), vegetables (CHENG *et al*. 2003), and apples (KIM *et al*. 2001, KAVDIR *et al*. 2002, XING *et al*. 2005A).

In this paper, the potential of using a hyper-/multi-spectral imaging system (400-1000 nm) is investigated for studying the quality of apples. Most efforts focus on the bruise detection on ‘Golden Delicious’ apples.

2 Theory

In the case of bruise detection on apples the algorithm should not only be able to detect whether there is a bruise, but also to localize where it is. The chemometric treatments of the hyperspectral imaging data are expected on the one hand to concentrate the information; and on the other hand to enhance the contrast between the damaged and sound tissue. After that, image processing techniques can be used to segment the bruised regions on apple surfaces.

2.1 Statistical methods

Statistical techniques were applied to summarize the spectral information obtained from the hyperspectral imaging system.

Principal components analysis (PCA). PCA is a very effective data reduction technique for spectroscopic data. It summarises data by forming new variables, which are uncorrelated, linear combinations of the original variables. A few of these new variables (principal components) represent the large part of the common variations to all the data. By only considering several principal components, the high dimensional spectral data can be reduced to a lower dimensionality with a minimal loss of information. In this study, PCA was used to aid in visualising the hyperspectral data and to develop criteria for selection of wavebands for multi-spectral bruise detection.

Partial Least Square Discriminant Analysis (PLSDA); The Partial Least Squares (PLS) regression is a bilinear modelling method in which information in the original X-variable is projected onto a small number of underlying variables called PLS factors or latent variables. The Y-variable is actively used in estimating the latent variables to ensure that the first one is most relevant for predicting the Y-variable. In particular, the objective with PLSDA is to find models that allow the maximum separation among classes of objects. A dummy variable can be constructed, representing the sample properties (*e.g.*, healthy = 1, bruised = 0) and then used as Y-variable. PLSDA is therefore a multivariate inverse least squares discrimination method used to classify samples. In this paper, the prediction values of the PLSDA procedure were surveyed. The prediction value is the predicted Y value for a new sample, which is the same as in the PLS regression.

2.2 Image processing methods

Image segmentation is one of the most important steps in image processing, as subsequent extracted data are highly dependent on the accuracy of this operation. Its main aim is to divide an image into regions that have a strong correlation with objects or areas of interest. Thresholding is a simple and fast technique for characterising image regions based on constant reflectivity or light absorption of their surfaces. It is a particularly effective technique for scenes containing solid objects resting upon a contrasting background, which distinguishes the object from the remaining part of an image with an optimal threshold value.

Two thresholding methods were tested in this experiment. The simple one is to choose a fixed threshold value for all images. The values of images are then compared with this threshold value. Ones are assigned to the regions with higher value and zeros for the region with lower values; and vice versa. The ‘moments’ is an automatic thresholding method, which is based on the hypothesis that the observed image is a blurred version of the theoretically binary original. The blurring that is produced from the acquisition process is treated as if the statistical moments (average and variance) were the same for both the blurred image and the original image. This function recalculates a theoretical binary image (NI-IMAQ).

3 Experimental

3.1 Software

The image capturing and automatic thresholding program was developed in Labview v7.1 (National Instrument Corporation, Austin, USA); while all computations, chemometric analyses and graphics were executed with programs developed in Matlab v6.5 (The MathWorks Inc., Natick, USA).

3.2 Materials and methods

Samples. From the local supermarket 59 'Golden Delicious' apples were purchased. They had a normal green colour. The apples were separated into two groups by visual inspection: non-bruised and bruised. Most of the bruises were detected on the cheeks of the apples and showed the typical browning symptoms. The other 69 'Golden Delicious' apples were harvested from the university orchard in Rillaar (Belgium). The apples were green and some of them had some yellowness. They were assumed to be free from bruises. One day after arrival at the laboratory, these apples were impacted with a pendulum in the midway between the calyx and stem end to get a controlled bruise. After the impact, the apples were stored at room temperature (22°C) for 24 hours before being measured.

Set-up. As shown in **Figure 1,** the hyperspectral imaging system mainly consists of a monochrome camera (Hitachi KP-F120) and a Specim V10 spectrograph (Spectral Imaging Ltd., Oulu, Finland). The wavelength sensitivity of the optical system ranges from 400 to 1000 nm. The resolution of the image acquisition system was 800×1040 pixels by 10 bits. The camera and spectrograph were used to scan the apples line-by-line as the transportation plate moved the apples through the field of view of the optical system. After finishing the scans on one entire apple, the spatial-by-spectral matrices were combined to construct a 3D spatial and spectral data space.
For more details about the construction and calibration of the hyperspectral imaging system, please refer to our paper (XING *et al*. 2005A).

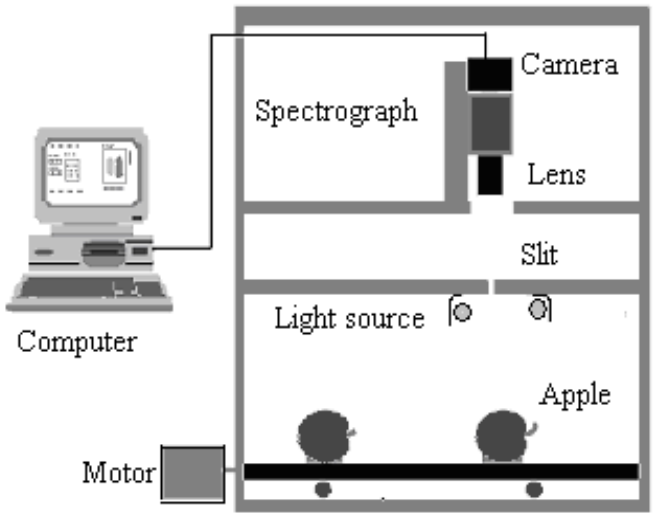

Figure 1: Schematic of hyperspectral imaging system

3.3 Results and discussion based on PCA

Principal components analysis on the full wavelength region. Each pixel on an apple corresponds to one spectrum. On each apple, more than 1,000 reflectance spectra can be recorded.

Principal components analysis was applied to the reflectance spectra of each apple. Then the scores of principal components were used to construct virtual images, which is called 'PCA scores image' in later text to distinguish it from the normal reflectance or intensity image. If the first principal component (PC1) scores were used, the resultant image was then called PC1 scores image. If the second principal component (PC2) scores were manipulated, it was called PC2 scores image; and so on. The advantage of using principal component scores images is that it can concentrate the information from multiple wavebands.

After visual inspection, PC1 scores images mainly demonstrate the uneven illumination for different distance of the surface to the lamps. PC2 or PC3 scores images demonstrate more the surface properties of the apple, *i.e.*, with(out) presence of bruises. They appear to provide the best discrimination between the sound and bruised tissue.

Selection of optimal wavebands. **Figure 2** shows the average loadings for the first three components from 20 apples across the entire spectral region. Although the first PC accounts for the larger part (more than 90%) of the variance in the image, it does not give evident features for the differences between the intact and damaged tissue. As most of the bruises could be inspected clearly from either PC2 or PC3 scores images, the loadings of PC2 and PC3 should be considered as the basis to select optimal wavebands for detecting bruises. Consequently, the wavebands (7 nm bandwidth) centred at 558 nm, 678 nm, 728 nm and 892 nm, respectively, were chosen as the optimal ones for bruise detection on 'Golden Delicious' apples.

Principal components analysis on the four effective wavebands. Principal components analysis was then carried out on the four effective wavebands instead of the full wavelength range. The resultant four-spectral PCA scores images appear very similar to those obtained on the full wavelength region (data not shown here). Therefore, the later analysis was based on the PCA results from the four wavebands. Similarly, PC1 scores images mainly accounts for the illumination condition, while PC2 or PC3 scores images are the best for discriminating bruises from sound tissue.

Classification results based on PCA. As described before, the bruises can be identified clearly either on PC2 or on PC3 scores images. To combine the information from these two principal components scores images, a normalisation and a combination algorithm were developed. More details about the classification algorithm can be found in XING *et al.* (2005A). **Figure 3** demonstrates the results after the image processing for sound and bruised apples.

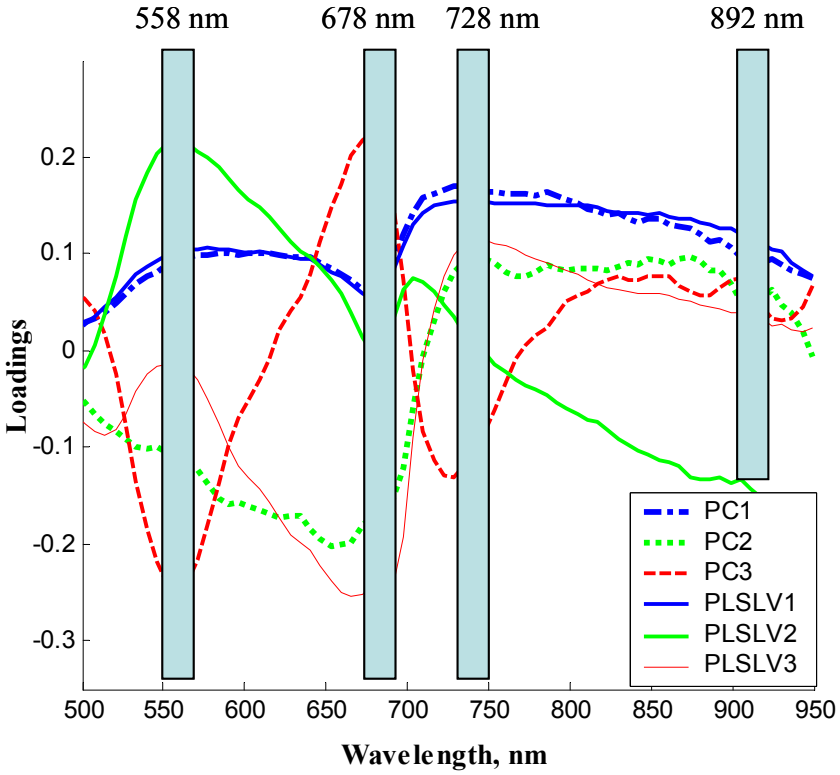

Figure 2: Suitable wavebands selection for bruise detection on 'Golden Delicious' apples

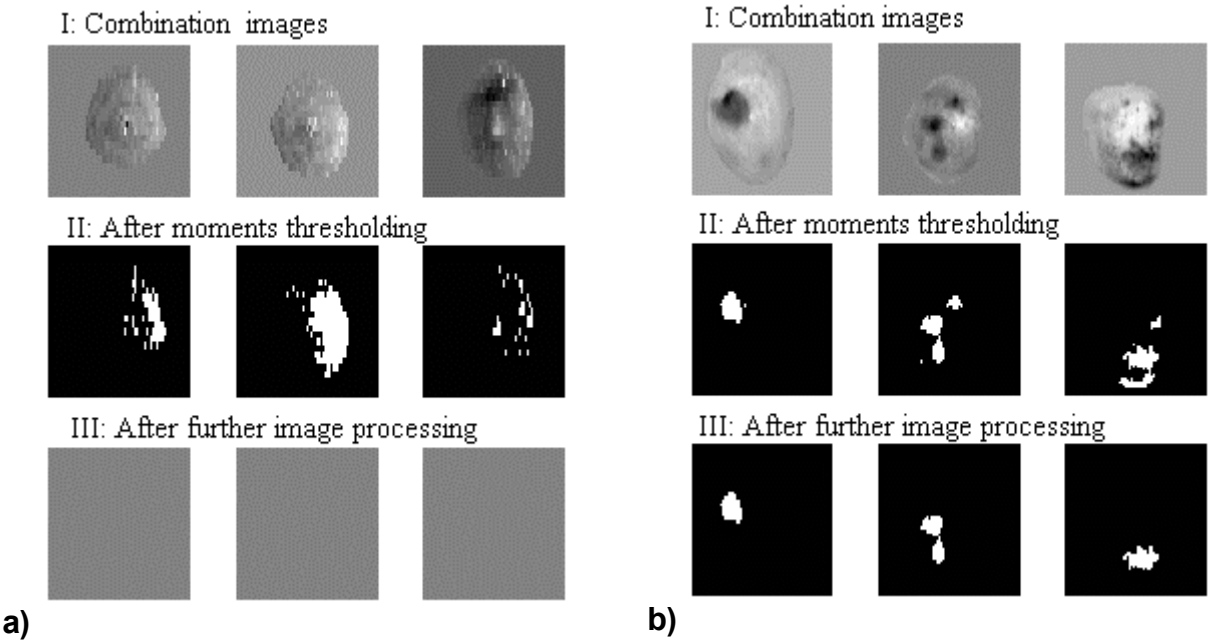

Figure 3: Results after applying image processing methods on the combination of PCA scores images (a) examples of sound apples; (b) examples of bruised apples

After applying this classification algorithm on the images obtained from the 128 apples, about 93.55% of the 62 non-bruised apples were recognised as sound; and about 86% accuracy for bruised apples was obtained (shown in **Table 1**).

Table 1: Classification results for 'Golden Delicious' apple using the algorithm based on PCA

Actual class	*Classified as*	
	Sound	*Bruised*
Sound (*n* = 62)	58 (93.55%)	4
Bruised (*n* = 66)	9	57 (86.36%)

* *n*, the number of samples

One issue that has to be noticed here is that, although the classification rate for the bruised apples is only 86%, all the bruised regions were remained in the 'moments' thresholding images. This indicates that this method is prospective for detecting bruises on 'Golden Delicious' apples, but that better feature selection or image processing methods have to be developed to recognise all the bruised regions.

3.4 Results and discussion based on PLSDA

Data preparation. Prior to doing the prediction for new samples, a PLSDA model has to be trained based on a calibration dataset. The training dataset includes 16,006 and 25,779 spectra collected from the bruised and sound tissue, respectively. To get rid of the irrelevant variations in the data, a maximum normalization pre-treatment was applied on the spectrum of each pixel on the apple surface, which means that each spectrum was divided by its own maximum value.

Calibration of PLSDA model. A dummy variable 'property', which consists of zeros and ones, was created for the purpose of regression. A value of 0 was assigned to the spectrum from bruised tissue and 1 for that from sound tissue. The ones and zeros are then used as regressand (Y-variable) in building the PLSDA model. The normalized reflectance spectra were taken as the regressors (X-variable).

Similar to what was done in the PCA procedure described in the previous section, the loadings plot of PLS latent variables (PLSLV) was used to determine the effective wavebands for discrimination. The peaks of the first four latent variables are quite similar to those of the principal components (Figure 2). Therefore, the four wavebands selected in the previous section will be used in this section as well in order to keep consistency between both analyses. Afterwards, the PLSDA model was rebuilt with these four wavebands only and it was saved for predicting new samples.

Prediction of bruises in new samples using PLSDA. For the prediction of bruises in new samples, the pre-treatment of maximum normalization was also applied on their spectra. The outcome of the model indicated then whether a new sample should be in the sound group or not.

Similar as conducted with the PCA scores image, PLS prediction values were used to construct virtual images. For this type of virtual images, there is no need for a sophisticated thresholding method, like 'moments'. The simple thresholding method was employed. The threshold value was set as half of the sum of maximum and minimum prediction of each apple. If the prediction value of a pixel is larger than the threshold value, this pixel will be assigned a '1' value; otherwise, it is given a '0' value.

Classification results from the PLSDA prediction images. **Figure 4** displays some example images of sound and bruised apples constructed with PLSDA prediction values, respectively. For clear demonstration, in the examples of binary image, the bruised spots are shown in white in the image and the sound tissues are in black in the image. The bruised samples are the same as those shown in Figure 3.

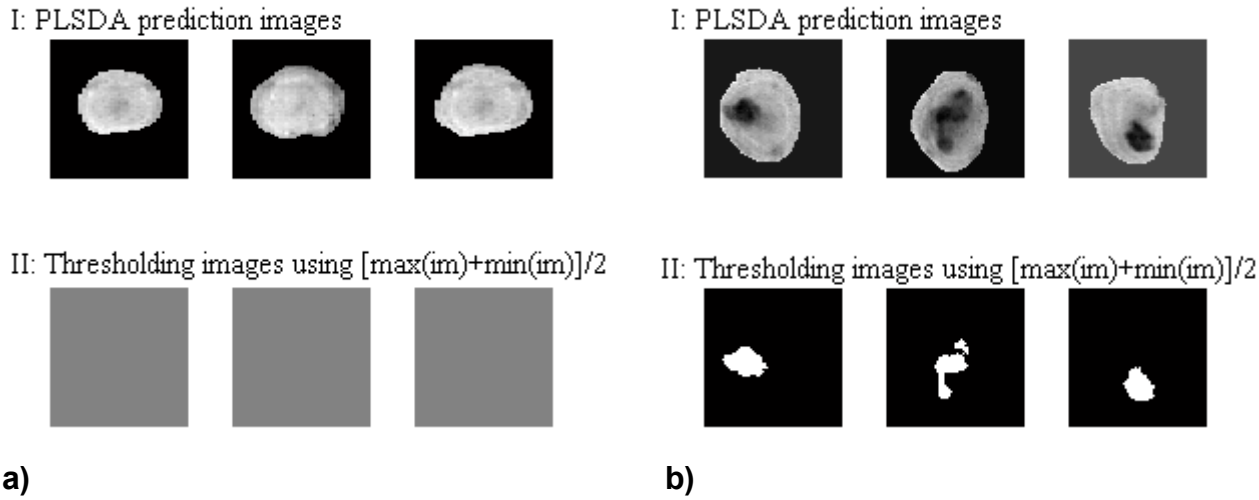

Figure 4: PLSDA prediction images and corresponding thresholding images of sound apples (a) and bruised apples (b)

It can be seen clearly that the PLSDA prediction images are different from the PCA scores images: the topographic information is no longer observable. The intensity change in the PLSDA prediction image is more dependent on the contrast of different tissues instead of the height profile. In the resultant images for the sound apples (Fig. 4a), the predicted value for each pixel is rather even and the illumination effects can no longer be observed. While, in the images of bruised apples (Fig. 4b), the injured regions have obvious contrast with the sound tissues, which lead to very clear and clean segmentation images with the simple thresholding method. This is an advantage of using the PLSDA technique for bruise detection on apple cheeks using multispectral imaging.

A total of 115 apples was tested with the PLSDA procedure for model validation (without including the apples used for calibration). The classification table is given in **Table 2**. All the sound apples and about 82.3% of the bruised apples were classified correctly.

Table 2: PLSDA classification results according to the prediction values

Actual class	*Classified as*	
	Sound	*Bruised*
Sound *n* = 53	53 (100%)	0
Bruised *n* = 62	11	51 (82.26%)

* *n*, the number of samples

3.5 Comparison of PCA and PLSDA procedures

Regarding to the classification accuracy obtained from this study, the algorithm based on PCA gives similar results to that of PLSDA (based on prediction values). PLSDA has the advantage that no complex image processing is needed. It may save some time in making a decision for the quality of apples on line. On the other hand, as reported in our paper (XING *et al*. 2005B), the topographic information is useful for separating the stem-end/calyx regions from the true damaged tissue. The PC1 scores images from the PCA procedure reveal this information well. However, the geometric information is not available in the PLSDA prediction images any more. The stem-end/calyx identification might demand for an extra analysis. This problem was investigated on 8 apples (data not shown here). After thresholding the PLSDA virtual images, the bruises and the stem-end/calyx regions are all retained in the image and it was difficult to separate them further. With PCA scores images no misclassifications between the stem-end/calyx and the bruises were obtained (XING *et al*. 2005B).

4 Conclusions

The experiments carried out on ‘Golden Delicious’ apples with the hyperspectral imaging system have been reported. Chemometric tools, such as PCA and PLSDA, were applied for extracting the useful information from the hyperspectral imaging data. Four sensitive wavebands (7 nm bandwidth), *i.e.*, centred at 558 nm, 678 nm, 728 nm and 892 nm, respectively, were chosen for bruise detection on apples. The results obtained from the chemometric techniques were used to construct virtual images for further analysis. Afterwards, some image processing methods were applied on these artificial images to aid in classifying samples.

PLSDA does not need complex image processing on the virtual images, which is good for speeding up the inspection speed. However, it needs a good training dataset to build a model prior to do the prediction for a new sample. The algorithm based on PCA results needs more processes for the virtual images to make a final decision about the properties

of samples, whether bruised or not. However, PCA is performed on each individual apple, which means the variations between different individuals are eliminated so that it is not necessary to make efforts for collecting a representative calibration dataset.

The chemometric tools do not only summarize and concentrate the information carried in the hyperspectral images, but they also enhance the contrast between the damaged and sound tissue on apples. The spatial features segmented by image processing methods can in turn help the expert to make a correct evaluation of the quality of apples. This study based on the hyperspectral imaging setup lays a foundation for later development of a computer vision system for bruise detection on 'Golden Delicious' apples, as well as for the other similar applications.

References

BARITELLE A.L., HYDE G.M. (2001): Commodity conditioning to reduce impact bruising. *Postharvest biology and technology*, 21: 331-339

CHAO K., CHEN Y.R., HRUSCHKA W.R., PARK B. (2001): Chicken heart disease characterization by multi-spectral imaging. *Transaction of the ASAE,* 17(1): 99-106

CHENG X., CHEN Y.R., WANG C.Y. (2003): Hyperspectral imaging and feature extraction methods in fruit and vegetable defect inspection. *An ASAE meeting presentation*, paper number: 033119

IMAQ vision builder turorial. National Instruments, USA; October 1999 edition

KIM M.S., CHEN Y.R., MEHL P.M. (2001): Hyperspectral reflectance and fluorescence imaging system for food quality and safety. *Transaction of the ASAE*, 44(3): 721-729

KAVDIR I., GUYER D.E. (2002): Apple sorting using artificial neural networks and spectral imaging. *Transaction of the ASAE*, 45(6): 1995-2005

LAWRENCE K.C., WINDHAM W.R., PARK B., BUHR R.J. (2003): A hyperspectral imaging system for identidication of faecal and ingrsta contamination on poultry carcasses. *Journal of near infrared spectroscopy*, 11: 269-281

LEEMANS V., DESTAIN M.-F. (2004): A real-time grading method of apples based on features extracted from defects. *Journal of Food Engineering*, 61: 83-89

LU R. (2003): Detection of bruises on apples using near-infrared hyperspectral imaging. *Transaction of the ASAE*, 46(2): 523-530

PARK B, LAWRENCE K.C., WINDHAM W.R., BUHR R.J. (2002): Hyperspectral imaging for detecting fecal and ingesta contaminants on poultry carcasses. *Transactions of the ASAE*; 45(6): 2017-2026

SCHUT A.G.T., KETELAARS J.J.M.H., MEULEMAN J., LORNET J.G., LOKHORST C. (2002): Noval imaging spectroscopy for grass sward characterization. *Biosystems Engineering*, 82(2): 131-141

SCHULTZ R.A., NIELSEN T., ZAVALETA J.R., RUCH R., WYATT R., GARNER H.R. (2001): Hyperspectral imaging: a novel approach for microscopic analysis. *Cytometry*, 43: 239-247

VOGT F., BANERJI S., BOOKSH K. (2004): Utilizing three-dimensional wavelet transforms for accelerated evaluation of hyperspectral image cubes. *J. Chemometrics*, 18: 350-362

XING J., BRAVO C., JANCSOK P., RAMON H., DE BAERDEMAEKER J. (2005A): Bruise detection on Golden Delicious apples by using hyperspectral imaging with multiple wavebands. *Biosystems Engineering*, 90(1): 27-36

XING J., DE BAERDEMAEKER J. (2005B): Bruises Detection on 'Jonagold' Apples Using Hyperspectral Imaging. *Postharvest Biology and Technology*, 37(2): 152-162

YANG C.C., CHAO L., CHEN Y.R. (2005): Develoment of multispectral image processing algorithms for identification of wholesome, septicemic and inflammatory process chickens. *Journal of Food Engineering*, 69: 225-234

YANG C.H., EVERITT J.H., MAO C.Y. (2001): A hyperspectral imaging system for agricultural applications. *An ASAE meeting presentation*, paper number 01-1107

„Chinese House“
in the "Deer Garden" of Sanssouci Park.

„Sanssouci Palace“

Phenolics and Antioxidant Activity of Wines During the Winemaking Process

Jaromír Lachman and Miloslav Šulc
Czech University of Agriculture in Prague, Department of Chemistry, Faculty of Agrobiology, Food and Natural Resources, Kamýcká 129, 165 21 Prague 6 – Suchdol, Czech Republic, E-Mail: lachman@af.czu.cz

Abstract: *Changes in the content of total polyphenols (TP) and antioxidant antiradical activity (AAA) affected by grape variety, wine-growing area and winemaking process in five white and four red varieties from three wine areas of Czech Republic (harvest 2004) were studied. Significant differences in TP among varieties were found. Analysis of variance showed statistically high differences among red and white wines and growing areas. Wines differed significantly in TP content and AAA increased significantly during wine making process. Statistically significant differences in AAA values were found among growing areas, wines and varieties. Significant positive correlations between TP and AAA were determined. Copyright © 2006 IFAC*

Keywords: *wine; variety; growing region; winemaking; total polyphenols; antioxidant activity*

1 Introduction

The French have low coronary heart disease mortality with high fat consumption; this epidemiological anomaly is known as the "French Paradox" and is commonly attributed to the consumption of red wine (VINSON *et al.* 2001). Red wine is a complex fluid containing grape, yeast, and wood-derived phenolic compounds, the majority of which have been recognized as potent antioxidants (BURNS *et al.* 2001). Antioxidative capacity of wine on human LDL oxidation is related to the content of polyphenols contained in wines (HURTADO *et al.* 1997), which improve aortic biomechanical properties (MIZUTANI *et al.* 1999). Content of polyphenols, composition of phenolic complex and antioxidative or antiradical capacity of wines could be affected by many extrinsic and intrinsic factors, as variety, wine growing area and climatic conditions, quality of wine, and not at least also technological procedures during wine-making (FAITOVÁ *et al.* 2004). Colour evolution during vinification and ageing has been attributed to the progressive changes of phenolic compounds extracted from grapes (VIVAR-QUINTANA *et al.* 2002). In last years many studies focused on the dynamics of polyphenol extraction during maceration processes of grape varieties (BUDIC-LETO *et al.* 2003, 2005). Important is the evolution of grape polyphenol oxidase activity and phenolic content during wine maturation and

vinification (VALERO *et al.* 1989), changes and evolution of polyphenols in young red wines (PELLEGRINI *et al.* 2000), changes of the hydrophilic and lipophilic antioxidant activity of white and red wines during the wine-making process (ALCOLEA *et al.* 2003). Some authors put more emphasis on maceration process (BUDIC-LETO *et al.* 2005), the other on grape maturation (JORDAO *et al.* 2001), when quantitative changes in oligomeric occur. Also changes in antioxidant capacity of Tannat red wines during early maturation were reported by ECHEVERRY *et al.* (2005). The aging of sparkling wines manufactured from red and white grape varieties (POZO-BAYON *et al.* 2003) and different copigmentation models by interaction of anthocyanins and catechins play during the aging process of wine important role (MIRABEL *et al.* 1999, ESPARZA *et al.* 2004, MONAGAS *et al.* 2005). Phenolic content and antioxidant activity could be also affected by storage conditions or conventional or ecological way of wine production (ZAFRILLA *et al.* 2003). To determine the importance and study factors influencing total polyphenol content (TP) and antioxidant antiradical activity (AAA) of red and white wines from different wine growing areas of Czech Republic, different viticulture, vinification and maturation processes of five white grape varieties and four red varieties were studied.

2 Material And Methods

2.1 Grape and wine samples

Five grape varieties for white wines production (Müller Thurgau, Moravian Muscat MOPR, Pinot Blanc, White Riesling, Traminer) and four grape varieties for production of red wines (Saint Laurent, Blauer Portugieser, Pinot Noir, Zweigeltrebe) from three wine production areas of Czech Republic (Kutná Hora, Mělník, Žernoseky) from the harvest 2004 were investigated. Samples were analysed in dates given in **Figures 1-4** in three parallel determinations. White varieties were immediately after harvest in October fermented, while red varieties were during October after harvest macerated and mashed and only after this procedure step fermented (both till the end of the year 2004). In the period January – March 2005 the wines maturated and in April they were bottled.

2.2 Determination of total polyphenol content

For the determination of total polyphenols (TP) adjusted method with Folin-Ciocalteau´s reagent was used. 1 mL of sample was pipetted into 50 mL volumetric flask and diluted with distilled water. Then 2.5 mL of Folin-Ciocalteau´s reagent was added and after agitation 7.5 mL of 20% sodium carbonate solution was added. After 2 hours standing at laboratory temperature absorbance of samples was measured on the spectrophotometer Heλios γ (Spectronic Unicam, GB) at wavelength λ=765 nm against blank. Extract of seeds was diluted before measuring at 1:50 ratio. Results were expressed as gallic acid

(in mg/kg dry matter – DM and in the case of must mg/L fresh must, gallic acid Merck, D). Average results were obtained from three parallel determinations.

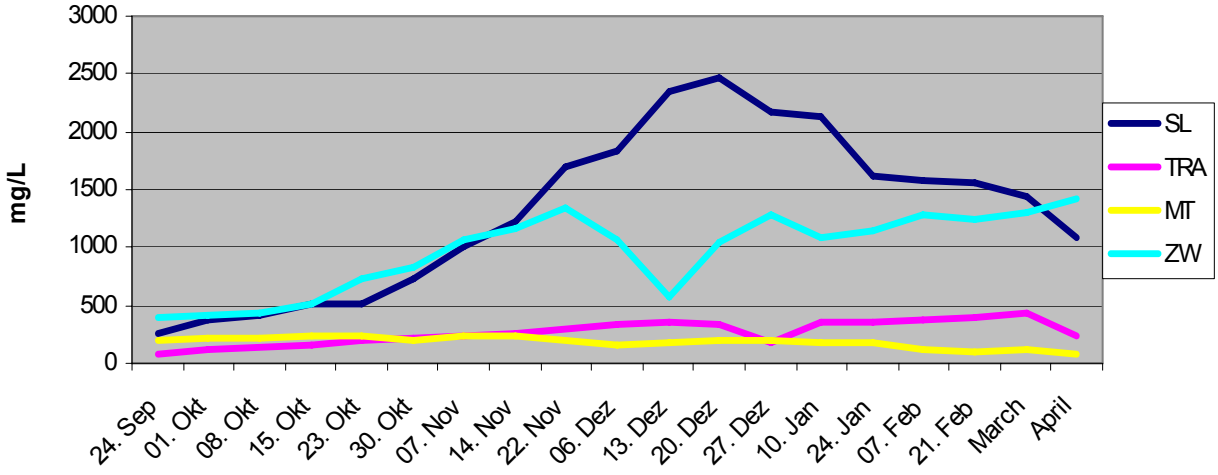

Figure 1: Content of total polyphenols during winemaking in wines from area Kutná Hora

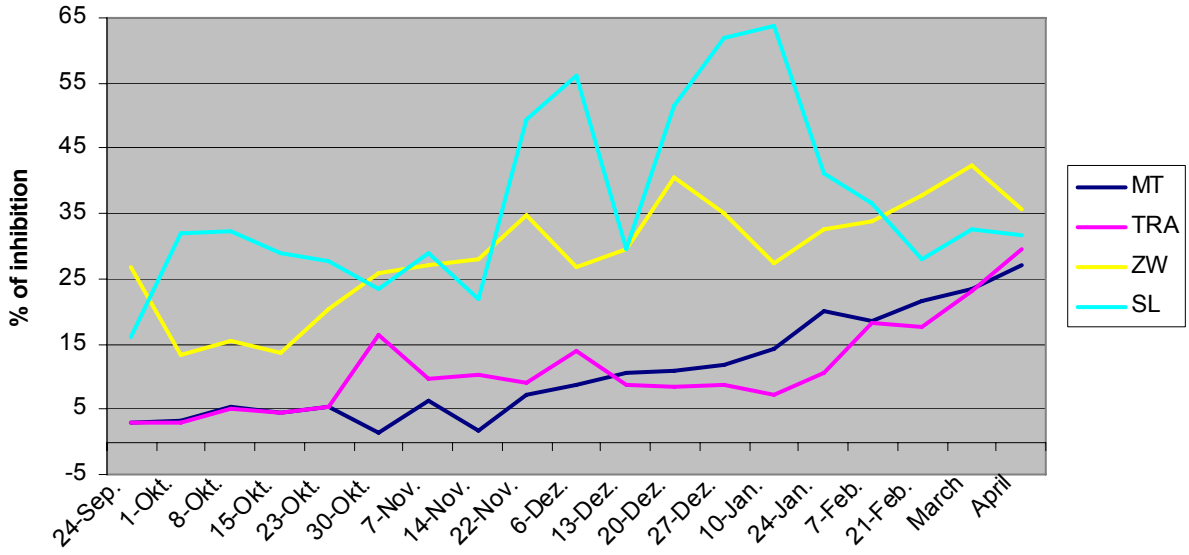

Figure 2: Content of total polyphenols during winemaking in wines from area Mělník

2.3 Determination of antioxidant antiradical activity (AAA) by DPPH method

AAA was measured after the reaction with free stable radical 1,1-diphenyl-2-picrylhydrazyl (DPPH·) according to MOLYNEUX (2004). Fresh solution of DPPH in concentration of 25 mg DPPH in 1 L of methanol should be prepared before the determination. 3 mL of violet DPPH·solution is pipetted into plastic cuvettes of 10 mm length and absorbance at wavelength λ = 515 nm on the spectrophotometer Heλios γ (Spectronic Unicam, GB) is measured. Then 5 μL of sample extract is added and after stirring with

the hand stirrer in cuvettes the reaction mixture is left to stand for 5 min. The absorbance is again measured and AAA is calculated from the decrease of absorbance in % according to relation:

$$\% \text{ of inactivation} = 100-[(A_{t5}/A_{t0})x100] \quad (1)$$

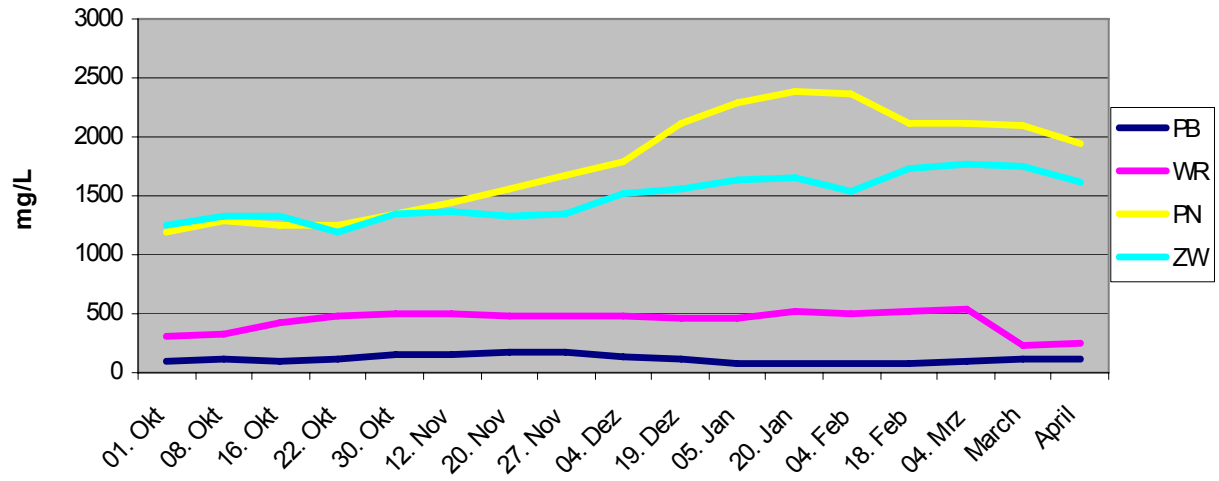

Figure 3: Changes of antioxidant antiradical activity of wines during winemaking from area Kutná Hora

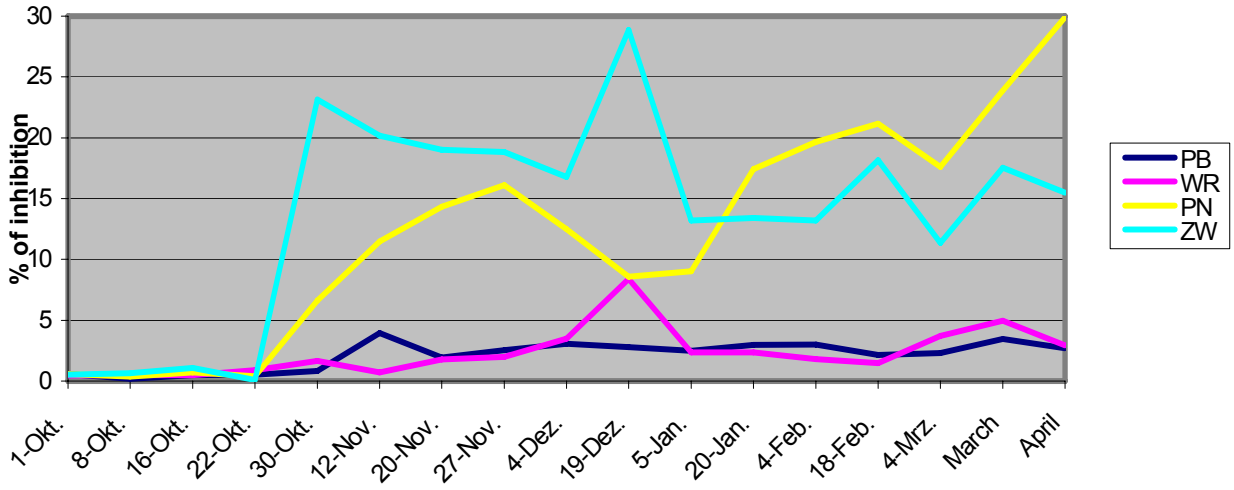

Figure 4: Changes of antiradical activity during wine making in wines from area Mělník
*MT – Müller Thurgau; SL – Saint Laurent; PB – Pinot Blanc; WR – White Riesling; PN – Pinot Noir; ZW – Zweigeltrebe; TRA – Traminer

Calibration curve of ascorbic acid (Sigma), tannic acid (Fluka) and gallic acid (Merck) were made. Results were expressed as % of inactivation and calculated to the concentration of standard AA (mg/mL), which could provide the same inactivation as studied sample. Results were obtained from seven parallel determinations.

2.4 Statistic evaluation

Statistic evaluation of obtained results was made by Statistica programme by the analysis of variance with multiple grouping. More detail evaluation was performed by Scheffé test at α = 0.05 and multiple regression analysis.

3 Results and Discussion

Significant differences in TP content (**Table 1**) among varieties were found after harvest (white varieties in av. 187.9 mg.L^{-1}, red var. 666.2 mg.L^{-1}. According to technological different winemaking procedures of white and red wines (in white wine vinification mashing is lacking) it was found, that at the end of wine making process red wines contained in av. 1425.6 mg.L^{-1} TP, whereas white wines only 161.6 mg.L^{-1}. Thus red wines contained in av. 2 times more TP in comparison with grape must at the beginning of winemaking, whereas TP content decreased to 86% of origin content in grape musts. The highest TP contents were found in Pinot Noir (1935 mg.L^{-1}), Zweigeltrebe (1522.2 mg.L^{-1}) and Blau Portugieser (1317.6 mg.L^{-1}). Analysis of variance (Scheffé test) at level of significance P<0.05 showed statistically high significance between red and white wines in TP content (P=0.000), Zweigeltrebe and all other varieties (P=0.000 – 0.013), Saint Laurent and Blauer Portugieser from all other varieties except Pinot Noir. Differences among white varieties were not significant. Variance analysis among wine growing areas confirmed highly significant differences (P ranged in interval 0.000 – 0.041, Tab. 3). Higher values were found in Mělník area (Zweigeltrebe 1257.7 mg.L^{-1}) as compared with Kutná Hora area (Zweigeltrebe 387 mg.L^{-1}). These results confirm the suggestions of BURNS *et al.* (2001) that the extraction of the phenolics was influenced by vinification procedure, grape quality, and grape variety. We can confirm high influence of winemaking techniques on the polyphenolic composition as BUDIC-LETO *et al.* (2003, 2005) referred in specific Croatian wines.

Table 1: Variance analysis between varieties and TP content (Scheffé test)

Variety	⟨1⟩	⟨2⟩	⟨3⟩	⟨4⟩	⟨5⟩	⟨6⟩	⟨7⟩	⟨8⟩	⟨9⟩
	390.15	1698.5	288.10	2315.5	116.41	436.79	1777.6	1211.1	263.52
1 Moravian Muscat		**0.0000***	0.9997	**0.0000***	0.9137	1.0000	**0.0000***	**0.0000***	0.9994
2 Saint Laurent	**0.0000***		**0.0000***	**0.0052***	**0.0000***	**0.0000***	0.9999	**0.0048**	**0.0000***
3 Müller Thurgau	0.9997	**0.0000***		**0.0000***	0.9863	0.9948	**0.0000***	**0.0000***	1.0000
4 Blauer Portugieser	**0.0000***	**0.0052***	**0.0000***		**0.0000***	**0.0000***	0.1254	**0.0000***	**0.0000***
5 Pinot Blanc	0.9137	**0.0000***	0.9863	**0.0000***		0.7929	**0.0000***	**0.0000***	0.9980
6 White Riesling	1.0000	**0.0000***	0.9948	**0.0000***	0.7929		**0.0000***	**0.0000***	0.9936
7 Pinot Noir	**0.0000***	0.9999	**0.0000***	0.1254	**0.0000***	**0.0000***		**0.0126***	**0.0000***
8 Zweigeltrebe	**0.0000***	**0.0048***	**0.0000***	**0.0000***	**0.0000***	**0.0000***	**0.0126***		**0.0000***
9 Traminer	0.9994	**0.0000***	1.0000	**0.0000***	0.9980	0.9936	**0.0000***	**0.0000***	

* Statistically significant at P<0.05

White and red wines differed significantly in TP content course during vinification process. In all measured cases from the preparation of must and its fermentation in October could be seen moderate increase followed by almost constant content during further fermentation and maturation (November – December 2004, January – February 2005), followed finally by moderate decrease in March – April 2005 during and after bottling. TP content changes in white wines during their vinification were insignificant. On contrary, the procedures of wine making of red wines are characterised by dramatic changes in their TP content. Maceration and mashing in October was characterised by moderate or medium TP increase, while during fermentation in November - December intense increase of TP occurred followed by constant content or its moderate decrease during January – March 2005 period (maturation of wine) and then decrease in April (bottling and aging.). As a final result an increase of TP and AAA esp. in red wines during vinification was found (Figures 1 and 2). As PELLEGRINI *et al.* (2000) suggested, aging is the main factor influencing the antioxidant activity and TP contents of wines. During maturation quantitative changes of catechins and oligomeric procyanidins were recorded (JORDAO *et al.* 2001). Relative constant total polyphenol content in our results is in accordance with results of ECHEVERRY *et al.* (2005), suggesting the relevance of qualitative changes of phenolics. It could be concluded that red and white wines differ not only in final contents of phenolics, but also in their extreme increase in red wines during fermentation. Different evolution patterns during aging depending on the grape variety were also confirmed by MONAGAS *et al.* (2005). Decrease is caused mainly by flavanols condensation reactions.

Another parameter investigated was antioxidant antiradical activity (AAA), which could be correlated with TP content. Statistically significant differences in AAA values were found in wine growing area, red and white wines and vine varieties (**Table 2**, **3**). Analysis of variance (Scheffé test) at level of significance P<0.05 showed statistically high significance between red and white wines in AAA content (P=0.000). AAA increased during wine making process, esp. in Zweigeltrebe, St Laurent and Pinot Noir wines

Table 2: Variance analysis between varieties and AAA (Scheffé test)

Variety	{1}	{2}	{3}	{4}	{5}	{6}	{7}	{8}	{9}
	3.385	29.070	7.073	16.573	2.108	2.348	12.373	21.634	11.183
1 Moravian Muscat		**0.0000***	**0.0000***	**0.0000***	0.9984	0.9997	**0.0000***	**0.0000***	**0.0000***
2 Saint Laurent	**0.0000***		**0.0000***	**0.0000***	**0.0000***	**0.0000***	**0.0000***	**0.0000***	**0.0000***
3 Müller Thurgau	0.2139	**0.0000***		**0.0000***	**0.0093**	**0.0184**	**0.0032**	**0.0000***	0.0590
4 Blauer Portugieser	**0.0000***	**0.0000***	**0.0000***		**0.0000***	**0.0000***	0.2315	**0.0088**	**0.0199**
5 Pinot Blanc	0.9984	**0.0000***	**0.0093**	**0.0000***		1.0000	**0.0000***	**0.0000***	**0.0000***
6 White Riesling	0.9997	**0.0000***	**0.0184**	**0.0000***	1.0000		**0.0000***	**0.0000***	**0.0000***
7 Pinot Noir	**0.0000***	**0.0000***	**0.0032**	0.2315	**0.0000***	**0.0000***		**0.0000***	0.9987
8 Zweigeltrebe	**0.0000***	**0.0000***	**0.0000***	**0.0088**	**0.0000***	**0.0000***	**0.0000***		**0.0000***
9 Traminer	**0.0000***	**0.0000***	0.0590	**0.0199**	**0.0000***	**0.0000***	0.9987	**0.0000***	

* Statistically significant at P<0.05

Table 3: Variance test between growing area and TP content or AAA (Scheffé test)

	TP			AAA		
Growing area	{1}	{2}	{3}	{1}	{2}	{3}
	1317.9	954.38	681.70	21.818	7.611	10.719
1 Žernoseky		**0.0056***	**0.0000***		**0.0000***	**0.0000***
2 Mělník	**0.0056***		**0.0411***	**0.0000***		**0.0005***
3 Kutná Hora	**0.0000***	**0.0411***		**0.0000***	**0.0005***	

* Statistically significant at P<0.05

(Figures 3 and 4), suggesting thus better AAA of wines compared with grape juices at the beginning of wine making process (ALCOLEA *et al.* 2003). The highest increase was determined during fermentation and maturation of wine. Multiple correlation coefficients between TP and AAA revealed significant correlations in Kutná Hora (R=0.4701) and Mělník (R=0.7379) wine-growing regions.

References

ALCOLEA J.F., CANO A., ACOSTA M., ARNAO M.B. (2003): Determination of the hydrophilic and lipophilic antioxidant activity of white- and red wines during the wine-making process. *Italian Journal of Food Science,* 15: 207-214

BUDIC-LETO I., LOVRIC T., VRHOVSEK U. (2003): Influence of different maceration techniques and ageing on proanthocyanidins and anthocyanins of red wine cv. Babic (*Vitis vinifera* L.). *Food Technology and Biotechnology,* 41: 299-303

BUDIC-LETO I., LOVRIC T., PEZO I., KLJUSURIC J.G. (2005): Study of dynamics of polyphenol extraction during traditional and advanced maceration processes of the babic grape variety. *Food Technology and Biotechnology,* 43: 47-53

BURNS J., GARDNER P.T., METTHEWS D., DUTHIE G.G., LEAN M.E.J., CROZIER A. (2001): Extraction of phenolics and changes in antioxidant activity of red wines during vinification. *Journal of Agricultural and Food Chemistry,* 49: 5797-5808

ECHEVERRY C., FERREIRA M., REYES-PARADA M., ABIN-CARRIQUIRY J.A., BLASINA F., GONZALES-NEVES G., DAJAS F. (2005): Changes in antioxidant capacity of Tannat red wines during early maturation. *Journal of Food Engineering* 69: 147-154

Esparza I., Salinas I., Caballero I., Santamaría C., Calvo I., García-Mina J.M., Fernández J.M. (2004): Evolution of metal and polyphenol content over a 1-year period vinification: sample fractionation and correlation between metals and anthocyanins. *Analytica Chimica Acta,* 524: 215-224

FAITOVÁ K., HEJTMÁNKOVÁ A., LACHMAN J., PIVEC V., DUDJAK J. (2004): The contents of total polyphenolic compounds and *trans*-reveratrol in white Riesling originated in the Czech Republic. *Czech Journal of Food Sciences,* 22: 215-221

Hurtado I., Caldu P., Gonzalo A., Ramon J.M., Minguez S., Fiol C. (1997): Antioxidative capacity of wine on human LDL oxidation in vitro: Effect of skin contact in winemaking of white wine. *Journal of Agricultural and Food Chemistry* 45: 1283-1289

JORDAO A.M., RICARDO-DA-SILVA J.M., LAUREANO O. (2001): Evolution of catechins and oligomeric procyanidins during grape maturation of Castelao Frances and Touriga Francesa. *American Journal of Enology and Viticulture,* 52, 230-234

MIRABEL M., SAUCIER C., GUERRA C., GLORIES Y. (1999): Copigmentation in model wine solutions: Occurrence and relation to wine aging. *American Journal of Enology and Viticulture,* 50: 211-218

MIZUTANI K., IKEDA K., KAWAI Y., YAMORI Y. (1999): Extract of wine phenolics improves aortic biomechanical properties in stroke-prone spontaneously hypertensive rats (SHRSP). *Journal of Nutritional Science and Vitaminology,* 45: 95-106

MOLYNEUX P. (2004): The use of the stable free radical diphenylpicrylhydrazyl (DPPH) for estimating antioxidant activity. *Songklanakarin Journal of Science and Technology*, 26: 211-219

MONAGAS M., BARTOLOME B., GOMEZ-CORDOVES C. (2005): Evolution of polyphenols in red wines from *Vitis vinifera* L. during aging in the bottle – II. Non-anthocyanin phenolic compounds. *European Food Research and Technology,* 220: 331-340

PELLEGRINI N., SIMONETTI P., GARDANA C., BRENNA O., BRIGHENTI F., PIETTA P. (2000): Polyphenol content and total antioxidant activity of Vini novelli (young red wines). *Journal of Agricultural and Food Chemistry,* 48: 732-735

POZO-BAYON M.A., HERNANDEZ M.T., MARTIN-ALVAREZ P.J., POLO M.C. (2003): Study of low molecular weight phenolic compounds during the aging of sparkling wines manufactured with red and white grape varieties. *Journal of Agricultural and Food Chemistry,* 51: 2089-2095

VALERO E., SANCHEZFERRER A., VARON R., GARCIACARMONA F. (1989): Evolution of grape polyphenol oxidase activity and phenolic content during maturation and vinification. *Vitis,* 28, 85-95

VINSON J.A., TEUFEL K., WU N. (2001): Red wine, dealcoholized red wine, and especially grape juice, inhibit atherosclerosis in a hamster model. *Atherosclerosis* 156: 67-72

VIVAR-QUINTANA A.M., SANTOS-BUELGA C., RIVAS-GONZALO J.C. (2002): Anthocyanin-derived pigments and colour of red wines. *Analytica Chimica Acta,* 458: 147-155

VRHOVSEK U., VANZO A., NEMANIC J. (2002): Effect of red wine maceration techniques on oligomeric and polymeric proanthocyanidins in wine, cv. Blaufrankisch. *Vitis,* 41: 47-51

ZAFRILLA P., MORILLAS J., MULERO J., CAYUELA J.M., MARTINEZ-CACHA A., PARDO F., NICOLAS J.M.L. (2003): Changes during storage in conventional and ecological wine: Phenolic content and antioxidant activity. *Journal of Agricultural and Food Chemistry,* 51: 4694-4700

This study was supported with Research Project of Ministry of Education, Youth and Sports of the Czech Republic MSM 6046070901.

Impact of Pulsed Electric Field Treatment on Polyphenolic Content of Grapes

A. Balasa, S. Toepfl and D. Knorr
Department of Food Biotechnology and Process Engineering, Berlin University of Technology, Germany

Abstract: *A novel process for Pulsed Electric Field (PEF) assisted enhancement of total polyphenolic content in grapes and grape products has been investigated. Total phenolic content has been measured in order to determine efficiency of PEF treatment as an external stimulus. Due to PEF induced permeabilization of cell membranes, higher yield of total polyphenolic content has been obtained. Copyright © 2006 IFAC*

1 Introduction

In recent years there has been an increased interest in natural antioxidants and their use in human health and nutrition. The importance of these compounds, characterized as plant secondary metabolites, does not only depend on their contribution to flavor and color characteristics of food, but also on their antioxidant characteristics, with mechanisms involving both free-radical scavenging and metal chelation. These mechanisms facilitate different biochemical and pharmacological effects contributing to human health. Polyphenolics are believed to play a significant role in preventing or delaying the onset of diseases including inhibition of human low-density lipoprotein oxidation, thereby decreasing the risk of heart diseases. Furthermore, they are claimed to have protective roles in carcinogenesis, atherosclerosis and thrombosis (GIRARD & MAZZA 1998).

The Pulsed Electric Field (PEF) treatment is a non-thermal food processing technology which involves application of short pulses of high electric field. Application of PEF can cause membrane permeabilization (electroporation) within very short time (in range of µs to ms) leading to formation of either permanent (irreversible permeabilization) or temporary (reversible permeabilization) pores (ZIMMERMAN 1986). Permeabilization of plant cells has been used to increase yield in the production of fruit juices (BAZHAL *et al*. 2001), or to enhance the extraction efficiency of intracellular metabolites (ESTHIAGHI & KNORR 2002, FINCAN *et al*. 2004, GUDERJAN *et al*. 2005). Industrial and agricultural residues are valuable source of natural antioxidants (MOURE *et al*. 2001). Grapes and grape products have been recognized as a rich source of polyphenolics (KAMMERER *et al*. 2005), which include phenolic acids, anthocyanins, flavonols, flavan-3-ols and tannins. Grape by-products obtained from the winemaking process contain large amount of phenolic compounds (BONILLA *et al*.

1999) that could be recovered as functional food ingredients. For the conventional extraction of these valuable compounds, organic solvents have been used, which are potential environmental and health hazard. Therefore, in the present study, the application of PEF treatment was used as an external stimulus followed by subsequent mild extraction with water. The aim of this research was not only to facilitate better extraction of polyphenolics from grape residues, but to also improve the quality of expressed juice by enhancing its nutritional value.

2 Materials and Methods

2.1 Raw material

Grapes (*Vitis Vinifera*, cultivar “Spät Burgunder”, vintage 2005) were obtained from the Sächsische Winzergenossenschaft Meissen e.G. (Meissen, Germany). Fresh samples have been stored in cold room environment at +4°C until treatment was preformed.

2.2 Pulsed Electric Field Treatment

Experiments were carried out with a high intensity pulsed electric field apparatus, connected as shown in **Figure 1**, with a maximum field strength of 20 kV. The grape samples were washed, weighed and placed in the treatment chamber between parallel stainless steel electrodes, with a gap of 7 cm. Grapes were hand squeezed to float in their own juice and pulsed with electric field strengths in the range of 0.5 to 2.4 kV/cm and 50 pulses, to induce cell permeabilization. After PEF treatment grapes were transferred to a 10L wine hand press (Vierka, Bad Königshofen, Germany) and pressed at ambient temperature in duration of 2 hours.

2.3 Extract preparation

Fifty grams of grape marc, obtained after pressing, were weighed and extracted with 200 ml of solvent (distilled water). The resultant mixture was shaken on a rotary shaker (150 rpm) for 2 hours at room temperature. To remove solids, subsequent filtration through glass wool was used.

2.4 Measurement of total polyphenols

Total polyphenolic content from both, fresh pressed juice and grape pomace extracts, was determined immediately using the Folin-Ciocalteu micro method modified by Waterhouse (http://waterhouse.ucdavis. edu/phenol/folinmicro.htm).

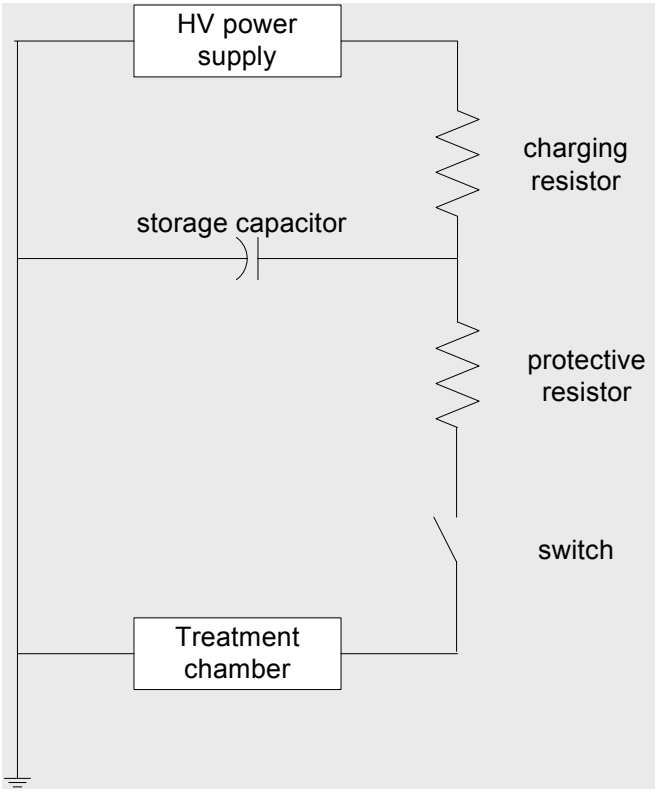

Figure 1: Schematic drawing of high intensity pulsed electric field apparatus

3 Results & Discussion

Efficiency of Pulsed Electric Field treatment was determined by measuring the yield of total polyphenolic content in fresh pressed juice and in grape pomace extracts. Results were expressed as milligrams per liter of Gallic Acid Equivalent (GAE) (**Figures 2** and 4). Polyphenolic content of both, grape pomace and grape juice, obtained from grapes treated with pulsed electric field has been shown to differ from untreated samples.

3.1 Effects of PEF on the total polyphenolic content of grape juice

Increase of total polyphenolic content in juice obtained from PEF treated grapes at field strength of 2.4 kV/cm was 28%, in comparison to untreated samples (Figure 2). Pores formed within the cell membrane seemed to enhance mass transfer out of the cells. Increase of total polyphenolic content of 22 and13% respectively, was reached when field strengths of 1 and 0.5 kV/cm were used (Figure2). Higher content of total polyphenolics in juice occurred with increasing electric field strength (**Figure 3**).

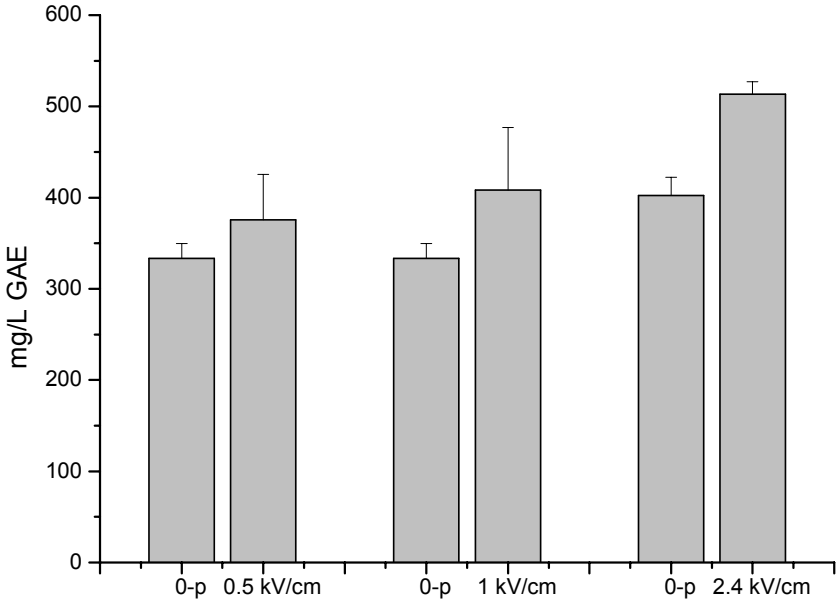

Figure 2: Total polyphenolic content of fresh pressed grape juice obtained from grapes treated with different PEF strengths (0-p: reference value)

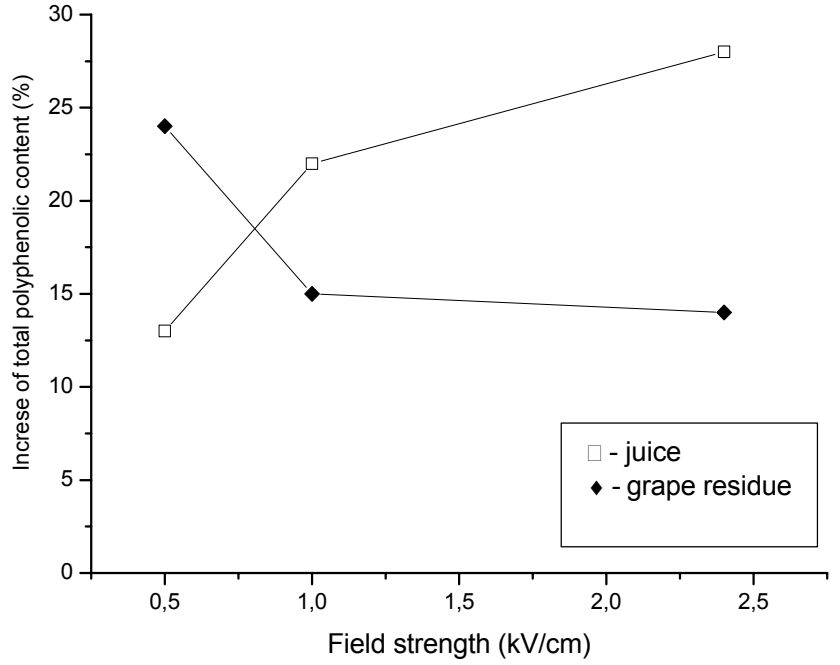

Figure 3: Increase of total polyphenolic content of grape juice (□) and grape pomace extracts (♦) obtained from grapes treated with different PEF strengths

Application of electric field pulses induced permeabilization of cell membranes which resulted in increased release of polyphenolics in juice. Enhanced permeabilization mechanism is responsible for increased diffusion and higher content of polyphenolics in juice treated with higher electric field strength.

3.2 Effects of PEF on the total polyphenolic content of grape pomace extracts

In addition, increase in total polyphenolic content of grape pomace of 14, 15 and 24% respectively was reached when field strengths of 2.4, 1 and 0.5 kV/cm were used (**Figure 4**). The higher yield indicated that transport process through permeabilized cellular membrane was facilitated. The highest yield increase occurred at the lowest field strength used (Figure 3).

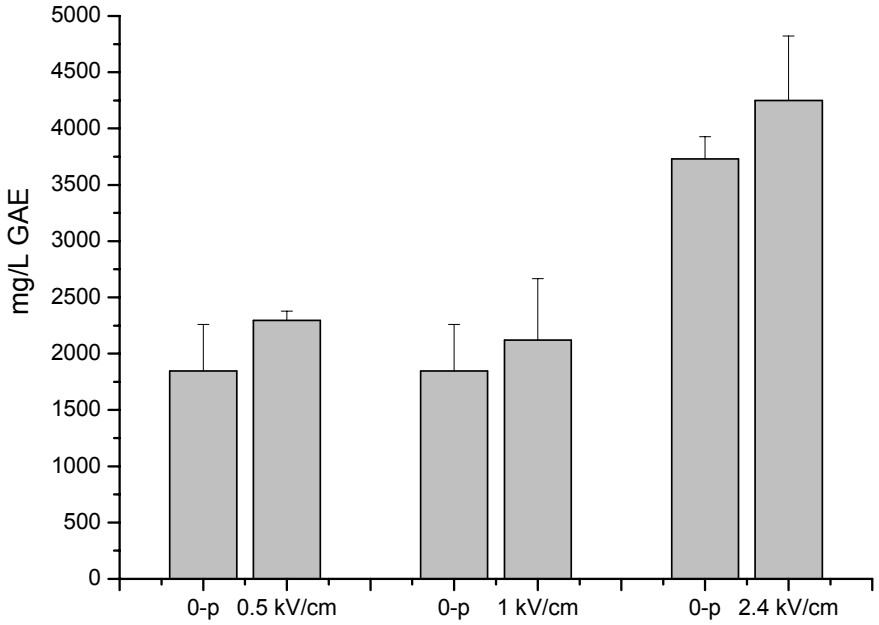

Figure 4: Total polyphenolic content extracted from grape pomace obtained from grapes treated with different PEF strength (Results were calculated as mg/L GAE on 1g of dry matter)

Comparing total polyphenolic content in juice and grape residue obtained from the same grape sample treated with PEF strength of 2.4 kV/cm, it was noticed that the juice had the highest total polyphenolic content, while the lowest polyphenolic content was observed in grape residue extracts. On the other hand, while pulsing with electric field strength of 0.5 kV/cm, less polyphenolics diffused in the juice and higher total polyphenolic content occurred in the grape residue extract. Reason for this phenomenon could be explained with the degree of cell membrane permeabilization, which most likely liberates intracellular compounds so that they can migrate into the external medium. Another reason for that increase could be a stress induction of the cells, followed by additional production of polyphenolics, as a plant response. Further investigation which involves enzyme activities and cell disintegration is necessary for a complete understanding of this phenomenon.

4 Conclusion

PEF treatment was found to be an effective pretreatment method for juice enrichment with polyphenolics. Simultaneously enhanced extraction of these valuable compounds from grape residue was reached. Therefore, extraction of specific cell metabolites via PEF treatment could be an alternative method for the recovery of polyphenolic compounds from "waste" products and as well nutritional quality of pressed juice by enhancing total polyphenolic content could be improved.

References

BAZHAL M.I., LEBOVKA N.I., VOROBIEV E. (2001): Pulsed Electric Field Treatment of apple tissue during compression for juice extraction. *Journal of Food Engineering*, 50: 129-139

BONILLA F., MAYEN M., MERIDA J., MEDINA M. (1999): Extraction of phenolic compounds from red grape marc for use as food lipid antioxidants. *Food Chemistry*, 66: 209–215

ESTIAGHI M.N., KNORR D. (2002): High electric field pulse pretreatment: potential for sugar beet processing. *Journal of Food Engineering*, 52: 265-272

FINCAN M., DEVITO F., DEJMEK P. (2004): Pulsed Electric Field Treatment of solid-liquid Extraction of red beetroot pigment. *Journal of Food Engineering*, 64: 381-388

GIRARD B., MAZZA G. (1998): Functional Grape and Citrus Products. In: *Functional Foods: Biochemical and Processing Aspects* (Mazza, G. (Ed)), 139-191. Technomic Publishing Co. Inc., Lancaster, Pennsylvania

GUDERJAN M., TÖPFL S., ANGERSBACH A., KNORR D. (2005): Impact of pulsed electric field treatment on the recovery and quality of plant oils. *Journal of Food Engineering*, 67: 281-287

KAMMERER D., CLAUS A., SCHIEBER A., CARLE R. (2005): A Novel Process for the Recovery of Polyphenols from Grape (*Vitis vinifera L*) Pomace. *Journal of Food Science*, 70: 157-163

MOURE A., CRUZ J.M., FRANCO D., DOMÍNGUEZ J.M., SINEIRO J., DOMÍNGUEZ H., JOSÉ NÚÑEZ M., PARAJÓ C. (2001): Natural antioxidants from residual sources. *Food Chemistry*, 72(2): 145-171

ZIMMERMAN U. (1986): Electrical breakdown, electropermeabilization and electrofusion. *Rev. Physiol. Biochem. Pharmacol*, 105: 176-250

Evaluation of Modified Phototransistor as Radiation Sensor

A. Wójcicki and I. Farkas
Department of Physics and Process Control, Szent István University
Páter K. u. 1., H-2103 Gödöllő, Hungary
Tel.:+36 28 52-055, E-mail: Farkas.Istvan@gek.szie.hu

Abstract: *The aim of the recent study is to find simple, compact, moderate cost solar radiation sensor suitable for monitoring global solar radiation flux for application in solar devices. Among further requirements it was no need for special electronic interfacing for readout and mechanical durability of the sensor to withstand vibrations during transport and in-situ assembly and usage of the drier. A modified production phototransistor was considered for qualifying a sensor. Long term measurements of output of three types of phototransistor were carried out and the gathered data was evaluated in terms of possibility of best calibration to certified radiation sensor. The evaluated sensors had original as well as modified surface shape and surface structure. The properties of the sensors were compared to preset tolerances on measurement fidelity. In result the suitable types were chosen and others rejected. Additionally, as a result of this work a proposition for design of improved radiation sensor emerged. Copyright© 2006 IFAC*

Keywords: *solar radiation, sensor, solar dryer, greenhouse, measurement, calibration.*

1 Introduction

Since the 1973 energy crisis the renewable energy sources, and among it solar energy have gained increased importance. Persisting effort to investigate practical means to utilize solar energy have led to development of numerous technological advances and scientific progress in the use of renewable energy in general. Energy demanding post-harvest processes benefit from use of solar energy where possible. One important aspect in utilization of solar energy is monitoring of incoming energy to more precisely control the process and ensure optimal process parameters. There are several ways to measure incoming solar radiation or in other means ensure desired process parameters including use of thermal sensors, photovoltaic sensors, simple thermal devices like bimetal switch plates and auto regulating passive design. The present article investigates properties of production phototransistor as in-field device to sense amount of incoming solar radiation for use in solar driers and solar operated greenhouses (WOJCICKI 1999).

In the practical development of devices used for different post-harvest processing of various agricultural crops there is emerging need to more closely monitor the process parameters. This in effect may yield in better characteristics of finished product and/or shorter treatment terms. Among such are the parameters of the dried substrate, like substrate humidity, temperature and mechanical, chemical and optical parameters of the substrate, as well as the parameters of the agents involved in the process; temperature and humidity of the air, the air flux and the amount, direction and spectrum of the solar radiation involved in the process.

For practical reasons in the production version of the solar drier and the solar operated greenhouse there is comparatively less possibility for use of sophisticated, laboratory grade measurement devices for monitoring the drying process, which leads to two possible design variations: purely passive version of the device without other than human monitoring of the process and a ″smart″ version, equipped with sensors and accompanying controlling electronics suitable for in-field function.

Thermal sensors have wide scientific use for measuring solar radiation, partly because they are able of attaining accuracy of 2 % in steady-state solar radiation measurements (NAST 1983).

As noticed by Suehrcke and others (SUEHRCKE *et al.* 1990), thermal sensors used for measuring solar radiation, such as Eppley or Kipp and Zonen sensor, behave as a dynamic heat transfer and storage systems. As such, they are unable to follow rapid changes of radiation associated with cloud shadowed - clear transitions during partly cloudy conditions.

The rate of change of the radiation can complicate the intrapolation and extrapolation of the output of the radiation sensors (FORGAN 1995).This has effect on calibration of one sensor to another if they have different time response constants and can result in different measurement values depending on the sensor dynamic behaviour during shade to exposition transitions.

In addition the thermal offset has influence on the output of pyranometers, and gains more significance at low direct radiance values. Various recent studies like (REDA *et al.* 2005) were carried out to take the effect into account and correct the output.

It is also a rather important issue the regular calibration of the solar radiation sensors as it is discussed by KOCSIS *et al.* (2005).

As solar driers and solar operated greenhouses themselves behave as dynamic heat transfer and storage systems too, so to use the input data from one dynamic system: the sensor to monitor and adjust behaviour of other dynamic system: greenhouse, is a complex numerical calculation and modelling task. Therefore one can argue that exact knowledge of instantaneous incoming radiation rather than time averaged, dynamic value from a thermal sensor allows more practical estimation of process parameters in the greenhouse.

2 Layout of the Measuring Set-Up

Five different solar radiation sensors were mounted next to each other on the terrace of Physics Department of the Szent Istvan University, Gödöllő. The output of each sensor was monitored using Adam-4017 data acquisition module.

The sensors were and Eppley sensor - Black & White Pyranometer, photovoltaic radiation sensor, BPV-17 phototransistor, and two STK-1KL phototransistors of which one had glossy hemispherical and one flat matt outer surface **Figure 1**.

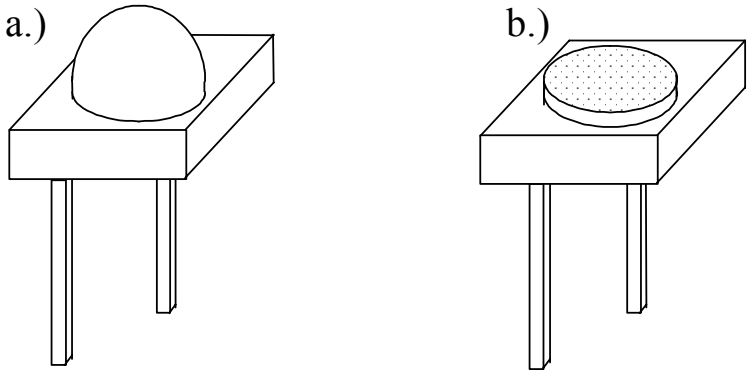

Figure 1: The shape of the hemispherical domed glossy (a.) and flat matt surfaced (b.) phototransistor head with cassis

The phototransistors (type BPV-17) were mounted in an electrical circuit showed in **Figure 2**, which was powered by a stabilised 5V power source. This an arrangement made it possible to attach the sensors directly to the input port of the data logger which was configured for input signals of 0-5V in amplitude on its ports.

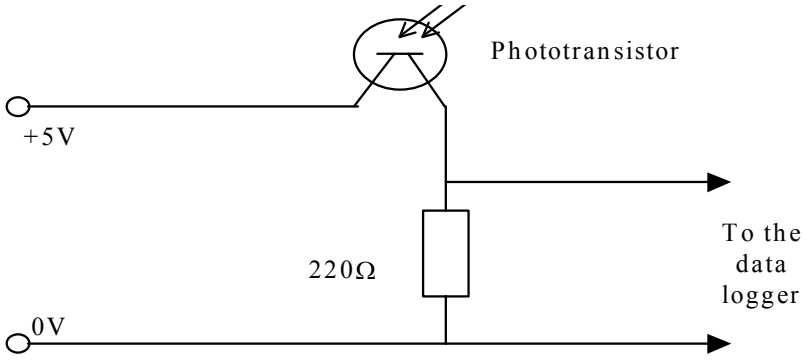

Figure 2: Schematic figure of the connection of the phototransistors to the data logging module

The output of the Eppley sensor having impedance of approximately 350 Ohms was directed to an 100x amplifier and collected by an Adam-4017 data acquisition module.

The Eppley sensor served as a reference - Black & White Pyranometer had a detector consisting of a differential thermopile with the hot-junction receivers blackened and the cold-junction receivers whitened. The sensor have built-in temperature compensation with thermistor circuitry which is to free the instrument from effects of ambient temperature.

According to the supplier's specifications the sensor operating in the temperature range -20 - +10 ^{o}C usually reach an linearity of about 1.5 % over ambient.

In the experiment two types of phototransistor were tested: STK-1KL type with maximal sensitivity at 940 nm, and BPV-17 with maximal sensitivity at 780 nm.

3 Results of the Measurements

The outputs of the sensors plotted against the reference sensor are shown in **Figure 3**. The phototransistor and photovoltaic sensor data is plotted against the irradiation values measured with a pyranometer.

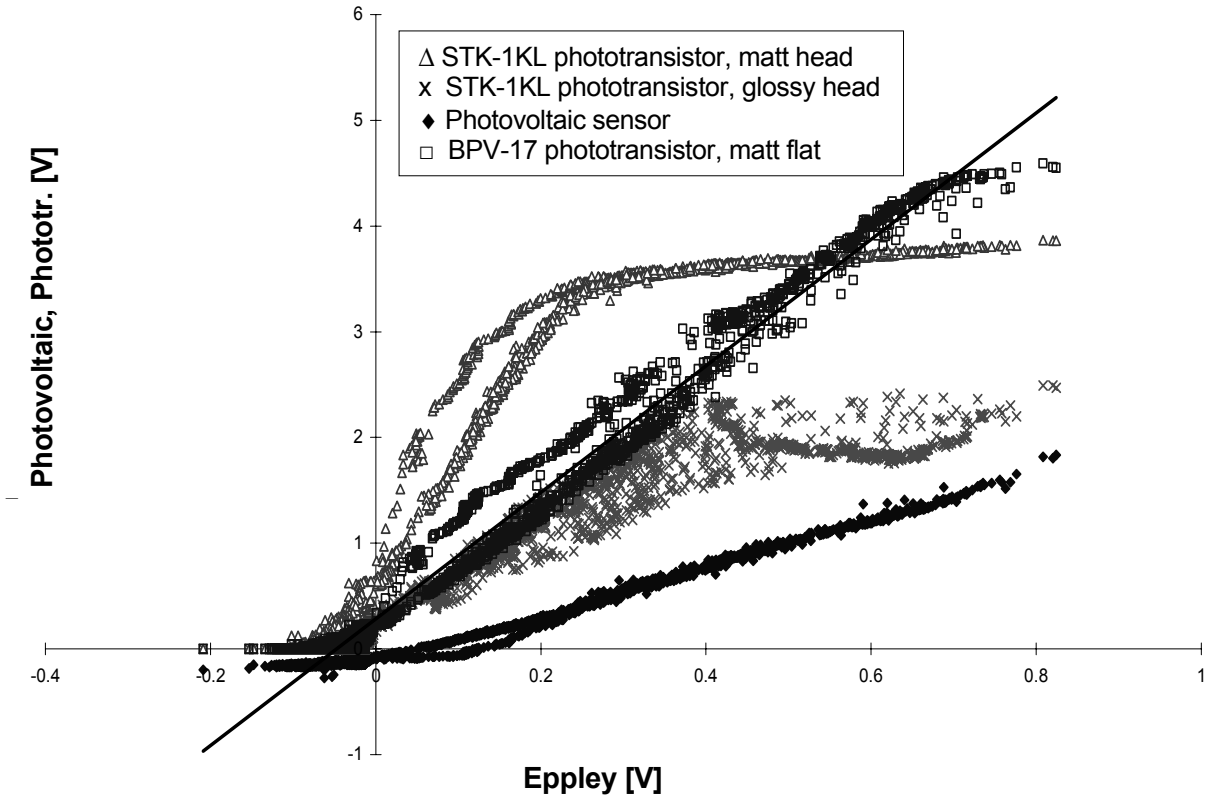

Figure 3: Output of four solar irradiation sensors plotted against the output of Eppley black and white pyranometer

As it can be seen, sensors with matt top surface, even without flat surface of the cassis, have better accuracy, probably due to neglecting the effects of the directional sensitivity of the measuring instrument.

The STK-1KL type phototransistors were saturated already at about 300 W m-2 total radiation (~0.2 V gived by Eppley sensor).

In Figure 3 substantial hysteresis of the sensors can be noticed. It is primarily due to the sensitivity temperature dependence of the phototransistors, causing the morning data show reasonably higher values than the real radiation. Another case is the spectrum change of the solar radiation during the day. An another reason could be the relatively long time coefficient of the Eppley pyranometer, causing hysteresis during partly cloudy conditions as an effect of cloud shadowed - clear transitions.

4 Conclusions

It can be concluded that the surface of the cassis of the phototransistor (gloss-matt) has big influence on the response of the sensor. Matt surfaced sensor could be more precisely calibrated. Above calibration data shows that production phototransistors can be calibrated to measure solar radiation values in certain spectra.

The shape of the phototransistor dome had big influence on the light directional sensitivity of the sensor, specially in case of glossy dome surface.

Both photovoltaic sensor and phototransistor showed temperature hysteresis which may need compensation. In case of photovoltaic sensor the maximal hysteresis was present in the low radiation range. The phototransistor showed higher amount of hysteresis in whole sensing range.

It can be deduced, that matt surface of the sensor helps distribute the incoming radiation more uniformly on the surface of the sensing semiconductor, thus helps avoiding development of areas of local saturation of the element coexisting with areas of shade.

As the measurements showed, all tested semiconductor sensors had nonlinear response, with more nonlinearity near top range (cropping) and low range (electron scarcity). It also means that the sensor as a whole has poor averaging capability to the incoming, non-uniformly distributed light, therefore it is beneficial to use such a surface which helps uniformly distribute the incoming radiation on the surface of the sensing semiconductor.

Further research using methods similar to (SCHOTLAND & COPP 1982) but perfomed on phototransistor can result in better estimation of the optical properties of the sensor head, its cosine error, differential polarization cosine error and the influence of the head properties on the measured radiation values.

Acknowledgements

The authors gratefully acknowledge for the technical and financial support of the German-Hungarian TÉT D-5/03 project.

References

FORGAN B.W. (1995): A New Method for Calibrating Reference and Field Pyranometers. *Journal of Atmospheric and Oceanic Technology*. Vol. 13, No. 3, pp. 638–645

KOCSIS L., FARKAS I., ELSNER B.V., TANTAU H.-J. (2005): Calibration of solar radiation measuring equipment, CD-ROM Proceedings of the 10th International Conference on Solar Energy in High Latitudes, NorthSun 2005,Vilnius, Lithuania, May 25-27, 2005, p. 8

NAST P.M. (1983): Measurements on the accuracy of pyranometers. *Solar Energy.* Vol. 31, pp. 279-283, Pergamon Press plc.

REDA I., HICKEY J., LONG C., MYERS D., STOFFEL T., WILCOX S., MICHALSKY J.J., DUTTON E.G., NELSON D. (2005): Using a Blackbody to Calculate Net Longwave Responsivity of Shortwave Solar Pyranometers to Correct for Their Thermal Offset Error during Outdoor Calibration Using the Component Sum Method. *Journal of Atmospheric and Oceanic Technology.* Vol. 22**,** No. 10, pp. 1531–1540

SCHOTLAND R.M., COPP J.D. (1982): Optical Properties of a Plastic Pyranometer Head. *Journal of Applied Meteorology*: Vol. 21, No. 5, pp. 735–739

SUEHRCKE H., LING C.P., MCCORMICK P.G. (1990): The dynamic response of instruments measuring instantaneous solar radiation. *Solar Energy.* Vol. 44 p. 145-148, Pergamon Press plc.

WOJCICKI A., FARKAS I., BIRÓ, A. (1999): Influence of shape structure on performance of plastic greenhouses, AGROTECH NITRA'99 International Conference, Nitra, Slovakia, September 8-10, Proceedings, Vol. 1, p. 63-70

Determination of Optimum Conditions for Half Fruit Drying Kinetics of Tomato

M. A. Hossain[1] and K. Gottschalk[2]
[1] Research Fellow and [2] Scientist
Department of Post Harvest Technology
Leibniz-Institut für Agrartechnik Potsdam-Bornim e.V. (ATB)
Max-Eyth-Allee 100, 14469 Potsdam, Germany
E-Mail: [1] ahossain@atb-potsdam.de [2] kgottschalk@atb-potsdam.de

Abstract: *Drying kinetics of half fruit tomatoes were investigated in a laboratory scale hot air dryer at an air velocity of 0.13 to 1.00 m/s and temperature range of 45 to 65°C to find out the optimum drying conditions. The selected tomatoes were Roma variety of medium size and weight. Moisture loss and shrinkage increased significantly with the increase in air temperature. But the value for green-red colour (a*) and lycopene content decreased significantly for increase in air temperature. Moisture loss increased with the increase of air velocity up to 0.75 m/s. Above this air velocity, moisture loss became independent of air velocity. Effect of air velocity was found insignificant on colour, lycopene content and shrinkage. The optimum drying air conditions was the temperature of 55°C and air velocity of 0.75 m/s, when both drying time and colour were considered. The moisture loss of over ripe tomato was found higher than that of optimum ripe and unripe (green) tomato. The experimental data were fitted to six different single layer drying models and the Midilli et al. model was found the best to predict the moisture content of tomato at different drying air conditions. Copyright © 2006 IFAC*

Keywords: *Air velocity, colour, moisture diffusivity, drying models, ripeness, shrinkage.*

1 Introduction

Tomato (*Lycopersicun esculentum* Mill.) is one of the most important vegetables in the world for its volume of production and its contribution to nutrition (KALOO 1993). Tomato is used in several forms and is widely used as a food ingredient. More than 80% of tomatoes are consumed in the form of processed products such as juice, paste, puree, ketchup, sauce etc.

Drying of tomato is carried out by open sun drying, solar drying or mechanical drying. Therefore, it is important to know the drying characteristics of tomato. The drying rate of tomato is closely associated with the drying air temperature, relative humidity and air velocity. One of the most important criteria of food is colour. Undesirable changes in the colour of food may lead to a decrease in consumers' acceptance as well as market value. So, it is essential to dry tomato in a suitable environment to produce a good qual-

ity dried products. The efficiency of the drying system can be improved by the analysis of the drying process. A generalized single layer tomato drying equation is therefore, needed for this purpose. The equation must be suitable for use at any temperature, relative humidity and air velocity of the drying air used in tomato drying.

Several thin layer drying models available in the literature for explaining thin layer drying characteristics of fruits and vegetables have been used by AFZAL & ABE (1999) for potato slices; KARATHANOS & BELESSIOTIS (1999) for fig; YALDIZ *et al*. (2001) for sultana grape; DANDAMRONGRAK *et al*. (2002) for banana; TOGRUL & PEHLIVAN (2003) for apricot and LAHSASNi *et al*. (2004) for prickly pear peel.

GIOVANELLI *et al*. (2002) studied the water diffusivity of tomato products at higher temperature (70-110°C), suitable for industrial drying. They calculated the apparent diffusivity including shrinkage of tomato products during drying. SACILIK *et al.* (2006) investigated the thin layer drying characteristics of half fruit organic tomato in solar tunnel drier. They fitted the experimental data to ten thin layer drying models and reported Approximation of diffusion equation was the best fitted model.

Little information is available in the literature on half fruit drying characteristics of tomato in single layer at different air temperature and air velocity without significant loss of colour. Therefore this work has been undertaken to study the half fruit drying kinetics of tomato in single layer, to evaluate the suitability of thin layer drying models and to optimise the drying conditions in terms of temperature, air velocity and colour.

2 Materials and Methods

2.1 Laboratory Dryer

The experiments of a single layer half fruit drying of tomato at various air temperature and air velocity were conducted in a laboratory scale dryer at the Leibniz-Institut für Agrartechnik, Potsdam-Bornim, Potsdam, Germany. The dryer mainly consisted of a blower, heating unit, plenum chamber, drying chamber, sample container, a digital balance and data logger. A thermostat was used to control the temperature and a controller was used to adjust the air velocity in the drying chamber. A series of sensors was inserted in the drying chamber to measure the air temperature and relative humidity. The sensors were connected with a PC via data logger for recording instantaneous data.

2.2 Sample Preparation

The fresh tomato of Roma variety (imported from the Netherlands) of medium size and weight aaccording to the classification of USDA (1991) was selected for this study. Before conducting each set of experiments, about one kilogram of fresh tomato was procured from a supermarket (Potsdam, Germany), washed with normal water, wiped and stored at

7-10°C and used within two weeks of purchase (LANA *et al*. 2005). For each experiment, a single half fruit tomato was used. The tomato was cut into halves with a sharp knife. Tomato was neither water blanched nor treated with any chemical before conducting the experiments.

2.3 Experimental Procedure

The ripeness of the tomato was determined by compression tests in term of hardness using Zwick Universal Testing Machine (type: BZ2.5/TS1S, Germany) with a flat plate probe was pressed on the full tomato with a constant speed of 2 mm/min. The deformation was calculated for 10 to 30% range of the rupture stress (FEKETE & FELFOLDI 2001). The stress and deformation were recorded during the test. From the results the rupture stress and the slope of the stress/deformation curve were determined. The colour of fresh and dried tomato surface was measured by a Minolta CR-300 Chromameter (Minolta Co., Japan) in L* (luminance), a* (red/green) and b* (yellow/blue) chromaticity coordinates using a Hunterlab colour difference meter. The colour was measured using CIELAB scale at D65 (Daylight–Neutral) illuminant. Though all the values L*, a* and b* were measured, the a* values were used which represents a measure of redness and greenness of tomato (HAHN 2002, SACILIK *et al*. 2006). Lycopene is an important carotenoid in tomato, which impart the red colour. Lycopene acts as an antioxidant during drying and storage of tomato. Due to the convenience and ease of using colour measurements instead of long, tedious and costly chemical methods, several studies (ZANONI *et al*. 1999, ARIAS *et al*. 2000) have correlated the colour with the lycopene content of tomato. The lycopene content of fresh and dried tomatoes were calculated using the following imperial equation (ZANONI *et al*. 1999).

$$LC = 0.67\,\frac{a^*}{b^*} - 0.04 \qquad (1)$$

Where, LC is Lycopene content (mg/g).

Thin-layer drying experiments were conducted at 45, 50, 55, 60 and 65 °C drying air temperatures and air velocity of 0.13, 0.25, 0.50, 0.75 and 1.00 m/s. Experiments were also conducted on different ripeness stages of tomato such as under, optimum and over ripe conditions. Before starting each experiment, all equipments were checked very carefully and were run for the required drying condition until the system had become stable. For each experiment a single half cut fruit with face upward was placed on the sample container in the drying chamber. Conditioned drying air flowed over and under the surfaces of tomato half and the weights, temperatures and relative humidity were recorded at every ten minutes with a data logger. The data-logging interval was adjusted at 10 minutes. The air off period for data recording was set at 30 seconds. After 9 minutes 30 seconds, the

blower was automatically off and the balance became stable and data was recorded in still air in 10 seconds. The initial moisture content of fresh tomato was determined by gravimetric method (AOAC 1975). Before and after completion of each experiment, the length, width, thickness and colour of half fruit tomato were measured.

2.4 Data Analysis and Model Development

Six commonly used thin layer drying equations (**Table 1**) available in the literature were used to fit the experimental data by the direct least square method using SPSS 9.0 software. The static equilibrium moisture content was obtained from the works of HUDA (2003).

Table 1: Different models used for experimental data fitting

Name of model	Model expression
1. Lewis	MR=exp(-kt)
2. Henderson and Pabis	MR=aexp(-kt)
3. Page	MR=exp(-kt^n)
4. Two term exponential	MR=aexp(-kt)+(1-a)exp(-kat)
5. Approximation of diffusion	MR=aexp(-kt)+(1-a)exp(-kbt)
6. Midilli *et al*.	MR=aexp(-kt^n)+bt

Where, $MR = \frac{M_t - M_e}{M_0 - M_e}$, M_t, M_0 and M_e are the moisture content at time t, initial moisture content and equilibrium moisture content respectively in kg/kg (dry basis). In the models, t is the drying time in minute, a, b, k and n are model constants. The equations were evaluated in terms of coefficients of determination (R^2) and root mean square errors (RMSE) in the following statistical forms:

$$R^2 = \frac{\left(\sum M_{\exp} M_{pred}\right)^2}{\sum M_{\exp}{}^2 \sum M_{pred}{}^2} \quad (2)$$

$$RMSE = \sqrt{\sum_1^N \left(\frac{M_{pred} - M_{\exp}}{df}\right)^2} \quad (3)$$

Where M_{exp} and M_{pred} represent the experimental and predicted moisture contents, df is degree freedom of regression model and N is the number of data points. Residuals of each model were plotted with experimental moisture contents. If residual plots indicate a

systematic pattern, the model should not be accepted (CHEN & MOREY 1989). A model was considered best when the residual plots indicated uniformly scattered points, RMSE at a minimum value and R^2 at a maximum value.

2.5 Moisture Diffusivity and Activation Energy

Fick's second law of the unsteady state diffusion, neglecting the effects of temperature and total pressure gradient, can be used to describe the drying behavior of fruits and vegetables as follows

$$\frac{\partial M}{\partial t} = Div\left(D\ grad\ M\right) \tag{4}$$

This equation can be solved for slab shape of the drying material as follows.

$$MR = \frac{8}{\pi^2}\sum_{n=1}^{\infty}\frac{1}{(2n-1)^2}\exp\left(-(2n-1)^2\frac{\pi^2 D_e t}{z^2}\right) \tag{5}$$

Where, D_e is the effective moisture diffusivity (m^2/s), t is drying time (s), z is half thickness of product (m) and n is number of order (1, 2, 3,…). For n=1, the Eqn (5) becomes

$$MR = \frac{8}{\pi^2}\exp\left(-\pi^2\frac{D_e t}{z^2}\right) \tag{6}$$

HAWLADER *et al*. (1991) proposed that z in Eqn (6) should be replaced with a modified thickness z´, related to the mass of sample by the following equation

$$\frac{z'}{z} = \left(\frac{W_t}{W_0}\right)^u \tag{7}$$

Where, W_0 and W_t are the mass of sample at time zero and t respectively, u is an index is obtained by optimising experimental data from $\ln[(M_t - M_e)/(M_0 - M_e)]$ as a function of t/z'^2. Then the Eqn (6) for modified thickness was fitted to the experimental data and the duffusivity was determined minimizing sum of squares of the deviations between the predicted and experimental moisture content.

The effective moisture diffusivity can be expressed by simple Arrhenius equation as a function of temperature as follows.

$$D_e = D_0 \exp\left(-\frac{E_a}{RT_a}\right) \quad (8)$$

Where, D_0 is constant equivalent to the diffusivity at infinitely high temperature (m^2/s), E_a is the activation energy (kJ/mol), R is the universal gas constant (8.314 $\times 10^{-3}$ kJ/mol K) and T_a is the absolute temperature. From Eqn (8), activation energy was calculated by non-linear regression analysis.

3 Results and Discussion

3.1 Effect of Temperature

The effect of air temperature on single layer drying of tomato is shown in **Figure 1**. Moisture loss increased with an increase in drying air temperature. There is no constant rate period of drying and drying took place only in the falling rate period. Time required for drying of tomato at 44.91, 51.13, 55.01, 61.06 and 64.30°C temperature were 101.67, 77.00, 61.00, 56.67 and 45.17 hours respectively. The increase in air temperature to accelerate the drying process is limited by the heat sensitivity of tomato. The effect of drying air temperature on colour and lycopene content of tomato is shown in **Table 2**. It is observed from the Table that due to drying, the colour and lycopene content of tomato decreased significantly from the fresh to dried tomato. This reduction is significant for the air temperature of 44.91 and 51.13 and highly significant for the temperature of 55.01, 61.06 and 64.30°C.

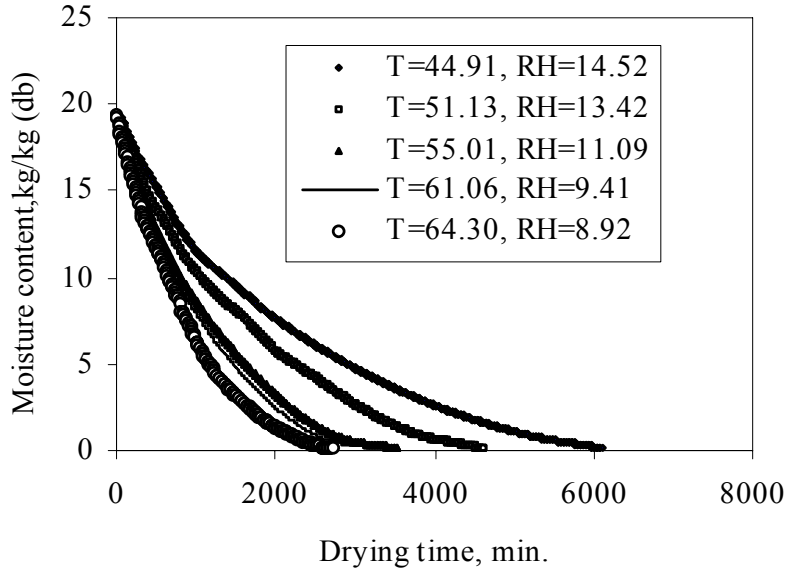

Figure 1: Single layer drying of tomato at different air temperatures (V=0.50 m/s).

Table 2: Variation of colour and lycopene content of tomato at different air temperatures

Temperature (°C)	Colour (a*)		Lycopene (mg/g)	
	Before drying	After drying	Before drying	After drying
44.91	23.01	21.51a	0.90	0.71a
51.13	22.14	19.11b	0.84	0.63b
55.01	22.51	17.98b	0.89	0.53c
61.06	22.53	12.87c	0.87	0.35d
64.30	22.11	9.11d	0.85	0.26c

There is significantly difference of colour and lycopene content after drying among the temperatures but for the temperatures of 51.13 and 55.01 °C the colour of dried tomato is statistically alike. ANDRITSOS *et al*. (2003) reported that lycopene content of tomato reduced with the increase of drying air temperature. But ZANONI *et al*. (1999) reported that lycopene content of tomato found stable during drying.

Values in the same row are significantly different from each other but values with the same letter in the same column are not significantly different at 1% level by DMRT.

3.2 Effect of Air Velocity

The effect of air velocity on the single layer drying of tomato is given in **Figure 2**. Moisture loss of tomato was faster at the higher air velocity and increased with the increase in air velocity. For an increase of air velocity from 0.12 to 0.75 m/s, the moisture loss of tomato increased but for an increase in air velocity from 0.75 to 1.00 m/s, the moisture loss was

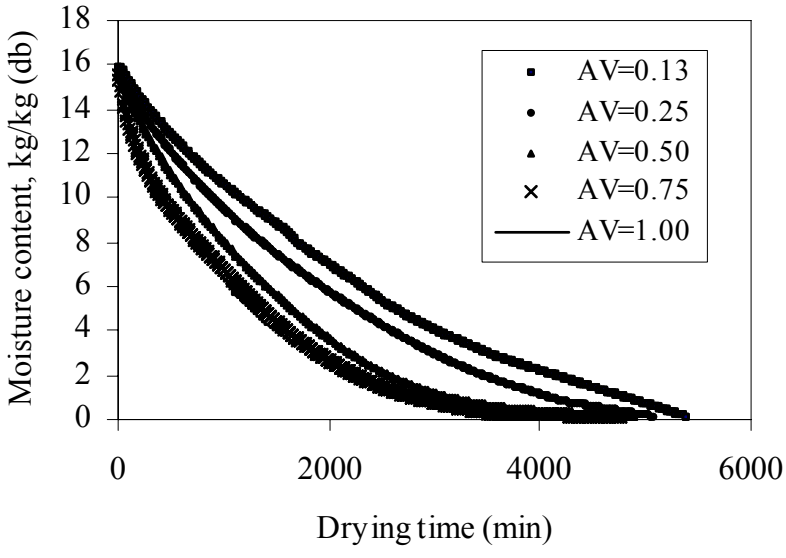

Figure 2: Single layer drying of tomato at different air velocities (T=50 °C, RH=10%)

almost constant. Time required for drying of tomato at 0.13, 0.25, 0.50, 0.75 and 1.00 m/s air velocity were about 89.83, 84.67, 81.5, 79.5 and 79.00 hours respectively. Hence, moisture loss became independent of air velocity for the value above 0.75 m/s. Air velocity above this value should be avoided to save energy. The effect of air velocity on colour and lycopene content of tomato is given in **Table 3**. There is no significant effect of air velocity on the red colour and lycopene content of tomato.

Values in the same column are not significantly different from each other but values with the different letter in the same row are significantly different at 1% level by DMRT.

Table 3: Variation of colour and lycopene content of tomato at different air velocities

Air velocity (m/s)	Colour (a*)		Lycopene (mg/g)	
	Before drying	After drying	Before drying	After drying
0.13	19.65	18.35	0.88a	0.62b
0.25	23.07	17.63	0.85a	0.57b
0.50	21.05	18.32	0.86a	0.59b
0.75	19.03	18.31	0.80a	0.56b
1.00	19.39	17.43	0.84a	0.55b

3.3 Effect of Ripeness

Effect of ripeness on drying rate of tomato is given in **Figure 3**. It is observed from the Figure that the over ripe sample dried faster than the optimum ripe and under ripe samples. This may due to that the cell walls and tissues of over ripe tomato became softer than optimum ripe and under ripe samples and hence the moisture diffusivity as well as drying rate became higher. The time required to reach final moisture content (about 15%, db) of over, optimum and under ripe samples were 39.83, 48.17 and 53.16 hours respectively.

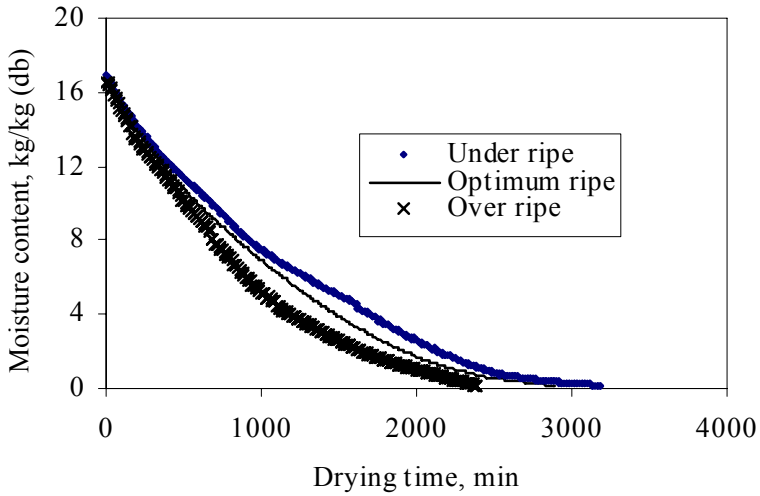

Figure 3: Half fruit drying characteristics of tomato at different ripeness stages

3.4 Optimisation of Drying Conditions

The drying air temperature, air velocity and ripeness were optimised based on the drying time and red colour value of dried samples. Scores were made based on the number of treatments. Lowest drying time got the highest score (5), highest drying time got the lowest score (1) and intermediated drying time got the intermediated scores ranged from 1 to 5. For colour, the scoring system was just opposite to drying time. The scores of drying time and red colour value of dried tomato samples at different drying conditions are tabulated in **Table 4**. It is observed from the Table that though the temperature 65°C got the highest score for drying time but it got the lowest score for colour. Similar scores were found for other temperatures, air velocities and ripeness. Hence, the overall drying conditions for optimum ripe half fruit tomato at the air temperature of 55 °C and air velocity of 0.75 m/s was the best when drying time, air velocity, ripeness and colour were considered. ANDRITSOS *et al.* (2003) reported that 50-55°C temperature is suitable for tomato drying for retaining colour and aroma in contrast to high temperature industrial drying (above 80°C) suffers from quality losses regarding colour and aroma and lead to case hardening.

Table 4: Scores of drying time and colour value of dried tomato samples at different drying conditions

Drying conditions		Drying time		Colour		Mean Score
		Hour	Score	a*	Score	
Temp (°C)	44.91	101.7	1.00	21.51	5.00	3.00
	51.13	77.00	2.18	19.11	4.03	3.11
	55.01	61.00	3.59	17.98	3.58	**3.58**
	61.06	56.67	3.98	12.87	1.52	2.75
	64.30	45.17	5.00	9.11	1.00	3.00
AV (m/s)	0.13	89.83	1.00	18.35	5.0	3.00
	0.25	84.67	2.38	17.63	2.08	2.23
	0.50	81.50	3.84	18.32	4.85	4.35
	0.75	79.50	4.77	18.31	4.78	**4.77**
	1.00	79.00	5.00	17.43	1.00	3.00
Ripeness	Un	53.16	1.00	-5.72	0.00	0.50
	Opt	48.17	1.87	16.69	3.00	**2.44**
	Over	39.83	3.00	9.28	1.67	2.33

3.5 Air and Tomato Temperatures

The drying air temperature, internal temperature, cut surface temperature and whole surface (on skin) temperature of half fruit tomato during single layer drying are shown in **Figure 4**. The drying air temperature was observed higher than the tomato temperature during the drying period. The whole surface temperature was found to be higher than the internal temperature followed by cut surface temperature but they were close to each other. At the beginning of the drying process, the tomato temperature was much lower than the drying air temperature. This is due to the evaporative cooling on the surface of the tomato. As the drying process proceeded, the moisture on the surface decreased and the evaporation zone moved from the surface into the tomato and evaporation took place mainly from the cut surface.

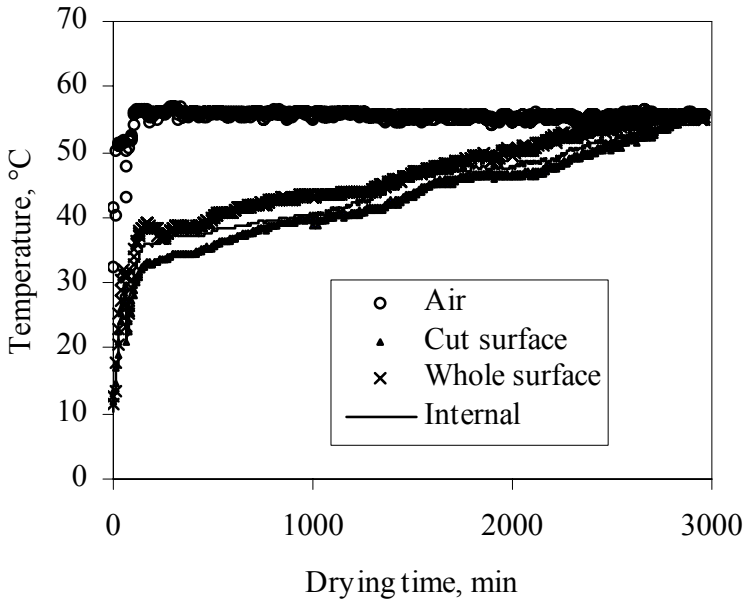

Figure 4: Temperature distribution at different position of a half fruit tomato during drying

3.6 Shrinkage

Volume, area and thickness shrinkages were calculated by direct measurement before and after drying of tomato samples. Effect of temperature on shrinkage of tomato is shown in **Figure 5**. Shrinkage took place linearly with the increase of temperature. Area shrinkage was found higher than thickness and volume shrinkage. There is no significant shrinkage observed due to air velocity. Over ripe sample shrinked more than the optimum and under ripe samples (**Figure 6**).

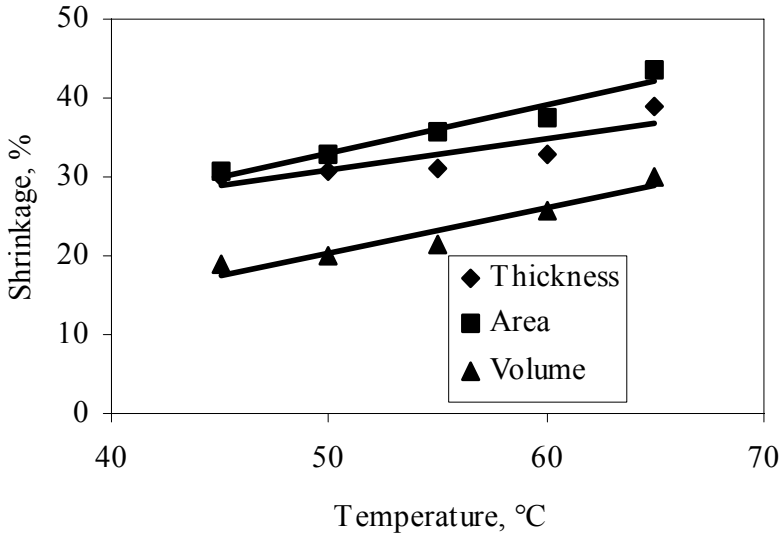

Figure 5: Effect of temperature on shrinkages of tomato

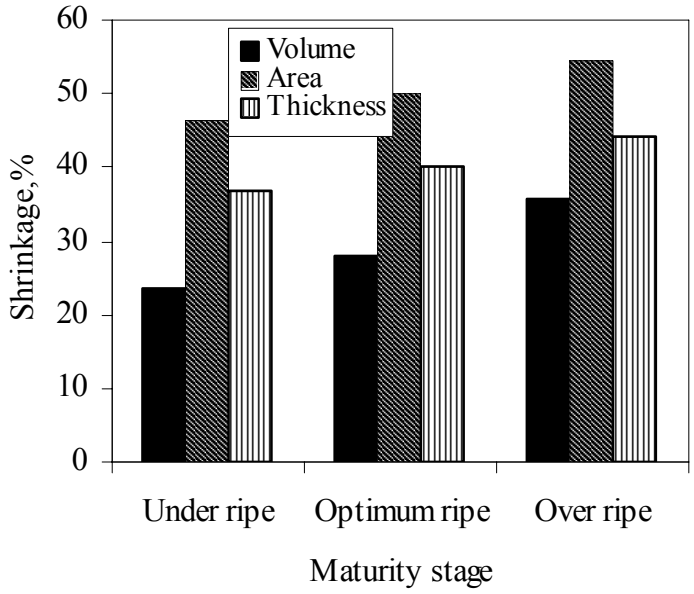

Figure 6: Effect of ripeness on shrinkages of tomato

3.7 Fitting of Experimental Data to the Models

Six thin layer equations were fitted to the experimental data for all experimental runs by direct least squares procedure. Average coefficient of determination (R^2), root mean square error (RMSE), grade and ranking of thin layer drying models at different air temperature and air velocity are presented in **Table 5** and **Table 6** respectively. From the Tables it is observed that MIDILLI *et al*. model gave the highest average R^2 and lowest RMSE followed by the Approximation of diffusion equation. Here, the highest R^2 and the lowest RMSE values indicated the lowest grade and the lowest ranked model are considered to be the best fitted model. Hence, MIDILLI *et al*. model got the lowest average grade and ranked one and Approximation of diffusion equation ranked two followed by two term exponential equation and Page equation.

Table 5: Average R^2, RMSE, grade and ranking of thin layer drying models at different temperatures

Models	R^2	RMSE	Grade	Ra nk
Lewis	0.9892	0.0288	5.9	6
Page	0.9952	0.0189	3.9	4
Henderson and Pabis	0.9910	0.0264	5.1	5
Approx. of Diffusion	0.9991	0.0083	1.6	2
Two term exponential	0.9934	0.0184	3.2	3
MIDILLI *et al.*	0.9995	0.0079	1.4	1

Table 6: Average R^2, RMSE, grade and ranking of thin layer drying models at different air velocities

Models	R^2	RMSE	Grade	Ra nk
Lewis	0.9892	0.0190	5.7	6
Page	0.9941	0.0141	4.4	4
Henderson and Pabis	0.9909	0.0186	4.8	5
Approx. of Diffusion	0.9972	0.0086	1.8	2
Two term expone ntial	0.9952	0.0121	3.4	3
MIDILLI *et al.*	0.9984	0.0070	1.1	1

Residual plots of different models for single layer drying of tomato is shown in **Figure 7**. For the MIDILLI *et al*. (2002) and the Approximation of diffusion models, the residual plots indicated a scattered pattern and the residuals are very close to X-axis leads to the interference that these models are suitable for predicting single layer drying of tomato. For other models, the residual plots indicated a systematic pattern and the residuals are not close to X-axis, which means that these models are not well fitted to experimental data. SACILIK *et al*. (2006) fitted the thin layer solar drying data of organic tomato in different thin layer models and reported that the Approximation of diffusion model was the best fitted model.

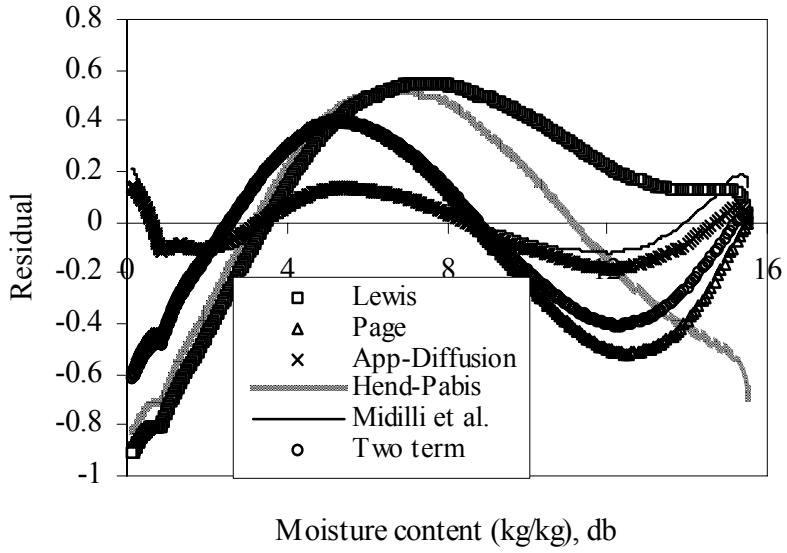

Figure 7: Residual plots of different models for single layer drying of tomato at T=50.87°C, RH=10.32% and AV=0.25 m/s

3.8 Development of models

Following regression equations were developed for the parameters of MIDILLI *et al* model as a function of temperature and relative humidity.

$a=1.454788-0.00393T+0.27268rh-0.04411rhT \quad (R^2=0.98)$ (9)

$b=-0.00016+2.25\times10^{-6}T+0.000924rh-1.41\times10^{-5}\,rhT \quad (R^2=0.99)$ (10)

$k=-0.005699+7.42\times10^{-6}T+0.044428rh-0.00171rhT \quad (R^2=0.99)$ (11)

$n=-0.61559+0.012895T-3,53225rh+0.214298rhT \quad (R^2=0.98)$ (12)

The parameters of MIDILLI *et al.* model at variable air velocities (0.13-1.00 m/s) are found to be a multiple function of air temperature, relative humidity and air velocities as follows.

$a=-373.65+7.71703T-173.601rh+17.3014V-168.013rhV \quad (R^2=0.99)$ (13)

$b=0.139496-.00287T+0.064258rh-0.00706V+0.06866rhV \quad (R^2=0.98)$ (14)

$k=-2.37436+0.048823T-1.05443rh+0.131201V-1.27387rhV \quad (R^2=0.99)$ (15)

$n=1678.467-34.5278T+764.7873rh-87.7295V+852.2098rhV \quad (R^2=0.99)$ (16)

Figures 8 shows the comparison the experimental and predicted moisture content from the MIDILLI *et al*. model. The predicted data mainly banded around the straight line which showed the suitability of the model in describing single layer drying behaviour of half fruit tomato. MIDILLI *et al*. (2002) fitted seven thin layer drying models to the experimental data of thin layer laboratory, forced solar and natural solar drying of mushroom,

pollen and pistachio. They reported that MIDILLI *et al*. model was the best fitted model among the tested models. MIDILLI *et al*. model is the modification of the Page model incorporating two more parameters. These additional parameters increased the flexibility and degree of freedom of the model for fitting ability of thin layer drying data.

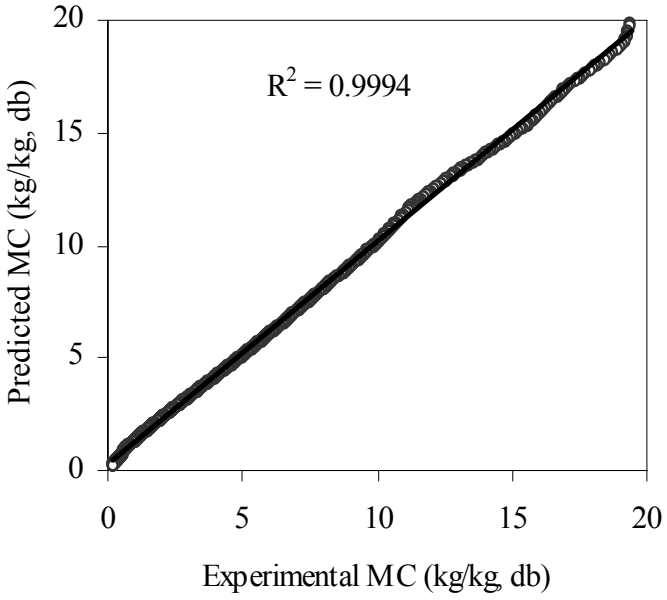

Figure 8: Experimental and predicted moisture content for single layer drying of tomato (T=44.91°C, RH=14.52%, V=0.50 m/s)

3.9 Moisture Diffusivity and Activation Energy

The effective moisture diffusivity of tomato increased linearly from 9.2214×10^{-9} to 2.1595×10^{-8} m^2/s as drying air temperature increased from 44.91 to 64.30 °C (**Table 7**). The effective moisture diffusivity of tomato also increased linearly from 8.3144×10^{-9} to 1.7072×10^{-8} m^2/s as drying air velocity increased from 0.13 to 0.75 m/s. For increased of air velocity from 0.75 to 1.00 m/s, the effective moisture diffusivity remained almost similar. GIOVANELLI *et al*. (2002) presented the effective diffusivity of tomato ranged from 2.3×10^{-9} to 9.1×10^{-9} m^2/s considering shrinkage. Again, SACILIK *et al*. (2006) reported the effective diffusivity of tomato neglecting shrinkage ranged from 1.07×10^{-9} to 1.31×10^{-9} m^2/s for solar and sun drying of organic tomato respectively.

During drying of tomato halves, an increase in air temperature increases diffusion and also increases shrinkage, but shrinkage reduces diffusion (HAWLADER *et al*. 1991). Since the first phenomenon is more substantial, the resulting effect of increase in air temperature the moisture diffusion increases which results in a drying rate increase.

The activated energy of tomato was calculated and found to be 37.72 kJ/mol. The activation energy value of tomato was in the range of values (15-40 kJ/mol) reported by RIZVI (1986) for various food materials such as green bean (37.716 kJ/mol), lettuce and cauliflower leaves (19.82 kJ/mol), Agaricus biporus (19.79 kJ/mol) and mushroom (23.59 kJ/mol).

Table 7: Moisture diffusivity of tomato at different air temperature and air velocity

Temp (°C)	AV (m/s)	Index u	Diffusivity (m^2/s)	R^2
44.91	0.50	0.702	9.2214×10^{-9}	0.943
51.13	0.50	1.016	1.1566×10^{-8}	0.922
55.01	0.50	1.343	1.6528×10^{-8}	0.929
61.06	0.50	1.471	1.8171×10^{-8}	0.931
64.30	0.50	1.922	2.1595×10^{-8}	0.929
50.76	0.13	0.814	8.3144×10^{-9}	0.911
50.87	0.25	0.891	1.0003×10^{-8}	0.919
50.86	0.50	1.024	1.3988×10^{-8}	0.939
50.64	0.75	1.094	1.7072×10^{-8}	0.970
50.76	1.00	1.148	1.7282×10^{-8}	0.965

4 Conclusions

Drying rate increased with an increase of drying air temperature. Air temperatures above 55°C affected significantly the red colour of tomato. The overall performance of the tomato dried at 55°C and was the best, when both drying time and colour were considered. Tomato should be dried at an air velocity equal to or just above 0.750 m/s. Above this air velocity, drying rate became independent of air velocity. There was no significant effect of air velocity on colour and shrinkage of tomato. Shrinkage of tomato increased with the increase of drying air temperature. The drying rate of over ripe tomato was found higher than that of optimum ripe and unripe (green) tomato. The experimental data were fitted to different single layer drying models and found that the MIDILLI *et al*. model was the best to predict the moisture content of tomato at different drying air conditions. The effective moisture diffusivity of tomato increased linearly from 9.2214×10^{-9} to 2.1595×10^{-8} m^2/s as drying air temperature increased from 44.91 to 64.30°C. The activated energy of tomato was calculated 37.716 kJ/mol. Hence, optimum ripe half fruit tomato may be dried at an air temperature of 55°C and air velocity of 0.75 m/s and MIDILLI *et al*. model may be recommended to describe the single layer drying of tomato.

Acknowledgement

The authors are thankful to Alexander von Humboldt Foundation, Germany for granting the Research Fellowship, Leibniz-Institut für Agrartechnik, Potsdam-Bornim, for providing working facility and Bangladesh Agricultural Research Institute, Gazipur for providing necessary leave.

References

AFZAL T.M., ABE T. (1999): Some fundamental attributes of far infrared radiation drying of potato. *Drying Technology*, 17: 137-155

ANDRITSOS N., DALAMPAKIS P., KOLIOS N. (2003): Use of geothermal energy for tomato drying. *GHC Bullein*, Mrach 2003: 9-13

AOAC (1975): *Official Methods of Analysis.* (12th ed.). Association of Official Analytical Chemists, Arlington, Virginia, USA

ARIAS R., LEE T., LOGENDRA L., JANES H. (2000): Correlation of lycopene measured by HPLC with the L*, a*, b* colour readings of a hydroponics tomato and the relationship of maturity with colour and lycopene content. *J. Agric. Food Chem.*, 48: 1697-1702

CHEN C., MOREY R.V. (1989): Comparison of four EMC/ERH equations. *Trans. of the ASAE*, 32(3): 983-990

DANDAMRONGRAK R., YOUNG G., MASON R. (2002): Evaluation of various pre-teatments for the dehydration of banana and selection of suitable drying models. *Journal of Food Engineering*, 55: 139-146

FEKETE A., FELFOLDI J. (2001): Determination of tomato ripeness by different test methods. *Proc. of the 6th International Symposium held in Potsdam on September 11-14, 2001.* Zude, M., B. Herold, and M. Geyer (Ed.), Institut für Agrartechnik Bornim e.V., 387-391

GIOVANELLI G., ZANONI B., LAVELLI V., NANI R. (2002): Water sorption, drying and antioxidant properties of dried tomato products. *Journal of Food Engineering*, 52: 135-141

HAHN F. (2002): Multi-spectral prediction of unripe tomatoes. *Biosystem Engineering*, 81(2): 147-155

HAWLADER M.N.A., UDDIN M.S., HO J.C., TENG A.B.W. (1991): Drying characteristics of tomatoes. *Journal of Food Engineering*, 14: 259-268

HUDA M.D. (2003): Air Flow Effects on Solar Drying. *PhD Thesis*, University of Newcastle upon Tyne, UK

KALOO G. (1993): Tomato. In: *Genetic Improvement of Vegetable Crops*. Kaloo, G. and B. O. Bergh (Eds), 645-666, Pergamon Press, Oxford, UK

KARATHANOS VAIOS J., BELESSIOTIS VSILIOS G. (1999): Application of a thin-layer equation to drying data of fresh and semi-dried fruits. *Journal of Agricultural Engineering Research*, 74: 355-361

LAHSASNI S., KOUHILA M., MAHROUZ M., IDLIMAM A., JAMALI A. (2004): Thin layer convective solar drying and mathematical modelling of prickly pear peel (*Opuntia ficus indica*). *Energy*, 29: 211-224

LANA M.M., TIJSKENS L.M.M., VAN KOOTEN O. (2005): Effects of storage temperature and fruit ripening on firmness of fresh cut tomatoes. *Postharvest Biology and Technology*, 35: 87-95

MIDILLI A., KUCUK H., YAPAR Z. (2002): A new model for single layer drying. *Drying Technology*, 20: 1503-1513

RIZVI S.S.H. (1986): Thermodynamic properties of foods in dehydration. In: Rao, M. A. and S. S. H. Rizvi (Ed.), *Engineering properties of foods* (pp. 190-193). Marcel Dekker Inc., New York

SACILIK K., KESKIN R., ELICIN A.K. (2006): Mathematical modelling of solar tunnel drying of thin layer organic tomato. *Journal of Food Engineering*, 73: 231-238

TOGRUL I.T., PEHLIVAN D. (2003): Modelling of drying kinetics of single apricot. *Journal of Food Engineering*, 58: 23-32

USDA (1991): *United States Standards for Grades of Fresh Tomatoes***.** United States Department of Agriculture, Agricultural Marketing Service, Washington DC

YALDIZ O., ERTEKIN C., UZUN H.I. (2001): Mathematical modelling of thin layer solar drying of sultana grapes. *Energy*, 26: 457-465

ZANONI B., PERI C., NANI R., LAVELLI V. (1999): Oxidative heat damage of tomato halves as affected by drying. *Food Research International*, 31(5): 395-401

A Simulation to Design Solar Dryer with Controlled Drying Air Conditions

B. M. A. Amer[1] and K. Gottschalk [2]

[1] Fac. of Agric., Cairo Univ. Egypt, Leibniz-Institut für Agrartechnik Potsdam-Bornim e. V. (ATB), Max-Eyth-Allee 100, 14469 Potsdam, Germany;
[2] Leibniz-Institut für Agrartechnik Potsdam-Bornim e. V. (ATB) Max-Eyth-Allee 100, 14469 Potsdam, Germany

Abstract: *A simulation of the drying process of fruits is presented for aiming to the design of a solar dryer. The drying profile of a fixed bed dryer has been simulated using a system of mathematical equations which describe the changes of the physical properties of the product, as well as the thermodynamic data of the drying air. The equations were solved using the thin-layer drying theory. Copyright © 2006 IFAC*

Key words: *solar dryer, design, simulation and controlled conditions.*

1 Introduction

The drying profile of fruits in dryers has been attempted in a previous work (AMER *et al.* 2003) based on the thin layer drying theory (AMER 1999). The results of this model were not satisfactory because it did not completely base on heat and mass balance. Also, there were some researchers such as: EXELL (1980), GRAINGER *et al.* (1981), SODHA *et al.* (1985), SHARMA *et al.* (1986), MAROULIS & SARAVACOS (1986), CHIRARATTANANON *et al.* (1988), RATTI & MUJUMDAR (1997), PRATOTO *et al.* (1997), BENNAMOUN & BELHAMRI (2003) and KARIM & HAWLADER (2005) which used the heat and mass balance to help in designing a solar dryer, but without using it to control the drying air conditions inside the dryer. Therefore, an improved and simplified model has been developed.

The main problem that should be faced was the fact that the a number of values of physical parameters as moisture content of fruits during drying are not constant due to the variation of drying air conditions during the drying process which in turn is caused by continuous variations in weather conditions and solar intensity.

Equations relating these parameters to drying condition variables, e.g. the moisture content, the temperature of the drying air, the drying air velocity and the relative humidity of the drying air, were developed to estimate the dimensions of the solar dryer. Also, this mathematical model has been developed using the heat and mass balance to control the drying air conditions inside the solar dryer and its storage unit.

The objective of this work was to introduce mathematically determined values of the aforementioned parameters into the equations, which describe the drying process of fruits.

2 Methodology of the Model

A set of mathematical equations is used to describe the drying process of a solar dryer of fruits under the following assumptions:

The change of bed volume during drying is negligible.

The solar collector walls are adiabatic, and some quantity of heat can be lost due to reflections of radiation from the glass.

The thermal processes at the chamber walls are adiabatic, with negligible heat capacity.

The heat capacities of moist air and of fruit are constant during short time periods.

The process can be considered as a one-dimensional problem.

The water temperature passing through the tube of the heat exchanger inside the solar drying unit equals the temperature of the tube surface.

2.1 Moisture to be removed from the fresh fruit

The moisture content of fresh fruits was determined by the vacuum oven drying method. Samples of the fresh fruit were dried in a vacuum oven at 70 °C until the weight of the dried sample became stable, according to A.O.A.C. (1984). It can be expressed as:

$$Mw_i = \frac{W_o - W_d}{W_o} \times 100 \qquad (1)$$

Mw_i moisture content, wet basis of the fresh fruit.
W_o weight of the fresh sample, (kg)
W_d weight of the dried sample, (kg)

Then, the total weight of moisture to be removed from the total weight of the fresh fruit is:

$$m_w = W_i \times \left[\frac{Mwi - Mwf}{100 - Mwf} \right] \qquad (2)$$

Where

m_w total weight of moisture to be removed from the fresh fruit, (kg).
W_i initial mass of the crop to be dried (kg)
Mw_f desired final moisture content of the fruit.

2.2 Energy Balance of the Drying process at the day time.

For controlling the drying air factors inside the solar dryer during the drying process, the heat and mass balance for the drying system should be used. It can be expressed mathematically

Heat gain "Q_U" = heat losses "Q_L" (3)

Energy requirements to evaporate moisture from the fresh fruits "Q_{L1}"

$$Q_{L1} = S + L_{total} \quad (4)$$

Q_{L1} Heat supplied to fruits
S Sensible heat to raise foodstuff temperature to the desired drying temperature
L Latent heat of water vaporization, (2400 kJ/kg).

$$S = W_i \times c_{p,\ fruit} \times (T_{f2} - T_{f1}) \quad (5)$$

$$L_{total} = m_w \times L \quad (6)$$

Where:

W_i the total initial weight of fruit to be dried, (kg).
m_w mass (weight) of water to be removed from the fresh fruit to be dried, (kg).

Heat loss for rejection of the moisture out of the solar drying unit "Q_{L2}".

$$Q_{L2} = \rho_a \ \dot{V}_{total} \ c_{p.a} \ (T_d - T_a) \times 35\% \quad (7)$$

Heat transfer by radiation from glass to outside the solar collector "Q_{L3}"

$$Q_{L3} = I \times 0.30 \quad (8)$$

Heat gain from the solar collector "Q_{U1}"

It is useful to determine the required air quantity to dry the agricultural product by the following method:

The total solar energy incident on the surface is:

$$I = I_T \ (\text{kW-hr/day.m}^2) \times 3600 \quad (9)$$

$$Q_{U1} = I \times \eta \quad (10\text{-a})$$

Where:

I_T total solar energy incident on the surface, (kW-hr /day.m^2)
I total solar energy incident on the surface, (kJ/day.m^2)
Q_{U1} total solar energy incident on the collector's surface (kJ/m^2)
η Efficiency of the solar collector (%)

Also, it can be expressed for the actual gain of the heat of the solar collector by another method:

$$\therefore Q_{U1} = I \times A \times t_s \quad (10\text{-b})$$

Q_{U1} actual gain of heat by the solar collector the total solar drying period for fruits (KJ)
t_s mean time of direct sun-shine period per day, (h)

The available heat gain from the quantity of recycled air "Q_{U2}":

The solar drying system will be working using a mixture of the ambient air and recycled air leaving the drying process, and the best of this mixture will be 35% ambient air and 65% recycled air (SAAD *et al.* 1992).

The available energy from the recycled air is determined as:

$$Q_{U2} = \rho_a \dot{V}_{total} c_{p.a} (T_d - T_a) \times 65\% \quad (11)$$

Q_{U2} available energy from the recycled air kJ/h
ρ_a density of drying air (kg/m^3)
m_a mass (or weight) of drying air (kg)
$c_{p.a}$ specific heat capacity of the air (kJ/kg.K).
T_i the ambient air temperature (^{o}C).
T_a the solar collector air temperature (^{o}C).
T_d the solar dryer air temperature (^{o}C).

Determination of the total air volume required for the whole drying process:

Determination of the quantity of air which is needed to heat the water to store in the water tank of the solar system:

$$V_{1,a} \times \rho_a \times c_{p,a} \times (T_d - T_i) = V_w \times \rho_w \times_{p.w} \times (T_w - T_i) \quad (12)$$

$$V_{1,a} = Q_w / \rho_a \times c_{p,a} \times (T_d - T_a) \quad (13)$$

Where

$V_{1,a}$ required air quantity to store heat in water
T_w the water temperature in storage tank (^{o}C).

The required quantity of air to evaporate the moisture from the fruits:

It can be determined by two methods;

the first method:

$$m_{2,a} \times c_{p.a} \times (T_d - T_f) = S + L_{total} \quad (14\text{-a})$$

or

$$V_{2,a} \times \rho_a \times c_{p.a} \times (T_d - T_f) = S + L_{total} \quad (14\text{-b})$$

$$V_{2,a} = (S + L_{total}) / (\rho_a \times c_{p.a} \times (T_d - T_f)) \quad (15)$$

Another method to determine the required quantity of air to remove the moisture of fruit outside the dryer is:

The air flow rate required for the drying operation may be estimated from three positions P_1 ,P_2 ,P_3 on the Psychrometric Chart, where: P_1 before heating, P_2 after heating and P_3 after adiabatic drying.

The difference between the two readings of the absolute humidity on the Psychrometric Chart is considered to be the quantity of moisture which can be carried away by one kilogram of air during the time interval Δt_i , from "t_{i-1}" to "t_i".

Since the fruit is placed on one layer (thin layer) of the drying tray the value of “i” can be considered as the same for the above three states of air.

From the Psychrometric Chart, it can be determined:

AH1 at T1 and RH1

AH2 = AH1 at T2 and RH2

AH3 at T3 and RH3

Where:

AH1 = absolute humidity of the air entering the drying system, (kg_{water} /$kg_{dry\ air}$).
AH2 = absolute humidity of the air entering the drying tray, (kg_{water} /$kg_{dry\ air}$).
AH3 = absolute humidity of the air coming out from the drying system, (kg_{water} /$kg_{dry\ air}$).

The required quantity of air to be able to remove the moisture to outside of the dryer will be:

$$m_{2,a} = m_w / (AH3_i - AH1_i) \quad (16)$$

$m_{2,a}$ required quantity of air to be able to remove the moisture outside the dryer ($kg_{dry\ air}$).

$$V_{2,a} = m_{2,a} \times V_C \quad (17)$$

V_C the specific volume of air (m^3/kg)

By using the mean of the drying time for fruits in hours, the rate of air which is required for drying can be determined as

$$\dot{V}_{2,a} = V_{2,a} / \text{N. of drying time} \quad (18)$$

Where:

$\dot{V}_{2,a}$ quantity of air to remove and evaporate water from the fruits (m^3/h)
$V_{2,a}$ volume of air to remove and evaporate the water from the fruits (m^3)
T_f the temperature of the fresh fruit (^{o}C).
w_c the width of the solar collector (m).
b_c the height of the solar collector (m).
u_c the air velocity inside the solar collector (m/s).

Hence,

$\dot{V}_{total} = \dot{V}_{1,a} + \dot{V}_{2,a} + \dot{V}_{3,a}$ (19)

$\dot{V}_{total}$ total quantity of air to remove and evaporate water from the fruits (m^3/h)

2.3 Dimensions of the solar collector:

Area of the solar collector:

$A_C = Q_L / Q_{U1}$ (20)

$\therefore$ air velocity inside the solar collector can be expressed as

$u_c = \dot{V}_{total} / A_C$ (21)

u_c air velocity inside the solar collector (m/s)

2.4 Heat exchanger heat transfer

This is known as Newton's Law of Cooling, and it can be expressed by the equation,

$q = h_s A (T_p - T_s)$ (22)

Where

h_s surface heat transfer coefficient,
T_c temperature of the fluid and
T_s temperature at the surface of the solid.

Applying the basic overall heat-transfer equations for the heat exchanger:

$q = UA \Delta T$ (23)

Following this reasoning, it may be seen that h_s can be considered as arising from the presence of another layer, this time at the surface, added to the case of the composite slab considered previously. The heat passes through the surface, then through the various elements of a composite slab and then it may pass through a further surface film. We can at once write the important equation:

$q = A \Delta T [(1/h_{s1}) + x_1/k_1 + x_2/k_2 + .. + (1/h_{s2})]$

$= UA \Delta T$ (24)

where

$1/U = (1/h_{s1}) + x_1/k_1 + x_2/k_2 + .. + (1/h_{s2})$

and h_{s1}, h_{s2} are the surface coefficients on either side of the composite slab,

x_1, x_2 ..... are the thicknesses of the layers making up the slab, and

k_1, k_2... are the conductivities of layers of thickness x_1, ...

The coefficient h_s is also known as the convection heat transfer coefficient

The overall coefficient *U* for a composite system, consisting of surface film, composite wall, surface film, in series, can then be calculated as in equation (25) from:

$$1/U = 1/(h_r + h_c)_1 + x_1/k_1 + x_2/k_2 + . + 1/(h_r + h_c)_2. \quad (25)$$

The water passing through inside tube of a good conductor, being heat transfer in air,

$$dQ = h_s A (T_s - T_p) dt \quad (26)$$

But this loss of heat cools the water in tube in accordance with the usual specific heat equation:

$$dQ = c_w \rho_w V dT \quad (27)$$

Where

c_w is the specific heat of the water in the tube,
ρ_w is the density of water and
V is the volume of the tube.

Since the heat passing through the surface must be equal the heat loss from the water inside tube, these two expressions for d*Q* can be equated:

$$c_w \rho_w V dT = h_s A(T_s - T_p) dt \quad (28)$$

Integrating between $T_s = T_1$ and $T_s = T_2$, the initial and final temperatures of the tube during the heat transfer period, t, we have:

$$- h_s At/ c_{p.w} \rho_w V = \log_e (T_2 - T_c)/(T_1 - T_c) \quad (29\text{-a})$$

or

$$(T_{w1}' - T_a)/(T_{w1} - T_a) = \exp(-h_s At/ c_w \rho_w V) \quad (29\text{-b})$$

or

$$(T_{a1}' - T_w)/(T_{a1} - T_w) = \exp(-h_s At/ c_w \rho_w V) \quad (29\text{-c})$$

By knowing of the dimensions of the solar drying unit, it is easy to know the dimensions of the heat exchanger as it has one length of its tubes equal the width of the solar collector. According to the diameter of the heat exchanger tube, distance between each two tubes according to connection curves and the length of the solar collector, it can be determined the number of the heat exchanger tubes.

$$N_t = l_c / x \quad (30)$$

$$t_a = x / u_c \quad (31)$$

t_a time needed to air passing above one tube (sec)
x distance between the centre of two tubes to the centre of next two tubes (m)

According to the number of tubes, the surface of the solar collector can be devided into slabs, with 4 mm width and 1.8 m length.

The area of solar collector for this time is

$$A_s = b \times l \qquad (32)$$

A_s area of solar collector from the centre of two tubes to the centre of next two tubes (m^2)

By using the heat balance between the heat added from the sun to the solar collector and the heat needed to raise the temperature of water passing through the tube of the heat exchanger inside solar collector, it can be determined from the difference of water temperature which comes from the solar radiation on the collector surface, assuming that the value of the solar radiation on the surface of the solar collector at the morning equals 20% from its maximum value and when the sun radiation will not fall perpendicular on the surface of collector

$$\Delta T_w = (Q_{U1} \times 0.2 \times t_a \times 3600 \times A_P) / (\dot{V}_w \times \rho_w \times c_{p.\,w}) \qquad (33)$$

ΔT_w the difference of water temperature before and after the solar radiation (°C)
A_P area of one tube inside the solar collector (m^2)

According to the rate between the area of one tube faced to the solar radiation and the rest of glass area the quantity of heat gain by solar radiation to air and water can be determined.

The new water temperature is:

$$T_{w1} = T_w + \Delta T_w \qquad (34)$$

T_w mean temperature of water in the morning time and at the beginning of the drying process (°C)

Similarly, the difference of air temperature caused by the solar radiation on the collector surface when air passing the first tube of the heat exchanger which contain water inside it, is calculated as:

$$\Delta T_a = (Q_{U1} \times 0.2 \times t_a \times 3600 \times (A_t - A_P)) / (\dot{V}_a \times \rho_a \times c_{p.\,a}) \qquad (35)$$

ΔT_a the difference of air temperature before and after the solar radiation (°C)

$$T_{a1} = T_a + \Delta T_a \qquad (36)$$

T_a mean temperature of air at the morning and the beginning of the drying process (°C)

But, there is heat transfer occuring during the contact between the air and the tube of water as (applying equation (29-c)):

$(T_{a1}' - T_w)/(T_{a1} - T_w) = \exp(-h_s A t / c_w \rho_w V)$

$T_{a1}' = [\exp(-h_s A t / c_w \rho_w V) \times (T_{a1} - T_w)] + T_w$ (37)

T_{a1}' actual new temperature of air passing inside collector (°C)

To determine the new temperature inside the water tube due to the heat transfer from the air passing over it, the heat balance of energy can be used.

In case of testing the solar drying unit without fruits:

$dq = \dot{m}_a c_{pa} dT_a + Q_{U2} = \dot{m}_w c_w dT_w + Q_{L2}$ (38)

$T_{w1}' = [((\dot{m}_a c_{p,a} dT_a) + Q_{U2} - Q_{L2})/(\dot{m}_w c_{pw})] + T_{w1}$ (39)

T_{w1}' actual new temperature of water passing inside tubes °C

In case of using the solar drying unit under conditions when loaded with plum fruits

$\dot{m}_a c_{p,a} dT_a + Q_{U2} = \dot{m}_w c_{p,w} dT_w + \dot{m}_f c_{p,f} dT_f + Q_{L2}$ (40)

$T_{w1}' = [((\dot{m}_a c_{p,a} dT_a) + (\dot{m}_f c_{p,f} dT_f) + Q_{U2} - Q_{L2})/(\dot{m}_w c_{p\,w})] + T_{w1}$ (41)

This seriesof equations were worked with Excel to determine the new air and water temperatures.

2.5 Energy balance of drying at the night period

The Energy Balance is expressed mathematically:

Heat gain Q_U' = heat losses Q_L' (42)

It was actually determined that the heat needed to evaporate the amount of moisture to be removed from the fresh fruit Q_{L1}' as equal to Q_{L1}. Also, heat transfers from water to raise the air temperature to the desired drying temperature Q_{L2}' equals Q_{L2}.

The energy available from the quantity of recycled air leaving the drying chamber and the air which is going again through the dryer Q_{U1}' equals Q_{U2}.

The energy available in the water storage of the solar energy and optionally heated by heating elements is Q_{U2}'.

In the time of sun-set the air temperature inside the drying unit is decreased due to the decreasing of the ambient air temperature. Then, the water temperature inlet to the first tube of heat exchanger inside the drying unit can be heated up by electric heating elements. The new water temperature is caused by the heat transfer occuring during the contact between the air and the tube of water and can be determined by applying equation (29-c)

$T_{a1}' = [\exp(-h_s A t / c_w \rho_w V) \times (T_{a1} - T_w)] + T_w$ (43)

By using the heat balance of energy, the new temperature of water tube due to the heat transfer with the air passing over it can be determined.

In case of testing the solar drying unit without fruits

$$dq = \dot{m}_a c_{p,a} dT_a + Q_{U2} = \dot{m}_w c_w dT_w + Q_{L2} \quad (44)$$

$$T_{w1} = [((\dot{m}_a c_{p,a} dT_a) + Q_{U2} - Q_{L2})/(\dot{m}_w c_w)] + T_{w1} \quad (45)$$

In case of using the solar drying unit under the conditions with loaded plum fruits

$$\dot{m}_a c_{p,a} dT_a + Q_{U2} = \dot{m}_w c_w dT_w + \dot{m}_f c_f dT_f + Q_{L2} \quad (46)$$

$$T_{w1} = [((\dot{m}_a c_{p,a} dT_a) + (\dot{m}_f c_f dT_f) + (Q_{U2} - Q_{L2}))/(\dot{m}_w c_w)] + T_{w1} \quad (47)$$

This series of equations were worked with Excel to determine the new air and water temperatures.

3 Results and Discussions

3.1 Determination of the quantity of water which must be removed from the fruit during drying

The intial moisture content of fresh plum fruits is around 87% (w.b.). Applying the equation no. (2) for plum fruits, taken W_i in range 32 kg gives:

$$m_w = 32 \times 0.825 = 26.4 \text{ (kg water)}$$

3.2 Energy balance of drying at the day time for the solar drying system

$S = 32 \times 3.8 \times (65 - 25) = 5472$ kJ

Since latent heat of evaporation at 65 °C is 2380 kJ/kg, it is:

$L_{total} = 26.4 \times 2380 = 62832$ kJ

$Q_L = 5472 + 62832 = 68304$ kJ

The required quantity of air to evaporate the moisture from fruits is

$V_{3,a} = 68304 / (65-25) = 1707.6$ m^3

This value of air volume can also be determined by using the Psychrometric Chart:

AH1=0.0115 kg_w/kg_{air} for T1 = 25°C and RH1 = 60% and T2 = 65°C and RH2 = 8%

AH3 =0.026 kg_w/kg_{air} for T3 = 35°C and RH3 = 75%

The required quantity of air to remove the moisture outside dryer will be:

$m_{2,\,a}$ = 26 / (0.026 – 0.0115) = 75.86 $kg_{dry\ air}$.

Average of V_C = 0.95 m^3/kg

$V_{1,\,a}$ = 75.86 × 0.95 = 72.07 m^3

Since the mean of drying time for half fruits of plums from laboratory experiments is 24 hours, then

$\dot{V}_{1,\,a}$ = 1707.6 / 24 = 71.15 m^3/h

When Cairo City, Egypt, is taken as an example, the total solar energy incident on the surface " I " is:

I = 5 kW-hr/day.m^2 = 18000 kJ/day.m^2

Assuming the efficiency of solar collector is 50%, and 30% from this heat is lost from the glass by radiation, the actual solar radiation on collector surface is

I_C = 18000 × 0.5 × 0.7 = 6300 kJ/m^2 per day

3.3 Determination of the air quantity which is needed to store in water the heat of the solar system

This required heat coming from solar energy through the day light time is stored in water and is used during the period from sunset until the sun shine in the next day, thus

Q_w = 0.5 × 4.19 × 1000 × (65 –25) = 83800 kJ

$V_{2,\,a}$ = 104750 / 1 × 1.005 × (65 –25) =2084.58 m^3

Since the direct sun-shine period is 10 hours per day, it is

$\dot{V}_{2,\,a}$ = 2084.58 / 10 = 208.5 m^3/h

There is some amount of heat loss in the air duct system as fan etc. and radiation. Also, there is some heat loss when rejecting the moisture inside the dryer. The total amount required to increase the total quantity of air forced by the fan is around 100 m^3/h

$\dot{V}_{total}$ = 71.2 + 208.5 + 100 ≈ 400 m^3/h

The available heat gain from quantity of recycled air:

Since the solar drying system is worked using a mixture of the ambient air and recycled air leaving the drying process and assuming the best of this mixture will be 35% ambient air and 65% recycled air (SAAD *et al.* 1992), the available energy from the recycled air is:

Q_{U2} = 1 × 4000 × 1 × (65-40) × 0.65 = 65000 kJ

3.4 Determination of the solar collector dimensions

The area of the solar collector which is needed to complete the drying requirements is

$A_C = (68304 + 83800 – 65000) / 6300 = 13.8\ m^2$

From the previous data, there are some choices to achieve the drying requirement

1. designing the area of the solar collector as 13.8 m^2
2. using the solar drying unit for more than 2 days with 5 m^2 as the area of the solar collector
3. storing a part of heat in water during the day time and also using an auxiliary heat resource at night period to complete the drying process continuously after using a solar collector area of 5 m^2 during the direct sun-shine period.

For saving construction costs and reducing drying time and considering the low cost of electricity in Egypt, it was found that the third choice is the most preferred one. Considering the dimensions of the solar drying system is (2.8 m $\times$ 1.8 m $\times$ 0.18 m) the cross section area of air passing inside the solar collector "A_C" is calculated as:

$A_C = 1.8 \times 0.18 = 0.32\ m^2$

Then, the drying air velocity inside the solar collector is

$\therefore\ u_c = \dot{V}_{total} / A_C = 400 / 0.32 = 1250\ m/h \approx 0.4\ m/s$

3.5 Heat transfer in the heat exchanger

Since the dimensions of the solar drying system is (2.8 m $\times$ 1.8 m $\times$ 0.18 m) the length of the tubes of the heat exchanger must be 1.8 m like the width of the solar collector. Also, as the a diameter of tube is 15 mm (0.015 m) and the distance between each one is 25 mm (0.025 m), then 70 tubes must be used to fill up the whole length of the solar collector, as is 2.8 m.

The distance from the centre between two tubes to the centre of the next two tubes is 40 mm (0.04 m). The air velocity inside the solar collector was determined as 0.4 m/s and then the time of air flow passing from the centre of 2 tubes to the centre of the next 2 tubes is

$t_a = 0.04 / 0.4 = 0.1\ sec$

The area of solar collector for this time is

$A_s = 0.04 \times 1.8 = 0.072\ m^2$

Since the mean of direct sun-shine period is 10 hours, the intensity is

$I = (6300 /10 \times 3600) \times 0.072 = 0.0126\ kJ/s$

By using the heat balance between the heat gained from the sun to the solar collector and the heat needed to raise the temperature of the water passing through the tube of the heat exchanger inside solar collector, the difference of water temperature can be determined. For the solar radiation on the collector surface it is assumed that the value

of the solar radiation on the surface of the solar collector in the morning time equals to 20% from its maximum value when it does not fall perpendicular on the surface of collector, hence

$\Delta T_w = 0.0008$ °C

(According to the rate between the area of tube faced to the solar radiation and the rest of glass area, it is considered that 62.5% of the solar energy is used to raise the temperature of the air passing through solar collector, and the rest of this energy, 37.5%, is used to raise temperature of the tube of the heat exchanger to store this heat inside water)

The mean temperature of air in the morning in Cairo, Egypt, when beginning the drying process is 25 °C, considering that the water temperature passing through the tube of the heat exchanger inside the solar drying unit equals the temperature of the air, then the new water temperature is:

$T_{w1} = 25 + 0.0008 = 25.0008$ °C

Similarly, the difference of air temperature due to the solar radiation on the collector surface, when air passing on the first tube of the heat exchanger which contain water, it gives:

$\Delta T_a = 0.0014$ °C

$T_{a1} = 25 + 0.0014 = 25.0014$ °C

Also, there is heat transfer occuring during the contact between the air and the tube of water.

Applying equation (29-b):

$h_s = 25$ W/ m^2 K, (Incropera and DeWitt, 1990),

$V = 3.14 \times 1.8 \times (0.015) / 4 = 0.00032$ m^3

$T_{a1}' = 25.0014$ °C

To determine the new temperature of water in the tube due to the heat transfer from the air passing over it, the heat balance of energy can be used.

In case of using the solar dryer without fruits

$T_{w1}' = 25.0008$ °C

In case of using the solar drying unit when loaded with plum fruits

$T_{w1}' = -0.00152 + 25.0014 = 24.9998$ °C

This series of equations were worked using Excel to determine the new air and water temperatures for each time step of 0.1sec.

It is shown in **Figure 1**, that during the sun-shine period and unloaded with fruits, the temperature of air passing through the solar drying unit can raise from 25 to 58 °C within 55

min. Due to the very slow velocity of water passing through the tubes of the heat exchanger, its temperature can raise from 15 to 55.8 °C , also within 55 min.

It is shown in **Figure 2**, when loading the solar drying unit with plum fruits during the sunshine period, the temperature of air passing through the solar drying unit can raise from 25 to 45 °C in 55 min. Due to the very slow velocity of water passing through the tubes of the heat exchanger inside the solar drying unit, its temperature can raise from 25 to 45 °C in 55 min.

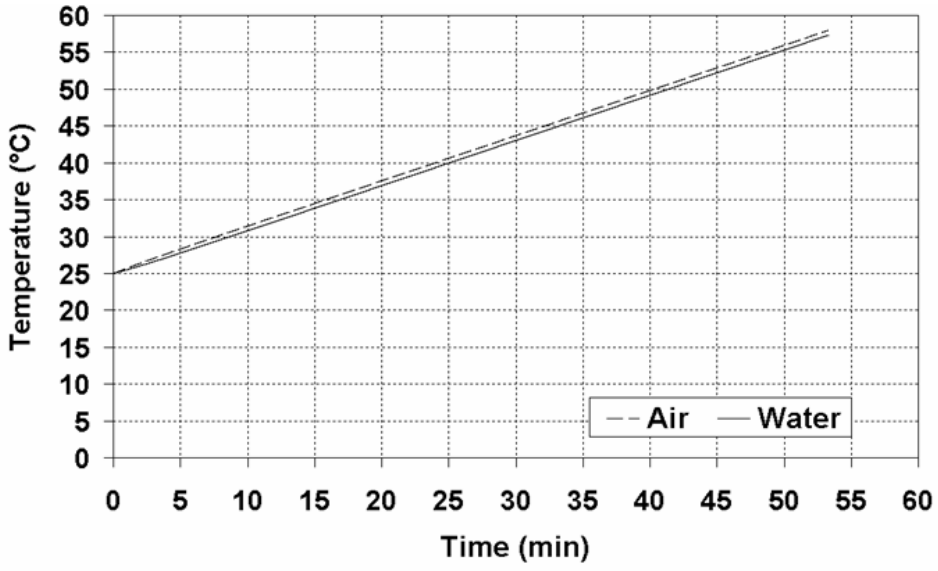

Figure 1: Simulation of the temperature profiles inside the solar drying system unloaded with fruits at day time under summer weather conditions in Egypt

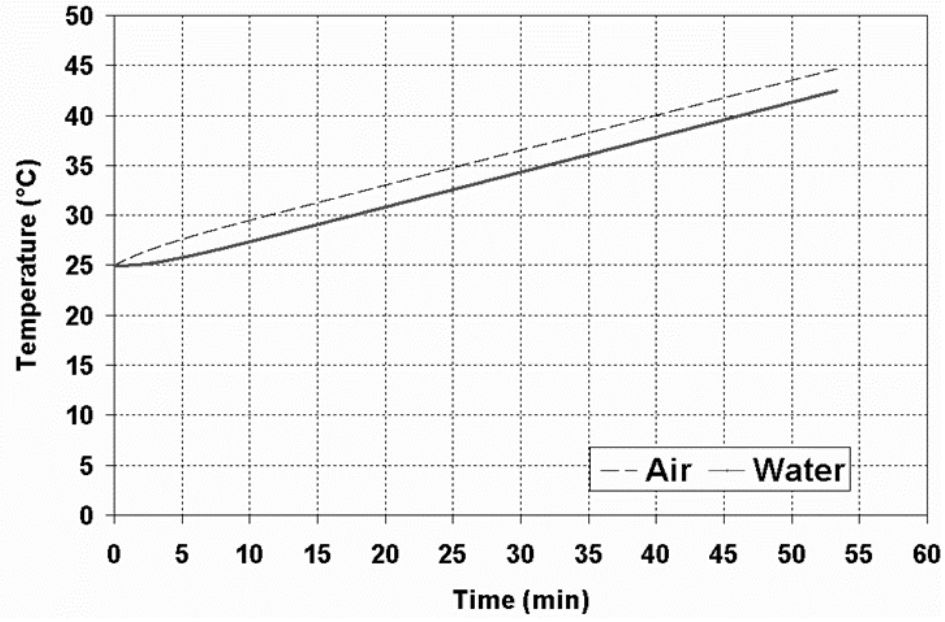

Figure 2: Simulation of the temperature profiles inside the solar drying unit with loaded plum fruits at day time under summer weather conditions in Egypt

3.6 Energy balance of drying at the night period

In the sun-set in Cairo, Egypt, the air temperature inside the drying unit is decreased to 50 °C due to the decreasing of ambient air temperature to 20 °C. Then the water temperature inlet to the first tube of the heat exchanger inside the drying unit is heated up by using the heating elements to 70 °C. The new water temperature is changing due to heat transfer during the contact between the air and the tube of water and can be determined by applying equation (29-c)

T_{a1}‘ = [0.99994353 × (50-70)] + 70= 50.005 °C

To determine the new temperature of water tube due to the heat transfer with the air passing over it, the heat balance of energy can be used.

In case of using the solar drying unit under unloading conditions

T_{w1}‘ = 69.992 °C

In case of using the solar drying unit loaded with plum fruits

T_{w1}‘ = 69.9928 °C

This series of equations were worked using Excel to determine the new air and water temperatures for each 0.1sec.

It is shown in **Figure 3**, that during the night period and unloaded conditions, its temperature can fall from 70 to 57 °C at 16 min due to the very slow velocity of water passing through the tubes. The heat is transferred from the water to the air passing through the solar drying unit and raises its temperature from 50 to 57 °C in 16 min.

Also, it is shown in **Figure 4**, when loading the solar drying unit with plum during the night period, its temperature can fall from 70 to 55 °C in 12 min. The heat is transferred from the water to the air passing through the solar drying unit and raises its temperature from 50 to 55 °C in 12 min.

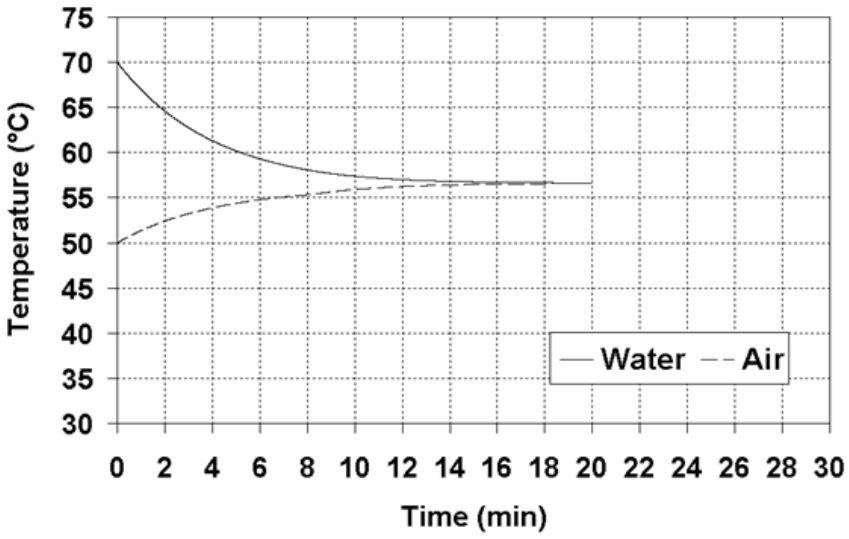

Figure 3: Simulation of the temperature profiles inside the solar drying unit when unloaded at night time under summer weather conditions in Egypt

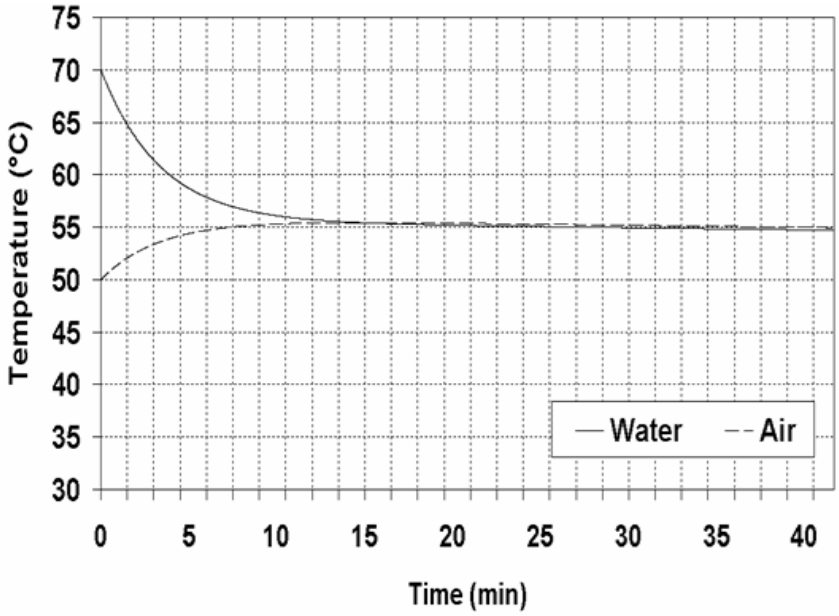

Figure 4: Simulation of the temperature profiles inside solar drying unit when loaded with plum fruits at night time under summer conditions in Egypt

4 Conclusion

The present mathematical modeling based on the heat balance can be used to determine the dimensions of the solar dryer and to predict the behavior of the air temperature inside it.

In addition, by using this modeling, the heat gain within the solar drying unit can be predicted for the air passing through it during the sun-shine period. Also, the stored heat by the water passing through the heat exchanger inside the drying unit can be predicted.

The quantity of heat transfer from water to air passing through the drying unit can be calculated to control the temperature of air to make it constant during the night period.

References

AMER B.M.A. (1999): Determination Of Drying Rate Of Fruits As A Function Of The Affecting Factors Under Conditions Suiting Solar Drying. M. Sc. Thesis, Ag. Eng. Dept., Fac. of Agic., Cairo Univ., Egypt

AMER B.M.A, MORCOS M.A., SABBAH M.A. (2003): A design for experimental drying apparatus for the determination of the impact of the affecting factors on the drying time and performance for fruits. Conference of New methods Means and Technologies for Applications of Agricultural Products. The International Conference Institute of Agricultural Engineering LUA Raudondvaris, Lithuania

BENNAMOUN L., BELHAMRI A. (2003): Design and simulation of a solar dryer for agricultural products. J. of Food Engineering; 59: 259-266

CHIRARATTANANON S., CHINPORNCHAROENPONG C., CHIRARATTANANON R. (1988): An steady-state model for the forced convection solar cabinet dryer. Solar Energy. Vol. 41(4), pp. 349-360

EXELL R.H. (1980): Grain drying. A simple solar rice dryer, basic design theory. Sunworld, Vol. 4, No. 6, pp. 186-191

GRAINGER W., OTHIENO H., TWIDEL J.W. (1981): Small Scale Solar Crop Dryers for Tropical Village Use – Theory and Practical Experiences. ISES; Solar World Forum, Brighton, UK; Pergamon Press, Oxford. pp. 989-996

INCROPERA F.P., DEWITT D.P. (1990): Fundamentals Of Heat And Mass Transfer. John Wiley & Sons. New York. pp. 645

KARIM M.A., HAWLADER M.N.A. (2005): Mathematical modelling and experimental investigation of tropical fruits drying. International Journal of Heat and Mass Transfer, Vol. 48, No. 23-24, pp 4914-4925

MAROULIS Z.B., SARAVACOS G. (1986): Solar Heating of Air for Drying Agricultural Products. Solar & Wind Technology. Vol. 3, No. 2, pp. 127 – 134

PRATOTO A., DAGUENET M., ZEGHMATI B. (1997): Sizing Solar-Assisted Natural Rubber Dryers. Solar Energy Vol. 61, No. 4, pp. 287 – 291

RATTI C., MUJUMDAR A.S. (1997): Solar Drying of Foods: Modeling and Numerical Simulation. Solar Energy. Vol. 60, (3/4), pp. 151 – 157

SHARMA V.K., SHARMA S., RAY R.A., GARG H.P. (1986): Design and performance studies of a solar dryer suitable for rural applications. Energy Convers. Mgmt. Vol. 26, No. 1, pp. 111-119

SAAD M.M.M., RIZAK S.S., MATWALY M.N.M.K. (1992): Using the solar Energy for drying the Agricultural Crops. Cairo, Egypt

SODHA M.S., DANG A., BANSAL P.K., SHARMA S.B. (1985): Analytical and experimental study of open sun drying and cabinet type drier. Energy-Conversion and Management. Vol. 25, No. 3, pp. 263 – 271

„Familie Flaschengrün“ in Potsdam
(at the corner Dortustraße and Brandenburger Straße)

„Mea Culpa“ Tapas Bar
(at the corner Hegelallee and Dortustraße)

Separation of Potato, Stones and Clods in the Air Flow

J. Fér and V. Mayer
Research institute of agricultural engineering
Drnovská 507, 161 01 CZ - Prague 6, Ruzyně

Abstract: *This paper is focused to the possibilities of potato, clods and stones separation from their mixture utilizing difference of the air flow lift speed. It describes theoretical principle and its verification in the reduced model for tubers in scale of 1 : 5.*

Results of the practical verification

Under operational conditions in stationary implementation the performance was around 30 t.h^{-1}, potato separation efficiency of 99.7 %, stones separation efficiency of 96.2 %. The two-row harvester performance was 0.39 ha.h^{-1}, separator passing rate of 99.6 – 99.8 %, stones separation efficiency of 87.0 – 91.6 %. Copyright © 2006 IFAC

Keywords: *Potato, stones, clods, air flow, lift speed*

1 Separation of Potato, Stones and Clods

In consequence of high occurrence of stones in soil within principal potato regions a significant injuries of tubers were observed during their harvest, transport and treatment. Possibility of their separation just in the harvester was limited as well as their treatment in stationary lines. Only the electronic separator E-691 was available utilizing difference of the x-ray radiation absorption with the separated mixture.

The experts in that field demanded better separating systems with a higher performance, efficiency and operational reliability. Therefore the work aimed to the pneumatic potato and stones principle has began with possibility of its application within the agricultural practice. But because there was no practical or theoretical information available, regarding this principle application the initial step was made – i.e. study of theoretical hypotheses and experimental solution. The starting point was an application of theory on the cereals lift speed developed for potato. The construction design was first verified in the reduced model for tubers in scale of 1 : 5.

The theoretical basis and knowledge of the reduced model verification were used for a design and experimental separator examination under the operational conditions. Results, performance data, separation efficiency, tubers injuries and air-conditioning parameters are included in this paper. A possibility how to reduce the tubers injury generating during a common tubers and stones transport was tested using the pneumatic separation with the potato harvester.

1.1 Determination of theoretical lift speed

For application of pneumatic separation of mixture components there are available extensive theoretical work and also practical experiences for cereals (ZUJEV 1976). But no published sudy is know regarding the potato and stones separation.

The theoretical presumption of separation is application of the lift speed differences of the separated particles. The generally valid equations define the presumption that the gravity caused by the particle mass m is at equilibrium with a force caused by another force acting to particle by the air vertical flow. This flow speed is called the lift speed v_0.

To describe the solid particles motion within the air vertical flow the following equation is applied:

That equation is based on simplified presumption of the spherical body within the large air flow. The following symbols are used in the equation:

m – mass of body placed in the air vertical flow (kg)
v – air speed (m.s^{-1})
v_0 – vertical flow speed when the body is not acting with power on surface and has a zero-speed, this speed is called the lift speed (m.s^{-1})
s – projection of body into a plane perpendicular to the air flow direction (m^2)
g – gravity acceleration (9.81 m.s^{-2})
c_x – coefficient of body aerodynamic resistance in the air flow ($c_x \cong 0{,}43$)
ρ_v – air specific weight (1,2 kg.m^{-3})
d – diameter of spherical body placed in the air flow (m)
ρ_t – body specific weight (kg.m^{-3})
ρ_{tb} – potato specific weight (1,1 . 10^3 kg.m^{-3})
ρ_{th} – clod specific weight (1,5 – 2) . 10^3 kg.m^{-3}
ρ_{tk} – stone specific weight (1,9 – 3) . 10^3 kg.m^{-3}

To determine the speed when its power acting effect on the spherical particle in the air vertical flow is balanced with the body gravity force, the body speed is assumed zero.

Determination of the lift speed is possible with adaptation of the previous equation:

$$v_0 = \sqrt{\frac{2mg}{c_x.S.\rho_v}} \quad \text{(m.s}^{-1}\text{)} \qquad (1)$$

This equation can be adapted:

$$v_0 = \sqrt{\frac{4gd.\rho_t}{3\rho_v.c_x}} \quad \text{(m.s}^{-1}\text{)} \qquad (2)$$

If the body placed in the vertical air flow is of irregular shape the equation can be adapted by substitution of the d value with so called equivalent diameter d_e calculated from the body volume V_t. Then it regards the spherical body diameter with identical both weight m and specific weight ρ_t:

$$d_e = \sqrt[3]{\frac{6m}{\pi.\rho_t}} = 1{,}24\sqrt[3]{\frac{m}{\rho_t}} = 1{,}24\sqrt[3]{V_t} \text{ (m)} \quad (3)$$

For particular components of the separated mixture (potato, clods, stones) the equation can be adapted for known interface of their specific weight ρ_t:

For potato (24 – 53 m.s^{-1}):

$$v_{0b} = 170\sqrt{d} \text{ (m.s}^{-1}\text{)} \quad (4)$$

For clods (28 – 74 m.s^{-1}):

$$v_{0h} = (200-235).\sqrt{d} \text{ (m.s}^{-1}\text{)} \quad (5)$$

For stones (32 – 95 m.s^{-1}):

$$v_{0k} = (220-300).\sqrt{d} \text{ (m.s}^{-1}\text{)} \quad (6)$$

From the graph (**figure 1**) is evident that the lift speeds interface is overlapped for considered interface of the components dimension of the separated mixture. The major part of the overlapping lift speeds v_o is between potato and clods. It may be anticipated that clod higher speed will increase the specific weight p_{th} and thus also the lift speed. More considerable difference of the lift speed is between potato and stones.

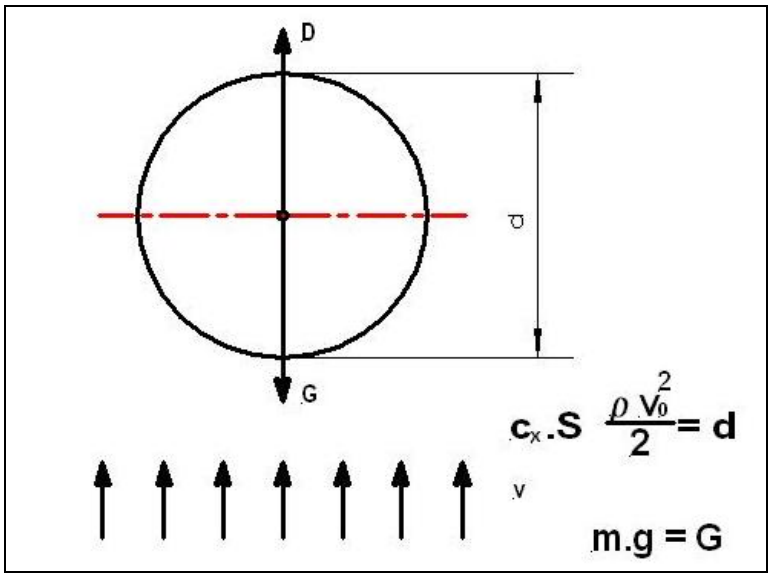

Figure 1: Air flow power acting on spherical body see (FÉR 1997)

1.2 Pneumatic separator

The potato and stones mixture is fed into the separator (**figure 2**) through the filling conveyer (8) and further on the inlet rod separator conveyer (3). Potatoes (11) having lower lift speed as compared with the admixtures (stones) (12) are entrained upward where are retained and by means of the rotating rod drum (2) further entrained into a space with the air speed lower than the potato lift speed. Potatoes are falling down on the cross outlet rib conveyer (4). The space where the rib conveyer is entering the separator box (1) is covered in the length corresponding with the direct pitch of two ribs. On the outlet side there is installed the top diaphragm which is pressed to the belt through the air pressure difference in – and outside the box (4). This system prevents the undesirable air penetration without the reverse tubers entraining and their injury.

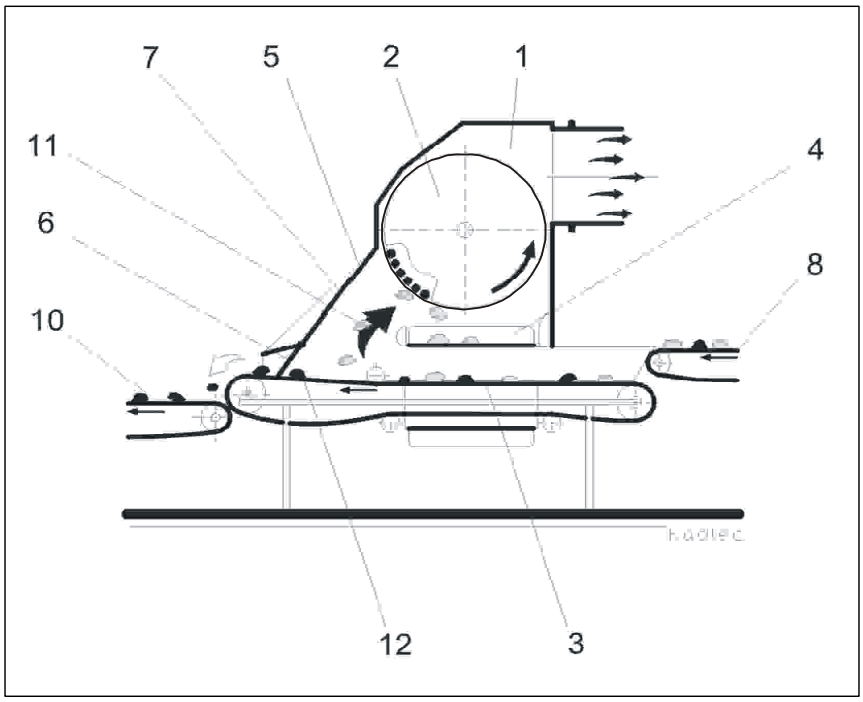

Figure 2: Experimental pneumatic separator – VÚZT see (FÉR 1997)

Stones with a higher lift speed remain laying on the inlet rod conveyer (3) and through the admixture conveyer are then removed out. The separator box is fitted with the swinging diagram (5). The cross- section of the separating channel can be changed within a certain range by means of its inclination influencing the lift speed. The bottom part of the diagram is attached to the swinging sheet flaps.

They prevent the undesirable air penetration and allow their deflection against the bigger stone. The air from the separator box is drawn out through the ventilator.

2 Verification of the Pneumatic Separation Principle by Means of Reduced Model

Prior to the proper construction of the pneumatic separator for required operational parameters there was built the functional model in scale of 1 : 5 (**figure 3**). To reach the lift speed in the separating channel there is used the drawing out radial ventilator with the moving wheel diameter of 315 mm. For testing were used the reduced models of tubers and small stones produced from modelite, adapted to identical specific weight as the natural potato.

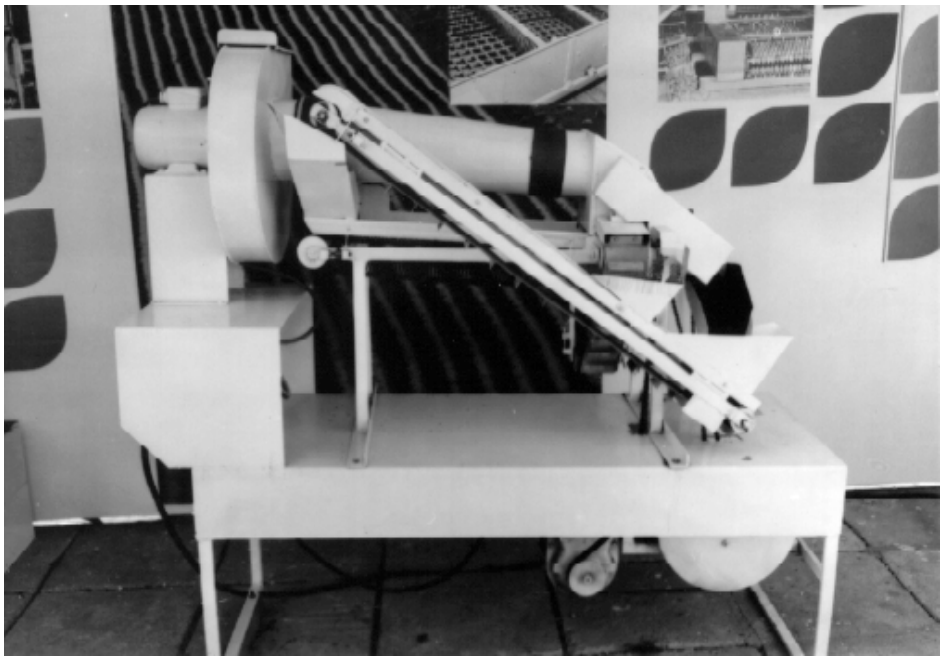

Figure 3: Model of pneumatic separator see (FÉR 1997)

For easier adjustment of the operational parameters the transport routes are designed in such way to allow to mix together the separated mixture and to lead it back to the separator inlet. The pipeline was attached to the air outlet from the ventilator for measuring of the air speed. From the ratio of both measuring and separation space the air speed in the separation space was calculated.

By means of the model the air speed change effect on the separation efficiency was investigated with different admixture amount. The tests were conducted in such way that the stones share was changed for different air speed and constant weight of the model potato in the place of the inlet. The purpose was to find out the incorrectly separated potato share (as related to the initial 100 %) into the admixture (x_b) and how many stones were incorrectly separated (as related to the initial 100 %) into potato ($x_{k.}$). The results are shown in the graph (**figure 4**). From the results is evident that:

- at the constant potato passage rate and higher share of admixtures the higher lift speed is necessary to reach lower percentage of incorrectly separated potato

- if the air speed in the separation space exceeds the stone lift speed the intensive increasing of the incorrectly separated stones will occur.

As the air speed exceeds the stone lift speed v_{ok} in the separating space the intense increasing of incorrectly separated stones (x_k) occurs.

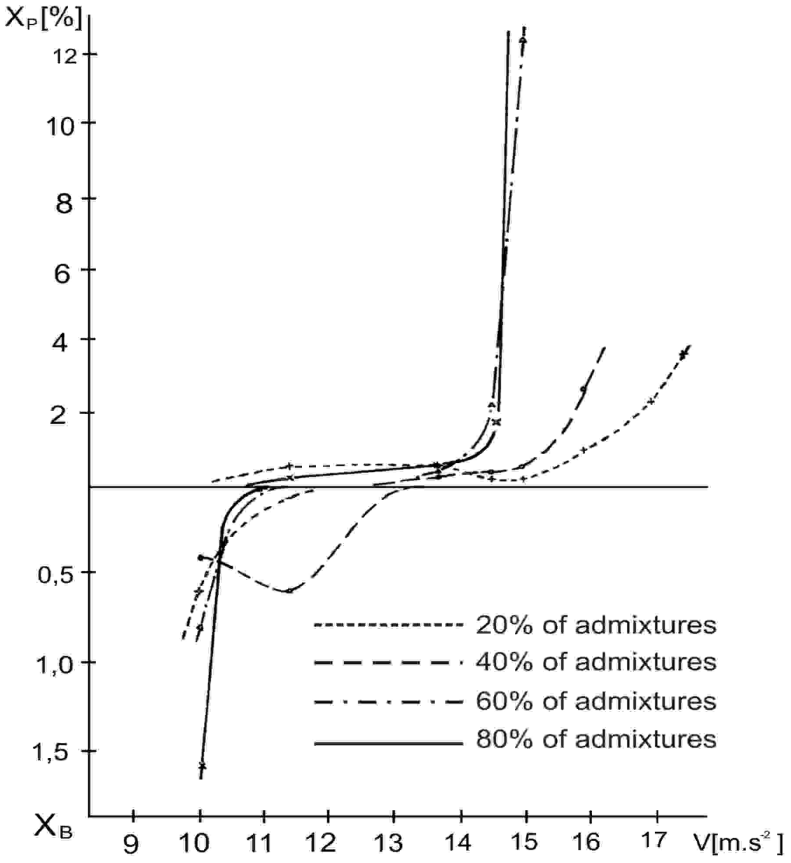

Figure 4: Error particles see (FÉR 1997)

3 Stationary separation

The separated mixture passing rate has reached of 30 $t.h^{-1}$ during the operational verification at the stationary working place (**figure 5**). Because the cross-section of the space where the separation is provided is filled during the operation with the separated mixture, the air speed of 26 $m.s^{-1}$ in the separation space (necessary for potato separation) is sufficient when considering that in the un-filled space this value is lower in comparison with the calculated lift speed of 28 – 53 $m.s^{-1}$. Therefore, in contrast to the theoretical presumptions, the necessary air volume and input are lower. The theoretical differences of the lift speed for various tubers size have not been confirmed. This is caused by a fact that the bigger tubers have more oval, irregular surface as compared with the smaller ones. They have thus a higher c_x coefficient and are better entrained with the air. The stones correct separation efficiency depends on their shape and specific weight. The separation efficiency of flat and hight stones (erinaceous marl) is worse (**table 1**).

Figure 5: Pneumatic separator see (FÉR 1997)

Table 1: Pneumatic separation performance

Inlet material passing rate $t.h^{-1}$	Stones admixture %	Separation efficiency	
		Potato %	Stones %
29.30	3.74	99.72	100.00
25.20	5.13	100.00	89.74
32.20	4.43	99.56	97.73
28.70	12.08	99.53	96.52
31.30	10.86	99.39	97.15
23.10	7.83	100.00	96.13
Average	7.34	99.70	96.21

4 Pneumatic Separation Performed With the Potato Harvesters

The knowledge obtained from the systems of potato and stones pneumatic separation with stationary lines has created presumptions of verification of this principle with the mobile potato harvesters. The aim was to exclude the tubers mechanical injury caused by stones during harvesting and transport.

The agricultural enterprises have equipped the potato harvesters with the pneumatic separator, based on the conception verified at the stationary working place (**table 2**). The reconstruction was implemented for harvesters of type E 671, E 684 and E 686 (**figure 6**).

Table 2: Pneumatic separation characteristics

Performance during testing	0,39 ha.h^{-1}
Separated mixture passing rate	12 760 – 23 510 kg.h^{-1}
Share of stones (potato 100%)	6,1 – 23,1 %
Potato separation efficiency	99,68 – 99,81 %
Stones separation efficiency	87,09 – 91,66 %
Potato losses caused by incorrect separation	0,19 – 0,32 %
Ventilator drive	motor Z-4001 equipped with starting clutch

Figure 6: Pneumatic separator attached to harvester E-686 see (FÉR 1997)

5 Conclusions

The results of the pneumatic separation research have resulted in serial production at the STS Pacov (type of separator TR-1-050) where more than 300 separators have been produced. This type is also produced in Germany. The pneumatic separation introduction has led to removal of all separators using the x-ray radiation from practical utilization.

The disadvantage of the pneumatic separation is in a high level of dustiness in more drought year and a low efficiency of clods separation.

At present, after the introduction of the soil bed stone removing before the potato planting, some agricultural enterprises utilize the pneumatic separators.

References

FÉR J. (1977): Pneumatic potato, clods and stones separation. Farm mechanization, 1977, No. 12

FÉR J., SEDLÁK J. (1977): Research of potato pneumatic separation. Research report VÚZT, Z-1392

ZUJEV F.G. (1976): Pneumatic transport of corn crops

A New Method to Model a 3D Shape of Biomaterials for Using in Post-Harvest Modelling

Jalal Kafashan[1,2], Bert Tijskens[1], Dimitrios Moshou[1], Cedric Bravo[1], Josse De Baerdemaeker[1], Herman Ramon[1]

[1] Division of Mechatronics, Biostatistics and Sensors, K.U.L., Kasteelpark Arenberg 30, B-3001, Belgium
[2] A.E.R.I. of I.R. of Iran
E-Mail: Jalal.kafashan@biw.kuleuven.be

Abstract: *Generally, shape is one of important factors in many products, crops, fruits and in most post-harvest processes such as handling, sorting, packaging etc for machine design, automation, control and modelling. A 3D modelling of biomaterials has therefore many applications in post-harvest processes. However, there are no realistic shape models available for most biomaterials. They have to be drawn manually which is extremely tedious and many important details are lost. Based on the applications, in this research, golden delicious has been selected as an example of biomaterials to propose a new modelling method for creating a three dimensional model. The apple is modelled as a 3D shape based on scanned slices using image processing and some mathematical methods. This method can be applied for biomaterials modelling such as pear, mango, quince etc. It is a new method involving application of image processing on real scanned slices of biomaterials. Copyright © 2006 IFAC*

Keywords: *3D, Apple, Image processing, Model, Shape, Slice, Post-harvest.*

1 Introduction

Three dimensional shape models of biomaterials can be used in modelling of mechanical damage caused by impact, constant load, friction, vibration and processes of harvesting, handling, sorting etc. It can also be used in some processes such as heat transfer and moisture transfer inside biomaterials. Moreover, it's very useful to use in product identification and measuring quality, quantity of products, automatic control, machine design, and etc. Briefly, while there are several published results on shape applications, shape models, image analysis, only a few exist on realistic 3D modelling. Some previous works that are relevant to the subject are given in the following;

KRANZLER (1985) presented a short introduction to image processing applications in agriculture. REHKUGLER & THROOP (1989) examined the defects of apples using a shape factor. GUYER *et al.* (1993) published several basic theories of plant identification by investigating shape. SINGH & DELWICHE (1994) described a system for grading peaches by their

shape and presence of the different defects (cut, scar, bruise and wormhole). CHENG & LING (1994) examined the shape and classified somatic coffee embryos. TOA *et al.* (1995) presented a shape grading system for potatoes based on the contour information. GHAZANFARI *et al.* (1997) used a vision system to grade and classify pistachio nuts into different size and shape (split and unsplit) categories. UMEDA *et al.* (1997) developed a watermelon harvester robot to identify and harvest watermelon. ZHANG *et al.*(1998) developed an automatic inspection system for tobacco leaves. Additionally to the colour, surface texture and vein information, the size and the shape were used to grade the leaves. MORIMOTO (1998) presented a fruit shape grading system based on chaos theory. CARRION *et al.* (1998) developed a vision system for citrus sorting. JANCSOK (1999) used a special device with CCD camera to make 3D modelling of biological products in order to produce finite element (FE) meshes based on image processing. Mulet *et al.* (2000) investigated the shape changes along the drying process of potato and cauliflower by image analysis and directly with a calliper. STEENHOEK & PRECETTI (2000) performed a study to evaluate the concept of two-dimensional image analysis for classification of maize kernels according to size. THROOP *et al.* (2001) used two conveyors to obtain performance and predictability of apple orientation based on shape characteristics. CHI *et al.* (2002) developed algorithms to extract the leaf boundary of selected vegetable seedlings by fitting Bezier curves. YING *et al.* (2003) used Fourier Transform and Inverse Fourier Transform pairs to descript shapes of Huanghua pears and applied artificial neural network (ANN) for classification. VAN ZEEBROECK (2005) used spherical shape to simulate impact damage of apple (Jonagold) during transport and handling using Discrete Element Method (DEM). He suggested some future works such as use of a more realistic shape to increase accuracy. KAFASHAN *et al.* (2005) proposed an algorithm to make a 3D shape model by image processing of the slices of some fruits. Hence, studying and researching about biomaterials' shape modelling and geometry of products will be continued due to the abundance of applications and the need to find realistic models.

2 Material and Methods

The Golden Delicious apples have been selected as an example of biomaterial in order to create a three dimensional shape model and also to develop the proposed algorithm (KAFASHAN *et al.* 2005) for 3D shape modelling. At the beginning, the apples were divided in 8 and 16 similar slices, respectively. It means the apples were divided using 45, and 22.5 degree steps around the stem/calyx axis, respectively. Then the slices were scanned using a colour image flat-bed scanner which is able to scan objects. The apples' slices are shown during the scanning process in **Figure 1**.

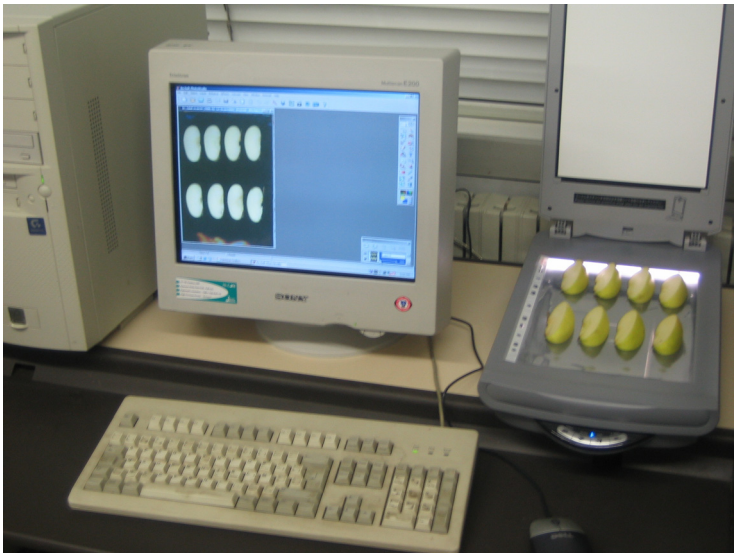

Figure 1: Scanner during scanning of the slices of an apple that was cut in eight slices around the stem/calyx axis. The slices have a step angle of about 45 degrees around stem/calyx axis in this case

The images of slices were saved into separated files as RGB images for image processing. The developed algorithm was used in MATLAB 6.5.1 as a program to carry out the image processing of the slice images. The program has several steps to perform image processing and to create the model as follows;

1- Reading all images of slices by the program.
2- Binarizing images of slices.
3- Removing spot or noise from images only around the object (which means from the slice).
4- Capturing the boundary of objects (as needed per application).
5- Converting the data from Cartesian into polar co-ordinate system in order to carry out a better analysis and to obtain the shape function (**Figure 2** shows the shape function for a slice of apple).
6- Converting the shape function (a wave shape) into a long periodic function (repetitive curve such as Fourier series).
7- Optimizing the periodic function by a general optimization method for removing some unfitted data from the curve.
8- Data filtering to extract very smooth curves.
9- Selecting a wave shape curve at the primary domain that we called processed shape function. This processed shape function is shown as a filtered curve in **Figure 3**.
10- Converting data from a polar into a Cartesian co-ordinate system results in slice images with very smooth edges. **Figure 4** is showing one reconstructed edge (white edge) in comparison with its original slice.
11- Finding a common axis as stem/calyx axis based on the tangential line for all slices.
12- Putting all slices together on one axis corresponding to the place of the original slices of the apple as a 3D shape.
13- Interpolation among all slices to a fit suitable surface over all.
14- Extracting data of final 3D shape.

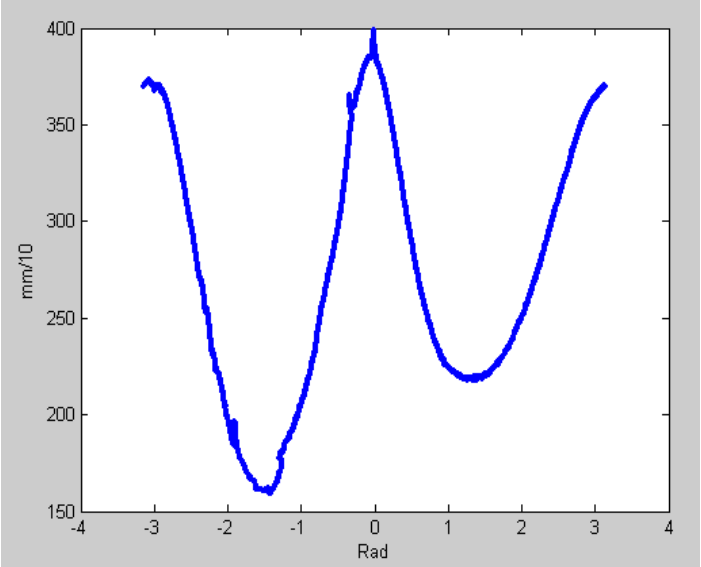

Figure 2: Shape function of a slice of an apple that was obtained by the method (before filtering)

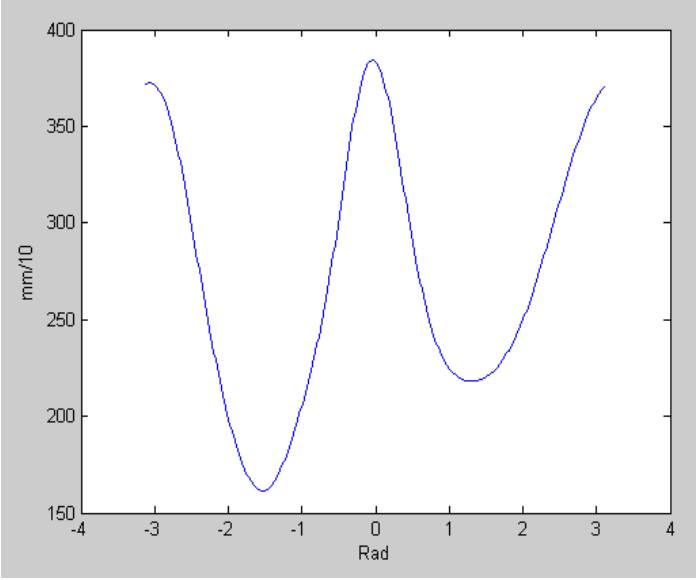

Figure 3: Shape function of a slice of an apple obtained by the proposed method (after filtering)

Figure 4: Comparing a reconstructed edge (using the method) with original scanned slice

3 Results

3D models of the apple were created using this algorithm (new method). There are several ways to cover a surface over these slices to make a 3D model. One way is using averages of slices based on data averaging. Another way is by matching 3D slices. This can be achieved in different ways depending on which surface interpolation technique is used. Step twelfth is shown in **Figure 5** as the wire frame of an apple (by 16 images of slices). Overall, the maximum error was about five percent in matching slices in a bad slice alignment situation which is acceptable and around ten percent in volume estimation.

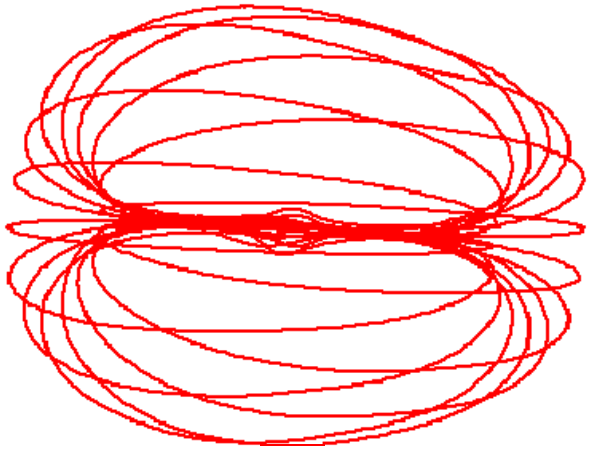

Figure 5: Wire frame of an apple (16 slices) created by the proposed method which constructs 3D shape and the location of the core is clear

4 Conclusion and Discussion

We can conclude that this method is able to make 3D model shapes of apples and is applicable in shape model creation of fruits such as pear, quince etc by changing a few parameters or procedure. In addition, it is a low-cost method without requiring any special devices and is easy to use in all lab works and also in many domains. These include post-harvest modelling such as using DEM, FEM, and ANN for process modelling, making a data base of 3D models of fruits for all cultivars/varieties etc. This can also be useful for machine design, automation and process control in classification and identification of quality, sorting or grading even in harvesting or for packaging. Meanwhile, the method has an additional advantage of recognizable core location. That can be used in certain modelling domains like heat transfer modelling for the storage process. It is necessary to mention that if the interior of the fruit is valuable as a modelling detail, it is better to use 8 slices. Otherwise, if details of the exterior of the fruit are more important, then using between 8 and 16 slices is preferred. However the direction of cutting is also very important in order to obtain fewer slices. Therefore, the method is destructive and it's not applicable for biomaterials that have high water content. These are its disadvantages. However the advantages for other types of materials are numerous. The method can be developed further for all biomaterials using additional devices, algorithms, or by optimization techniques. It is a

new method involving application of image processing on real scanned slices of biomaterials for creating 3D shape models. As future work, it would be better to compare several interpolation methods at the final step, using flat instead of embowed slices and also using this method for modelling more diverse types of biomaterials.

References

Carrion J., Torregrorosa A., Orti E., Molto E. (1998): First results of an automatic citrus sorting machine based on an unsupervised vision system.In: Proceedings of AgEng98, International Conference on agricultural engineering, Paper No. 98-F-019,Oslo.Norway

Cheng Z., Ling P.P. (1994): Machine vision techniques for somatic coffee embryo morphological feature extraction. Transaction of the ASAE. 37(5):1663-1669

Chi Y.–T., Chien C.–F., Lin T.–T. (2002): Leaf shape modeling and analysis using geometric descriptors derived from Bezier curves. Transactions of the ASAE. 46(1): 175–185

Ghazanfari A., Irudayaraj J., Kusalik A., Romaniuk M. (1997): Machine vision grading of pistachio fruits using Fourier descriptors. Journal of Agricutural Engineering Research. 68: 247-252

Guyer D.E., Miles G.E., Gaultney L.D., Schreriber M.M. (1993): Application of machine vision to shape analysis in leaf and plant identification. Transaction of the ASAE. 36(1): 163-171

Jancsok P.T. (1999): Geometrical model generation for finite element meshes of biological products based on digital image processing. PhD thesis. Faculty of agricultural and applied biological sciences, K.U. Leuven. Belgium. 44-49

Kafashan J., Tijskens B., Ramon H. (2005): Shape modelling of fruit by image processing. Comm. Appl. Biol. Sci. Ghent University. 70(2): 161-164

Kranzler G.A. (1985): Applying digital image processing in agriculture. Agricultural Engineering. 66(3): 11-13

Mulet A., Garcia-Reverter J., Bon J., Berna A. (2000): Effect of shape on potato and cauliflower shrinkage during drying. Drying Technology. 18(6): 1201–1219

Morimoto T., Takeuchi T., Miyata H., Hashimoto Y. (1998): Pattern recognition of fruit shape on the basis of chaos using neural networks. In: Proceedings of Control Applications in Post-Harvest and Processing Technology 1998. (CAPPT'98) 109-114. Budapest, Hungary

Rehkugler G.E., Throop J.A. (1989): Image processing algorithms for apple defect detection. Transaction of the ASAE. 32(1):267-272

Steenhoek L., Precetti C. (2000): Vision sizing of seed corn. In: 2000 ASAE Annual International Meeting, Paper No. 003095 ASAE, Milwaukee, Wisconsin, USA

Singh N., Delwiche M.J. (1994): Machine vision methods for defect sorting stonefruit. Transaction of the ASAE. 37(6): 1989-1997

Tao Y., Morrow C.T., Heinemann P.H., Sommer H.J.I.I.I. (1995): Fourier-based separation technique for shape grading of potatoes using machine vision. Transactions of the ASAE. 38(3): 949-957

Throop J.A., Aneshansley D.J., Upchurch B.L., Anger B. (2001): Apple orientation on two conveyors performance and predictability based on fruit shape characteristics. Transactions of the ASAE. 44(1): 99–109

UMEDA M., LIDA M., KUBOTA S. (1997): Development of Watermelon Harvesting robot "STORK" In : Proceedings of Bio-robotics 97: International Workshop on Robotics and Automated Machinery for Bio-production.(F. Juste, G. Andreu, J.M.Valiente and J.V. Benlloch (Ed.)), 137-142. Valencia, Spain

VAN ZEEBROECK M. (2005): The discrete element method (DEM) to simulate fruit impact damage during transport and handling. PhD thesis. Faculty of bioscience engineering, K.U.Leuven.Belgium. 231-238

YING Y., JING H., TAO Y., ZHANG N. (2003): Detecting stem and shape of pears using Fourier transformation and an artificial neural network. Transactions of the ASAE. 46(1): 157–162

ZHANG J., SOKHANSANJ S., WU S., FANG R., YANG W., WINTER P. (1998): A transformation technique from RGB signals to the Munsell system for color analysis of tobacco leaves. Computers and Electronics in Agriculture. 19(2): 155-166

Crop Conceptual Model for Predicting Productivity of Bread Wheat in Semi-Arid Kenya

P.K. Kimurto[1], K. Gottschalk[2], J.B.O. Ogola[3], M.G. Kinyua[4] , J.K. Macharia[5] and W. Herppich[2]

[1] Dept. of Crop and Soil Sciences, Egerton University, P.O. Box 536, Njoro, Kenya
E-Mail: pkimurto@yahoo.co.uk
[2] Leibniz-Institut für Agrartechnik Potsdam-Bornim e.V. ATB, Max-Eyth-Allee 100, 14469 Potsdam, Germany
[3] Dept. of Plant Production, University of Venda, Private bag X5050, Thohoyandou South Africa.
[4] National Plant Breeding Research Center, Njoro, P.O. Njoro, Kenya
[5] Dept. of Biological Science, Egerton University, P.O. Box 536, Njoro, Kenya

Abstract: *The data generated from the rain shelter by measurement of evapotranspiration (ET) together with weather variables in Katumani, Kenya were used to develop a conceptual model that can predict wheat yields in that site. The amount of water transpired by the crop and water loss beneath the canopy (E_{sc}) was estimated from the relationship between normalised transpiration efficiency (TE), obtained from seasonal vapour pressure deficits (VPD) and total dry matter yield (DM). The response of yield to water supply was quantified through the yield response factor (Ky) which relates relative yield decrease (1-Ya/Ym) to relative evapotranspiration deficit (1-ETa/ETm). Water deficit was expressed as the ratio of actual evapotranspiration (ETa) and maximum evapotranspiration (ETm) that occurred during the individual growth periods of establishment, vegetative, flowering and yield formationd, while ETo was used as the reference evapotranspiration. ETa was estimated from the soil water balance equation measured using Neutron probe under rain shelter. Crop coefficients (kc) used for different growth stages of wheat were, 0.35, 0.75, 1.1, and 0.45, for crop establishment, development stage, mid-season stage, and late season stage respectively, while the crop periods considered were between 10-20, 25-35, 45-55, and 20-40 days for crop establishment, development stage, mid-season stage and late season stage. Maximum yield (Ym) of the wheat genotype considered for genotype Chozi under ideal conditions was 5 t ha^{-1} and actual grain yield (Ya) was obtained from the relationship (1-Ya/Ym) = ky*(1-ETa/ETm), where ky is the yield response factor of 1.22. Total above-ground biomass (DM) was obtained from the relationship: HI = GY/DM, where HI is harvest index and GY is grain yield to be predicted by the model. Transpiration was estimated from the relationship between total dry matter production and normalised TE expressed as TE = DM/T, where T is transpiration (mm). Predicted grain yield using low ETa in the short rains season of 2001 and 2002 and long rains of 2003 and 2004 at same site for cultivar Chozi were 1530.3, 2792.7, 2281.2 and 1453.4 kg ha^{-1} respectively, actual yield were 1315, 1754, 1125 and 1296 kg ha^{-1} respectively. The results shown indicate that yields obtained from the conceptual model compare very well with realised yields from actual field experiments conducted at the same site and other semi-arid areas of Kenya.*

To improve the accuracy of prediction other variables like soil factors need to be incorporated. To increase wheat production in these areas measures that conserve water and/or make more water available to the crop such as prevention or minimisation of run-off, and rain water harvesting for supplemental irrigation are necessary. The present results show that it's possible to select drought tolerant wheat genotypes for semi-arid tropics through drought simulation and modelling with consequent reduction in cost of dryland research, enhanced development of drought tolerant germplasm and reduced food insecurity and donor food-aid. Copyright © 2006 IFAC

Keywords: *Wheat, conceptual model, drought, Evapotranspiration, yield response factor.*

1 Introduction

World-wide arid and semi-arid lands are diverse and widespread (REYNOLDS *et al*. 2001, TURNER 2001, Blum 1996). In Kenya, drought conditions are frequent and widespread, covering 83% of total land area mainly in northern districts, southern Rift valley, parts of Coastal and Eastern regions. Therefore carrying out dryland research is usually very expensive and time consuming due to the travelling required from one location to another (KINYUA *et al.* 2002, KIMURTO *et al*. 2003). It is also dependent on annual weather changes, which are usually very unreliable. Despite being the second most important cereal after maize in Kenya, the current domestic wheat production meets only 50% of the annual national demand of approximately 700,000 tons (MINISTRY OF ECONOMIC PLANNING 2002-2005) while the rest is imported, which drains the country of enormous and scarce foreign exchange. Average yields is 2 tons/ha which is below world average of 4 tons/ha (FAO 2004). There is need therefore to increase domestic wheat production by intensifying production in traditional high potential areas and movement to less favourable areas (KARI 1994), mainly semi-arid areas. But annual rainfall in these areas is low (200-400 mm), unreliable (40-50 days) and highly erratic (KEATING *et al*. 1992), causing frequent crop failures and related famine. Given this scenario developing drought tolerant cultivars would be an economic and efficient means of increasing food production in dry areas world-wide (ASHRAF *et al.* 1992). This will offer a means of stabilising grain yields, reduce food insecurity and hunger at no additional cost to the poor-resource small scale farmers mainly living in Arid and semi-arid areas of Kenya. However, carrying out field trial-research is expensive and costly for the National wheat programme, development of a simulation model for predicting the performance of the crop in actual marginal area would reduce costs of carrying out dryland. Since shortage of water is a chief cause of variation and low yields in wheat yields in these areas, it is desirable to predict the likely effects of variation in rainfall. Development of a simulation model for predicting the crop performance in actual marginal area would reduce costs of carrying out dryland and also provide appropriate tool for economical testing, screening and evaluating the productivity of wheat in semi-arid areas. But before theses models can be used, they must be validated using data from field experi-

ments (ASADI & CLEMENTE 2001). Crop simulation models such as CERES-wheat are useful when incorporated into decision support system (DSS) (RITCHIE 1995). Elsewhere also, CERES model have been used to investigate the role of water stress on plant development and growth and methodologies to determine optimal variable rate for N and populations across several fields have been developed (PAZ *et al.* 1999). Phasic development in most models is quantified with respect to the physiological age of the plant and potential growth is dependent of photosynthetically active radiation (PAR) and its interception as influenced by leaf area index, row spacing and conversion efficiency (ASADI & CLEMENTE 2001).

This paper attempts to develop a model that predicts the yield of bread wheat in Katumani a semi-arid area in Kenya (**Figure 1**). Earlier studies under the Rain shelter (KIMURTO *et al*. 2003) at Kenya Agricultural Research Institute (KARI), Njoro, Kenya (**Figure 2**) showed that crop water use increases with water supply. The data generated from the rain shelter by measurement of evapotranspiration (ET) together with weather variables in Katumani (**Table 1**) were used to predict wheat yields in that site. Katumani is located in Machakos, Kenya (1° 33′ S, 37° 14′ E and 1560 m above sea level) about 60 km East of Nairobi (Figure 1).

Figure 1: Map of Kenya showing Katumani the experimental site

Figure 2: Rain out shelter showing neutron access tubes and drip irrigation at KARI Njoro, Kenya

Katumani is semi-arid with an annual average rainfall of 755 mm (SD = 150), high rainfall variability between years and seasons and average annual pan evaporation of 1800 mm. There are two distinct rainy seasons, with 330 mm (SD = 150 mm) in the 'long rains' (March to July) and 365 mm (SD = 125 mm) in the 'short rains' (October to February). The mean annual temperature is 19.2°C, August being the coldest month with a mean monthly temperature of 17.1°C while March is the warmest month with a mean monthly temperature of 21.3°C. The soils are Alfisols, Kandic Rhodustalfs (USDA soil taxonomy). Daily weather data for the different seasons were obtained from an automatic weather station located within the area. The following climatic variables were recorded each day; rainfall (mm), pan evapotranspiration (mm), maximum (T_{max}) and minimum (T_{min}) air temperatures (°C), solar radiation (MJ m^{-2} d^{-1}) and relative humidity (%). Table 1 shows the monthly totals or means for these weather variables over the growing period during the various seasons.

Table 1: Monthly total (rainfall and E_{pot}) and daily mean of weather variable during the 2001- 2002 growing seasons at Katumani, Kenya

	Total Rainfall (mm)	Mean $E_{pot.}$ (mm)	Maximum Daily Temp (°C)	Minimum Daily Temp (°C)	Mean* Temp (°C)	Solar Radiation (Lang leys m^{-2} d^{-1})	Relative Humidity (%)
2001							
October	7.3	180.3	27.1	13.6	20.4	630.0	51.5
November	169	126.1	24.0	14.6	19.3	573.9	69.0
December	43.6	127.6	24.2	14.4	19.3	552.7	72.5
January (02)	79.5	148.2	26.9	14.1	20.0	624.4	65.5
February	7.5	179.0	27.1	13.9	20.0	676.4	53.0
Mean/Total	**306.9**	**761.2**	**24.7**	**14.0**	**19.5**	**611.5**	**62.4**
2002							
October	21.2	188.2	26.7	14.1	20.4	517.9	38
November	144	167.8	24.9	15.1	20.0	499.0	51
December	183	117.2	24.0	15.2	19.1	452.6	63
January (03)	31.6	130.2	25.3	12.9	19.6	547.7	52
February	17.2	95.9	28.8	12.7	21.4	691.0	32
Mean/Total	**397**	**699.3**	**24.7**	**14.0**	**19.5**	**541.6**	**48.4**
2003							
January	31.6	130.2	25.3	12.9	19.6	547.7	52.0
February	17.2	95.9	28.8	12.7	21.4	691.0	32.0
March	115.2	172.9	28.6	13.3	20.9	730.1	38.0
April	153.2	151.3	26.8	14.1	20.6	684.3	47.0
May	133.8	107.8	23.9	14.5	19.1	614.9	68.0
June	Nil	52.0	23.2	11.9	21.5	613.2	57.0
July	Nil	97.5	22.2	10.1	16.1	595.2	51.0
August	26.3	110.8	22.8	10.4	16.2	622.3	55.0
September	21.5	187.3	24.9	11.8	18.6	736.5	43.0
October	30.8	190.8	26.4	13.3	20.1	791.9	42.0
November	121.1	148.1	24.5	13.8	19.1	784.1	55.0
December	24.1	169.1	25.1	13.4	19.2	800.3	50.0
Mean/Total	**674.6**	**1613.2**	**25.2**	**13.6**	**19.5**	**684.3**	**51.4**
2004							
January	48.0	169.0	25.9	14.4	20.1	796.7	54.0
February	47.9	165.4	26.6	14.4	20.5	853.3	47.0
March	83.1	188.9	27.3	14.7	21.0	867.6	42.0
April	121.5	147.5	25.3	15.2	20.2	840.7	58.0
May	59.8	123.8	25.1	13.3	19.1	830.7	51.0
June	0.7	59.0	23.4	11.2	16.4	790.4	47.0
July	Nil	92.5	24.3	9.4	16.1	838.5	40.0
August	Trace	120.8	23.6	10.7	17.2	807.9	46.0
September	1.0	165.3	26.4	12.1	19.1	836.5	39.0
October	47.6	150.8	25.9	13.7	19.9	799.9	45.0
November	161.3	148.1	24.7	14.6	19.2	804.1	53.0
December	89.5	160.1	24.4	14.0	19.2	800.3	56.0
Mean/Total	**660.4**	**1693.2**	**24.7**	**14.0**	**19.5**	**834.3**	**48.4**

*The mean of daily maximum and minimum temperature *Temp- temperature

2 Theoretical Aspects of the Conceptual Model

The complex growth control mechanisms related water use, water use efficiency (WUE) and yield is concisely represented with equation:

$$\Delta W = k(ET - Es)/(e* - e) \quad (1)$$

where ΔW is growth (kg/ha), ET is evapotranspiration (mm), Es is soil evaporation (mm), $e*$ is saturated vapour pressure (kPa), and e is actual vapor pressure (kPa). The value of ET is obtained from soil balance equation, which covers whole life cycle of the crop. Pioneer workers (BRIGGS & SHANTZ 1916) working on transpiration ratio showed that the yield of plants was linearly related with evapotranspiration. They later separated the ET from Es in the field and concluded that ET-Es represents transpiration (T). BRIGGS & SHANTZ (1916) observed that transpiration efficiency (TE) was low when atmospheric evaporative demand was high. MORISON & GIFFORD (1983) later showed that TE was linearly related to vapour pressure deficit (VPD), which is defined as the difference between saturated vapour pressure, $e*$, and actual vapour pressure, e, at same temperature. VPD is proposed as the most appropriate field measure of the evaporative demand because it approximates the gradient in vapour concentration between saturated leaf mesophyll and the atmosphere (MORISON & GIFFORD 1983). Because the value of $e*$-e can vary greatly throughout the season, the above equation should be evaluated at short intervals, such as a day or week, if it is used to predict growth. In this study $e*$- e is presented as mean value for the daylight hours. Similarly, the findings of MORISON & GIFFORD (1983 and TURNER & JONES 1981) showed that the relation between growth of a given crop and water use (expressed as transpiration) varied between seasons and environments. For example, in potatoes TURNER (1981) reported a linear relationship between transpiration and dry matter production. However, the slope of this relation, the transpiration efficiency (TE), was found to vary, showing a scatter with season and environmental conditions (TURNER & JONES 1981, GREGORY 1988). Also, PILBEAM *et al.* (1995) reported a linear relationship between dry matter production and normalised (by the average seasonal vapour pressure deficit) transpiration in maize and beans grown in semi-arid Kenya.

SINCLAIR *et al*. (1984) showed how climate can influence the TE of crops. In particular, they, together with GREGORY (1988) and GREGORY & SIMMONDS (1992), showed that a strong correlation exists between biomass production and normalised transpiration (ratio of actual transpiration to the vapour pressure deficit of the air). In practice, if the influence of the VPD regime on transpiration is accounted for, the scatter shown by TE will be reduced to a single linear relation, with a constant slope, κ (kPa). In potatoes, however, the value of κ (normalized TE) has been found to vary considerably from 15 Pa (RIJTEMA & ENDRODI 1970) to 55-65 Pa (TURNER 1981), and to 15-26 Pa (TREBEJO & MIDMORE 1990). These differences were attributed primarily to: the methodology used to calculate VPD (TURNER 1981); errors in assuming leaf temperature to be close to air temperature (TREBEJO & MIDMORE 1990); and to changes in maintenance respiration. In maize and wheat

the value of κ has been found to vary little. For example, OGOLA *et al*. (2002) found k values of 8.4-10.5 Pa in Kenya, 9.1 Pa in Bushland USA (HOWELL *et al.* 1998) and 11.8 Pa while RICHARDS *et al.* (2002) found k values of 5-8.2 Pa in wheat. However, PILBEAM *et al*. (1995) found a much lower value of κ (5.4 Pa) for maize grown in semi-arid Kenya. The slight variation in the value of normalised TE in maize could also be attributed to the different methods used to calculate VPD (TURNER 1981), errors in assuming leaf temperature to be close to air temperature (TREBEJO & MIDMORE 1990), and possibly to changes in maintenance respiration.

In spite of these shortcomings, the value of κ (normalised TE) is still considered to be fairly constant for any given crop (OGOLLA *et al*. 2002, PILBEAM *et al*. 1995). It is thus possible to estimate TE for a given crop and environment provided that mean seasonal VPD for that particular site can be determined and normalised TE has been obtained for a given location. More recently OGOLA *et al.* (2002) predicted yield of maize at Katumani Kenya using data evapotranspiration and TE obtained from studies in UK using a conceptual model. The same concept will be used in this study to predict yield of wheat in the same site using data obtained from Rain shelter (Figure 2) located at Njoro, Kenya. This principle will be used in this paper to attempt to estimate productivity of a wheat crop grown in semi-arid Kenya. The ETa obtained from rain shelter and TE obtained from literature with same conditions, as current location will be normalised using seasonal VPD and used to develop crop simulation model. The VPD was calculated for hourly intervals from the saturated vapour pressure at temperatures interpolated from daily maximum and minimum and from the vapour pressure measured in a standard Meteorological screen at Katumani local recording time of 0900 hrs.

3 Method

The response of yield to water supply is quantified through the yield response factor (Ky) which relates relative yield decrease (1-Ya/Ym) to relative evapotranspiration deficit (1-ETa/ETm). Water deficit of a given magnitude, expressed in the ratio of actual evapotranspiration (ETa) and maximum evapotranspiration (ETm), may either occur continuously over the total growing period of the crop or it may occur during any one of the individual growth periods, i.e. establishment, vegetative, flowering, yield formation, or ripening period. The magnitude of water deficit refers in the former to the deficit in relation to crop water requirements over the total growing period of the crop and in the latter to the deficit in relation to the crop water requirements of the individual growth period (FAO 1986).

The ky values for most crops are derived on the assumption that the relationship between relative yield (Ya/Ym) and relative evapotranspiration (ETa/ETm) is linear and is valid for water deficits of up to about 50 % or 1-ETa/ETm = 0.5. This value of ky for wheat is 1.22 for the total growing period and is based on an analysis of experimental field data covering

a wide range of growing conditions, with high-producing varieties, well-adapted to the growing environment and grown under a high level of crop management (FAO 1998). The yield response factor will be used in this case to estimate actual grain yield and consequently total above-ground biomass. The amount of water transpired by the crop (and hence E_{sc}) will then be estimated from the relationship between normalised TE (using seasonal VPD) and total dry matter yield.

3.1 Model Input Variables, Calculations and Assumptions

It is assumed that planting was done on 29th October 2001 and 25th Oct 2002 respectively and 50% crop emergence was recorded on 5th November and 1st Nov respectively. Final harvesting (crop maturity) was done on 27th 2001 and 20th February 2002 (90DAE).

The major inputs of the model were:

1. Reference evapotranspiration representing the mean value in mm day^{-1} was obtained by:

   $$ETo = k_{pan} * E_{pan} \quad (2)$$

   Where E_{pan} is evaporation in mm day^{-1} from an unscreened class A evaporation pan (obtained from the automatic weather station at Katumani between Oct-Feb growing period), and k_{pan} is pan coefficient which was estimated to be 0.8 for the site and period considered here (FAO, 1986).

2. Maximum evapotranspiration (ETm) was calculated from the relationship

   $$ETm = kc.ETo \quad (3)$$

   Where kc is an empirically-determined crop coefficient and ETo is the reference evapotranspiration (evaporative demand of the atmosphere). For most crops, the kc value increases from a low value at time of crop emergence to a maximum value during the period when the crop reaches full development, and declines as the crop matures. The kc for different growth stages of wheat is: crop establishment 0.25-0.45 (10-20 days), the development stage 0.7-0.80 (25-35 days), the mid-season stage 1.05-1.2 (45-55 days), and during the late season stage 0.8-0.9 (20-40 days) (FAO 1985a, FAO 1998). The kc values used in this study are 0.35, 0.75, 1.1, and 0.45, for crop establishment, development stage, mid-season stage, and late season stage respectively.

3. Actual evapotranspiration (ETa) was estimated from the soil water balance equation measured using Neutron probe under rain shelter at Njoro as:

   $$ETa = -\Delta S + P - D - R \quad (4)$$

Where ∆S is the change in storage, P is precipitation, D is drainage, and R is runoff. Drainage was assumed to be negligible. Runoff was obtained from the equation:

$$R = 0.482*P - 4.640 \quad (5)$$

This equation relating runoff to precipitation was developed from a tilled plot of maize and sorghum in semi-arid Kenya and India (RAO *et al*. 1998, OGOLA *et al*. 2002, KARI 1999) that had the same soil type as that under consideration in this study. The ETa values were divided into 4 growth stages as described above (establishment, development, mid-season and late season respectively).

4. Maximum yield (Ym) of the wheat genotype considered for genotype Chozi under ideal conditions is 5 t ha^{-1} (KINYUA *et al.* 2002, KARI 2003).
5. Actual grain yield (Ya) was obtained from the relationship:

$$(1-Ya/Ym) = ky*(1-ETa/ETm), \quad (6)$$

Where ky is the yield response factor of 1.2 (FAO 1986)

6. Total above-ground biomass (DM) was obtained from the relationship:

$$HI = GY/DM, \quad (7)$$

Where HI is harvest index, and a value of 0.45 was used as obtained in various CIMMYT varieties between 1962-1986 and other related studies (REYNOLDS *et al.* 2002), and GY is grain yield to be predicted.

7. The transpiration efficiency (TE) reported in literature ranged between 6.2 to 9.7 (REYNOLDS *et al.* 2002, CARLOS & PINTO 1998, FAO 1998, GODWIN & ALLEN 1991). Mean TE of 7.8 Pa will be used in the study.
8. Mean seasonal VPD (kPa) as suggested by and SINCLAIR *et al.* (1984) was calculated as difference between the saturated VPD of the air and actual VPD using daily maximum and minimum temperature and daily maximum and minimum RH following earlier procedure (FAO 998). VPD obtained from Katumani during the growing season was used to normalise measured ETa and TE. Several authors working in similar conditions like Katumani, in the UK, Bushland US, Australia, Syria and have reported seasonal VPD ranging between 0.66 to 1.8 kpa (TURNER & JONES 1981 and HOWELL *et al*. 1998). The values to be used for 2001, 2002, 2003 and 2004 are 1.3, 1.01, 0.87 and 1.12, respectively (KARI 2004).
9. Transpiration was estimated from the relationship between total dry matter production and normalised TE (7.8 Pa) as expressed below:

$$TE=DM/T, \quad (8)$$

T is transpiration (mm).

10. Direct evaporation from soil beneath the crop canopy (E_{sc}) was obtained by assuming that the two components of ET are independent and additive, hence if any two terms are known then the third can be determined by difference:

$$T = ET - E_{sc} \quad (9)$$

4 Results and Discussion

Calculation of crop water need; Crop stages were divided into 4 stages (15 days-initial stage; 25days-crop development; 50days-Mid-stage and 30days-late season) (FAO 1998). The initial stage, crop development, mid-stage and late season stage respectively covered Nov, Nov-Dec, Dec and Jan-Feb for year 2001 and 2002 and while 2003 and 2004 covered April-May, May-Jun, July and August respectively as shown by calculations. Actual evapotranspiration (ETa) of cultivar Chozi measured at rain shelter under low, medium and high moisture are 97.9, 132 and 164.8mm respectively. These values were normalized before using in the simulation with VPD (kPa) of Katumani, which were 1.3, 1.01, and 0.87 for 2001, 2002, 2003 and 2004 respectively. Maximum evapotranspiration (ETm) was calculated from sum total of crop coefficient (Kc) for 4 stages; crop establishment 0.35 for 15 days, the development stage 0.75 for 25days, the mid-season stage 1.15 for 50 days and 0.45 for 30days during the late season stage 0.8-0.9 (20-40 days) (FAO 1998). In 2001 for example, HI used was 0.45 resulting in DM of 4163 kg/ha (HI=Ya/DM) and actual harvested yield of 1315 tons/ha. If Low moisture ETa is used in the prediction, then yield for 2001, 2002, 2003 and 2004 were 1112.5, 1297, 1196 and 1534 Kg/ while actual yield were 1315, 1754, 1129nand 896 kg/ha respectively. This shows that using low moisture regime to calculate ETa would be more reliable as shown in **Figure 3** than medium and high ETa (**Figure 4-6**). Transpiration was obtained using equation TE=DM/T and normalized using VPD, resulting in approximately 41.2 mm of water transpired through the plant

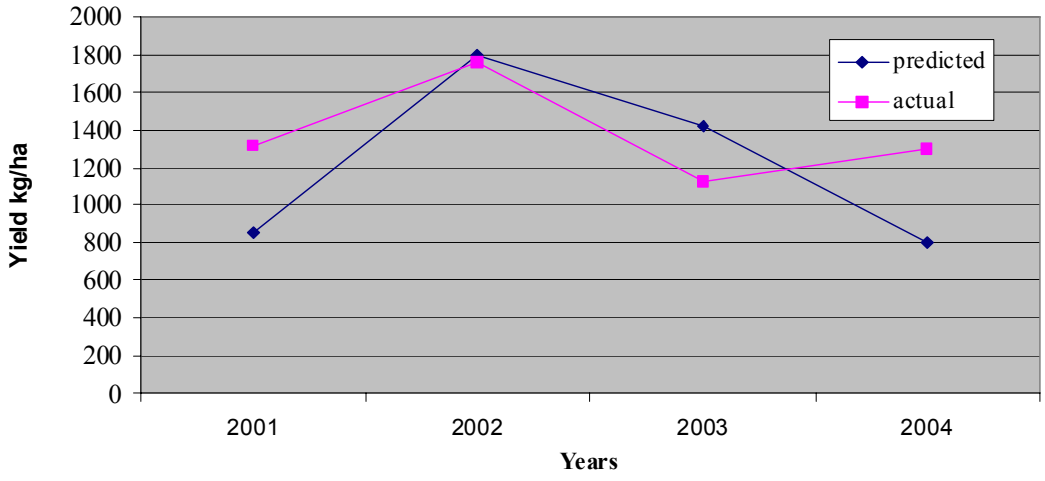

Figure 3: Predicted and actual yield oytest genoytpe under low Eta

in 2001. Direct evaporation from soil beneath the crop canopy (E_{sc})=ET-T, resulting in about 109.8 mm lost through surface evaporation. The results obtained from this conceptual model compare very well with results from actual field experiments conducted at the same site and other semi-arid areas of Kenya. This is in agreement with reports on usefulness of crop models elsewhere (RITCHIE 1991, RITCHIE & OTTER 1985).

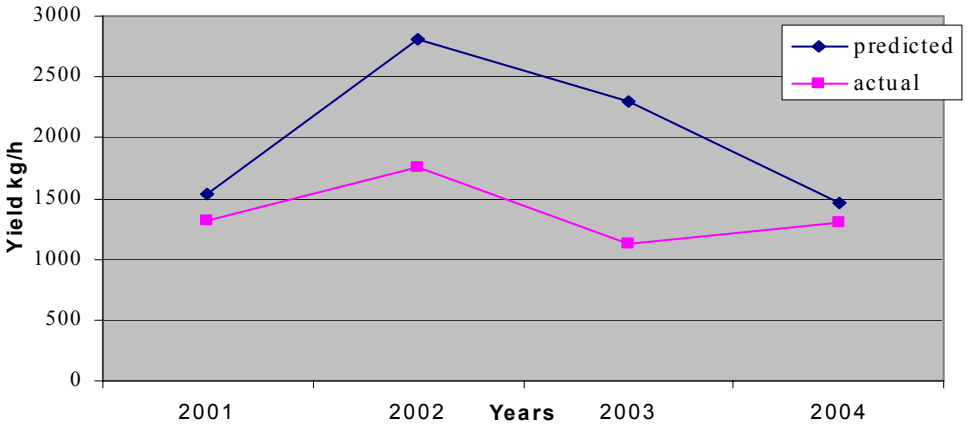

Figure 4: Predicted and actual yield of test genotype under medium Eta

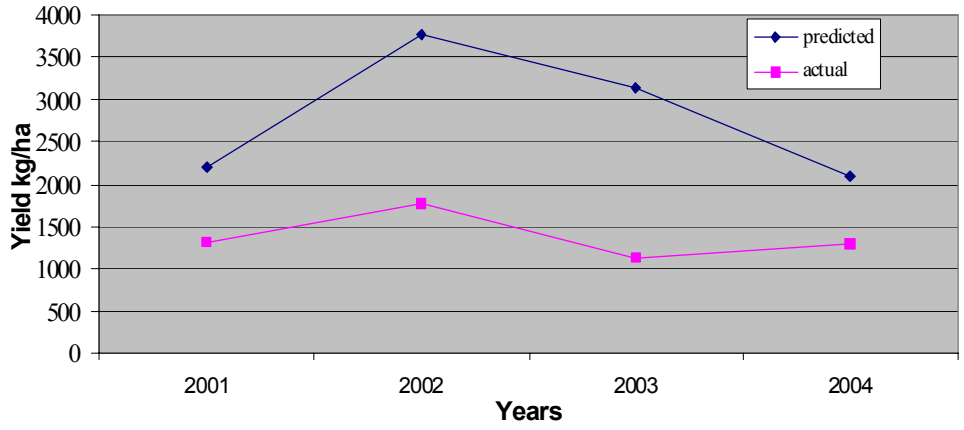

Figure 5: Predicted and actual yield of test genotype under high ETa

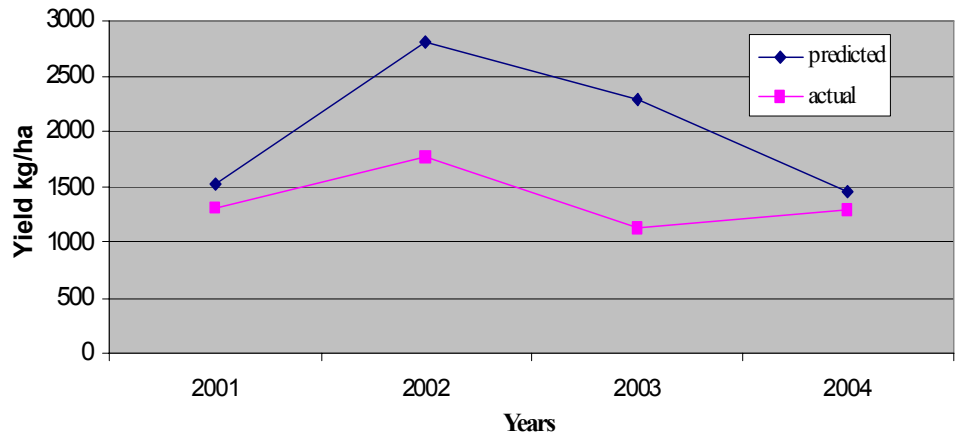

Figure 6: Mean yields of predicted and actual yield of test genotype

Table 2: Results of derived values of ETa, ETo, and predicted ad actual yield for variety Chozi in Katumani, Kenya for 4 years (2001-2004)

Year	Year 2001						
Month	ETo (mm)	Crop coefficient	ETm (mm)	Normalized ETa (ETa*vpd)	Normalized TE (kPa) (TE*vpd)	Predicted Yield (kg/ha)	Actual Yield Kg/ha
Nov	0.8*126.1=100.88	0.35*15/30+10/30*0.75=0.42	0.29* 100.88=42.8	127.3	10.14	857.7	1315
Dec	0.8*127.6mm=102.1	0.75*15/30+15/30*1.15=0.9	0.95*102.08=96.9	171.6		1538.9	
Jan	0.8*127.6mm=102.1	30/30*1.15=1.15	1.15*118.6=136.3	214.2		2194.7	
Feb	0.8*179mm=143.2	5/30*1.15+22/30*0.405=0.52	0.52*143.2=74.7				
Total/ Mean	**464.72 mm**		**350.8**	**171.0**		**1530.2**	**1315**
			Year 2002				
Nov	0.8*144=115.2	0.35*15/30+15/30*0.75=0.55	0.55*115.2=63.36	98.8	7.78	1796.5	1754.8
Dec	0.8*188=150.4	10/30*0.75+20/30*1.15=1.02	1.02*150.4=152.9	133.33		2805.5	
Jan	0.8*31.6=25.28	30/30*1.15=1.15	1.15*25.28=29.1	166.4		3775.9	
Feb	0.8*17.2=13.74	30/30*0.45=0.45	1.15*25.28=29.1				
			13.74*0.45=6.2				
Total/ Mean	**304.64**		**251.5**	**132.8**	**7.78**	**2792.7**	**1754.8**
			Year 2003				
April	0.8*151.3=121.04	0.35*15/30+10/30*0.75=0.43	0.43*121.04=51.4				
May	0.8*107.8=86.24	0.75*15/30+15/30*1.15=0.95	0.95*86.24=81.92	85.17	6.79	1416.4	1125.9
June	0.8*52=41.6	1.15*30/30=1.15	1.15*41.6=47.84	114.84		2293.0	
July	0.8*97.5=78	1.15*5/30+25/30*0.45=0.49	0.49*78=38.35	143.37		3136.1	
Aug.	0.8*110.8=88.64	5/30*0.45=0.15	0.15*88.64=6.6				
Total/ Mean	**415.5**		**216.4**		**6.79**	**2281.8**	**1125.9**
			Year 2004				
			0.35*117.04=44.2				
April	0.8*147..3=117.84	0.35*15/30+10/30*0.75=0.35	0.95*99.24=109.35	85.17	8.74	800.9	1296.1
May	0.8*107.8=99.04	0.75*15/30+15/30*1.15=0.75	1.15*47.6=67.85	114.84		1462.4	
June	0.8*52=47.2	1.15*30/30=1.15	0.49*74=41.6	143.37		2099.1	
July	0.8*97.5=74	1.15*5/30+25/30*0.45=0.45	0.15*96.6=54.35				
Aug.	0.8*110.8=96.6	5/30*0.45=0.45					
	434.72		**317.38**	**147.56**	**8.74**	**1453.9**	**1296.1**

Seasonal rainfall received during that period was 306, 398, 335 and 264 mm, which correlates with grain yield obtained. The results presented are based on the assumption that all agronomic conditions like weed control, disease and fertilizer levels were optimal. The predicted biomass and yield were however, higher than the actual or observed yield, from this study especially when moisture supply in increased (medium and high ETa). The high predicted values from medium and high ETa from the rainshelter, could be used to predict wheat productivity in other sites like Naivasha, Narok and other areas which are wetter than Katumani. However the discrepancy may be attributed to at least in part, to the high

irradiances characteristic of the region which may lead to photo inhibition and hence a reduction in photosynthetic efficiency and dry matter production as reported earlier elsewhere (JONES & KINIRY 1986). Similarly the presence of uncontrolled factors in the trials like pest, weeds and disease damage, soil-limiting factors, and micronutrient deficiencies, not accounted for in the estimation and could have contributed to decrease in observed yield as earlier reported elsewhere (JONES *et al*. 1986, ASADI & CLEMENTE 2001 and THORNTON *et al*. 1995). The water budget was also well predicted by the model in all the seasons (Table 2). For example in 2001, the total crop ET was 151 mm, out of which only 42 mm (27%) was transpired by the plant and the rest 109 mm (72%) was lost as E_{sc}. Of the total rainfall received (306mm) (Table 1), crop evapotranspiration (ETa) represented about 49%, with transpiration accounting for about 13% and E_{sc} representing 35%. Similar variation was also observed in 2002, 2003 and 2004 growing seasons. These results show that to improve wheat production in such regions, measures that conserve water and/or making more water available to the crop may be of more importance. Such measures may include prevention or minimisation of run-off, and rain water harvesting to be used for supplemental irrigation. Also developing and sowing varieties with higher early season biomass accumulation to utilize the initial available moisture may be desirable. This will reduce Esc and increase transpiration.

5 Conclusion

The results presented suggested that this simple conceptual model having developed with evapotraspiration (ETa) obtained from rain shelter experiments and calibrated and evaluated with weather variables, performed adequately well for tested location in Katumani, Kenya. It's possible to apply with confidence this model to predict the productivity of bread wheat in semi-arid areas of Kenya. But further work is needed to improve the accuracy and capability of the model by adding more biotic (disease, weeds) and abiotic (radiation, temperature) conditions and other factors affecting growth of the crop. Also the model should be tested and validated with data from other areas with more cooler and drier weather conditions, soil conditions and cultivars with varied yield potential. The comparison between observed and simulated results over the three moisture regimes (ETa) and four growing years showed that the model could be applicable in simulating yields in continuous runs and therefore it can reduce the costs of travelling and time spend in carrying out dryland research.

References

ASADI M.E., CLEMENTE R.S. (2001): Simulation of maize yield and nitrogen uptake under tropical conditions with CERES-Maize model. *Tropical Agriculture (Trinidad),* 78 (4): 211-217

ASHRAF M., BOKHARI H., CRISTITI S.N. (1992): Variation in osmotic adjustments of lentil *(Lens Culimaris medic*) in response to drought. *Acta Botania Neerlandica* 41: 51-62

BRIGGS L.J., SHANTZ, H.L. (1913): The water requirement of plants. II. A review of the literature. *US Department of Agriculture Bureau. Plant Bulletin* 285: 1-96

BLUM A. (1996): Crop responses to drought and the interpretation of adaptation. *Plant Growth Regulation* 20: 135-148

CARLOS P.C., PINTO P.A. (1998): Linking DSSAT V3 to a relational database the AGROSYS-DSSAT interface, *Computers And Electronics In Agriculture* (21)1*,* pp. 69

FAO (1995a): *Irrigation in Africa in figures*, FAO Water Report 7, Rome, Italy

FAO (2004): FAO quarterly bulletin of statisitcs Vol. 3 No. 3. Food and Agriculture Organisation of the United Nations, Rome, Italy

FAO (1986): Yield response to water. *FAO Irrigation and Drainage Paper 33*

FAO (1998): *Crop evapotrans piration - Guidelines for computing crop water requirements*, Allen, R.G., L.S. Pereira, D. Raes and M. Smith (Eds.), FAO Irrigation and Drainage Paper 56, Rome, Italy

GODWIN D.C., ALLEN J. (1991): Nitrogen dynamics in soil-plant systems. pp. 287-322. In J. HANKS and J.T. RITCHIE (eds.) Modelling plant and soil systems. *Agron. Monogr. 31*. ASA, CSSA, and SSSA, Madison, Wisconsin

GREGORY P.J. (1988): Water and crop growth. In. Russel's Soil Conditions and Plant Growth, 338-377. (Ed A. Wild). Longman Group UK Ltd. 11th edition

GREGORY P.J., SIMMONDS L.P. (1992): Water relations and growth of potatoes. In. The Potato Crop. The Scientific Basis for Improvement. 214-246. (Ed. P.M. HARRIS). London: Chapman & Hall. 2nd edition

HOWELL T.A., TOLK J.A., SCHNEIDER A.D., EVETT S.R. (1998): Evapotranspiration, yield, and water use efficiency of corn hybrids differing in maturity. *Agronomy Journal* 90: 3-9

JONES C.A., KINIRY J.R. (1986): CERES-Maize: A simulation model of maize growth and development. Texas A&M University Press, College Station

JONES J.W., MISHOE K.J., WILKERSON G.G., JAGTAP S.S. (1986): SOYGRO v. 5.3: Soybean crop growth and yield model,IBSNAT version. Technical documentation, University of Florida, Gainesville

KARI (1994, 1999, 2002, 2004): Kenya Agricultural Research Institute Annual Report. KARI, Nairobi, Kenya

KEATING B.A., SIAMBI J.K., WAFULA B.M. (1992): The impact of climatic variability on cropping research in semi-arid Kenya between 1955 and 1985. In: ACIAR Proceedings 1992. Search for strategies for sustainable dryland cropping in semi-arid eastern Kenya. pp 16-25, No. 41

KIMURTO P.K., KINYUA M.G., NJOROGE J.M. (2003): Response of bread wheat genotypes to drought simulation under a mobile rain shelter in Kenya. *African Crop Sci. .Journal* 11: 16-25

KINYUA M.G., OTUKHO B., ABDALLA O.S. (2000): Developing wheat varieties for the drought-prone areas of Kenya: 1996-1999 In: CIMMYT. 2000. The 11th Regional wheat workshop for Eastern, Central and Southern Africa. Addis Ababa, Ethiopia, CIMMYT

MINISTRY OF ECONOMIC PLANNING (various issues) (2002-2005): National Development Plan. Government Printers, Nairobi, Kenya

MORISON J., GIFFORD R.M. (1983): Stomatal sensitivity to carbon dioxide and humidity. *Plant Physiology* 71: 789-796

OGOLA J.B.O., WHEELER T.R., HARRIS P.M. (2002): Water use of maize in response to planting density and irrigation. *Field Crops Research* 12: 24-33

OTTER N.S., GODWIN D.C., RITCHIE J.T. (1986): Testing and validating the CERES-Wheat Model in diverse environments, AgRISTARS YM-15-00407, 146 pp

PAZ J.O., BATCHER W.D., BABCOCK B.A., COLVIN T.S., LOGSDON S.D., KASPAR T.C., KARLEN D.L. (1999): Model based techniques to determine variable rate nitrogen for corn. Agric syst 61: 69-75

PILBEAM C.J., SIMMONDS L.P., KAVILU A.W. (1995): Transpiration efficiencies of maize and beans in semi-arid Kenya. *Field Crops Research* 41: 61-69

RAO K.P.C., STEENHUIS T.S., COGLE A.L., SRINIVASAN S.T., YULE D.F., SMITH G.D. (1998): Rainfall infiltration and runoff from an alfisol in semi-arid tropical India. II. Tilled sytems. *Soil and Tillage Research* 48: 61-69

REYNOLDS M.P., NAGARAJAN S., RAZZQUE M.A., AGEEB O.A.A. (2001): Heat tolerance In: REYNOLDS M.P., ORTIZ-MONASTERIO J.I. and MCNABS A. (eds.). Application of Physiology in wheat Breeding. Mexico, D.F.: CIMMYT

REYNOLDS M.P., TRETHOWAN R., CROSSA J., VARGAS M., SAYRE K.D. (2002): Physiological factors associated with genotype and environment interaction in wheat. *Field Crops Research* 75. (2/3): 139-160

RIJTEMA P.E., ENDRODI G. (1970): Calculation of production of potatoes. *Netherlands Journal of Agricultural Science* 18: 26-36

RICHARDS R.A., REBETZKE G.J., CONDON A.G., VAN HERWAARDEN A.F. (2002): Breeding opportunities for increasing the efficiency of water use and crop yield in temperate cereals. *Crop Sci.* 42: 111-121

RITCHIE J.T. (1991): Wheat phasic development. pp. 31-54. In J. Hanks and J.T. Ritchie (eds.) Modeling plant and soil systems. Agron. Monogr. 31. ASA, CSSA, and SSSA, Madison, WI

RITCHIE J.T. (1995): International consortium for agric systems applications (ICASA); Establishment and purpose, Agrl systems 49: 329-335

RITCHIE J.T., OTTER N.S. (1985): Description and performance of CERES-Wheat: A user-oriented wheat yield model, USDA-ARS, ARS-38, pp. 159-175

SINCLAIR T.R., TURNER C.B., BENNETT J.M. (1984): Water use efficiency in crop production. *Bioscience* 34: 40-60

THORNTON P.K., SAKA A.R., SINGH U., KUMWENDA J.D.T., BRINK J., DENT J.B. (1995): Application of a maize crop simulation model in Central region of Malawi, Expt Agric 31: 213-226

TREBEJO I., MIDMORE D.J. (1990): Effects of water stress on potato growth, yield and water use in a hot and cool tropical climate. *Journal of Agricultural Science*, *Cambridge* 114: 321-334

TURNER N.C., JONES M.M. (1981): Turgor maintenance by osmotic adjustments: A revie and evaluation. In TURNER N.C and KRAMER P.J. (eds). Adaptation of plants to water and high temperature stress. New York. Wiley and Sons : 87-104

TURNER N.C. (2001): Optimizing water use. In: NOSBERGER J., GEIGER H.H. and STRUIK P.C. (eds.). Crop Science Congress Proceedings, Australia. CAB International

TURNER C.B. (1981): Transpiration efficiency of potato. *Agronomy Journal* 73: 56-74

Mathematical Model of Mixed-Flow Grain Drying, Experimental Validation and Concept of a Model-Based Control

J. Mellmann, I.-G. Richter and W. Maltry
Department of Post Harvest Technology
Leibniz Institut für Agrartechnik Potsdam-Bornim (ATB)
Max-Eyth-Allee 100, Potsdam, D-14469, Germany
Tel.:+49 331 5699321, E-Mail: jmellmann@atb-potsdam.de

Abstract: *Farmers in Central Europe succeed to harvest the grain dry for the most part but still about 1/3 of it must be dried. Although mixed-flow dryers are widely used for hot-air grain drying there is still a need to optimize the process control as well as the dryer apparatus. For instance, fluctuations of the grain moisture content at the dryer entrance are still a major problem resulting in quality and economic losses due to under-drying or over-drying. Therefore, the objective of this work is to develop a mathematical model for heat and mass transfer in a mixed-flow dryer. It is applied to a new model-based control system which shall enable the operator to equalize the fluctuations of the moisture content of the dried grain and, hence, to reduce losses and to save quality. To validate the model a semi-technical dryer test station was constructed and practical drying experiments have been carried out the results of which are presented.*

Keywords: *grain drying, mixed-flow dryer, mathematical model, experiments, control*

1 Introduction

Mixed-flow dryers are the most popular continuous hot-air grain dryers in Europe and are also widely used in North and South America. With it large mass flows of grain, rice, and maize are preserved. The dryer capacity can reach up to 100 tons per hour. The mixed-flow dryer consists of a vertical shaft through which the grain flows down by gravity. It is charged at the top and the grain mass flow is controlled by a discharge device at the bottom. Rows of ducts are located in the dryer shaft through which air is supplied to and removed from the moving grain bed. The ducts are mainly located in horizontal planes such that every inlet air duct is surrounded by four exit air ducts and vice versa. Due to its design the mixed-flow dryer provides a more uniform thermal treatment to the grain than does a cross-flow dryer. Because of its importance the mixed-flow dryer was a matter of research in many papers so far, e. g. MALTRY (1966), BRUCE (1984), MCFARLANE & BRUCE (1991), BROOKER *et al.* (1992), NELLIST & BRUCE (1995), and GINER *et al.* (1998). Recent publications on the modelling of hot-air grain drying are mainly concerned with other types of dryers and single kernel drying; see for example RUMSEY & ROVEDO (2001), SITOMPUL *et al.* (2003), and WU *et al*. (2004).

2 Mathematical model

In a mixed-flow dryer air and grain are guided through the dryer shaft in co-current, counter-current and cross flow modes at the same time (PABIS *et al.* 1998). To calculate this complex drying process a mathematical model of the coupled heat and mass transfer has been developed consisting of two parts: a thin-layer drying model for the heat and mass transfer within a single grain kernel (single grain model) and a drying model for the bed material (deep-bed model). For the single grain model it is assumed that the grain has the shape of a sphere which can be subdivided into up to ten shells. The differential equations of air flow and grain flow are coupled in the deep-bed model. The differential equation system obtained is solved using a difference technique.

Industrial mixed-flow dryers often work in a quasi-stationary record-by-record mode of operation. In this case, the grain is at rest during almost the whole drying time. The standing time between two discharges may reach several minutes whereas the discharge time – the period of time at which the discharge device is opened – amounts to few seconds. The grain is transported stepwise downwards the dryer shaft. At each discharge it is assumed that the grain bed moves in plug flow pattern. During the standing time the drying process can be considered as unsteady batch drying. The bed material is assumed to be a connection in series of single grain layers the drying behaviour of which is described by means of a single grain model (FARKAS & RENDIK 1996, ZIEGLER 1999). In this way the exit air of a certain layer is the inlet air of the next layer and so on. Therefore, the drying process in a mixed-flow dryer can be described as follows:

1. Modelling of the drying behaviour of a single grain layer by heat and mass transfer in a single grain kernel,
2. Modelling the drying process of the grain bed using a connection in series of single grain layers.

The mathematical model and the differential equation system for the heat and mass transfer between air and grain obtained are further described in MELLMANN *et al.* (2005) and (2006).

3 Experimental validation

To validate the mathematical model a semi-technical test station of a mixed-flow dryer has been constructed, see **Figure 1**. For the drying experiments a quasi-stationary record-by-record operation was chosen. As drying bed material charges of farm-fresh wheat with initial moisture contents of 20% w. b. and 16% w. b. were used. The mass flow rate of dried grain varied between 100 kg/h and 200 kg/h. The drying air temperatures employed were 60°C and 70°C. The volume flow rate of the drying air was held constant corresponding to an air velocity within the void fraction of the grain bed of about 0.25 m/s. The standing time of the dryer was fixed to 5 minutes whereas the discharge time amounted to a few seconds depending on the grain mass flow rate. For

example, to achieve a grain mass flow rate of 200 kg/h a grain mass of 16.7 kg per discharge has been adjusted according to the feed characteristic of the slide bottom.

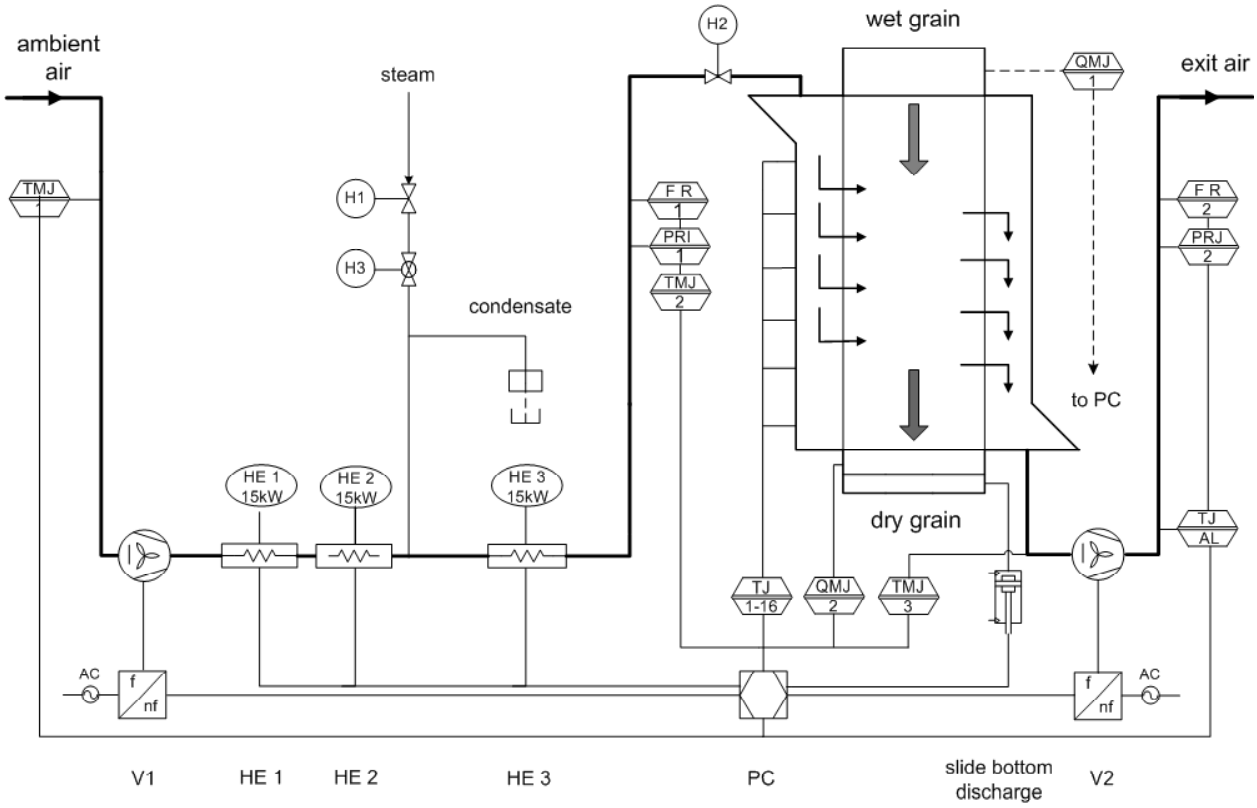

Figure 1: Flow sheet of the mixed-flow dryer test station

In **Figure 2a** the inlet and outlet grain moisture contents are depicted in dependence on the drying time. The inlet m. c. was measured by a grain moisture immediate-measuring system (Granomat, Pfeuffer) based on an infrared analyzer. The outlet m. c. was continuously detected with a microwave moisture sensor (TRIME-GW, Imko) based on the time-domain-reflectometry.

The experiment was started with dry grain bed material used as initial dryer filling. Therefore, the outlet m. c. measured at the beginning (at 09:40 the discharge system was started) is at a low level of about 10.8% w. b. After it, the outlet m. c. decreases displaying that the initial dryer filling is over-dried followed by a period of continuous increase. From 11:40 when the moist inlet grain completely replaced the initial dryer filling the moisture content at the dryer discharge reaches an almost constant value of about 12.8% w. b. In **Figure 2b** the measured temperature and relative humidity of the total exit air are shown as a function of the drying time. Both curves steeply increase or decrease from the start, respectively, due to the dry initial bed material passing through the dryer. At about 11:30 the variables attain nearly constant values of 28.4°C and 57.5% r. h., respectively. The exit air temperatures measured inside the dryer shaft in different exit air ducts are depicted in **Figure 2c** versus drying time. The exit air ducts

No. 1, 4, and 7 represent the top section, middle section, and the lower section of the dryer, respectively. From 11:30 all dryer sections are in steady state operation.

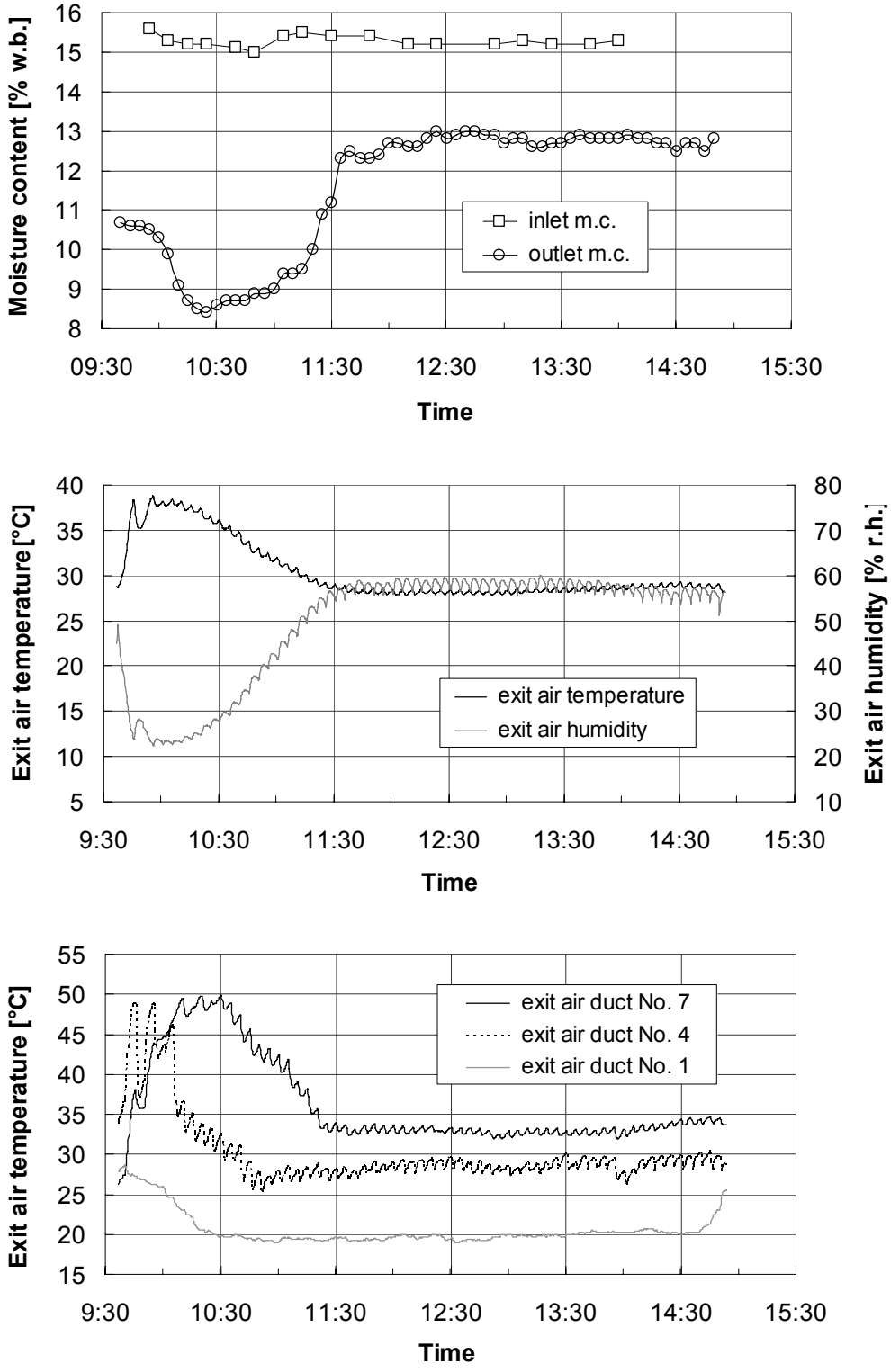

Figure 2: Measured values from drying experiment 7: M_0 = 15.3% w. b., $\dot{M}_G$ = 200 kg/h, ϑ_{Air} = 60°C, φ_{Air} = 5.3% r. h., $w_{Air,\psi}$ = 0.25 m/s. a) Inlet and outlet grain moisture content; b) Temperature and relative humidity of the total exit air; c) Exit air temperatures measured in different air ducts over the height of the dryer

To compare model and experiment measured and predicted grain m. c. at the dryer discharge are shown in **Figure 3** in dependence on drying time. In this experiment moist grain of nearly 15.7% w. b. was used as bed material from the beginning. At 13:25 after a heating-up period of about 2 hours the discharge device was set into operation resulting in a decrease of the moisture content. For the next two hours the unsteady dried initial dryer filling was discharged leading to a strong fluctuation of the grain moisture curve. At about 15:40 the mixed-flow dryer reached stationary operation. As can be seen from the figure, the predicted results are in relative good agreement with the measurements in the stationary operation period. However, existing discrepancies show that the model must be improved.

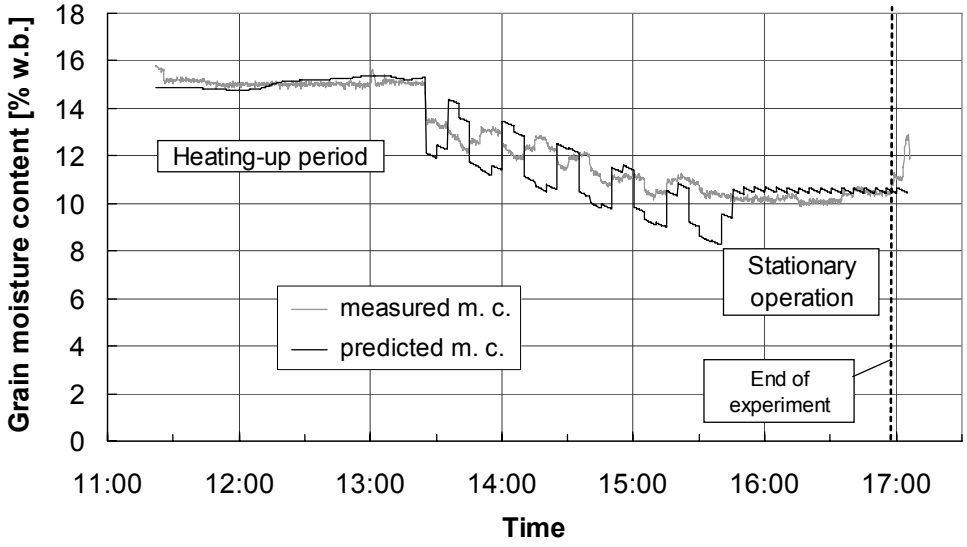

Figure 3: Measured and predicted outlet moisture contents versus drying time for experiment 5: M_0 = 15.7% w.b., $\dot{M}_G$ = 100 kg/h, ϑ_{Air} = 70°C, φ_{Air} = 2.9% r.h., $w_{Air,\psi}$ = 0.25 m/s.

4 Concept of model-based control

The concept of the model-based control system for the mixed-flow grain dryer is shown in **Figure 4**. As can be seen from the figure in model-based control the mathematical model of the drying process (process model) is at the outset part of the controller itself as against other control principles. That's why it is called Internal Model Control (IMC). The process model is connected in parallel to the real control process.

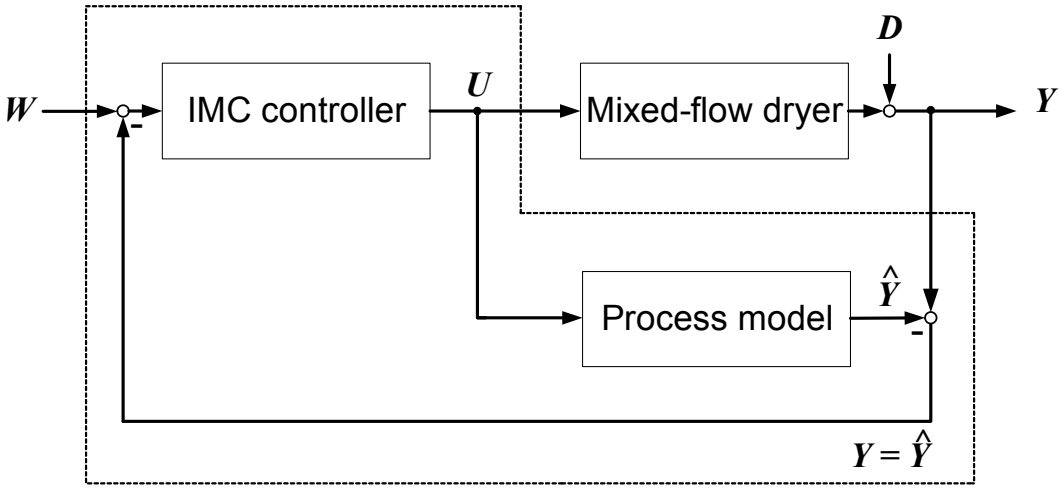

D	disturbance variable	inlet grain moisture content / distribution
U	control variable	grain mass flow rate (discharge device)
W	command variable	target grain moisture content
Y	controlled variable	outlet grain moisture content
Ŷ	predicted controlled variable	

Figure 4: Structure of the Internal Model Control (IMC) system

The IMC control system proposed has not yet been experimentally tested by now. In further investigations drying experiments at the mixed-flow dryer test station (Figure 1) in reversing operation mode are carried out to estimate model parameters and to prove the control system.

5 Conclusions

In order to predict the drying process in a mixed-flow grain dryer a mathematical model of the coupled heat and mass transfer has been developed. To validate the model a semi-technical test station of a mixed-flow dryer has been constructed and a series of quasi-stationary drying experiments in record-by-record operation have been carried out. As the model testing revealed experimental and predicted results are in relative good agreement in the stationary operation period which is relevant for practice. Due to the complexity of the mixed-flow drying process a comparison with other models has been refrained from. However, the model needs refinement in order to more accurately predict unsteady and reversing operation modes which may occur if for instance the inlet grain moisture content is intensely fluctuating or the type of grain, the grain mass flow rate, the air temperature, and other operation variables are changing. Further drying experiments are necessary to prove the model-based control concept.

Acknowledgements

The authors are grateful to the German Federal Ministry for Education and Research for the financial support (BMBF/PTJ Project No. 0339992, TP5558).

References

BROOKER D.B., BAKKER-ARKEMA F.W. AND HALL, C.W. (1992): Drying and Storage of Grains and Oilseeds. Van Nostrand Reinhold, New York

BRUCE D.M. (1984): Simulation of Multiple-Bed Concurrent-, Counter-, and Mixed-Flow Grain Driers. Journal of Agricultural Engineering Research, Vol. 30, pp. 361-372

FARKAS I., RENDIK Z. (1996): Block oriented modeling of drying processes. Mathematics and Computers in Simulation, Vol. 42, pp. 213-219

GINER S.A., BRUCE D.M., MORTIMORE S. (1998): Two-Dimensional Simulation Model of Steady-State Mixed-flow Grain Drying. Part 1 and 2: Journal of Agricultural Engineering Research, Vol. 71, pp. 37-66

MALTRY W. (1966): Einige Untersuchungen zur Aufklärung des Verhaltens von Getreide im Dächer-Schachttrockner. Archiv für Landtechnik, Vol. 5(3), S. 223-264

MCFARLANE N.J.B., BRUCE D.M. (1991): Control of Mixed-flow Grain-driers: Development of a Feedback-plus-Feed forward Algorithm. Journal of Agricultural Engineering Research, Vol. 49, pp. 243-258

MELLMANN,J., RICHTER I.-G., MALTRY W. (2005): Optimierte Steuerung von Getreide-Schachttrocknern. Bornimer Agrartechnische Berichte, No. 52, Leibniz-Institute of Agricultural Engineering Potsdam-Bornim

MELLMANN J., RICHTER I.-G., MALTRY W. (2006): Experiments on hot-air drying of wheat in a semi-technical mixed-flow dryer. 15th International Drying Symposium (IDS), Budapest, Hungary, 20-23 August 2006

NELLIST M.E., BRUCE D.M. (1995): Heated-Air Grain Drying. In: Jayas D.S., White N.D.G., Muir W.E.: Stored-Grain Ecosystems. Marcel Dekker Inc., New York

PABIS S., JAYAS D.S., CENKOWSKI S. (1998): Grain Drying. Wiley & Sons, New York

RUMSEY T.R., ROVEDO C.O. (2001): Two-dimensional simulation model for dynamic cross-flow rice drying. Chemical Engineering and Processing, Vol. 40, pp. 355-362

SITOMPUL J.P., STADI I., SUMARDIONO S. (2003): Modelling and Simulation of Momentum, Heat, and Mass Transfer in a Deep-Bed Grain Dryer. Drying Technology, Vol. 21, pp. 217-229

WU B., YANG W., JIA C. (2004): A Three-dimensional Numerical Simulation of Transient Heat and Mass Transfer inside a Single Rice Kernel during the Drying Process. Biosystems Engineering, Vol. 87, pp. 191-200

ZIEGLER T. (1999): Modellierung und Simulation der solar unterstützten Schüttguttrocknung am Beispiel Weizen. PhD Dissertation, Techn. Univ. Dresden

In der Reihe
Bornimer Agrartechnische Berichte

sind bisher erschienen:

Heft 1	Technik und Verfahren der Landschaftspflege	1992
Heft 2	Beiträge zur Lagerung und Verarbeitung pflanzenbaulicher Produkte	1993
Heft 3	Technik und Verfahren in der Tierhaltung	1993
Heft 4	Technik und Verfahren der Landschaftspflege und für die Verwendung der anfallenden Materialien	1994
Heft 5	Verfahrenstechnik der Aufbereitung, Lagerung und Qualitätserhaltung pflanzlicher Produkte	1994
Heft 6	Biokonversion nachwachsender Rohstoffe und Verfahren für Reststoffbehandlung	1994
Heft 7	Preußische Versuchs- und Forschungsanstalt für Landarbeit und Schlepperprüffeld in Bornim 1927 bis 1945	1995
Heft 8	Qualitätssicherung und Direktvermarktung	1996
Heft 9	Konservierende Bodenbearbeitung auf Sandböden	1996
Heft 10	Anwendung wärme- und strömungstechnischer Grundlagen in der Landwirtschaft	1996
Heft 11	Computer-Bildanalyse in der Landwirtschaft Workshop 1996	1996
Heft 12	Aufbereitung und Verwertung organischer Reststoffe im ländlichen Raum	1996
Heft 13	Wege zur Verbesserung der Kartoffelqualität durch Verminderung der mechanischen Beanspruchung	1997
Heft 14	Computer-Bildanalyse in der Landwirtschaft Workshop 1997	1997
Heft 15	Technische und ökonomische Aspekte der Nutztierhaltung in großen Beständen	1997
Heft 16	11. Arbeitswissenschaftliches Seminar	1997
Heft 17	Nachwachsende Rohstoffe im Land Brandenburg Stand Aktivitäten und Perspektiven einer zukunftsfähigen und umweltgerechten Entwicklung	1998
Heft 18	Qualität von Agrarprodukten	1998
Heft 19	Computer-Bildanalyse in der Landwirtschaft Workshop 1998	1998
Heft 20	Beiträge zur teilflächenspezifischen Bewirtschaftung	1998
Heft 21	Landnutzung im Spiegel der Technikbewertung – Methoden Indikatoren, Fallbeispiele	1998

Heft 22	Kriterien der Nachhaltigkeit in der Verfahrensentwicklung für die Nutztierhaltung	1999
Heft 23	Situation und Trends in der Landtechnik / Erneuerbare Energien in der Landwirtschaft	1999
Heft 24	Institut für Landtechnik der Deutschen Akademie der Landwirtschaftswissenschaften zu Berlin 1951 bis 1965	1999
Heft 25	Computer-Bildanalyse in der Landwirtschaft Workshop 1999 / 2000	2000
Heft 26	Computer-Bildanalyse in der Landwirtschaft Workshop 2001	2001
Heft 27	Approaching Agricultural technology and Economic Development of Central and Eastern Europe	2001
Heft 28	6th International Symposium on Fruit, Nut, and Vegetable Production Engineering	2001
Heft 29	Measurement Systems for Animal Data and their Importance for Herd Management on Dairy Cow Farms	2002
Heft 30	Produktion, Verarbeitung und Anwendung von Naturfasern	2002
Heft 31	Computer-Bildanalyse in der Landwirtschaft Workshop 2002	2002
Heft 32	Biogas und Energielandwirtschaft - Potenzial, Nutzung, Grünes Gas^{TM}, Ökologie und Ökonomie	2003
Heft 33	Sozioökonomische Aspekte zu Perspektiven des Offenlandmanagements	2003
Heft 34	Computer-Bildanalyse in der Landwirtschaft Workshop 2003	2003
Heft 35	Energieholzproduktion in der Landwirtschaft Potenzial, Anbau, Technologie, Ökologie und Ökonomie	2004
Heft 36	High-Tech Innovationen für Verfahrensketten der Agrarproduktion. Statusseminar 2003	2004
Heft 37	Computer-Bildanalyse in der Landwirtschaft Workshop 2004	2004
Heft 38	Die Landmaschinenprüfung in der DDR 1951-1991 und ihre Vorgeschichte	2004
Heft 39	Energieverlust und Schimmelpilzentwicklung bei der Lagerung von Feldholz-Hackgut	2005
Heft 40	Computer-Bildanalyse in der Landwirtschaft Workshop 2005	2005
Heft 41	Demonstration der Langzeitwirkung bedarfsorientierter Fungizidbehandlung mit dem CROP-Meter	2005

Heft 42	Biochemicals and Energy from Sustainable Utilization of herbaceous Biomass (BESUB)	2005
Heft 43	Ozontes Waschwasser zur Qualitätssicherung leichtverderblicher Produkte - Entwicklung einer *Fuzzy-Logic*-Steuerung des Waschprozesses	2005
Heft 44	Messsystem zur Bewertung des Unkrautvorkommens	2005
Heft 45	Anwendung der Thermographie zur Optimierung der Belüftungssteuerung bei der Lagerhaltung landwirtschaftlicher Produkte	2005
Heft 46	Membranbioreaktor zur Aufbereitung von Schlachthofabwässern	
	Prozesssteuerung von Biogasanlagen mit Kofermentation	2005
Heft 47	Verschleißeinfluss auf das Förderverhalten von Drehkolbenpumpen	2005
Heft 48	Qualitätserhaltung und Qualitätssicherung von Bioobst und Biogemüse in der Nachernte	2005
Heft 49	Miniaturisiertes Datenerfassungs-System zum Implantieren in Früchte und zur Messung ihrer mechanischen Belastung durch Ernte- und Nachernteverfahren	2005
Heft 50	Prozesskontrolle der Qualität von frischem Obst und Gemüse mit Hilfe eines Multigas-Sensors	2005
Heft 51	Entwicklung eines Echtzeitsensors für die Stärkebestimmung bei Kartoffeln als funktionaler Bestandteil eines optoelektronischen Verleseautomaten	2005
Heft 52	Optimierte Steuerung von Getreide-Schachttrocknern	2005
Heft 53	Möglichkeiten und Grenzen der energetischen Nutzung von Rizinusöl	2005
Heft 54	Non-Destructive Methods for Detecting Health-Promoting Compounds COST Action 924 Working Group Meeting	2005
Heft 55	Control Applications in Post - Harvest and Processing Technology (CAPPT 2006) 4th IFAC / CIGR Workshop	2006

Interessenten wenden sich an:

Leibniz-Institut für Agrartechnik Potsdam-Bornim e.V.
Max-Eyth-Allee 100
14469 Potsdam

Tel.: (0331) 5699-820
Fax.: (0331) 5699-849
E-Mail: atb@atb-potsdam.de

Schutzgebühr: 13,- €